

INVESTIGATING THE ROLE OF GLYOXAL  
USING SATELLITE AND MAX-DOAS  
MEASUREMENTS

LEONARDO M. A. ALVARADO BONILLA



Dissertation zur Erlangung des Grades  
*Doktor der Naturwissenschaften*

Institut für Umweltphysik  
Fachbereich Physik und Elektrotechnik  
UNIVERSITÄT BREMEN  
Mai 2016





**1. GUTACHTER:** Prof. Dr. John P. Burrows  
**2. GUTACHTER:** Prof. Dr. Mihalis Vrekoussis

**BETREUER:** Dr. Andreas Richter

**DATUM DES KOLLOQUIUMS:** 21. Juni 2016



*Para mi esposa e hija.*



# Abstract

Volatile Organic Compounds (VOC) are key species in tropospheric chemistry, air pollution and climate. The largest fraction of VOC is emitted from natural sources, but significant contributions are also attributed to anthropogenic emissions and vegetation fires. Despite many studies estimating VOC amounts in the atmosphere and identifying their sources, the uncertainties in estimation are large. Glyoxal ( $\text{CHOCHO}$ ), the smallest and most abundant of the alpha-dicarbonyls in the atmosphere, is an intermediate product in the oxidation of most VOC and an indicator of secondary aerosol formation in the atmosphere. Glyoxal in combination with other VOC (e.g. formaldehyde:  $\text{HCHO}$ ) can be used for source identification of VOC. Glyoxal has been measured from space since 2003 by the SCIAMACHY and GOME–2 (MetOp–A) instruments and provides a unique global long-term dataset. The focus of this thesis is to retrieve glyoxal from measurements by the OMI instrument, to improve the SCIAMACHY and GOME–2 (MetOp–A and–B) analysis, and to investigate the resulting long-term datasets.

The first part of this thesis focuses on the development of an improved retrieval for glyoxal from OMI measurements. From sensitivity tests, optimized fit parameters are determined. Two different approaches to reduce the interference of liquid water absorption over oceanic regions are evaluated, achieving a significant reduction of the number of negative columns over clear water regions. The impact of using different absorption cross-sections for water vapour is evaluated and only small differences are found. Finally, a high temperature (boundary layer ambient 294 K) absorption cross-section of nitrogen dioxide ( $\text{NO}_2$ ) is introduced in the DOAS retrieval to account for potential interferences with  $\text{NO}_2$  over regions with large anthropogenic emissions, leading to improved fit quality over

these areas. In a sensitivity test, a spectrum of backscattered solar radiation over the Pacific Ocean is used as a reference spectrum, in order to reduce the offsets (“stripes”) that sometimes are observed between viewing directions in the OMI instrument. The new retrieval has also been applied to measurements from SCIAMACHY and GOME–2 (MetOp–A and–B) instruments.

Using the new CHOCHO dataset, the combination of four instruments provides more than 12 years of glyoxal measurements, which are used for the investigation of the temporal variability of VOC on a global scale. The link between vegetation, fires, anthropogenic activity, and glyoxal columns is investigated both globally and locally. This provides a general picture of where glyoxal comes from and what its temporal behaviour is depending on the region. CHOCHO and HCHO are used synergistically for the identification of VOC emission sources by computing their ratio and correlating it with indicators of biogenic emissions, fires, and anthropogenic activities, giving important information for assigning the ratios of glyoxal to formaldehyde to emission sources of VOC.

In a case study, mapped averages are computed for a fire event in Russia between mid-July and mid-August 2010. Enhanced CHOCHO levels are found in close spatial and temporal proximity to elevated levels of fire radiate power, demonstrating that pyrogenic emissions can be clearly identified in the new CHOCHO data product. Also, for the first time long-range transport of glyoxal in the atmosphere has been clearly identified, where elevated levels of glyoxal follow the trajectories of simulated air masses.

Finally, CHOCHO, HCHO, and NO<sub>2</sub> columns have been retrieved from ground based measurements for two MAX-DOAS stations, which are part of the BRE-DOM network. Diurnal and seasonal variations have been computed for the three species and also the glyoxal to formaldehyde and formaldehyde to nitrogen dioxide ratios. The results have been compared to results from the satellite observations and with other studies.

# Publications

Some parts of this thesis, including figures, tables and text passages, have appeared previously in publications, conference talks or conference posters. Those sections of this thesis that contain such figures, tables and text passages from one of these articles are indicated with an appropriate footnote. Also, the abstract of this thesis is an extended and combined version of the abstracts from those publications.

## Articles

- **Alvarado, L. M. A.**, Richter, A., Vrekoussis, M., Wittrock, F., Hilboll, A., Schreier, S. F., and Burrows, J. P.: Investigating the link between glyoxal and biogenic activities. In Lohmann G., Meggers H., Unnithan V., Wolf-Gladrow D., Notholt J., and Bracher A. (Eds.), Towards an Interdisciplinary Approach in Earth System Science, Springer International Publishing, pp. 59–65, doi:10.1007/978-3-319-13865-7\_25, 2015
- Peters, E., Wittrock, F., Richter, A., **Alvarado, L. M. A.**, Rozanov, V. V., and Burrows, J. P.: Liquid water absorption and scattering effects in DOAS retrievals over oceans, *Atmos. Meas. Tech.*, 7, 4203-4221, doi:10.5194/amt-7-4203-2014, 2014
- **Alvarado, L. M. A.**, Richter, A., Vrekoussis, M., Wittrock, F., Hilboll, A., Schreier, S. F., and Burrows, J. P.: An improved glyoxal retrieval from OMI measurements, *Atmos. Meas. Tech.*, 7, 4133-4150, doi:10.5194/amt-7-4133-2014, 2014

## Selected presentations

- **Alvarado, L. M. A.**, Richter, A., Vrekoussis, M., Wittrock, F., Schreier, S. F., and Burrows, J. P.: Investigating the temporal variation of VOC using a homogenized glyoxal retrieval for different satellite platforms. Presented at the *7th International DOAS Workshop*, Brussels, Belgium, July 2015
- **Alvarado, L. M. A.**, Richter, A., Vrekoussis, M., Wittrock, F., Schreier, S. F., and Burrows, J. P.: What can we learn from glyoxal. Presented at the *Helmholtz Research School on Earth System Science Retreat*, Bremerhaven, Germany, November 2014
- **Alvarado, L. M. A.**, Richter, A., Peters, E., Wittrock, F., Burrows, J. P., Vrekoussis, M., Gratsea, M., Gerasopoulou E.: MAX-DOAS observation of HCHO and CHOCHO over Athens and Nairobi. Presented at the *EGU General Assembly*, Vienna, Austria, April 2014
- **Alvarado, L. M. A.**, Richter, A., Vrekoussis, M., Wittrock, F., Schreier, S. F., and Burrows, J. P.: Glyoxal columns retrieved from OMI data as an indicator of fire emissions. Presented at the *DPG spring meeting*, Berlin, Germany, March 2014
- **Alvarado, L. M. A.**, Richter, A., Vrekoussis, M., Wittrock, F., Schreier, S. F., and Burrows, J. P.: Glyoxal retrieval from satellite observations as indicator of fires emission and biogenic activities. Presented at the *Seminar of University of El Salvador*, San Salvador, February 2014

## Selected posters

- **Alvarado, L. M. A.**, Richter, A., Wittrock, F., Vrekoussis, M. Burrows, J. P.: Insvestigating the sources of VOC using the ratio of glyoxal to formaldehyde from satellite and ground based measurements. Presented at the *DPG Spring meeting*, Regensburg, Germany, March 2016
- **Alvarado, L. M. A.**, Richter, A., Peters, E., Wittrock, F., Burrows, J. P., Vrekoussis, M., Gratsea, M., Gerasopoulou E.: MAX-DOAS observation of CHOCHO, HCHO and NO<sub>2</sub> over Nairobi and Athens. Presented at the *DPG Spring meeting*, Heidelberg, Germany, March 2015

- **Alvarado, L. M. A.**, Richter, A., Vrekoussis, M., Wittrock, F., and Burrows, J. P.: Comparison of OMI and GOME–2 CHOCHO columns since 2007. Presented at the *EUMETSAT Meteorological Satellite Conference*, Geneva, Switzerland, September 2014
- **Alvarado, L. M. A.**, Richter, A., Vrekoussis, M., Wittrock, F., and Burrows, J. P.: An improved glyoxal retrieval from OMI data and intercomparison with GOME-2 data. Presented at the *Helmholtz Research School on Earth System Science Retreat*, Bremen, Germany, November 2013
- **Alvarado, L. M. A.**, Richter, A., Vrekoussis, M., Wittrock, F., and Burrows, J. P.: Sensitivity study on glyoxal retrieval from OMI data. Presented at the *6th International DOAS workshop*, Boulder, USA, August 2013
- **Alvarado, L. M. A.**, Richter, A., Vrekoussis, M., Wittrock, F., and Burrows, J. P.: An improved glyoxal retrieval from OMI satellite data. Presented at the *EGU-General Assembly*, Vienna, Austria, April 2013



# Acknowledgements

I am very grateful to have had the opportunity to do my PhD at the *Institut für Umweltphysik* (IUP) in Bremen and to be part of the wonderful DOAS group. I would especially like to express my appreciation and thanks to Prof. Dr. John P. Burrows. Thank you for making me part of this excellent research institute and for your advice and support during all these years.

I am thankful to Prof. Dr. Mihalis Vrekoussis who kindly accepted to review this PhD thesis as a second examiner. Thanks also for the fruitful discussions, valuable comments, and support you gave me.

I am deeply thankful to Dr. Andreas Richter for being my thesis supervisor, you have been a tremendous mentor for me. I would like to thank you for all your support, for encouraging my research, for allowing me to grow as a research scientist, and for always being there in my times of ignorance. Your advice on research, my career, as well as on life, have been priceless.

I would also like to thank Dr. Michel Van Roozendaal for serving as a member in my PhD committee, for the valuable comments, and for the time spent on my research.

My PhD has been funded by the German Academic Exchange Service (DAAD) and by the University of Bremen. Also, financial support for attendance at conferences and soft skill trainings has been provided by the Earth System Science Research School (ESSReS), an initiative of the Helmholtz Association of German Research Centres (HGF) at the Alfred Wegener Institute for Polar and Marine Research (AWI). Thanks to Klaus Grosfeld, Helge Meggers, Stefanie Klebe, and all the other members of ESSRES. The courses, seminars, excursions and soft skill trainings will be in my memories as part of a fantastic time during my PhD.

This adventure could not have been possible without the support of all members of the DOAS group (present and past members, which are too many to write down). Many thanks for all your advice, discussions, and comments which helped to improve my work. Thanks for the hours of fun and relaxation, for the pleasant (working) environment, for making my stay in Bremen very comfortable, for being part of my family, and for helping me when needed.

A special thanks to A. Hilboll and A. Meier, my officemates and dear friends, whom have always been there for me by supporting, advising, answering hundreds of questions, and sharing all the fun in the office. Thank you to E. Peters for many fruitful discussions and for all the support in both research and life. Also thanks to S. Schreier for the unconditional support, the shared frustration, the happy times, and for being like a brother to me during this journey.

A special thanks to H. van Asperen, A. Hilboll, J. Iraheta, E. Peters, and N. Ryan for the proof-reading of this manuscript.

I would like to thank Johannes Kaiser and the MACC team for providing the GFASv1.0 FRP product. Also, I would like to thank several institutions for their data and support: OMI lv1, MODIS FRP, and EVI data have been provided by NASA, GOME-2 lv1 data have been provided by EUMETSAT, and SCIAMACHY lv1 data have been provided by ESA through DLR. Also thanks to the Atmospheric Physics and Chemistry Group of the National Observatory of Athens and UNEP Nairobi for hosting the BREDOM stations.

I was lucky to be part of the IUP Bremen and of the ESSReS research school which are not only scientifically stimulating environments, but which also gave me the opportunity to meet wonderful people, of which some became great friends. Thanks for all the moments of fun and great stories which we shared. A special thanks goes to Hella, Jia, Matthias, and Ola for always being there when I needed them.

I would like to thank Dr. Carlos Rudamas for support me during my PhD, despite of distance he always found a way to helping me when needed.

Last but not least, I would like to thank all my friends and family for their unconditional support, for this reason I will write some a few words to them in Spanish: A mis padres, Wilfredo Alvarado y Marta Bonilla, gracias por su apoyo incondicional, sus consejos y su amor hacia mí a pesar de la distancia. A mis hermanos y hermanas, Marta, Leonides, Mercedes y Wilfredo, gracias por apoyarme y escucharme siempre que lo he necesitado. También, gracias a mis

abuelos y abuelas, algunos ya no estan con nosotros, pero siempre me motivaron a seguir adelante con todas mis metas. A mis tíos, tías y demás familia, gracias por apoyarme siempre en todo lo que he necesitado. Finalmente, a mi esposa e hija, Vicky y Maybelline, gracias por ser mi apoyo y sostén durante estos años.



# Contents

<b>Contents</b>	<b>xvii</b>
<b>List of Figures</b>	<b>xx</b>
<b>List of Tables</b>	<b>xxiv</b>
<b>1 Introduction</b>	<b>1</b>
<b>2 Scientific background</b>	<b>5</b>
2.1 Volatile organic compounds . . . . .	5
2.2 Introduction to Earth's atmosphere . . . . .	8
2.3 Tropospheric chemistry . . . . .	11
2.3.1 Formaldehyde (HCHO) . . . . .	12
2.3.2 Glyoxal (CHOCHO) . . . . .	13
2.3.3 Nitrogen dioxide (NO <sub>2</sub> ) . . . . .	15
2.4 Absorption spectroscopy . . . . .	17
2.4.1 Electromagnetic radiation . . . . .	17
2.4.2 Energy levels and transitions in molecules . . . . .	18
2.4.3 Solar radiation . . . . .	20
2.4.4 Radiative transfer in the atmosphere . . . . .	21
2.4.5 Scattering processes in the atmosphere . . . . .	22
2.4.6 Absorption in the atmosphere . . . . .	25
2.4.7 Differential Optical Absorption Spectroscopy (DOAS) . . .	27
2.4.8 The Air mass factor . . . . .	30
2.5 Description of instruments . . . . .	32
2.5.1 Ground based instruments . . . . .	33
2.5.2 Satellite instruments . . . . .	34
<b>3 Glyoxal retrieval from satellite measurements</b>	<b>37</b>

## CONTENTS

3.1	Introduction . . . . .	37
3.2	Optimization of the glyoxal retrieval from satellite measurements . . . . .	40
3.2.1	Dependence on the fitting window . . . . .	41
3.2.2	Dependence on the polynomial order . . . . .	48
3.2.3	Interference with liquid water absorption . . . . .	50
3.2.4	Interference with NO <sub>2</sub> absorption . . . . .	53
3.2.5	Dependence on the water vapour cross-section . . . . .	55
3.2.6	The effects of clouds on the glyoxal retrieval . . . . .	58
3.2.7	The reference spectrum . . . . .	62
3.3	Glyoxal detection limits and errors . . . . .	68
3.4	Summary . . . . .	72
<b>4</b>	<b>Observations of glyoxal from space</b>	<b>73</b>
4.1	Introduction . . . . .	73
4.2	Global observations and satellite intercomparison . . . . .	75
4.2.1	Interannual variability . . . . .	79
4.2.2	Seasonal variation . . . . .	79
4.3	Identification of glyoxal sources . . . . .	81
4.3.1	Biogenic emissions . . . . .	81
4.3.2	Pyrogenic emissions . . . . .	83
4.3.3	Anthropogenic emissions . . . . .	85
4.4	“Hot-spot” areas of glyoxal and comparison with indicators of different sources . . . . .	87
4.4.1	North and Central America . . . . .	87
4.4.2	South America . . . . .	90
4.4.3	Europe and Western Sahara . . . . .	92
4.4.4	Africa . . . . .	94
4.4.5	Asia . . . . .	95
4.4.6	Oceania . . . . .	97
4.5	Summary . . . . .	99
<b>5</b>	<b>Identification of VOC sources and case studies</b>	<b>101</b>
5.1	Introduction . . . . .	101
5.2	Ratio of glyoxal to formaldehyde (R <sub>GF</sub> ) . . . . .	102
5.3	Case studies . . . . .	107
5.3.1	Glyoxal as an indicator of pyrogenic emissions: Russian fires in summer 2010 . . . . .	107
5.3.2	Glyoxal transport event . . . . .	109

## CONTENTS

5.4 Summary . . . . .	111
<b>6 Glyoxal, formaldehyde, and nitrogen dioxide retrievals from MAX-DOAS measurements</b>	<b>113</b>
6.1 Introduction . . . . .	113
6.2 Measurement sites . . . . .	115
6.2.1 Athens . . . . .	115
6.2.2 Nairobi . . . . .	116
6.3 Sensitivity study on the retrievals of CHOCHO, HCHO and NO <sub>2</sub>	120
6.4 Results and Discussion . . . . .	128
6.4.1 Athens . . . . .	128
6.4.2 Nairobi . . . . .	137
6.4.3 Comparison between Athens and Nairobi . . . . .	144
6.5 Summary . . . . .	145
<b>7 Conclusions and Outlook</b>	<b>147</b>
<b>Bibliography</b>	<b>155</b>

# List of Figures

Figure 2.1 Chemical and transport processes in the atmosphere . . . . .	6
Figure 2.2 Estimates of global VOC emissions from different sources .	7
Figure 2.3 A typical vertical temperature profile of the atmosphere . .	9
Figure 2.4 Global distribution of formaldehyde . . . . .	11
Figure 2.5 Global distribution of glyoxal . . . . .	14
Figure 2.6 Global distribution of tropospheric nitrogen dioxide . . . . .	16
Figure 2.7 Electromagnetic spectrum . . . . .	18
Figure 2.8 Diagram of rotational-vibrational energy levels in two electronic states of a molecule . . . . .	20
Figure 2.9 Example of solar spectrum measured by SCIAMACHY instrument . . . . .	22
Figure 2.10 Polar diagram of the Rayleigh scattering phase function .	24
Figure 2.11 Representation of the Beer-Lambert law . . . . .	26
Figure 2.12 The DOAS principle . . . . .	28
Figure 2.13 DOAS configurations . . . . .	31
Figure 2.14 The ground-based DOAS instrument . . . . .	33
Figure 3.1 Glyoxal wavelength dependence for synthetic spectrum .	42
Figure 3.2 Cross-sections of species used in the glyoxal retrieval . .	44
Figure 3.3 Glyoxal retrieved over different environments . . . . .	45
Figure 3.4 Glyoxal wavelength dependence for the GOME-2 and SCIAMACHY measurements . . . . .	47
Figure 3.5 RMS obtained in the glyoxal retrieval to different wavelengths from OMI, SCIAMACHY and GOME-2 (A) measurements . . . . .	48
Figure 3.6 Glyoxal retrieved for different polynomials . . . . .	49
Figure 3.7 Comparison of different liquid water corrections . . . . .	50
Figure 3.8 Latitudinal dependence of glyoxal SC over oceans . . . . .	52
Figure 3.9 Longitudinal variation of glyoxal SCs for latitudes 14°–28° N	53

## LIST OF FIGURES

Figure 3.10 Glyoxal and NO <sub>2</sub> over highly populated areas . . . . .	54
Figure 3.11 Seasonal variation of glyoxal SCs including and excluding the high-temperature NO <sub>2</sub> absorption cross-section . . . . .	56
Figure 3.12 Chi-square relative differences between glyoxal retrievals with different water vapour cross-sections . . . . .	57
Figure 3.13 Comparison of CHOCHO SCs using different cloud fractions	60
Figure 3.14 Glyoxal SC dependence on the cloud fraction for selected regions . . . . .	61
Figure 3.15 OMI orbit example: the Pacific region as a reference spec- trum . . . . .	63
Figure 3.16 RMS relative differences: Sun vs Pacific region . . . . .	63
Figure 3.17 Glyoxal comparison: Sun vs Pacific region . . . . .	65
Figure 3.18 Glyoxal SC relative differences: Sun vs Pacific region . . .	66
Figure 3.19 Correlation coefficients: Sun vs Pacific region . . . . .	67
Figure 3.20 Comparison of GOME–2A glyoxal SCs over Pacific: daily Sun vs daily Pacific . . . . .	68
Figure 3.21 Glyoxal SCs over Pacific: fix Sun reference . . . . .	70
Figure 3.22 Distribution of CHOCHO SCs over a clean equatorial ocean region . . . . .	71
 Figure 4.1 Global glyoxal means from SCIAMACHY, OMI, and GOME– 2 (A and B) . . . . .	77
Figure 4.2 Global glyoxal absolute differences between instruments .	77
Figure 4.3 Comparison of monthly averaged CHOCHO VCs from OMI, GOME–2 (A and B) and SCIAMACHY instruments . . . . .	78
Figure 4.4 Yearly averages maps of CHOCHO VCs between 2007 and 2014 . . . . .	80
Figure 4.5 Glyoxal seasonal variation from GOME–2A instrument .	81
Figure 4.6 Correlation map between glyoxal VC and EVI . . . . .	82
Figure 4.7 Time series over regions with high correlation coeffiente between glyoxal VCs and EVI . . . . .	83
Figure 4.8 Correlation map between CHOCHO VC and FRP . . . . .	84
Figure 4.9 Time series over regions with high correlation coeffiente between glyoxal VC and FRP . . . . .	85
Figure 4.10 Averaged maps of glyoxal and tropospheric NO <sub>2</sub> VCs .	86
Figure 4.11 Density correlation plots between glyoxal and tropospheric NO <sub>2</sub> VCs . . . . .	88
Figure 4.12 Selected glyoxal “hot-spots” over different continental regions	89

## LIST OF FIGURES

Figure 4.13 Seasonal means of glyoxal, FRP, EVI and NO <sub>2</sub> from morning and afternoon instruments over North and Central America . . . . .	90
Figure 4.14 Seasonal means of glyoxal, FRP, EVI and NO <sub>2</sub> from morning and afternoon instruments over South America . . . . .	91
Figure 4.15 Seasonal means of glyoxal, FRP, EVI and NO <sub>2</sub> from morning and afternoon instruments over Europe and Western Sahara . . . . .	93
Figure 4.16 Seasonal means of glyoxal, FRP, EVI and NO <sub>2</sub> from morning and afternoon instruments over Africa . . . . .	95
Figure 4.17 Seasonal means of glyoxal, FRP, EVI and NO <sub>2</sub> from morning and afternoon instruments over South America . . . . .	96
Figure 4.18 Seasonal means of glyoxal, FRP, EVI and NO <sub>2</sub> from morning and afternoon instruments over Australia and New Guinea . . . . .	98
Figure 5.1 Global average maps of glyoxal and formaldehyde VCs from 2007 to 2014 from GOME–2A measurements . . . . .	104
Figure 5.2 Global averaged ratio of glyoxal to formaldehyde from GOME–2A data . . . . .	105
Figure 5.3 Ratios of glyoxal to formaldehyde for nine selected regions	106
Figure 5.4 Global land cover map with the different biomass types . .	107
Figure 5.5 CHOCHO detected over large fire event over Russia during summer 2010 . . . . .	108
Figure 5.6 High CHOCHO levels detected over Myanmar-Thailand-Laos . . . . .	110
Figure 6.1 Overview map of locations where MAX-DOAS instruments are measuring . . . . .	116
Figure 6.2 Average temperature for Athens . . . . .	117
Figure 6.3 Average rainfall for Athens . . . . .	118
Figure 6.4 Location of the MAX-DOAS instrument in Athens . . . .	118
Figure 6.5 Average temperature for Nairobi . . . . .	119
Figure 6.6 Average rainfall for Nairobi . . . . .	119
Figure 6.7 Location of the MAX-DOAS instrument in Nairobi . . . .	120
Figure 6.8 Mean RMS for formaldehyde retrievals over all possible fitting windows . . . . .	122

## LIST OF FIGURES

Figure 6.9 Mean RMS for glyoxal retrieval over all possible fitting windows . . . . .	123
Figure 6.10 Mean RMS for nitrogen dioxide retrieval over all possible fitting windows . . . . .	124
Figure 6.11 Formaldehyde, glyoxal, and nitrogen dioxede wavelength dependence for MAX-DOAS measurements . . . . .	125
Figure 6.12 Example fits for HCHO, CHOCHO, and NO <sub>2</sub> . . . . .	127
Figure 6.13 Time series of HCHO DSCs retrieved from the MAX-DOAS measurements over Athens . . . . .	128
Figure 6.14 Time series of CHOCHO DSCs retrieved from the MAX-DOAS measurements over Athens . . . . .	129
Figure 6.15 Time series of NO <sub>2</sub> DSCs retrieved from the MAX-DOAS measurements over Athens . . . . .	130
Figure 6.16 Monthly means HCHO, CHOCHO, and NO <sub>2</sub> VCs over Athens . . . . .	132
Figure 6.17 Diurnal variation of HCHO, CHOCHO, and NO <sub>2</sub> VCs over Athens for cloud free days . . . . .	133
Figure 6.18 Monthly means of HCHO, CHOCHO, and NO <sub>2</sub> VCs over Athens for different azimuth directions for 2013–2014 . . .	135
Figure 6.19 Monthly means R <sub>GF</sub> in the S direction over Athens . . . .	136
Figure 6.20 Monthly means R <sub>FN</sub> in the S direction over Athens . . . .	137
Figure 6.21 Time series of HCHO DSCs retrieved from the MAX-DOAS measurements over Nairobi . . . . .	138
Figure 6.22 Time series of CHOCHO DSCs retrieved from the MAX-DOAS measurements over Nairobi . . . . .	139
Figure 6.23 Time series of NO <sub>2</sub> DSCs retrieved from the MAX-DOAS measurements over Nairobi . . . . .	140
Figure 6.24 Diurnal variation of HCHO, CHOCHO, and NO <sub>2</sub> VCs over Nairobi for cloud free days . . . . .	141
Figure 6.25 Monthly means of HCHO, CHOCHO, and NO <sub>2</sub> VCs over Nairobi . . . . .	142
Figure 6.26 Monthly means R <sub>GF</sub> over Nairobi . . . . .	143
Figure 6.27 Monthly means R <sub>FN</sub> over Nairobi . . . . .	144

Figure A.1 Comparison of monthly averaged CHOCHO VCs from OMI, GOME–2 (A and B) and SCIAMACHY instruments for 21 selected “hot-spots” . . . . .	154
---	-----

## List of Tables

Table 2.1 Most relevant gaseous constituents of the Earth’s atmosphere	10
Table 3.1 Regions selected for Fig. 3.3 . . . . .	43
Table 3.2 Chi-square relative difference and $P$ values obtained from the Wilcoxon signed-rank test . . . . .	57
Table 3.3 Regions selected for testing the dependence on cloud frac- tion (Fig. 3.14) . . . . .	59
Table 3.4 CHOCHO retrieval settings for the reference spectrum in- tercomparison . . . . .	64
Table 3.5 Regions selected for Fig. 4.3 . . . . .	65
Table 4.1 Homogenized glyoxal retrieval settings for the instrument intercomparison . . . . .	76
Table 6.1 Parameters used in the HCHO, CHOCHO, and NO <sub>2</sub> re- trievals . . . . .	126

# 1

## Introduction

The fact that plants, in particular trees, emit volatile organic compounds (VOC), mainly in the form of isoprenes ( $C_5H_8$ ) and monoterpenes (varieties of molecules with two isoprene units) has been well established for many years (Guenther et al., 1995; Atkinson and Arey, 2003; Kansal, 2009). However, the uncertainties in total emissions are very high since the amounts emitted depend on several parameters, e.g. on plant species, temperature, humidity and also condition of the plants (Guenther et al., 2000). Furthermore, VOC are present in the atmosphere as a result of many anthropogenic activities, being mainly emitted by the oil industry. In urban areas, VOC from anthropogenic (AVOC) emissions are emitted from mobile and stationary sources (Kansal, 2009). Additionally, burning of biomass emits large quantities of trace gases and aerosols into the atmosphere. Depending on the type of biomass burned and the temperatures of the fire, VOC are emitted in varying amounts and compositions. Similar to biogenic emissions the total amount of the pyrogenic emissions of VOC have large uncertainties (Stavrakou et al., 2009b).

The role and importance of VOC in ambient atmospheric composition and its impact in climate change was established many years ago (Williams, 2004; Curci et al., 2010; Vrekoussis et al., 2010), most notably for tropospheric ozone ( $O_3$ ) formation (Houweling et al., 1998). In the presence of sunlight, enhanced levels of VOC in combination with oxides of nitrogen ( $NO_x=NO+NO_2$ ; NO: nitrogen oxide) lead to the photochemical formation of ozone in the troposphere. Another topical issue is the formation of secondary organic aerosols (SOA) (Fu et al.,

2008), which potentially are relevant for cloud formation (Yu, 2000), heterogeneous chemistry, and can also contribute to the long-term transport of otherwise short lived VOC by first acting as a sink and later re-emitting VOC.

The inhomogeneous spatial and temporal distribution of VOC, resulting in a large variability of VOC fluxes into the atmosphere, led several research groups to study the global distribution of smaller molecules such as formaldehyde and glyoxal, which are produced from precursor biogenic VOC (BVOC) and AVOC species. Additionally, pyrogenic emissions can produce HCHO and CHOCHO both directly and indirectly (Stavrakou et al., 2009a). CHOCHO and HCHO are often used as tracers of hydrocarbons over areas with enhanced VOC emissions, the so-called photochemical “hot-spot” regions due to their short lifetime. They are intermediate products in the oxidation of most VOC (Volkamer et al., 2005a; Wittrock et al., 2006; Sinreich et al., 2007; De Smedt et al., 2008). Also, CHOCHO is an indicator of SOA formation (Sinreich et al., 2007; Fu et al., 2008; Vrekoussis et al., 2009).

Atmospheric HCHO and CHOCHO columns can be determined by remote sensing using the Differential Optical Absorption Spectroscopy (DOAS) method in the ultraviolet and visible spectral regions (Platt and Stutz, 2008). This sensitive technique has been used both from the ground, applying active and passive DOAS (e.g. Volkamer et al., 2005a; Heckel et al., 2005; Sinreich et al., 2007), and from satellites (e.g. Wittrock, 2006; De Smedt et al., 2008). Satellite observations, including the GOME (Global Ozone Monitoring Experiment) (Burrows et al., 1999), the SCanning Imaging Absorption spectrometer for Atmospheric CHartographY (SCIAMACHY) (Burrows et al., 1995; Bovensmann et al., 1999), the second Global Ozone Monitoring Experiment (GOME-2) (Calley et al., 2000), and the Ozone Monitoring Instrument (OMI) (Levelt et al., 2006) have been used to derive the spatial distribution of HCHO and CHOCHO at a global scale, to study individual fire episodes and to identify sources of VOCs. The satellite data have also been used in combination with chemical transport models to estimate isoprene emissions in the Eastern United States and Europe. Ground-based DOAS measurements have been used for both local pollution studies and validation of satellite HCHO columns. While sources and chemistry of glyoxal and formaldehyde are similar in many respects, the variation in production efficiency for different sources can be used to better constrain source attribution of VOCs e.g. by analysing the ratio of CHOCHO to HCHO. In addition, comparison of satellite observations and model results has revealed a missing source for glyoxal from a biogenic precursor with a longer lifetime.

## 1. INTRODUCTION

In addition, VOC may have direct and indirect impacts on human health (Kampa and Castanas, 2008). The indirect impact is due to the photochemical ozone formation in the troposphere, and the direct impact on human health is through the different effects of some organics compounds. These effects include: acute respiratory diseases, nose and skin irritation, nervous system impairment, asthma, and lung and nasal cancer.

This study aims at develop an improved CHOCHO retrieval from different platforms (satellite-based and ground-based) and to investigate its temporal variability over areas with dense vegetation, fire events, and with high populations, at identifying VOC sources by constraining the ratio of glyoxal to formaldehyde and by correlating time series with indicators of different emissions.

This thesis is structured as follows: scientific background information about VOC sources and their atmospheric chemistry, an introduction to the Earth's atmosphere, tropospheric chemistry of relevant trace gases, absorption spectroscopy, and a description of instruments are given in Chapter 2. A complete description of improved glyoxal retrievals from different instruments, the optimization of fitting parameters, the corrections needed due to interferences with different absorber species, error estimation, and an intercomparison of glyoxal retrieved from different instruments are present in Chapter 3. In Chapter 4, a description of seasonal behaviour and temporal evolution of glyoxal, and identification of different sources by correlation with indicators of biogenic, pyrogenic and anthropogenic activities are presented. In Chapter 5, computation of CHOCHO to HCHO ratios for sources identification of VOC and two case studies are presented. In Chapter 6, glyoxal, formaldehyde and nitrogen dioxide are retrieved from MAX-DOAS measurements taken at two different locations, and discussed. Finally, a summary of the main findings and conclusions obtained in this study are presented, as well as an outlook for further analysis and improvements in the retrievals of VOC and suggestions for future studies.



# 2

## Scientific background

### 2.1 Volatile organic compounds

VOC are organic chemicals that play an important role in the atmosphere. Organic chemical compounds originate from biogenic, pyrogenic, and anthropogenic emissions and have a significant influence on atmospheric composition (Vrekoussis et al., 2010; Curci et al., 2010). VOC include non-methane hydrocarbons (NMHC) and oxygenated NMHC (e.g., alcohols, aldehydes and organic acids), and are emitted from different sources such as vegetation and oceans, fossil fuel burning, biomass burning, and geochemical processes (Kansal, 2009). Most VOC have a short atmospheric lifetime ranging from fractions of a day to months Volkamer et al. (2005a). On a global scale, the biogenic emissions exceed the anthropogenic emissions by around a factor of 10 (Atkinson and Arey, 2003). The biogenic contribution of VOC is estimated to be around  $1150 \text{ Tg C yr}^{-1}$  (Guenther et al., 1995). BVOC are emitted by oceans and plants, in particular trees, as part of a complex system (see Fig. 2.1) (Guenther et al., 1995; Atkinson and Arey, 2003; Kansal, 2009). The uncertainties in total emissions are very high since the amounts emitted depend on plant species, temperature, humidity and also the condition of the plant. In urban areas, there are also contributions of VOC from anthropogenic emissions by mobile and stationary sources (Kansal, 2009). AVOC sources include fuel production, distribution, and combustion, with the largest source from motor vehicles due to either evaporation or incomplete combustion of fuel, and from biomass burning. However, estimated AVOC emis-

## 2.1 VOLATILE ORGANIC COMPOUNDS

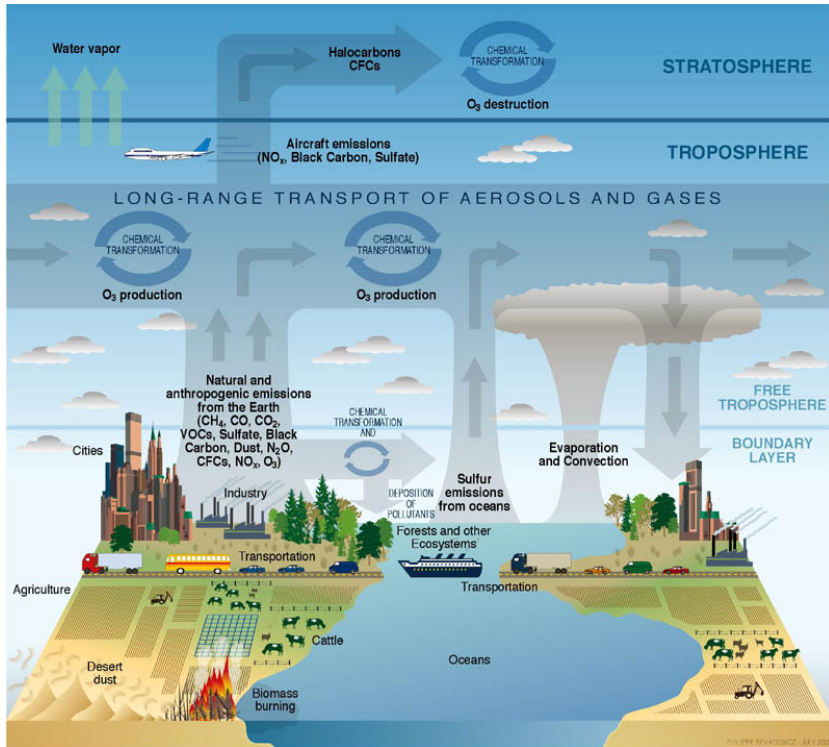


**Figure 2.1:** Schematic description of chemical and transport processes in the atmosphere, showing the relations between atmospheric processes and other components of the Earth system such as the oceans, land, and terrestrial and marine plants and animals (from USGCRP, 2003).

sions between 161–186 Tg C yr<sup>-1</sup> are ten times lower than the respective BVOC (Stavrakou et al., 2009b). In addition, 33–49 Tg C yr<sup>-1</sup> emanate from pyrogenic emissions (Andreae and Merlet, 2001). Lastly, the oceanic sources emit about 0.5–5 Tg C yr<sup>-1</sup> (Koppmann, 2007) (see Fig. 2.2).

VOCs in the presence of NO<sub>x</sub> are precursors of O<sub>3</sub> formation in the troposphere, with the hydroxyl (OH) radical as initiators of oxidation (Atkinson and Arey, 2003; Cook et al., 2007; Martin, 2008; Stavrakou et al., 2009b; Kansal, 2009). They also play a role in the formation of organic aerosols (Atkinson, 2000).

## 2. SCIENTIFIC BACKGROUND

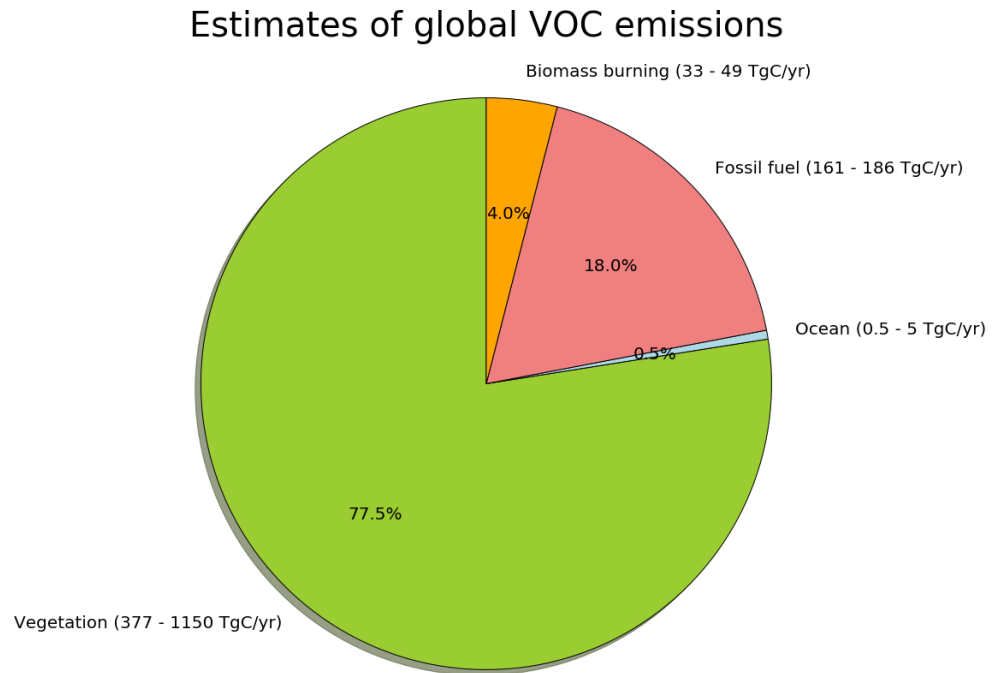
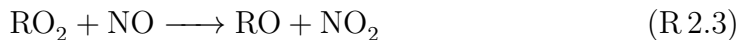


**Figure 2.2:** Estimates of global VOC emission from biogenic, anthropogenic and pyrogenic sources. The dominant emission of VOC into the atmosphere is from biogenic sources in the form of isoprene and monoterpene.

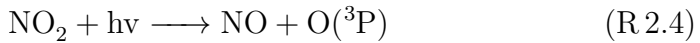


The conversion of NO to  $NO_2$  is the key reaction in the VOC oxidation cycle, and takes place through a transfer reaction with NO.



R can also be produced by photolysis and usually involves only VOC with molecules containing the carbonyl bond ( $C=O$ ). The most common VOC molecule containing the carbonyl bond is HCHO (see Sect. 2.3.1). Following this,  $O_3$  is formed from the photolysis of  $NO_2$ ,

## 2.2 INTRODUCTION TO EARTH'S ATMOSPHERE



However,  $\text{O}_3$  reacts quickly with NO,



and reactions R 2.4, R 2.5 and R 2.6 do not lead to the net formation or loss of  $\text{O}_3$ . In rural areas (less anthropogenic emissions) where the  $\text{NO}_x$  concentration is small,  $\text{O}_3$  can actually be removed by VOC. However, in urban areas  $\text{NO}_x$  concentrations are often at levels that allow the formation of  $\text{O}_3$  in the presence of sunlight. This is because organic peroxy ( $\text{RO}_2$ ) radicals are intermediate products in the degradation of BVOC and AVOC, and these radicals react with NO to form  $\text{NO}_2$  (reaction R 2.3), which then leads to net  $\text{O}_3$  formation (Atkinson, 2000).

Moreover, VOC have an important role in the global carbon cycle and can enhance the global greenhouse effect as these emissions play a major role in the increasing rate of methane ( $\text{CH}_4$ ) and carbon monoxide (CO) concentrations in the atmosphere. Consequently, there are changes in the global radiation balance of the Earth and climate in general (Fehsenfeld et al., 1992; Guenther et al., 1995).

## 2.2 Introduction to Earth's atmosphere

The atmosphere together with the hydrosphere form the fluid layered system of the Earth, whose dynamics are closely related. The Earth's atmosphere is divided into five layers, the troposphere, stratosphere, mesosphere, thermosphere, and exosphere, which are defined by vertical changes in temperature (see Fig. 2.3). The lowest layer (troposphere) extends from the Earth's surface up to 10–17 km in altitude, depending on latitude and season, and its temperature decreases with altitude. In addition, it is dominated by  $\text{H}_2\text{O}$  produced by evaporation of water from rivers, lakes, and oceans due to the solar radiation that reaches the Earth's surface, which also contributes to cloud formation in the

## 2. SCIENTIFIC BACKGROUND

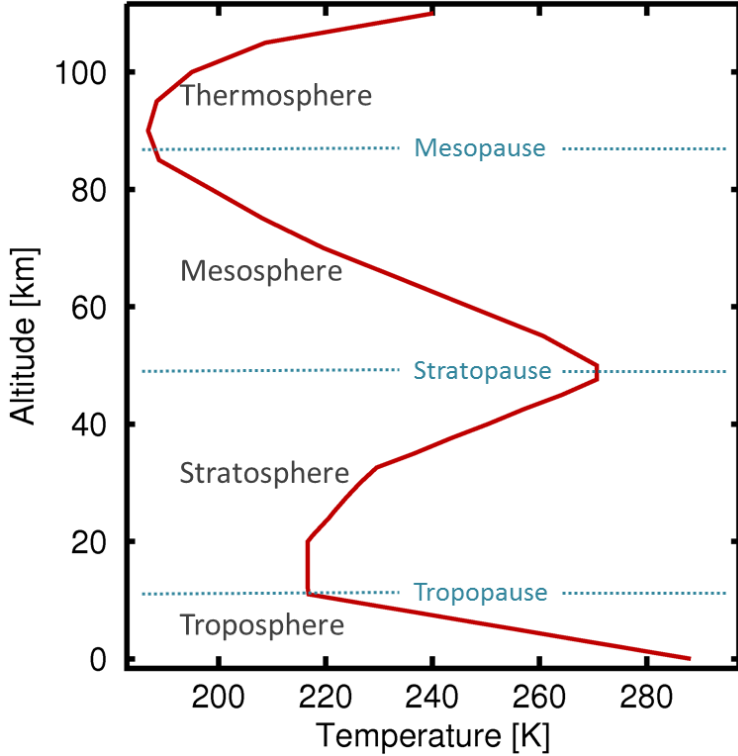


**Figure 2.3:** A typical vertical temperature profile of the atmosphere at mid-latitude (U.S. Standard Atmosphere).

atmosphere. This layer can be subdivided into boundary layer (BL) and free troposphere. The VOC chemistry is mainly taking place in the boundary layer. In Fig. 2.3, the stratosphere layer is extended from 12 km to 50 km with an increase in temperature with altitude, due to absorption of ultraviolet radiation by O<sub>3</sub> molecules. These two layers (troposphere and stratosphere) account for 99.9% of the atmosphere's mass. In the next layer (mesosphere), the temperature drops with increasing altitude; this is the coldest of the layers. Similar to the stratosphere, the thermosphere shows an increase in temperature with altitude, which is caused by the absorption of a huge amount of strong UV solar radiation by nitrogen (N<sub>2</sub>) and oxygen (O<sub>2</sub>). Finally, the last layer (exosphere) extends up to space and is almost at vacuum.

The Earth's atmosphere contains a variety of gases and suspended particles in its layers. These gases vary in quantities, nitrogen (N<sub>2</sub>: 78.08%) and oxygen (O<sub>2</sub>: 20.95%) being the dominant constituents, which do not change with altitude,

## 2.2 INTRODUCTION TO EARTH'S ATMOSPHERE

**Table 2.1:** Most relevant gaseous constituents of the Earth's atmosphere (adapted from Wallace and Hobbs, 2006, pp. 8).

<b>Gas specie</b>	<b>Fractional concentration</b>
<b>by volume</b>	
Nitrogen ( $\text{N}_2$ )	78.08%
Oxygen ( $\text{O}_2$ )	20.95%
Argon (Ar)	0.93%
Water vapour ( $\text{H}_2\text{O}$ )	0-5%
Carbon dioxide ( $\text{CO}_2$ )	380 ppm
Neon (Ne)	18 ppm
Helium (He)	5 ppm
Methane ( $\text{CH}_4$ )	1.75 ppm
Krypton (Kr)	1 ppm
Hydrogen ( $\text{H}_2$ )	0.5 ppm
Nitrous oxide ( $\text{N}_2\text{O}$ )	0.3 ppm
Ozone ( $\text{O}_3$ )	0-0.1 ppm

while Argon (Ar: 0.93%) is the noble gas having the largest concentration (see Table 2.1). Water vapour ( $\text{H}_2\text{O}$ ) has large variability in concentration around 0–5% and depends on the atmospheric conditions (e.g temperature and humidity). Also, other constituents are present in small concentrations and are known as trace gases. Among these trace gases can be found the VOC, such as HCHO and CHOCHO, as well as  $\text{NO}_2$ , which are of interest for this study.

In addition, some gas species more strongly absorb the outgoing infrared radiation,  $\text{H}_2\text{O}$ , carbon dioxide ( $\text{CO}_2$ ) and  $\text{O}_3$  being the most importants. These species are called greenhouse gases. Also,  $\text{CH}_4$ , nitrous oxide  $\text{N}_2\text{O}$ , CO, and chlorofluorocarbons (CFCs) are contributors to the so-called greenhouse effect, which is a process by which the outgoing radiation from Earth's surface is absorbed and re-emitted by these greenhouse gases. Since part of this re-emitted

## 2. SCIENTIFIC BACKGROUND

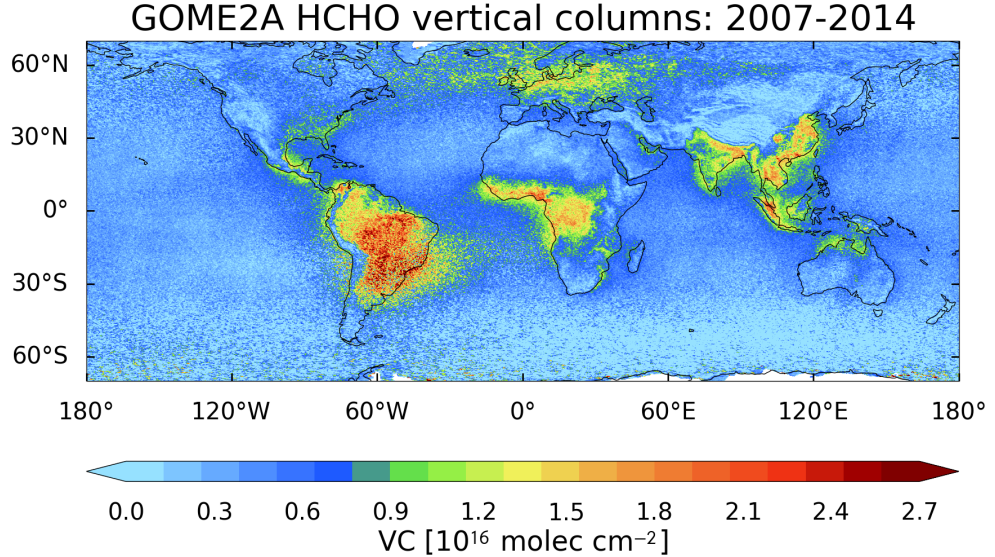


**Figure 2.4:** Global distribution of HCHO vertical columns from GOME-2 (MetOp-A) instrument for the time period of 2007–2014. Formaldehyde is mainly located in the tropical and sub-tropical regions over areas with large vegetation, also large amounts of HCHO vertical columns are located in Europe and Southeastern of USA.

radiation is directed back towards the surface and the boundary layer, it results in an increase of the average surface temperature. While this study is not directly linked to the greenhouse effect, the VOC are related to it mainly by their impact on the ozone.

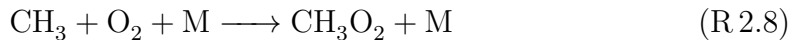
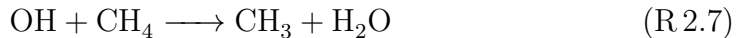
### 2.3 Tropospheric chemistry

The atmosphere is composed of a wide variety of gases. Among these gases are the so called trace gases, which are found in low concentrations compared to those of  $\text{N}_2$  or  $\text{O}_2$ . Both VOC and  $\text{NO}_x$  are trace gases and are mainly located in the troposphere.

## 2.3 TROPOSPHERIC CHEMISTRY

### 2.3.1 Formaldehyde (HCHO)

Atmospheric formaldehyde originates from a wide number of natural and anthropogenic sources and is the most abundant among the carbonyls in the atmosphere. While primary emissions from biomass burning and fossil fuel combustion exist (Wittrock, 2006; Boeke et al., 2011), most production is secondary. In the troposphere, HCHO varies commonly from 0.2 parts per billion by volume (ppbv) to 20 ppbv (Fried et al., 2002). HCHO is an indicator of photochemical activity and an intermediate product of the process of degradation of VOC (Fu et al., 2007; De Smedt et al., 2008; Stavrakou et al., 2009b). This is because atmospheric HCHO concentrations are mainly determined by the oxidation of methane and non-methane hydrocarbons. During their oxidation to carbon monoxide (CO), carbon dioxide (CO<sub>2</sub>) and water (H<sub>2</sub>O), almost all VOC lead to the formation of HCHO as an intermediate product in the presence of sunlight (Wittrock, 2006; Platt and Stutz, 2008). As the simplest example, the process of oxidation of CH<sub>4</sub> in the atmosphere is as follows:

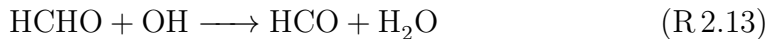


The levels of HCHO are therefore indicative of the overall VOC concentrations, at least for regions without significant direct emissions of HCHO due to anthropogenic activities (e.g. traffic). HCHO has a short lifetime (a few hours during daytime) as a result of photolysis,



and reaction with OH

## 2. SCIENTIFIC BACKGROUND



The hydroperoxyl radical ( $\text{HO}_2$ ) is generated by reaction R 2.14, and the OH radical (consumed in reaction R 2.13) returns in reaction R 2.15 to complete the cycle. Moreover, reaction R 2.15 produces the  $\text{NO}_2$  required for  $\text{O}_3$  formation, as described in section 2.1. In addition, CO generated by reaction R 2.14 can react like an organic molecule to yield another hydroperoxyl radical.



There is also a significant contribution to HCHO removal from the atmosphere by dry and wet deposition (Hak et al., 2005). HCHO plays a main role in odd hydrogen radical chemistry,  $\text{HO}_x$  ( $\text{OH} + \text{HO}_2$ ), and in  $\text{O}_3$  production. This occurs due to the fact that HCHO is a source of  $\text{HO}_2$  radicals in the presence of enough  $\text{NO}_x$  by converting NO to  $\text{NO}_2$ , in particular in the upper troposphere where water vapor is found at low concentrations (Fried et al., 2002; Hak et al., 2005; Wittrock, 2006; Platt and Stutz, 2008; Dufour et al., 2009).

For humans, HCHO in concentrations larger than 100 ppbv can cause irritation to the nose, the eyes, the throat, and the skin. Even higher concentrations of HCHO in air are toxic and classified as potentially carcinogenic (ATSDR, 1999).

### 2.3.2 Glyoxal (CH<sub>2</sub>OCHO)

Glyoxal originates from natural and anthropogenic activities similar to HCHO (Wittrock et al., 2006; Wittrock, 2006; Fu et al., 2008; Stavrakou et al., 2009a). It is the smallest of the alpha-dicarbonyls and the most predominant in the atmosphere (Myriokefalitakis et al., 2008). It is an intermediate product in the oxidation of most VOC (Volkamer et al., 2005a; Wittrock, 2006; Sinreich et al., 2007) and an indicator of SOA formation in the atmosphere (Sinreich et al., 2007;

## 2.3 TROPOSPHERIC CHEMISTRY

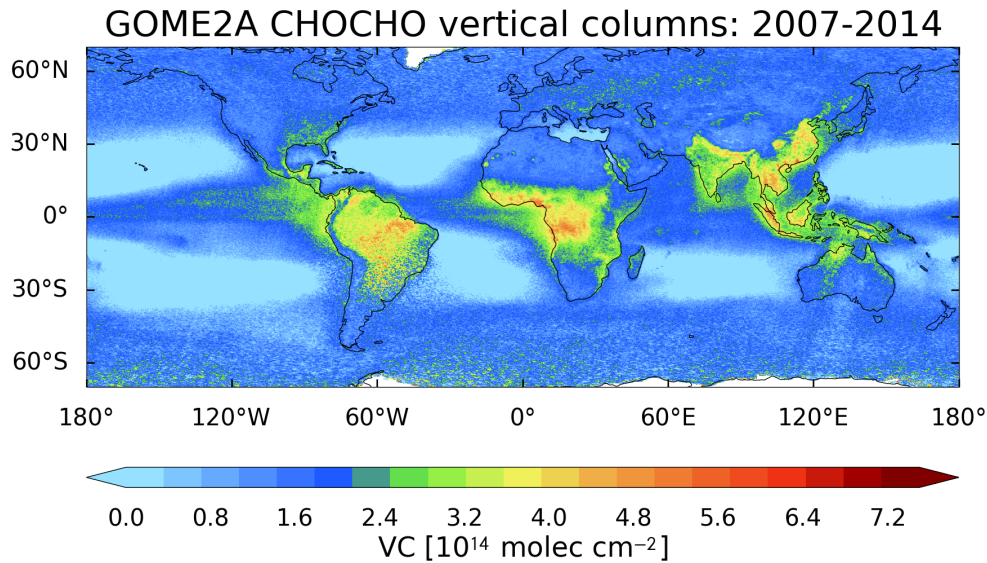
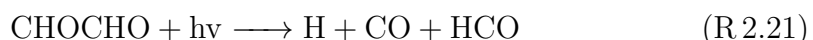
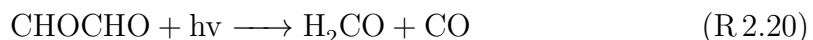


**Figure 2.5:** Global distribution of CHOCHO vertical columns from GOME–2 (MetOp–A) instrument for period of 2007–2014. Glyoxal, similar to formaldehyde, is mainly located in the tropical and sub-tropical regions over areas with large vegetation and fire events. Also, some “hot-spots” of CHOCHO vertical columns are located over regions with large anthropogenic emissions.

Fu et al., 2008; Vrekoussis et al., 2009). Among others, CHOCHO is a product of the oxidation of isoprene, alkyne, and aromatic hydrocarbons. CHOCHO is not influenced directly by vehicle emissions (Volkamer et al., 2005a), because these are believed to be small. Glyoxal has a short lifetime (a few hours) in the presence of sunlight (Atkinson, 2000), because of its removal from the atmosphere by photolysis (Tadić et al., 2006),



and reacts with OH (Setokuchi, 2011).

## 2. SCIENTIFIC BACKGROUND

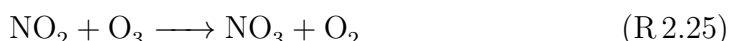
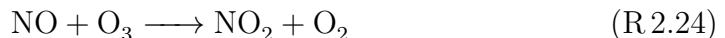


Additionally, CHOCHO is removed by SOA, OH oxidation, and by dry and wet deposition (Fu et al., 2008; Stavrakou et al., 2009a). For atmospheric observations, CHOCHO is of interest as it has slightly different sources than HCHO, and can be used as an indicator of the rate of photochemical VOC processing, because in contrast to HCHO it is not produced in the oxidation of CH<sub>4</sub> (Myriokefalitakis et al., 2008).

At high concentrations, CHOCHO is harmful for humans, causing irritation to the eyes and skin (Wittrock, 2006).

### 2.3.3 Nitrogen dioxide (NO<sub>2</sub>)

Nitrogen dioxide is one of the most important trace gases in the atmosphere. It is emitted by a wide variety of natural and anthropogenic sources (Platt and Stutz, 2008). The majority of NO<sub>2</sub> comes from fossil fuel combustion in industries, vehicle emissions, home heating, and power stations. However, there are also contributions from biomass burning and soils, as well as situ formation from lightning and photochemical reactions in the troposphere (Atkinson, 2000). NO<sub>x</sub> lead to the formation of nitrate (NO<sub>3</sub>) radicals in the troposphere by the reactions,



However, NO<sub>3</sub> photolyzes rapidly with a lifetime of around 5 s in the presence of sunlight (Atkinson, 2000),



## 2.3 TROPOSPHERIC CHEMISTRY

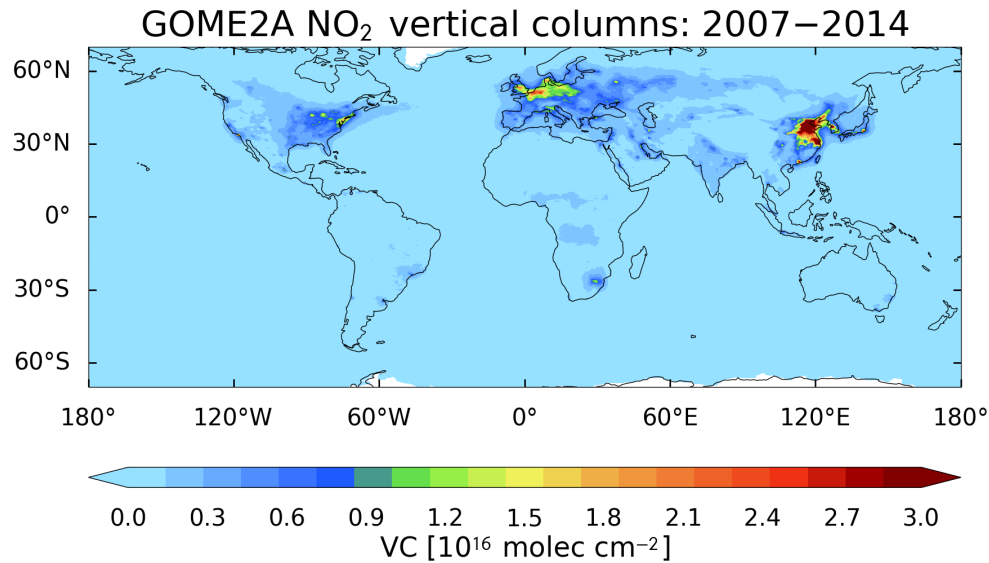
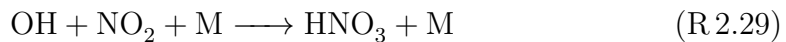
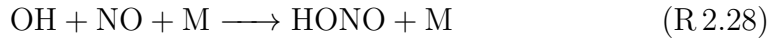


**Figure 2.6:** Global distribution of tropospheric NO<sub>2</sub> vertical columns from GOME-2 (MetOp-A) instrument for period of 2007–2014. High levels of nitrogen dioxide are located over large agglomerations, which are characterized by large anthropogenic emissions.

NO<sub>2</sub> in the presence of sunlight is a catalyst for ozone formation in the troposphere (reaction R 2.4 and R 2.5). In the stratosphere, in contrast to the troposphere, NO<sub>2</sub> plays an important role in the destruction of ozone, and also in the formation of halogen reservoirs such as chlorine nitrate (Richter et al., 2011, and references therein).

NO<sub>2</sub> is destroyed in the atmosphere mainly by its reaction with OH during the daytime, and at high concentrations it can have an important impact on OH levels (Atkinson, 2000). At night, NO<sub>3</sub> takes over the role of OH.



The reaction of OH with NO is in photoequilibrium with the photolysis of nitrous acid (HONO),

## 2. SCIENTIFIC BACKGROUND



HONO is also formed during the night-time in urban areas and this is attributed to the heterogeneous hydrolysis of NO<sub>2</sub> on aerosol and particulate matter surfaces (Jacob, 2000). This being the case, HONO is important because its photolysis early in the morning enhances photo-oxidation processes due to rapid production of OH radicals.

NO<sub>2</sub> is a pulmonary irritant primarily affecting the upper respiratory system. Individuals with asthma, respiratory disorders, and lung diseases are more sensitive to the effects of NO<sub>2</sub>. At higher concentrations it can irritate the lungs, cause bronchitis and pneumonia, and lower resistance to respiratory infections (EPA).

## 2.4 Absorption spectroscopy\*

### 2.4.1 Electromagnetic radiation

Electromagnetic radiation consists of oscillating waves of electric and magnetic fields, which propagate at the speed of light ( $c \approx 2.998 \times 10^8 \text{ ms}^{-1}$ ). These waves are always in phase and perpendicular to each other. Electromagnetic radiation is distinguished by its wavelength ( $\lambda$ ) or frequency ( $\nu$ ), which are related by,

$$c = \nu \cdot \lambda \quad (2.1)$$

The electromagnetic radiation is subdivided in different regimes depending on wavelength. These regimes are  $\gamma$ -radiation, X-radiation, ultraviolet (UV), visible (Vis), infrared, and radio waves (see Fig 2.7). The ultraviolet spectral range extends from about 100 nm to 400 nm, while the visible ranges from 400 nm to 780 nm. Wavelengths shorter than 100 nm correspond to the  $\gamma$  and X-radiation range and longer than 780 nm to the infrared, while radiation of even longer wavelength ( $\lambda > 1 \text{ mm}$ ) corresponds to microwave and radio wave radiation.

---

\*This section is based on Seinfeld and Pandis (2006) and Platt and Stutz (2008)

## 2.4 ABSORPTION SPECTROSCOPY

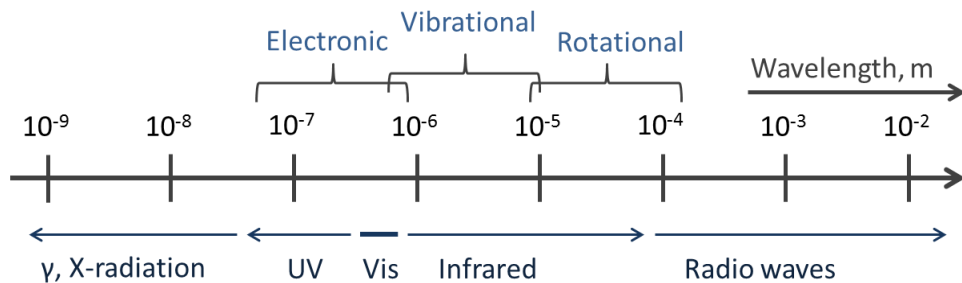


**Figure 2.7:** Diagram of the electromagnetic spectrum showing the different wavelength ranges from radio waves to X-rays. The different types of transition in atoms and molecules induced by electromagnetic radiation are indicated at the corresponding wavelength range.

From quantum mechanics it is well-known that some aspects of electromagnetic radiation can be described as waves, and others can only be understood as particles. Depending on the energy ( $E = h\nu = hc/\lambda$ ;  $h \approx 6.626 \times 10^{-34}$  Js denoting Planck's constant) of photons, different forms of interactions of radiation with the matter can take place. For example, UV and visible radiation can lead to reconfiguration of the electron shell of atoms or molecules, which is commonly called electronic excitation, while less energetic radiation will excite vibrational or rotational states in molecular gases. Atoms or molecules in an excited state can return to the ground state by converting the absorbed photon into heat (collisions with other molecules) or by re-radiating a photon. The energy of an excited state can also be used in chemical reactions to overcome the activation barrier.

### 2.4.2 Energy levels and molecular transitions

Molecules are electrically neutral groups of two or more atoms connected by chemical bonds. The individual energy states in atoms and molecules are discrete, because they are quantum multi-particle systems. For molecules, two additional excitation states are found, which are not present in atoms. Therefore, there are three energy states in molecules: rotational (rotation of the complete molecule), vibrational (vibration of the atoms in the molecule) and electronic (change in the configuration of the electrons). The typical transitions energies are on the order of about 1 eV for electronic, 0.1 eV for vibrational, and between  $10^{-3}$  and  $10^{-2}$  eV

## 2. SCIENTIFIC BACKGROUND

for rotational transitions. Electronic transitions correspond to wavelengths of the visible and near UV spectral range, vibrational transitions to wavelengths in the infrared spectral range, and the rotational lines to wavelengths in the microwave range (see Fig 2.7).

The rotational energy levels in a molecule are calculated by,

$$E_j = B \cdot J(J + 1) \quad (2.2)$$

where  $B$  is the rotational constant of the molecule, and  $J$  the rotational quantum number. The energy difference between two consecutive states is given by,

$$\Delta E_j = E_{j+1} - E_j = 2B(J + 1) \quad (2.3)$$

which represents the photon energy of the allowed transitions. Thus, in absorption spectra rotational lines are equally spaced. Most molecules are rotationally excited at room temperature, because these differences of energies are in the order of the thermal kinetic energy ( $10^{-3} - 10^{-2}$  eV).

The vibration of atoms in molecules can be described by the harmonic oscillator and the energy levels can be given by,

$$E_n = (n + \frac{1}{2}) \cdot \hbar\omega_0 \quad (2.4)$$

where  $n$  is the vibrational quantum number and  $1/2\hbar\omega_0$  is the zero-point energy of the molecular oscillator. Therefore, for the different vibrational states the energies vary proportional to the vibrational quantum number. In these vibrational states it is very likely that the molecules are also rotationally excited at ambient temperature. Therefore, each vibrational state splits into a series of rotational lines (see Fig 2.8).

Electronic transitions occur when the configuration of the electrons in a molecule change from one energy level to another, which also leads to changes in the intermolecular force and length. Thus, each electronic state has its own set of vibrational and rotational states. Figure 2.8 shows an example of an electronic

## 2.4 ABSORPTION SPECTROSCOPY

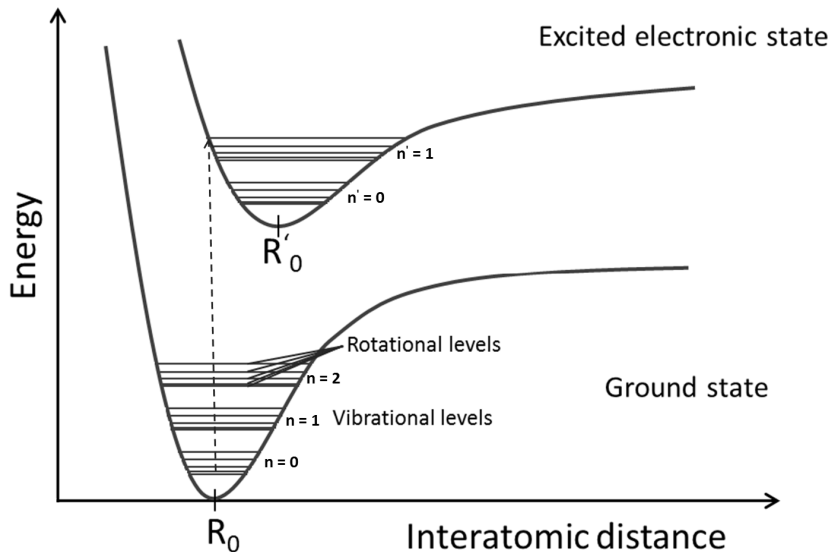


**Figure 2.8:** Diagram of rotational-vibrational energy levels in two electronic states of a molecule. Electronic energies are given as a function of interatomic distance. These energies are minimal at a certain distance ( $R_0$  and  $R'_0$ ), which is different for each different electronic state. The groups of equidistant horizontal lines represent the lowest rotational levels of the vibrational states (ground state:  $n = 0, 1, 2$ ; excited state:  $n' = 0, 1$ ).

transition, which represents a potential energy diagram with the rotational-vibrational energy levels of two electronic states in a molecule. The electronic transition occurs vertically, as is governed by the *Franck-Condon principle* describing the absorption or emission of a photon. This principle states that when a molecule undergoes an electronic transition, no significant change is experienced in the nuclei position during the electron reconfiguration.

### 2.4.3 Solar radiation

Electromagnetic radiation is reaching the Earth from space, mainly from the Sun and is emitted back into space. The Sun is a gaseous body of about  $1.99 \times 10^{30}$  kg mass and a radius around  $6.96 \times 10^5$  km. It is mainly composed of hydrogen (around three parts) and helium (one part). The energy in the outer layers of the Sun is coming from the core, which is believed to be mainly trans-

## 2. SCIENTIFIC BACKGROUND

ferred by electromagnetic radiation and produced by nuclear reactions in the core, the fusion of four hydrogen atoms into one helium atom being the dominating process. The solar radiation received by the Earth is emitted in the photosphere (around 500 km outer of the Sun), the emission of which can be approximated by black-body radiation corresponding to its temperature of  $\approx 5800$  K. The spectral distribution is described by Planck's law, which describes the radiation emitted by a black-body in thermalequilibrium at a given temperature,

$$P_e(\lambda, T) = \frac{2\pi hc^2}{\lambda^5} \frac{1}{exp(\frac{hc}{\lambda k_B T}) - 1} \quad (2.5)$$

Here,  $\lambda$  denotes the wavelength,  $T$  the temperature,  $c$  is the speed of light,  $h$  is the Planck constant,  $k_B \approx 1.381 \times 10^{-23}$  JK $^{-1}$  is the Boltzmann constant. However, the Sun does not emit radiation as a perfect black-body. The Sun's atmosphere emits and absorbs radiation at characteristic wavelengths. Figure 2.9 shows a solar spectrum measured by the SCIAMACHY instrument outside the atmosphere. Many absorption lines are observed in the solar spectrum, which are called *Fraunhofer lines* and are caused by absorption at characteristic wavelength for different species (see Fig. 2.9). The solar spectrum shown is similar to the one used in this study as reference spectrum.

### 2.4.4 Radiative transfer in the atmosphere

Radiative transfer in the atmosphere describes all processes that influence the propagation of radiation in a medium that absorbs and scatters it, such as the atmosphere. Understanding these processes is required for the interpretation of measurements with passive DOAS. As will be described in Sect. 2.4.7, the DOAS analysis results in the slant column density, which depends on the effective optical light path  $s$  through the absorbing layer. The propagation of radiation in the atmosphere is a complex process and is dominated by the interaction of radiation with matter, such as absorption, scattering and emission. These processes are expressed in the equation of radiative transfer ("RTE: Radiative Transfer Equation"). The RTE describes the changes of radiation while passing through the atmosphere ( $I(\lambda)$ ). When the RTE is applied in the ultraviolet/visible spectral range, as is done in this work, the thermal emission can be neglected and the RTE is given by,

## 2.4 ABSORPTION SPECTROSCOPY

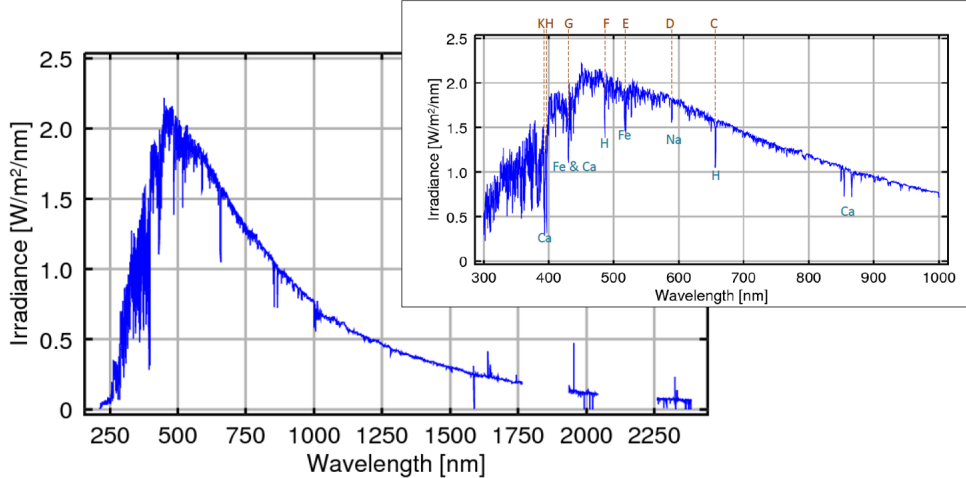


**Figure 2.9:** Example of solar spectrum measured by the SCIAMACHY instrument.

In addition, some of the Fraunhofer absorption lines have been pointed out for wavelengths between 300 and 1000 nm with their responsible species (from Schönhardt, 2009).

$$\frac{dI(\lambda)}{ds} = -I(\lambda)\varepsilon(\lambda) + \varepsilon(\lambda)B(\lambda) \quad (2.6)$$

The left side of the equation represents the change of radiation along the effective optical light path  $ds$ , while the first term on the right side describes the attenuation of radiation due to absorption and scattering,  $\varepsilon$  being the extinction coefficient, which is the sum of the absorption and scattering coefficients. The second term represents the gain through scattering, where  $B(\lambda)$  is the scattering source function (Rozanov et al., 2013).

### 2.4.5 Scattering processes in the atmosphere

In the atmosphere, incoming radiation can be scattered by large molecules of atmospheric gases and suspended particles. The scattering process can be divided into two main different types: elastic (no change of photon energy due to the scattering process) and inelastic (change in the photon energy during the process). The elastic scattering usually occurs on time scales of  $10^{-14}$  seconds, this scattering depending on the ratio of the particles size to the wavelength of incident radiation and can be referred as Rayleigh or Mie scattering. While the

## 2. SCIENTIFIC BACKGROUND

inelastic scattering by air molecules is referred to as Raman scattering.

### **Rayleigh Scattering**

Rayleigh scattering describes the dominant elastic scattering of light by particles which are small compared to the wavelength of the scattered light. In the atmosphere, Rayleigh scattering is responsible for blue sky during a clear day, because shorter wavelengths are scattered more efficiently by air molecules (e.g. N<sub>2</sub> and O<sub>2</sub>). Thus, most of the ultraviolet radiation is scattered before reaching the Earth's surface. Rayleigh scattering results from electric polarizability of air molecules, being reached the maximum of polarisation at 90° scattering angle. The dependence of the Rayleigh scattering cross-section ( $\sigma_{Ray}$ ) with wavelength ( $\lambda$ ) is very strong and given by (Platt and Stutz, 2008),

$$\sigma_{Ray}(\lambda) = \frac{8\pi^3}{3\lambda^4 N_{air}^2} \cdot (n_0(\lambda)^2 - 1)^2 \cdot F_K(\lambda) \quad (2.7)$$

where  $n_0(\lambda)$  represents the index of refraction of air as a function of wavelength,  $N_{air}$  is the number density of air, and  $F_K(\lambda)$  is the polarisability factor of air molecules, which expresses the influence of molecular anisotropy. However, equation 2.7 can be simplified using an analytic expression for the dependence of refraction index with wavelength and thus, Rayleigh scattering cross-section can be written as (Nicolet, 1984),

$$\sigma_{Ray}(\lambda) = \frac{4.02 \times 10^{-28}}{\lambda^{4.04}} \text{ cm}^2 \quad (2.8)$$

The distribution of scattered light can be described by the phase function, which gives the distribution probability of scatter intensity as a function of scattering angle, which is measured with respect to the direction of incoming radiation. For Rayleigh scattering, the phase function is given by,

$$P(\theta) = \frac{3}{4} (1 + \cos^2(\theta)) \quad (2.9)$$

where  $(\theta)$  is the scattering angle. For Rayleigh scattering, the distribution of intensity of scattered radiation is equally distributed between forward and backward directions (see Fig. 2.10).

## 2.4 ABSORPTION SPECTROSCOPY

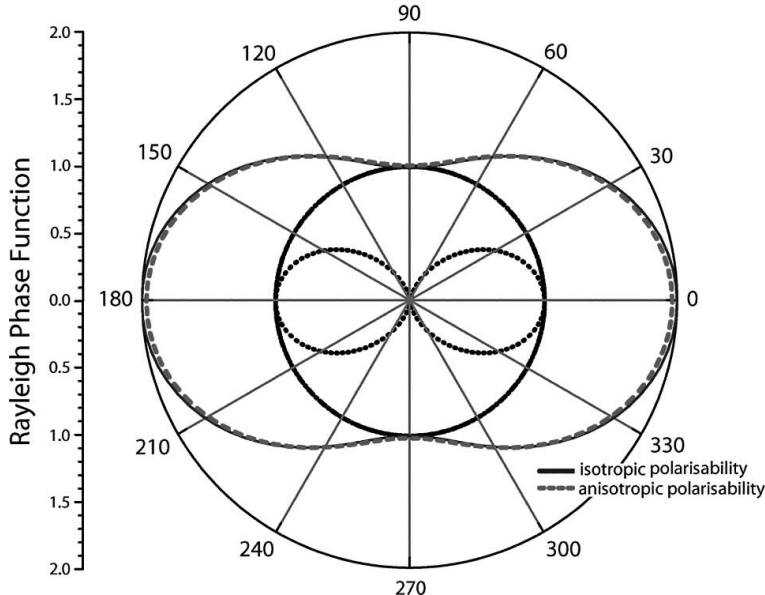


**Figure 2.10:** Polar diagram of the Rayleigh scattering phase function  $P(\theta)$  for non-polarised incident radiation (from Platt and Stutz, 2008, pp. 94).

## Mie Scattering

When light is scattered by a particle comparable in size to the wavelength of the incident light, it is known as Mie scattering. This scattering occurs mainly on “large” particles, e.g. aerosol, cloud droplets, suspended matter in liquids. In the atmosphere, there are a large variety of aerosols and their sizes and shapes among them varies, thus performing calculations using the scattering phase function can be complex. This problem can be addressed by the Mie theory, which describes the solution of Maxwell’s equations for the scattering of light on spherical particles. Mie scattering is mainly differentiated from Rayleigh scattering by its weaker dependence on the wavelength. Similar to Rayleigh scattering, Mie scattering can be defined as (Platt and Stutz, 2008),

$$\sigma_{Mie}(\lambda) \propto \frac{1}{\lambda^\alpha} \quad (2.10)$$

Where  $\alpha$  is the Ångström exponent. Small particles have larger values for  $\alpha$ . For large particles  $\alpha$  decreases. A normal distribution of particles in the atmosphere have a characteristic value of  $\alpha \approx 1.3$ .

## 2. SCIENTIFIC BACKGROUND

In the atmosphere, the distribution of scattered light for Mie scattering depends on aerosol types and particle size, as well as wavelength of scattered light, resulting in different shape of phase functions. Also, depending on  $\alpha$ , the distribution of scattered radiation has a strong dominance in the forward direction in comparison to Rayleigh scattering, being stronger for larger particles. In addition, Mie scattering is not polarising in contrast to the Rayleigh scattering.

### Raman Scattering

The inelastic scattering of photons by air molecules is known as Raman scattering and is the inelastic version of Rayleigh scattering. It can be described as the interaction of light with an air molecule that changes its energy state of excitation during the scattering process. The photon transfers part of its energy to the molecule (Stokes lines) or loses part of its energy (Anti-Stokes lines). The term rotational Raman scattering is used, if it is affected by the rotational excitation only, and if also the vibrational state changes, the term is called rotational-vibrational Raman scattering. Only discrete amounts of energy can be transferred between the photon and the molecule defined by the difference between discrete excited levels. The rotational-vibrational Raman scattering is an order of magnitude smaller than the rotational Raman scattering. In addition, rotational Raman scattering has important effects on the spectrum of scattered solar radiation in the atmosphere in comparison to direct sunlight (unscattered radiation). As a consequence of Raman scattering at air molecules, the presence of absorption features such as Fraunhofer lines changes the spectrum of scatter radiation (Brinkmann, 1968). This results in systematically less deep and strong Fraunhofer lines in the scattered sunlight in comparison to unscattered sunlight. This filling-in of absorption lines is not exclusive to the Fraunhofer structures but also occurs for other absorbers such as ozone. This effect was named as the *Ring effect*, which has been discovered by Grainger and Ring (1962) and explained by Brinkmann (1968).

#### 2.4.6 Absorption in the atmosphere

With the absorption of a photon by a molecule, electronic, vibrational and rotational transitions can occur by absorbing energy, an electron "jumps" from a lower energy state  $E_1$  to another higher energy state  $E_2$  (now the molecule is in an excited state). Classically, the absorption process is described by the

## 2.4 ABSORPTION SPECTROSCOPY

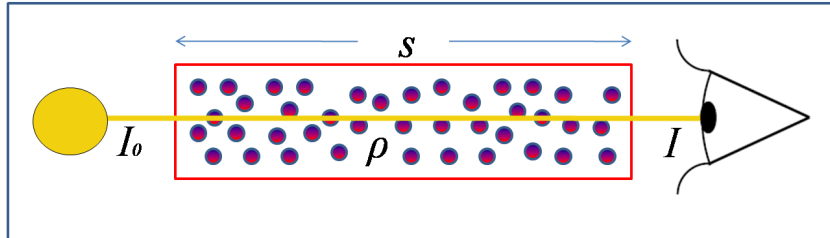


**Figure 2.11:** Representation of the Beer-Lambert law. Intensity after passing through the sample is collected by a detector. Its intensity decreases by an exponential function as  $s$  increases (from Alvarado Bonilla, 2011).

Beer-Lambert law (Platt and Stutz, 2008),

$$I(\lambda) = I_0(\lambda) \exp[-\sigma(\lambda)\rho s] \quad (2.11)$$

Where  $I_0(\lambda)$  represents the initial intensity,  $I(\lambda)$  the intensity after passing through the portion of material (see Fig. 2.11),  $\lambda$  the wavelength,  $\rho$  the uniform material concentration,  $s$  the optical path and  $\sigma(\lambda)$  represents the absorption cross-section, which is characteristic of each material.

Rewriting equation 2.11, the concentration for a uniform and homogeneous material is given by,

$$\rho = \frac{\ln(I_0/I)}{\sigma(\lambda)s} \quad (2.12)$$

where  $\ln\left(\frac{I_0}{I}\right)$  is known as optical depth or absorbance of a certain material. The optical depth is the basis for most applications of absorption spectroscopy (Platt and Stutz, 2008).

In the atmosphere the equation should include all the processes of absorption by all molecules. It also needs to account for the processes of light scattering. Although the scattering process is not an absorption process, it can be treated as an absorption in the Beer-Lambert law (Platt and Stutz, 2008). Therefore, adding the terms for Rayleigh, Mie, and Raman (by the Ring effect) scatterings, equation 2.11 can be rewritten as follows,

## 2. SCIENTIFIC BACKGROUND

$$\frac{I(\lambda)}{I_0(\lambda)} = \exp \left[ - \int ds \left( \sum_{i=1}^n \rho_i(s) \sigma_i(\lambda, s) + \rho_{Ray}(s) \sigma_{Ray}(\lambda, s) + \rho_{Mie}(s) \sigma_{Mie}(\lambda, s) + \rho_{Ring}(s) \sigma_{Ring}(\lambda, s) \right) \right] \quad (2.13)$$

where  $I_0(\lambda)$  represents the initial intensity (extra-terrestrial solar spectrum),  $I(\lambda)$  the intensity after passing through the atmosphere,  $\rho_{i,Ray,Mie,Ring}(s)$  are the number densities of the absorbers and the scattering molecules and particles, and  $\sigma_{i,Ray,Mie,Ring}(\lambda)$  are the absorption and scattering cross-sections, which are specific to each species and integration is along the light path  $s$ . The so-called Ring effect is related to rotational Raman scattering on air molecules, which produces wavelength shifts in the ultraviolet and visible wavelength range comparable to the width of Fraunhofer lines and results in an apparent filling-in of the Fraunhofer lines (more details in Sect. 2.4.5). Thus, the Ring effect is treated as an additional absorber. Here, the differential form of Beer-Lambert law is used, because  $\rho_i$  varies along the light path as it changes with altitude.

### 2.4.7 Differential Optical Absorption Spectroscopy (DOAS)

DOAS has been frequently applied to measure trace gases in the troposphere and stratosphere (Platt and Stutz, 2008). This technique allows the determination of atmospheric amounts of trace gases with narrow absorption bands in the ultraviolet and visible. The method analyses the intensity of the absorption bands using the Beer-Lambert law in the atmosphere. From equation 2.13 and not taking into account any dependence of the cross-section on location along the light path ( $s$ )<sup>1</sup>, we can exchange the integral with the sum and can define the slant column density (SC) as,

$$SC_i = \int \rho_i(s) ds \quad (2.14)$$

---

<sup>1</sup>This is considered as an approximation, because the cross-sections normally are temperature dependent, and thus depend on altitude. Sometimes, cross-sections at different temperatures are used in the retrieval to take into account the temperature dependence of the trace gas retrieved (e.g. ozone in the UV and NO<sub>2</sub> in the visible), because the gases normally are not spread across the whole atmosphere, but located at some specific altitude.

## 2.4 ABSORPTION SPECTROSCOPY

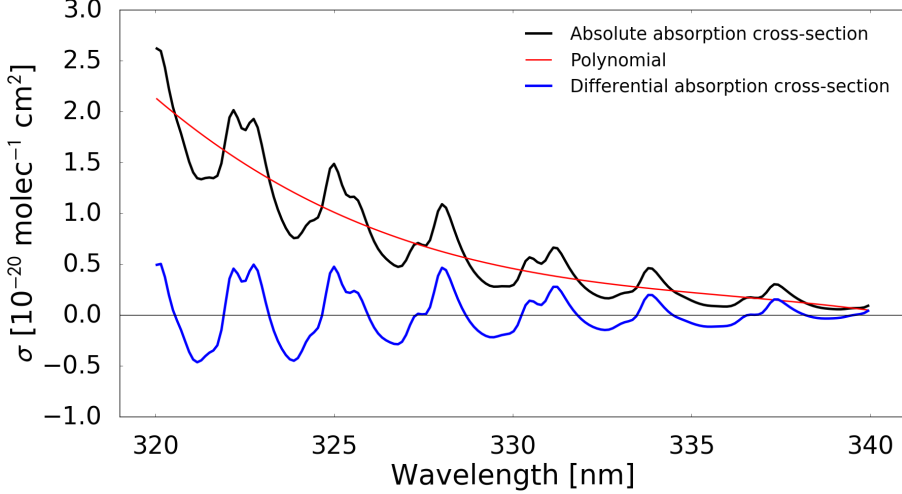


**Figure 2.12:** Principle of DOAS:  $\sigma_i^0$  and  $\sigma_i^*$  are separated by a filtering procedure, the black line represent the absolute absorption cross-section, the red line (polynomial) describe the slowly varying with wavelength, and the blue line is rapidly varying with wavelength (differential absorption cross-section).

The basic idea of the DOAS method is to decompose the cross-section into a component that varies “slowly” with wavelength,  $\sigma_i^0$ , and another component,  $\sigma_i^*$ , that shows a “fast” variation with wavelength ( $\sigma_i = \sigma_i^* + \sigma_i^0$ ).

The rapidly varying part  $\sigma_i^*$  is representative of narrow band structures in the absorption of trace gases, while  $\sigma_i^0$  includes low frequency variations of the spectrum (see Fig. 2.12, broad band structures). The latter, together with the Rayleigh scattering ( $\sigma_{Ray} \sim \lambda^{-4}$ ) and Mie scattering ( $\sigma_{Mie} \sim \lambda^{-k}, 0 \leq k \leq 2$ ), can be substituted by a polynomial proportional to  $\lambda^p$ , due to its slow variation with wavelength. With these considerations we obtain,

$$\frac{I(\lambda)}{I_0(\lambda)} = \exp \left[ - \sum_{i=1}^n \sigma_i^*(\lambda) SC_i - \sum_p a_p \lambda^p \right] \quad (2.15)$$

where  $\sigma_i^*$  is called *differential* absorption cross-section (see Fig. 2.12). As a consequence of the separation of absorption into slow and fast variation, only gases with narrow band structures in the spectral window of interest can be retrieved by the DOAS method (e.g. ozone in the UV, see Fig. 2.12). Taking the

## 2. SCIENTIFIC BACKGROUND

natural logarithm of Eq. 2.15, we obtain the optical depth ( $\tau(\lambda)$ ),

$$\tau(\lambda) = \ln \left( \frac{I_0(\lambda)}{I(\lambda)} \right) = \sum_{i=1}^n \sigma_i(\lambda) SC_i + \sum_p a_p \lambda^p \quad (2.16)$$

If  $I(\lambda)$ ,  $I_0(\lambda)$ , and the absorption cross-sections  $\sigma_i$  are known, the  $SC_i$  can be determined by a least-squares fit. The absorption cross-section of the species can be obtained from the literature or measured in the laboratory. Equation 2.16 only consider the ideal case, because the measurements are affected by noise, which can not be calculated. Thus, the measured optical depth,  $\tau(\lambda)$ , needs to be replaced by the fitted,  $\tau_{fit}(\lambda)$ , which differs from the measured optical depth as,

$$r(\lambda_k) = \tau(\lambda_k) - \tau_{fit}(\lambda_k) \quad (2.17)$$

where  $\lambda_k$  represents the wavelength at discrete spectral point, because the measure spectra ( $I$  and  $I_0$ ) are measured in discrete points as well. The slant columns of interest as well as the polynomial coefficients are obtained as fit parameters, which are adjusted in the DOAS fit routine to yield the best fit result ( $\tau_{fit}$ ) as close as possible to the measured optical depth ( $\tau$ ),

$$\sum_k r_k^2 \rightarrow \text{minimize} \quad (2.18)$$

$r(\lambda_k)$  is the residual spectrum at the respective wavelength point. Therefore,

$$\begin{aligned} \tau(\lambda) &= \tau_{fit}(\lambda) + r(\lambda) \\ \tau(\lambda) &= \sum_{i=1}^n \sigma_i(\lambda) SC_i + \sum_p a_p \lambda^p + r(\lambda) \end{aligned} \quad (2.19)$$

A small residual without remnants of absorption structures are request for a most successful retrieval. Thus, in order to judge the fit performed, the root mean square (RMS) is used as a quality criterion,

## 2.4 ABSORPTION SPECTROSCOPY

$$RMS = \sqrt{\frac{1}{N} \sum_{k=1}^N r_k^2} \quad (2.20)$$

This describes the deviation of measurement from the theory for each pixel, where  $N$  represent the total number of pixels in the fitting window. The data analysis is performed using the in-house software *NLIN* developed by Richter (1997). Additionally, the DOAS principle can be applied in a variety of arrangements and observation modes. These can be classified according to their light sources as active or passive DOAS. The first one uses an artificial light, while the second has a natural source light (e.g. sun, moon). This discussion is limited to explaining some of the passive DOAS configurations. Among these passive DOAS configurations, direct sunlight DOAS, multi axis DOAS (MAX-DOAS), and satellite borne DOAS (see Fig. 2.13) can be found (Platt and Stutz, 2008). For satellite DOAS, the measurements of  $I_0$  do not contain any absorption of traces gases due to the presence of Earth's atmosphere, because it usually is measured out of atmosphere. However, for ground-based DOAS the  $I_0$  measurement is performed in the zenith direction at the small solar zenith angle (SZA), because the light path through the Earth's atmosphere is shorter and thus, the absorption of different species is smaller as is showed in the Fig. 2.13, A and C. As a consequence, the slant column is not absolute, but it is the difference between the slant column ( $SC$ ) of spectrum  $I$  and the slant column of the reference spectrum  $I_0$  ( $DSC = SC - SC_{ref}$ ).

### 2.4.8 The Air mass factor

As the SC depends strongly on observation geometry and the sun's elevation above the horizon, it is often useful to compute the vertical column which is defined as the trace gas concentration integrated along vertical path,

$$VC = \int \rho_i(z) dz \quad (2.21)$$

where  $\rho_i(z)$  is the concentration of the species and  $dz$  is the vertical path through the atmosphere. The vertical and slant columns are related by the air

## 2. SCIENTIFIC BACKGROUND

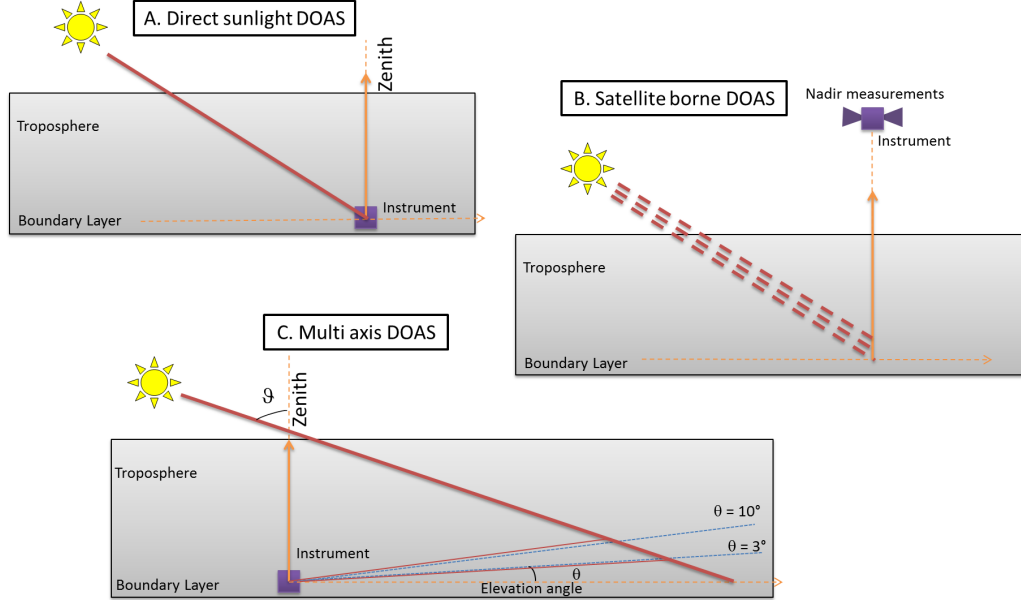


**Figure 2.13:** Schematic representation of some passive DOAS configurations: (A) direct sunlight DOAS observations, (B) satellite borne DOAS (nadir observation), and (C) multi axis DOAS observations.

mass factor (AMF). The AMF is defined as the ratio of SC and VC, and depends on the radiative transfer in the atmosphere (Platt and Stutz, 2008),

$$AMF = \frac{SC}{VC} \quad (2.22)$$

It depends on the wavelength, trace gas profile, air pressure, surface spectral reflectance (albedo), temperature, ozone and aerosol profiles, clouds, as well as on the SZA and the measurement geometry. In the computation of the AMF, an a priori assumption of the profile shape is needed. However, if the trace gas profile is not known, large uncertainties can be introduced in the conversion of SC to VC. As the measurements are functions of altitude, the so called Block-AMF (BAMF) concept is used, in order to characterize the altitude-dependent sensitivity. This describes the partial AMF within an individual atmospheric layer,

## 2.5 DESCRIPTION OF INSTRUMENTS

$$BAMF_i = \frac{SC_i}{VC_i} \quad (2.23)$$

where  $SC_i$  and  $VC_i$  represent the partial slant and vertical columns within the layer. Then, the total SC can be defined as,

$$SC = \sum_{i=0}^{TOA} BAMF_i \cdot VC_i \quad (2.24)$$

The total SC up to the top of the atmosphere is expressed as the sum of partial slant columns from the surface to the top of the atmosphere (TOA). The advantage of BAMF in contrast to the AMF is that these are independent of the trace gas profile. Thus, AMF can be computed from BAMF as,

$$AMF = \frac{\sum_{i=0}^{TOA} BAMF_i \cdot VC_i}{VC} \quad (2.25)$$

where  $VC_i/VC$  gives the relative trace gas concentration profile or shape factor (Palmer et al., 2001). As the AMFs no longer depend on the absorber profile, these can be applied to different a-priori profiles (e.g. from atmospheric chemistry models or retrieved from measurements). In addition, this approach is convenient when a large number of air mass factors have to be computed as in the case of satellite observations.

In this work, AMFs have been calculated using the radiative transfer model SCIATRAN (Rozanov et al., 2013) assuming typical glyoxal profiles as described in Wittrock (2006), page 96.

## 2.5 Description of instruments

In the following, a brief description of the instruments used in this thesis to obtain the data for the retrieval of columns of atmospheric species by the DOAS technique from ground and satellite is given.

## 2. SCIENTIFIC BACKGROUND

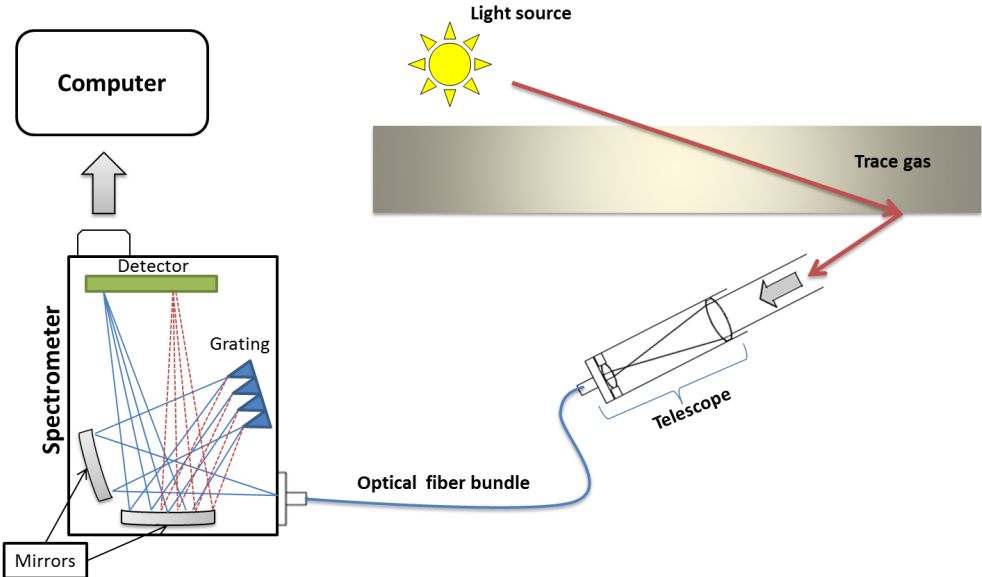


**Figure 2.14:** Schematic representation of main parts of ground-based DOAS instrument.

### 2.5.1 Ground based instruments

Currently there is a wide variety of designs of ground-based passive DOAS instruments and these designs are based on many requirements such as high sensitivity, spectral resolution and practical aspects such as the cost, weight and power consumption (Platt and Stutz, 2008).

In general, a MAX-DOAS instrument consists of a telescope coupled to a spectrograph by a fibre bundle (see Fig. 2.14). It also has a temperature controller and a telescope that can be pointed at different elevation angles. Two MAX-DOAS instruments are used in this work and both have a telescope with a field of view of  $1.2^\circ$  and an optical fiber bundle with 76 single fibers, one is coupled to two spectrometers (38 fibers for each). One spectrometer is for the ultraviolet range (315–384 nm) with a two-dimensional CCD (512x2048 pixels) and a spectral resolution of 0.4 nm. The second spectrometer also has a two-dimensional CCD ( $100 \times 1340$  pixels) for the visible range (400–570 nm) with a spectral resolution of 0.8 nm. The second MAX-DOAS instrument has a spectrometer that covers the ultraviolet and visible range (332–508 nm) with a two-dimensional CCD ( $512 \times 2048$  pixels) with a spectral resolution of 0.8 nm. Moreover, the

## 2.5 DESCRIPTION OF INSTRUMENTS

telescope contains a video camera and a Mercury/Cadmium (HgCd) lamp for wavelength calibration measurements. For more details see Peters et al. (2012).

### 2.5.2 Satellite instruments

The GOME, SCIAMACHY, OMI, and GOME-2 instruments are nadir viewing spectrometers providing the spectral coverage and resolution needed for DOAS retrievals of atmospheric trace gases. These instruments measure the light scattered by the atmosphere and reflected by the surface in the UV and visible range. The principal characteristics of each of these instruments are explained below.

#### GOME instrument

The Global Ozone Monitoring Experiment was carried by the European Remote Sensing platform (ERS-2). It had a double monochromator with a pre-disperser prism and four holographic grating channels as dispersing elements. These channels had wavelength intervals of 237–316 nm, 311–405 nm, 405–611 nm and 595–793 nm. The spatial resolution was 320 km×40 km and the spectral resolution was between 0.2 nm to 0.4 nm. The instantaneous field of view was  $2.9^\circ \times 0.14^\circ$  (40 km×2 km). The GOME instrument had a global coverage of three days and an equator crossing time of 10:30 LT (Local Time). The main objective of the GOME mission was to observe the global O<sub>3</sub> distribution and several other atmospheric compounds that are related to global change issues (Burrows et al., 1999). GOME data are available from April 1995 to July 2011.

#### SCIAMACHY instrument

The Scanning Imaging Absorption spectroMeter for Atmospheric ChartographY instrument was launched on the ENVISAT satellite in March 2002. It was an enhanced version of the GOME instrument, designed for a wavelength operating range of 214–2386 nm with spatial resolution of 60 km×30 km and a spectral resolution of 0.2–1.5 nm. SCIAMACHY performed solar and lunar occultation measurements and limb scans. It had an equator crossing time of 10:00 LT (half an hour earlier than the GOME instrument), and an instantaneous field of view of  $1.8^\circ \times 0.045^\circ$  (ground pixel size of 25 km×0.6 km). Global coverage was achieved in six days at the equator (Bovensmann et al., 1999). SCIAMACHY

## 2. SCIENTIFIC BACKGROUND

has been used for retrieval of many trace gases including O<sub>3</sub>, NO<sub>2</sub>, SO<sub>2</sub>, HCHO, CHOCHO, BrO, OCIO, H<sub>2</sub>O and also aerosol properties, cloud cover and cloud top high (Ladstätter-Weißenmayer et al., 2003; Wittrock et al., 2006, and references therein). The SCIAMACHY instrument provided data from April 2002 to April 2012.

### OMI instrument

The Ozone Monitoring Instrument is a nadir viewing imaging spectrograph that measures backscattered radiation in the wavelength range from 270 to 500 nm with an average spectral resolution of about 0.5 nm and a spatial resolution of 13 km×24 km at nadir that can be zoomed to 13 km×13 km. The radiation entering the telescope is split into two channels, the UV channel (270–365 nm) and the visible channel (365–500 nm). The UV channel is subdivided into two full performance ranges of 270–310 nm and 310–365 nm with spectral resolutions of 0.42 nm and 0.45 nm, respectively. The UV channel enables retrieval of O<sub>3</sub>, HCHO, SO<sub>2</sub>, BrO, and OCIO (González Abad et al., 2015), while the visible channel enables retrieval of NO<sub>2</sub> and CHOCHO (Chan Miller et al., 2014; Alvarado et al., 2014; Anand et al., 2015). OMI has a swath width of 2600 km due to its wide field of view of 114°, which provides global coverage in one day (14 orbits). This has a sun-synchronous polar orbit with an equator crossing time at 13:45 LT (ascending node). The OMI instrument consists of a two-dimensional CCD, one used for detecting spectral information (780 pixels) and the other for spatial information (576 pixels). Thus, this does not use a scan mirror as GOME, GOME-2(MetO-A and-B) and SCIAMACHY instruments for recording spatial information. In addition, OMI does not have polarization sensitivity, because it uses a polarization scramble which depolarizes the radiation over all wavelength ranges. Moreover, OMI does not have a spectral lamp onboard for the spectral calibration, but this is performed using a spectrum of Fraunhofer lines and a spectral slit function measured on the ground. This calibration is only performed for the nadir row, because the calibration for every single spectrum using this procedure would consume too much time (Levelt et al., 2006). The OMI instrument provides data from October 2014 until today.

## 2.5 DESCRIPTION OF INSTRUMENTS

### **GOME–2 instrument**

The second Global Ozone Monitoring Experiment is one of the European instruments carried by the MetOp platforms, and consists of a series of three satellites which carry 11 different scientific instruments with a mission duration of six years for each one. The GOME–2 instrument consists of a double monochromator with a predisperser prism and four holographic gratings. The spectral range is from 240 to 790 nm in four different channels (1. 240–315 nm, 2. 311–403 nm, 3. 401–600 nm, and 4. 590–790 nm) with a spatial resolution of 80 km×40 km and a spectral resolution of 0.2–0.4 nm. The instantaneous field of view is  $0.286^\circ \times 2.75^\circ$  (4 km×40 km), and the instrument provides nearly daily global coverage (Callicies et al., 2000). The GOME–2 instrument on board the MetOp–A platform provides data from January 2007 until today, and the GOME–2 instrument on board the MetOp–B since September 2012. MetOp–C is scheduled to launch in August 2018. For now, we will refer to GOME–2 (MetOp–A and–B) as GOME–2 (A and B).

# 3

## Glyoxal retrieval from satellite measurements

### 3.1 Introduction

In the last decades, the applications of remote sensing from space and in particular by the DOAS technique have had a rapidly growing and important role in the observations of atmospheric composition. There are many satellite based studies of HCHO and somewhat fewer on CHOCHO. However, the exact amounts of VOC emissions from anthropogenic, pyrogenic and biogenic sources are unfortunately still unknown. The studies from satellites have been performed using different instruments such as GOME (Burrows et al., 1999), SCIAMACHY (Burrows et al., 1995; Bovensmann et al., 1999), OMI (Leveld et al., 2006), and GOME–2 (Callies et al., 2000), which when combined provide a continuous data set covering a period of 20 years. Below, a chronological overview of VOC retrievals from satellite measurements is presented. The first results reported of HCHO retrieval from space were presented by Thomas et al. (1998) and Burrows et al. (1999). Thomas et al. (1998) published results of HCHO slant columns over southeast Asia from GOME measurements between August and October 1997, finding slant column values in the range  $2.5$  to  $4.0 \times 10^{16}$  molec cm $^{-2}$ . Burrows et al. found tropospheric HCHO VCs up to  $2.0 \times 10^{16}$  molec cm $^{-2}$ , over Indonesian biomass burning in summer-fall 1997, also from GOME measurements. Soon

### 3.1 INTRODUCTION

after, Chance et al. (2000) published results of HCHO observations over North America for July 1996, also from the GOME instrument. This study reported values of HCHO in the range  $2$  to  $3.0 \times 10^{16}$  molec cm $^{-2}$  over North America. These values were compared by Palmer et al. (2001) with global chemistry transport model (CTM) results that showed an overestimation of 30% in simulated HCHO VCs compared to GOME results. Abbot et al. (2003) and Martin et al. (2004b) reported results from satellite observations over North America, the first one presenting an evaluation of a multi-year (1995–2001) time series of HCHO columns from the GOME instrument for determination of the seasonal and interannual variability of isoprene emissions, showing a good consistency between known isoprene emissions and HCHO columns from GOME over this region. The latter study reported a comparison of NO<sub>2</sub> and HCHO from the GOME instrument with insitu measurements from aircraft of tropospheric NO<sub>2</sub> and HCHO columns over eastern Texas and the southeast United States. These results showed a mean absolute difference between both techniques of  $6.0 \times 10^{14}$  molec cm $^{-2}$  for NO<sub>2</sub> and  $5.5 \times 10^{15}$  molec cm $^{-2}$  for HCHO.

Hewson et al. (2013) reported a characterisation of GOME–2 (A) HCHO retrieval based on sensitivity tests for minimisation of the fitting residual, performing an evaluation in the spectral fitting window for HCHO, as well as testing the major parameters such as polynomial order, I<sub>0</sub> correction, fitted ancillary absorbers and offset corrections. The results showed that changes in the spectral fitting window produce variations in the retrieved HCHO SC around 190 and 390% globally. These tests provided an optimal group of parameters for HCHO retrievals, based on the minimisation of error.

The most recent study by González Abad et al. (2015) focused on a new HCHO retrieval from OMI measurements. They present an updated algorithm, including a new high-resolution solar reference spectrum, additional interfering species such as O<sub>4</sub> and O<sub>3</sub> at 295 K, a new fitting window. In addition, they use a model reference sector over the remote Pacific Ocean to correct for possible biases and their temporal drift in the retrieved SC, leading to improvements in the fit residual and reductions in the noise.

In order to improve our understanding of VOC sources and extend the amount of data available, Wittrock et al. (2006) published the first global simultaneous observation of HCHO and CHOCHO by the SCIAMACHY instrument. The highest concentrations of both species were found over areas with large biogenic isoprene emissions and also in regions with anthropogenic emissions and

### 3. GLYOXAL RETRIEVAL FROM SATELLITE MEASUREMENTS

biomass burning. Both HCHO and CHOCHO showed similar global patterns and ratios of CHOCHO to HCHO around 0.05 in regions with biogenic emissions. The study also presented a comparison of results from ground-based DOAS and SCIAMACHY measurements, finding good agreement between both datasets. In addition, Wittrock (2006) reported on the comparison of HCHO between the SCIAMACHY and GOME instruments for January to March 2003 over Africa, showing a correlation of 0.73 and a consistent agreement between both instruments.

Kurosu et al. (2007) reported on the first CHOCHO retrieval from OMI observations, presenting seasonally resolved global distributions of HCHO and CHOCHO during twelve months (2005–2006) over regions of biomass burning and anthropogenic sources. These results were compared with ground-based measurements as well as with simulations from CTM.

De Smedt et al. (2008) published results of tropospheric HCHO from the GOME and SCIAMACHY instruments during 1996–2007 using a new retrieval, which led to a reduction in the columns over tropical forests of about 20–30% compared to previous studies and also to reduce fitting errors.

Vrekoussis et al. (2009) reported on a new retrieval of CHOCHO from SCIAMACHY measurements, where the largest values over tropical and sub-tropical regions were found as part of a study of temporal and spatial variability of CHOCHO. This result was associated with high biological activity and plumes from vegetation fires. Also, they found in the seasonality highest values during the warm and dry periods due to the enhancement of biogenic activities and/or biomass burning from natural and man-made fires. A study by Stavrakou et al. (2009a) confirms the high emissions of CHOCHO from natural sources, however the amount of these sources is still unknown and the comparison with simulated CHOCHO columns led to a good agreement between both, but with an underestimation in the simulated columns.

Vrekoussis et al. (2010) published the firsts retrievals of HCHO and CHOCHO columns from the GOME–2 (A) instrument over regions with enhanced biogenic emissions. They used the ratio of CHOCHO to HCHO to classify different sources. These results were compared with SCIAMACHY observations showing good agreement for the period 2007–2008. Lerot et al. (2010) reported an improved retrieval for CHOCHO and compared the results with model calculations. They presented for the first time a retrieval algorithm with a two-step approach to reduce interferences in the CHOCHO analysis over some oceanic

### 3.2 OPTIMIZATION OF THE GLYOXAL RETRIEVAL FROM SATELLITE MEASUREMENTS

regions caused by liquid water absorption. The latter approach resulted in an improvement of the fit quality and less unphysical negative CHOCHO columns over clear water regions. The highest CHOCHO values were found over continental tropical regions and the comparison with simulated results from a CTM showed that there are probably missing CHOCHO sources in the CTM.

A study over China by Liu et al. (2012) compared CHOCHO satellite observations with model simulated values. This comparison showed a large unknown source of CHOCHO over China. They attributed this missing source to an underestimation of aromatics emissions.

Chan Miller et al. (2014) reported on OMI retrievals of CHOCHO. They showed that CHOCHO is very sensitive to the settings of the retrieval. Also, Chan Miller et al. (2014) used a two-step approach similar to Lerot et al. (2010) to reduce the interferences with liquid water over ocean regions. In addition, they used a normalization region over the Sahara instead of the Pacific Ocean region, which is used in other studies (Vrekoussis et al., 2009; Lerot et al., 2010).

In this chapter, results of an improved CHOCHO DOAS retrieval applied to the radiances measured by OMI are presented. These results are extended to data from the GOME–2 (A and B) and SCIAMACHY instruments. Sensitivity tests have been performed aiming at the optimization of the CHOCHO retrieval parameters, and at reducing spectral interferences with liquid water absorption over ocean regions and with tropospheric NO<sub>2</sub> absorption over areas with large NO<sub>x</sub> emissions. Part of these results have been published in Alvarado et al. (2014).

## 3.2 Optimization of the retrieval from satellite measurements\*

For the retrieval of weak absorbers such as CHOCHO, an appropriate selection of the fitting window is a prerequisite for deriving accurate SCs. Most retrievals focus on avoiding spectral regions where interfering species have significant absorption lines. Retrievals of CHOCHO are usually performed in the spectral region between 420 and 460 nm, with polynomials of order 2, 3, or 4 for removal of broad-band signatures, and including the respective interfering species

---

\* Parts of this section have been previously published as part of Alvarado et al. (2014).

### 3. GLYOXAL RETRIEVAL FROM SATELLITE MEASUREMENTS

(Wittrock et al., 2006; Vrekoussis et al., 2009). As mentioned above, Lerot et al. (2010) showed that absorption by liquid water interferes with CHOCHO retrievals over oceans, and a pre-fitting of the liquid water signature using a larger fitting window was suggested to improve the CHOCHO retrievals. Despite these efforts to achieve better CHOCHO retrievals, the results are still affected by large uncertainties. Here, a new retrieval algorithm for the OMI measurement is presented based on detailed sensitivity tests, which has been extended to GOME–2 (A and B) and SCIAMACHY measurements.

For the glyoxal retrieval, the OMI, GOME–2 (A and B), and SCIAMACHY level 1B calibrated data have been used, which are provided by NASA, EU-METSAT, and ESA through DLR respectively. Also, a two-step wavelength calibration has been applied which first aligns the irradiance spectrum to a high-resolution Fraunhofer spectrum (Chance and Kurucz, 2010) and then the radiance spectrum to the irradiance. An intensity offset is fitted as well. Additionally, the quality flags provided by NASA are used to reduce problems with the row anomaly in the OMI data<sup>2</sup>.

The additional settings used in the glyoxal retrievals within this work are described in detail below.

#### 3.2.1 Dependence on the fitting window

Systematic errors can be introduced into the glyoxal retrieval by possible cross-correlations between reference cross-sections, by the influence of instrumental features, and by shifts in the wavelength calibration. Thus, a dependence on the fitting window can be observed in the retrieved CHOCHO SCs, because all these systematic errors exhibit a dependency on the wavelength interval.

In order to test the sensitivity of the retrieval on the wavelength interval selected and to find an appropriate fitting window for the CHOCHO retrieval, a synthetic measurement spectrum of backscattered Earthshine was computed using the radiative transfer model SCIATRAN (Rozanov et al., 2013). A satellite measurement in nadir geometry, at solar zenith angle of 41°, and at constant surface reflectance of 5 % was simulated in the wavelength range of 365–500 nm at a spectral sampling of 0.2 nm. Absorption cross-sections of CHOCHO and

<sup>2</sup>The row anomaly is a dynamic anomaly, which changes over time and corresponds to row on the CCD detectors. This anomaly affects the quality of the level 1B radiance data at all wavelength of particular OMI viewing direction and shows differences between channels.

### 3.2 OPTIMIZATION OF THE GLYOXAL RETRIEVAL FROM SATELLITE MEASUREMENTS

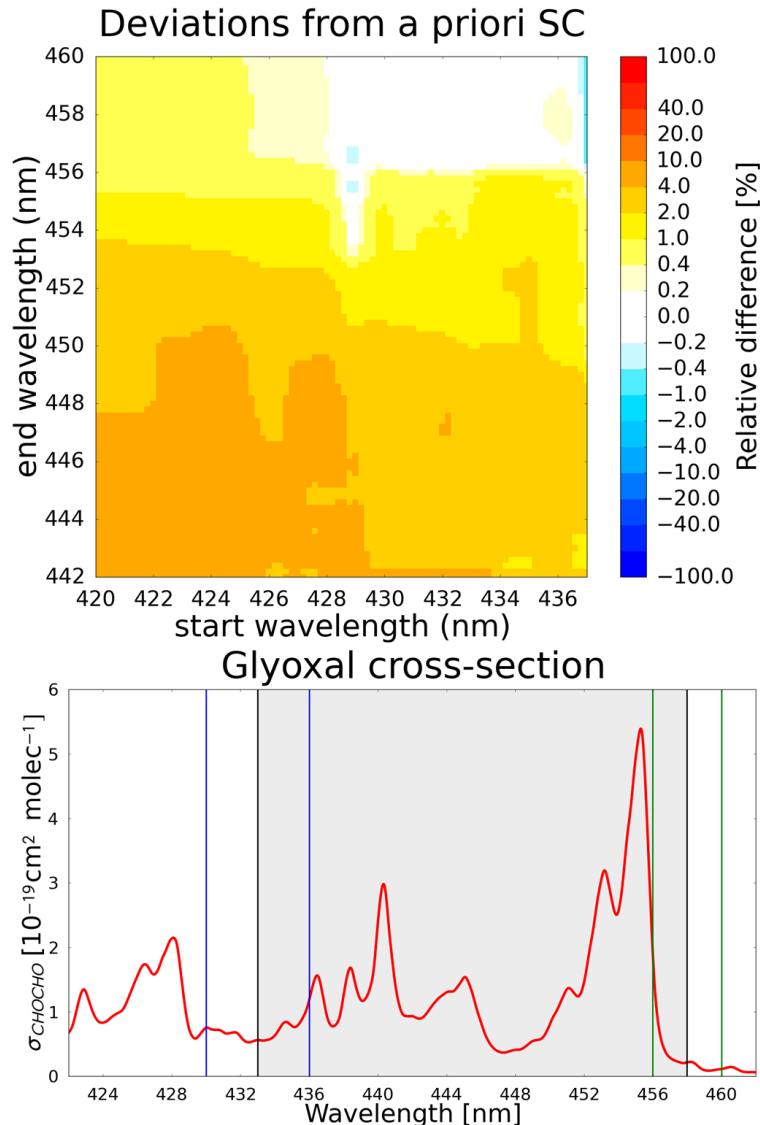


**Figure 3.1:** Colour mapping of the relative difference of CHOCHO SCs with respect to the a priori (“true value”) ( $\frac{\text{SC}_{\text{fitted}} - \text{SC}_{\text{true}}}{\text{SC}_{\text{true}}} \times 100$ ) retrieved from a synthetic spectrum for wavelength intervals with start limits of 420–437 nm and end limits 442–460 nm (top). Glyoxal absorption cross-section at 296 K (Volkamer et al., 2005b); blue and green lines mark the start and end of the favourable wavelength intervals, respectively, with the main absorption bands in the shaded area (bottom).

### 3. GLYOXAL RETRIEVAL FROM SATELLITE MEASUREMENTS

**Table 3.1:** Regions selected for Fig. 3.3.

	Latitude [°]	Longitude [°]	Date
Africa	$-5.0 \pm 3.0$	$13.5 \pm 0.5$	9 Aug 2007
Brazil	$-8.5 \pm 3.5$	$-64.5 \pm 2.5$	19 Aug 2007
Europe	$49.5 \pm 3.5$	$7.0 \pm 5.0$	20 Aug 2007
NA	$31.0 \pm 3.0$	$-82.5 \pm 1.5$	14 Aug 2007
Desert	$22.0 \pm 3.0$	$20.0 \pm 4.0$	15 Aug 2007
Ocean	$25.0 \pm 1.0$	$144.0 \pm 1.0$	1 Aug 2007

interfering species ( $\text{NO}_2$ ,  $\text{O}_3$ ,  $\text{H}_2\text{O}_{\text{vap}}$ , and  $\text{O}_4$ ; see Fig. 3.2), degraded to the OMI spectral resolution, were used to model absorption processes in the light path. However, rotational Raman scattering (Ring effect) was not included in the model simulation. For the atmospheric profiles, the assumption was made of a CHOCHO concentration profile, exponentially decreasing with altitude, and no stratospheric contribution. The sensitivity test consists of retrievals of glyoxal SCs in different wavelength intervals. The results are shown in Fig. 3.1 (top), where each pixel corresponds to one CHOCHO SC retrieved using one particular wavelength range and is colour coded according to the relative difference between the retrieved and a priori SC ( $2.69 \times 10^{15}$  molec  $\text{cm}^{-2}$ ). The wavelength intervals have start limits of 420–437 nm, end limits of 442–460 nm, the limits have steps of 0.2 nm, and a polynomial of order 3 is used in the retrievals. This test follows the method developed in Vogel et al. (2013).

In general, the observed deviations are mostly rather small (i.e.  $< 4\%$ ). The largest deviations are found for wavelength ranges with start limits between 420–430 nm and end limits of 442–448 nm, which correspond to the wavelength region where glyoxal only has weak absorption bands and consequently the interference with the strong absorbers (e.g.  $\text{NO}_2$  and  $\text{O}_3$ ) is more significant. These deviations decrease for start and end wavelengths in the ranges 430–437 and 448–454 nm, respectively, as these ranges include an additional glyoxal band with greater absorption than those found between 420 and 430 nm. Nevertheless, interferences with the absorption bands of  $\text{NO}_2$ ,  $\text{O}_3$ ,  $\text{O}_4$ , and  $\text{H}_2\text{O}_{\text{vap}}$  are present in these wavelength ranges (see Fig. 3.2), the last two being the dominant species. Consequently, the deviations decrease when the strongest absorption band of glyoxal

### 3.2 OPTIMIZATION OF THE GLYOXAL RETRIEVAL FROM SATELLITE MEASUREMENTS

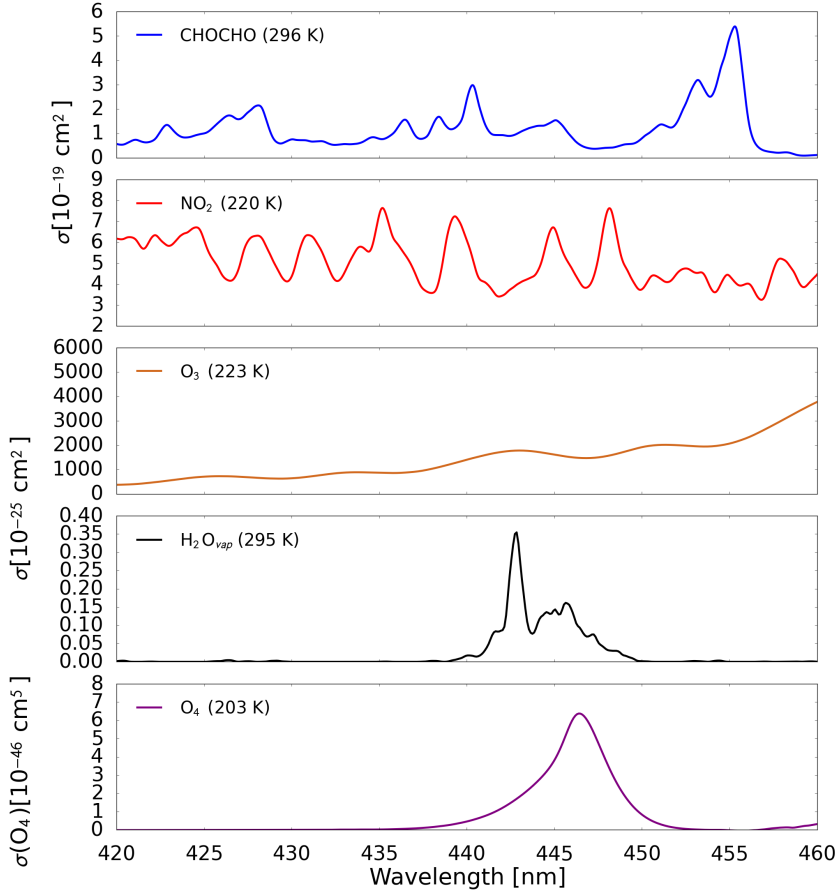


**Figure 3.2:** Different absorption cross-sections degraded to the OMI resolution included in the glyoxal retrieval. CHOCHO at 296 K (Volkamer et al., 2005b); NO<sub>2</sub> at 220 K (Vandaele et al., 1998), O<sub>3</sub> at 223 K (Bogumil et al., 2003), H<sub>2</sub>O at 295 K (Rothman et al., 2005), and O<sub>4</sub> at 203 K (Thalman and Volkamer, 2013).

is included, the most accurate retrievals being found in the wavelength intervals with start limits of 430–436 nm and end limits of 456–460 nm. Thus, the best wavelength intervals for the retrieval of glyoxal from synthetic spectra simulated for the specific scenario described above, have start limits of 430–436 nm and end limits of 456–460 nm, corresponding to deviations close to zero from the a priori SC. In Fig. 3.1 (bottom), the blue lines mark these start limits and the green lines the end limits.

To compare these results with real data, a similar test was performed for

### 3. GLYOXAL RETRIEVAL FROM SATELLITE MEASUREMENTS

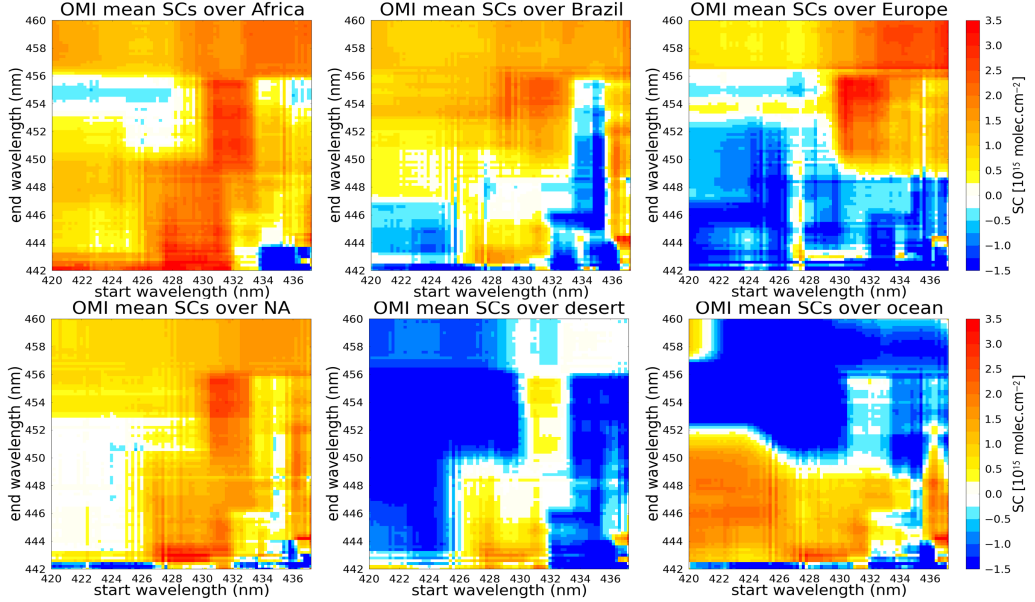


**Figure 3.3:** CHOCHO SC means retrieved over selected regions from OMI measurements for wavelength windows with start limits of 420–437 nm and end limits of 442–460 nm, during different days on August 2007 (see Table 3.1).

selected relatively small areas over Africa, Europe, North America (NA), Brazil, a desert region, and an oceanic area (see Table 3.1). These regions were selected to be representative for different CHOCHO levels and sources, as well as for possible interfering effects (sand, liquid water absorption). For each region, more than 100 spectra measured by OMI were included to obtain significant results and to limit the effect of measurement noise (with SC detection limits between  $0.5 \times 10^{14}$  molec cm $^{-2}$  and  $2.0 \times 10^{14}$  molec cm $^{-2}$ ). The retrieval settings were identical to the synthetic test described above; additionally, the Ring cross-section and an intensity offset were included. Figure 3.3 shows averages of the retrieved SCs for each region and for all wavelength ranges. The variation in retrieved SCs is large on real data for all regions selected, highlighting the fact that glyoxal retrievals are very sensitive to details of the fitting parameters selected. A similar variability in the results is found for ground-based data (see Sect. 6.3) as well as for SCIAMACHY and GOME-2 (A) measurements over two selected regions (see Fig. 3.4), but the observed pattern of deviations varies. This indicates that both interference between absorption from different absorbers

### 3.2 OPTIMIZATION OF THE GLYOXAL RETRIEVAL FROM SATELLITE MEASUREMENTS

and also instrumental effects may play a role. In the absence of validation data, the true columns are not known for this test on real measurements. However, some consistency considerations can help to make a choice for the fitting range. First, the strongest absorption band of glyoxal should be included in the fitting window, because without this band, interferences with other species in the wavelength range of weak glyoxal absorption bands (420–450 nm) are stronger and sometimes lead to unphysical results. This restricts our intervals to start wavelengths of 420–437 nm and end wavelengths of 456–460 nm. Second, the SC averages obtained over the desert in the restricted region are mostly negative for start wavelengths below 432 nm (larger fitting windows, Fig. 3.3), most likely due to soil interferences (Richter et al., 2011). In addition, large CHOCHO SCs are retrieved from the SCIAMACHY data, and SCs around zero from the GOME–2 (A) data for wavelength windows with start limits below 432 nm over the desert region. Under normal circumstances, however, no CHOCHO can be expected in the desert atmosphere. Thus, the fit windows can be limited to start wavelengths between 432 and 437 nm, which correspond to mean values close to zero for the three instruments, and also correspond to lower root mean square (RMS) values of the spectral fit for the Africa region (see Fig. 3.5). Then, the chosen wavelength intervals can be restricted again to start limits between 432 to 437 nm and end limits between 456 to 460 nm, which also show homogeneous patterns for Africa, Brazil, Europe, and the North America region within the chosen wavelength ranges and also have limits similar to the wavelength ranges obtained from the synthetic spectrum. However, over the ocean region, negative SC means are obtained, probably as a consequence of interference with liquid water absorption (Lerot et al., 2010; Alvarado et al., 2014). Additionally, the fitting windows used for glyoxal retrievals in previous studies are found in these chosen wavelength intervals (Vrekoussis et al., 2010; Lerot et al., 2010; Alvarado et al., 2014). Despite the good consistency found for OMI data over the selected regions, the glyoxal retrieval appears to be sensitive to small changes in wavelength and it is a challenge to determine the most appropriated fitting window.

### 3. GLYOXAL RETRIEVAL FROM SATELLITE MEASUREMENTS

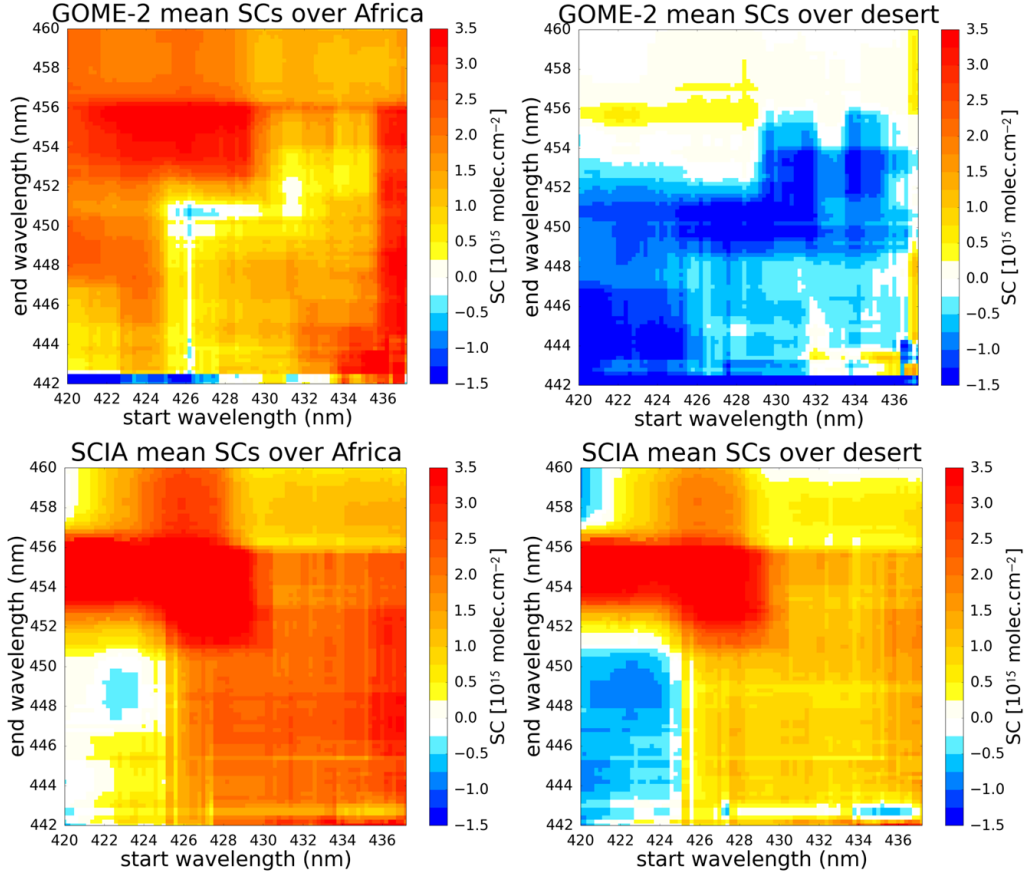


**Figure 3.4:** Colour mapping of absolute CHOCHO SCs for different wavelength with start limits of 420–437 nm and end limits 442–460 nm retrieved from the GOME-2 (A, top) and SCIAMACHY (bottom) measurements over two Africa regions (large forest and desert), during different days in August 2007.

In the following, we will use a fitting window extending from 433 to 460 nm (within the chosen wavelength intervals), as indicated by the shaded area in Fig. 3.1 (bottom), which is slightly larger than the fitting windows used in previous studies (e.g. Vrekoussis et al., 2010; Alvarado et al., 2014). In addition, when the liquid water cross-section is included in the glyoxal retrieval (see Sect. 3.2.3), a reduction in the number of negative glyoxal SCs is observed over ocean using this wavelength range in comparison to a smaller fitting window (e.g. 434–458 nm) for all three instruments. This wavelength range covers the strong CHOCHO absorption bands, which have already been used to retrieve glyoxal from ground

### 3.2 OPTIMIZATION OF THE GLYOXAL RETRIEVAL FROM SATELLITE MEASUREMENTS

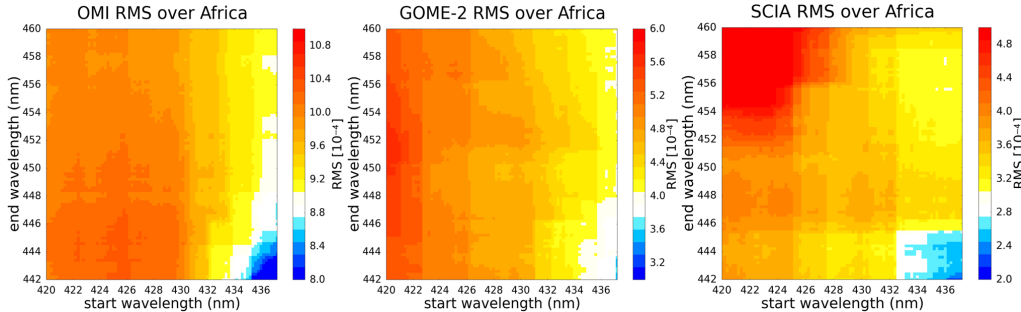


**Figure 3.5:** RMS obtained in the glyoxal retrieval from OMI (left), the GOME-2 (A, middle) and SCIAMACHY (right) measurements for different fitting intervals, with start limits of 420–437 nm and end limits 442–460 nm over large forest area (Africa) during a day in August 2007.

and ship-based instruments (Sinreich et al., 2007, 2010) as well as from satellite measurements (Wittrock et al., 2006; Vrekoussis et al., 2009, 2010; Lerot et al., 2010).

#### 3.2.2 Dependence on the polynomial order

Another main parameter in the DOAS retrieval is the order of the polynomial accounting for broadband features in the measured spectra. Experience shows that a low-order polynomial helps to avoid instability in the fit, while increasing the degree usually improves the fitting residual, in particular for large fitting windows. In order to evaluate the dependence of the fit results on the polynomial degree, the glyoxal retrievals were performed for both cases (i.e. using the synthetic spectrum and real data) for polynomial orders 2, 3, and 4. For the synthetic spectrum, Fig. 3.6 (top) shows the deviations of the CHOCHO SCs from the a priori SC, for polynomial degrees 2, 3, and 4. For the specific conditions of the simulated spectrum, the results are similar for polynomial orders 3 and 4, while the SCs retrieved with polynomial order 2 show larger deviations from the true value for most wavelength intervals and more variability for the wavelength ranges where the deviations are close to zero for the polynomial orders 3 and 4.

For comparison, glyoxal columns from OMI measurements over two small regions (Africa and North America) have been retrieved for August 2007, as high glyoxal levels are expected over these areas in summer, which are attributed to biogenic activity and biomass burning. Figure 3.6 (middle and bottom) shows

### 3. GLYOXAL RETRIEVAL FROM SATELLITE MEASUREMENTS

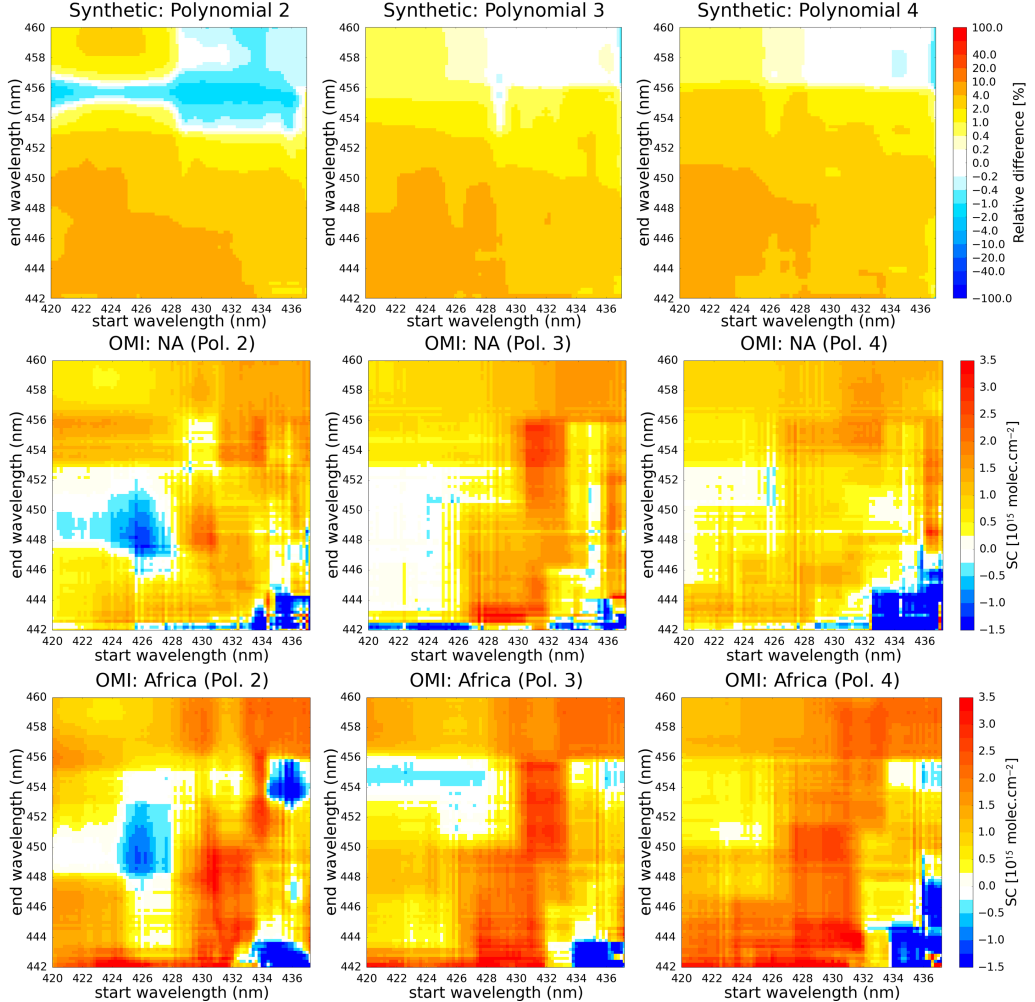


**Figure 3.6:** Colour mapping of CHOCHO SC deviation with respect to the a priori (“true value”), retrieved from a synthetic spectrum for wavelength intervals with start limits of 420–437 nm, end limits 442–460 nm, and polynomial degrees 2, 3, and 4 (top). CHOCHO SC means retrieved over Africa and North America for August 2007 (see Table 3.1) from OMI measurements for different wavelength ranges and polynomial orders (middle and bottom).

similar patterns for polynomial order 3 in both regions and a more homogeneous behaviour than polynomial order 4 for the chosen wavelength ranges, while results using polynomial degree 2 show more variability in the CHOCHO SCs for the wavelength area of interest. However, among the instruments, the polynomial

### 3.2 OPTIMIZATION OF THE GLYOXAL RETRIEVAL FROM SATELLITE MEASUREMENTS

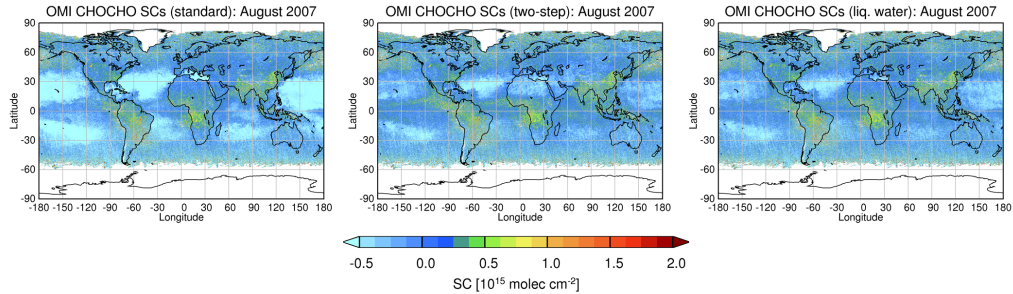


**Figure 3.7:** Maps of monthly averaged glyoxal slant columns retrieved from OMI measurements for August 2007 (top). Cloud screening has been applied in all maps (see Sect. 3.2.6). CHOCHO SCs obtained using the standard CHOCHO retrieval without liquid water absorption cross-section (left), by using the two-step fit (centre), and including the liquid water absorption cross-section in the standard CHOCHO retrieval (right).

degree 4 show a more consistent result than polynomial degree 2 and 3. In view of small differences found between polynomial degrees 3 and 4, and more consistency in the result among instruments for polynomial degree 4, in the following a polynomial order of 4 is selected in the glyoxal retrieval for all instruments. The differences in the polynomial for the different instruments is probably the result of instrument calibration issues.

#### 3.2.3 Interference with liquid water absorption

One of the main problems in glyoxal retrievals found by Vrekoussis et al. (2009) was the negative CHOCHO SC values over the remote Pacific Ocean, possibly due to interferences from the absorption by liquid water. Later, similar results were found by Lerot et al. (2010), who proposed a two-step retrieval to reduce the negative values over ocean regions. In a first step, they retrieved liquid water SCs from a large fitting window (405–490 nm). In a second step, they then retrieved glyoxal SCs in the wavelength range of 435–460 nm, fixing the liquid water SC to the results from the first step. This method worked well for GOME–2 fits, significantly reducing the impact of liquid water absorption on the glyoxal fits. Similar problems of interferences over ocean regions were found in the glyoxal retrieval from OMI measurements.

### 3. GLYOXAL RETRIEVAL FROM SATELLITE MEASUREMENTS

In order to reduce the number of negative glyoxal SCs over the remote Pacific Ocean, two different approaches were tested. First, the approach proposed by Lerot et al. (2010) is followed and a two-step fitting procedure is applied, where the absorption by liquid water is determined in a pre-fit using a wavelength range of 410–495 nm. Second, the liquid water cross-section is introduced in the standard glyoxal fit. Figure 3.7 shows a comparison of monthly global maps of CHOCHO SCs for August 2007, standard (left), two-step(centre), and including the liquid water absorption cross-section (right).

All three maps show a similar pattern over ocean, with negative values of varying amplitude over clear water regions. Clearly, SCs obtained from the standard retrieval without the liquid water absorption cross-section have more negative results over oceans than the two retrievals that add this cross-section. In addition, the standard glyoxal retrieval shows a dependence of CHOCHO SCs on latitude in comparison to those that include the liquid water cross-section in the retrieval. Figure 3.8 shows CHOCHO SC means retrieved over a small oceanic region at different latitudes (latitude:  $55.0^{\circ} \pm 1.0^{\circ}$ ,  $25.0^{\circ} \pm 1.0^{\circ}$ ,  $0.0^{\circ} \pm 1.0^{\circ}$ ,  $-25.0^{\circ} \pm 1.0^{\circ}$ ,  $-55.0^{\circ} \pm 1.0^{\circ}$ ; longitude:  $144.0^{\circ} \pm 1.0^{\circ}$ ) for different wavelength intervals. As can be seen from the figures showing the dependence on fitting window, the two-step approach and including the liquid water cross-section reduce the number of negative glyoxal SCs and their latitudinal dependence over the oceans, however the two-step approach has slightly more variability in the wavelength ranges chosen as optimal in the Sect. 3.2.1.

The two-step approach and including the liquid water cross-section in the fit show similar behaviour over ocean and both significantly reduce the number of unphysical negative values over these regions. The approaches show some differences in CHOCHO SCs over land (see Fig. 3.7), mainly over desert regions, most likely due to spectral interferences with sand (Richter et al., 2011). Figure 3.9 shows CHOCHO SC averages for the standard fit, the two-step fit, and including the liquid water cross-section retrievals as function of longitude for the latitude range of  $21.0^{\circ} \pm 7.0^{\circ}$ . The two-step approach and including the liquid water cross-section show a significant reduction of the number of negative SCs over ocean (Longitudes  $< -17.0^{\circ}$ ) in comparison to the standard retrieval, similar to the observation made from the global maps. However, large differences are found over land (Longitudes  $> -17.0^{\circ}$ ) between the two-step approach and the other two retrievals, most likely as a consequence of interferences with sand.

Based on the global behaviour, the smallest number of negative values is

### 3.2 OPTIMIZATION OF THE GLYOXAL RETRIEVAL FROM SATELLITE MEASUREMENTS

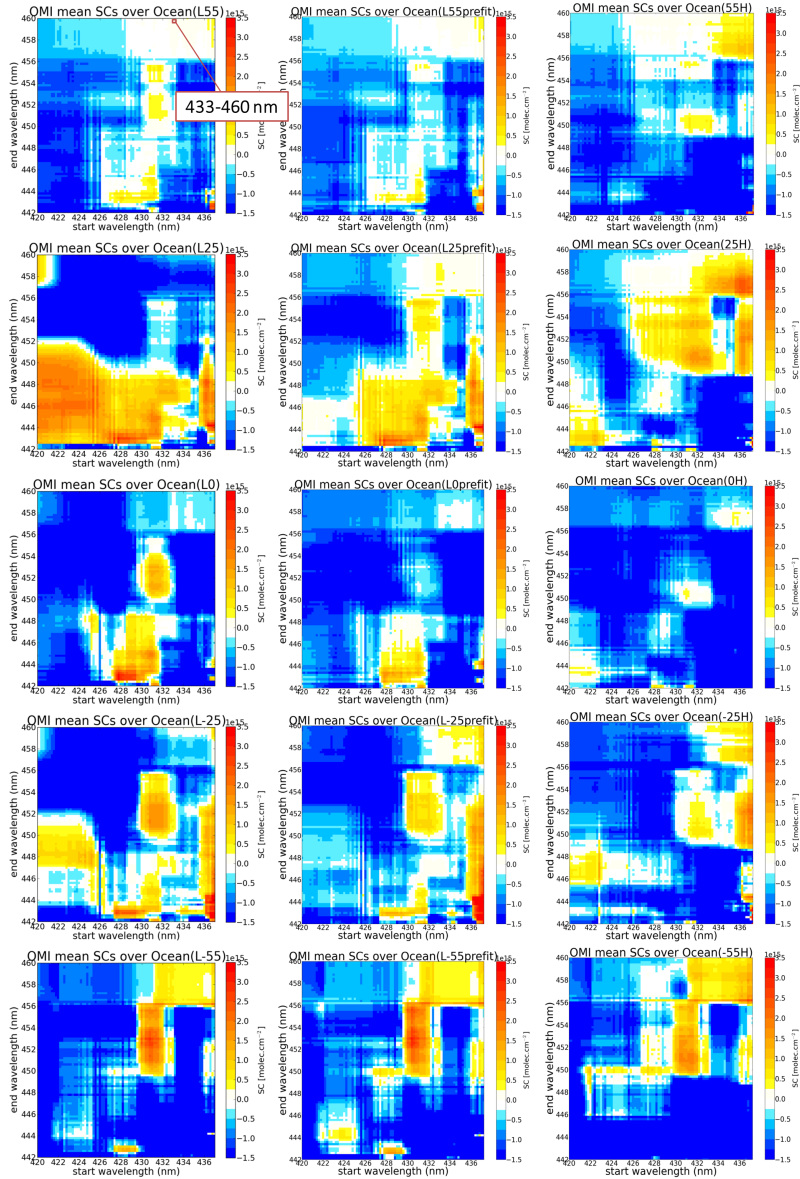


**Figure 3.8:** CHOCHO SC means retrieved using the standard retrieval without liquid water absorption cross-section (left), by using the two-step approach (centre), and including the liquid water absorption cross-section (right) at different fit windows with start limits of 420–437 nm and end limits 442–460 nm over ocean (latitudes of 55° N–55° S and longitudes of  $144.0^\circ \pm 1.0^\circ$ ) from OMI measurements on 1 August 2007.

### 3. GLYOXAL RETRIEVAL FROM SATELLITE MEASUREMENTS

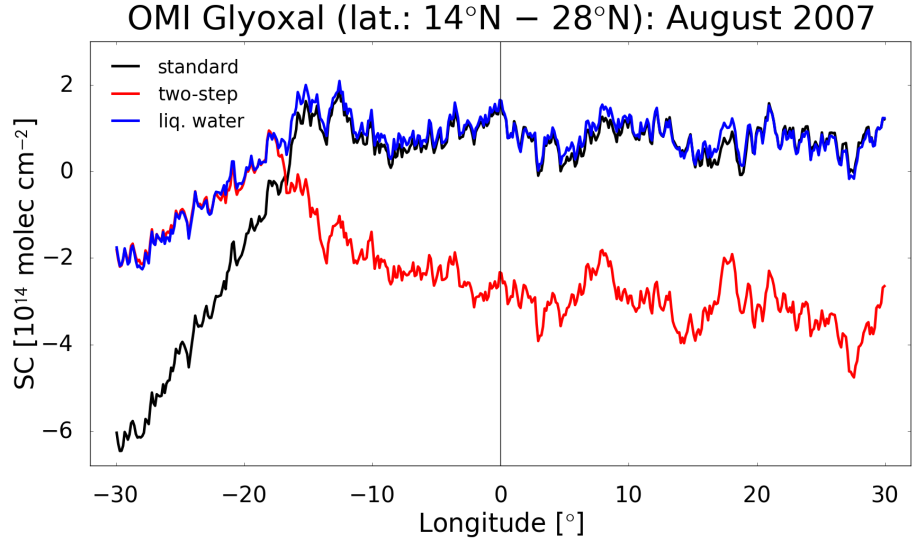


**Figure 3.9:** CHOCHO SC means retrieved using the standard CHOCHO retrieval (black), by using the two-step fit (red), and including the liquid water absorption cross-section in the standard CHOCHO retrieval (blue) for latitudes ( $21.0^{\circ}$  N $\pm 7.0^{\circ}$ ) as function of longitude from OMI measurements in August 2007.

obtained when including the liquid water cross-section directly in the fit. As no significant differences with respect to the standard retrieval are observed over land as a consequence of introducing this cross-section, this option was selected for the final data product.

Although the CHOCHO SCs retrieved by including the liquid water cross-section are improved over the oceans, the interference with liquid water is still present to a lesser degree, judging from the fact that some regions with negative CHOCHO SC values still remain over ocean. Whether this is the result of non-optimal cross-sections for liquid water (Peters et al., 2014) or other effects such as vibrational Raman scattering in the ocean water cannot be determined at this point.

#### 3.2.4 Interference with NO<sub>2</sub> absorption

Some urban and industrial regions show high levels of glyoxal (e.g. the large urban agglomerations Johannesburg, Los Angeles, Beijing, and Guangzhou) due

### 3.2 OPTIMIZATION OF THE GLYOXAL RETRIEVAL FROM SATELLITE MEASUREMENTS

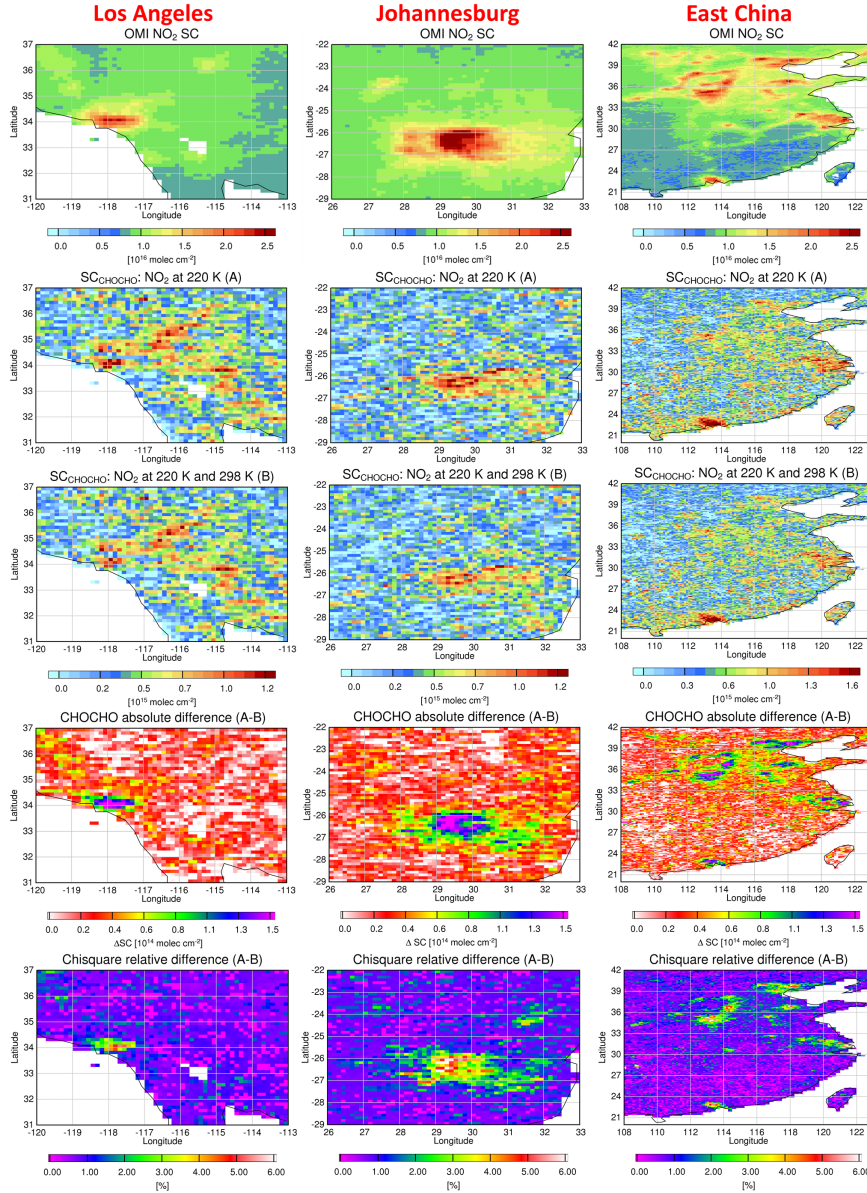


**Figure 3.10:** Monthly maps of NO<sub>2</sub> SCs, CHOCHO SCs, SC absolute and chi-square relative differences between retrievals with and without high-temperature NO<sub>2</sub> absorption cross-section over Los Angeles, Johannesburg, and East China for September 2007. **(A)** CHOCHO SCs retrieved with 220 K NO<sub>2</sub> cross-section. **(B)** An additional NO<sub>2</sub> cross-section at high temperature (294 K) is included in the retrieval.

### 3. GLYOXAL RETRIEVAL FROM SATELLITE MEASUREMENTS

to the production of CHOCHO from aromatics and acetylene (Volkamer et al., 2007; Myriokefalitakis et al., 2008; Liu et al., 2012). However, the observed CHOCHO signal could potentially also be influenced by spectral interferences with tropospheric NO<sub>2</sub>, which is very abundant in these regions (see Fig. 3.10, top) and also shows strong absorption lines inside the CHOCHO fitting window. To test this, an additional NO<sub>2</sub> absorption cross-section measured at high temperature (i.e. typical for the surface, 294 K) was included in the glyoxal retrieval to better represent near-surface NO<sub>2</sub>.

Monthly maps of glyoxal SCs for September 2007 are shown in Fig. 3.10. Including the high-temperature NO<sub>2</sub> absorption cross-section in the fit leads to decreased glyoxal SC values over pollution hot-spots and improves the fitting residuals. The improvement of chi-square values over these regions is up to 5% and even larger in some cases. However, glyoxal values still remain high in all cases, indicating that the observed enhancements are not artefacts but rather indicate genuine anthropogenic sources.

To further investigate the effect of including the high-temperature cross-section of NO<sub>2</sub>, a comparison between the glyoxal seasonal variation including and excluding this additional term is presented in Fig. 3.11 (top and middle), retrieved from the OMI and SCIAMACHY instruments for the regions of Beijing (latitude:  $37.5^{\circ} \pm 2.5^{\circ}$ ; longitude:  $115.5^{\circ} \pm 1.5^{\circ}$ ) and Congo (latitude:  $-4.0^{\circ} \pm 2.0^{\circ}$ ; longitude:  $18.0^{\circ} \pm 2.0^{\circ}$ ).

The results show similar seasonal variability. However there are large differences (larger than 30 %) observed during winter especially in Beijing, where the anthropogenic emissions of NO<sub>x</sub> are higher than in Congo (see Fig. 3.11, bottom), because the latter is mainly influenced by biogenic sources and fires. Moreover, these differences between datasets are observed for both instruments. This result shows that the temperature dependence of the NO<sub>2</sub> absorption cross-section should be taken into account in case of large tropospheric NO<sub>2</sub> columns to limit as much as possible the seasonal dependent systematic errors of the glyoxal column caused by spectral interferences.

#### 3.2.5 Dependence on the water vapour cross-section

From ground-based observations, potential interferences of water vapour with glyoxal have been identified pointing at possibly insufficient quality of existing water vapour cross-sections. In some cases, measured water vapour cross-sections

### 3.2 OPTIMIZATION OF THE GLYOXAL RETRIEVAL FROM SATELLITE MEASUREMENTS

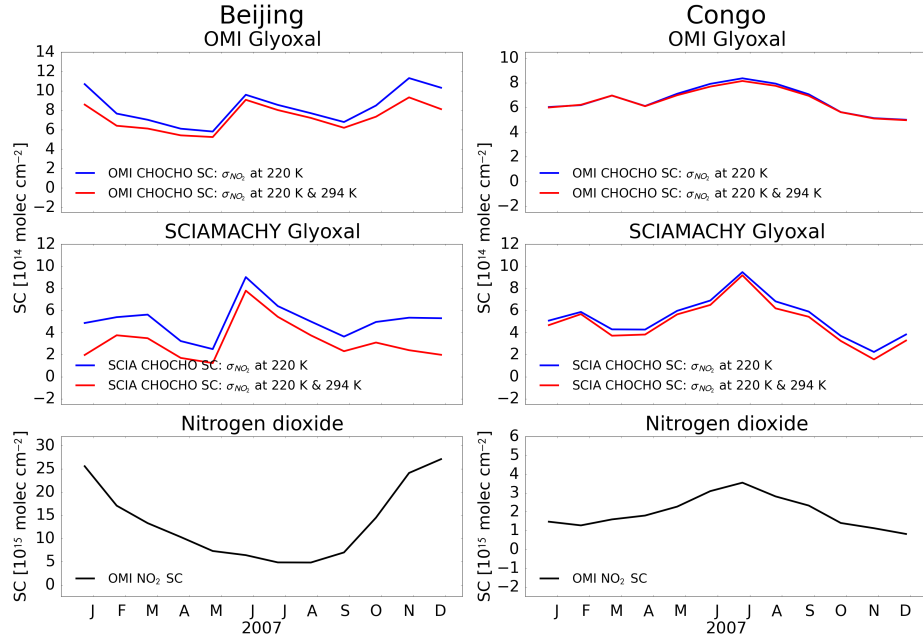


**Figure 3.11:** Seasonal variation of glyoxal SCs including and excluding the high-temperature NO<sub>2</sub> absorption cross-section from OMI and SCIAMACHY instruments (top and middle), and NO<sub>2</sub> SCs (bottom) over Beijing (left: latitude,  $37.5^\circ \pm 2.5^\circ$ ; longitude,  $115.5^\circ \pm 1.5^\circ$ ) and Congo (right: latitude,  $-4.0^\circ \pm 2.0^\circ$ ; longitude,  $18.0^\circ \pm 2.0^\circ$ ) for 2007.

have been used to improve the glyoxal retrieval (Sinreich et al., 2007, 2010). However, evidence for problems with water vapour cross-sections in satellite observations has not been published so far. In order to evaluate the potential influence of the choice of water vapour cross-section on the glyoxal retrieval, four different water vapour cross-sections were tested in the glyoxal retrieval from OMI data (i.e. Rothman et al., 2005, 2009, 2010, 2013) and the results were compared. First, the relative differences of chi-square between retrievals using the different water vapour cross-sections are computed, assuming the database HITRAN–2005 (Rothman et al., 2005) as reference. The relative differences between the glyoxal–HITRAN–2005 retrieval and those using the other cross-sections led to global differences no larger than 2.0 % (see Table 3.2). At closer inspection, the comparison between retrievals using HITRAN–2005 and HITEMP (Rothman et al., 2010) water vapour cross-section led to relative differences in the chi-square no large than 2.0 %, which does not indicate a significant improvement

### 3. GLYOXAL RETRIEVAL FROM SATELLITE MEASUREMENTS

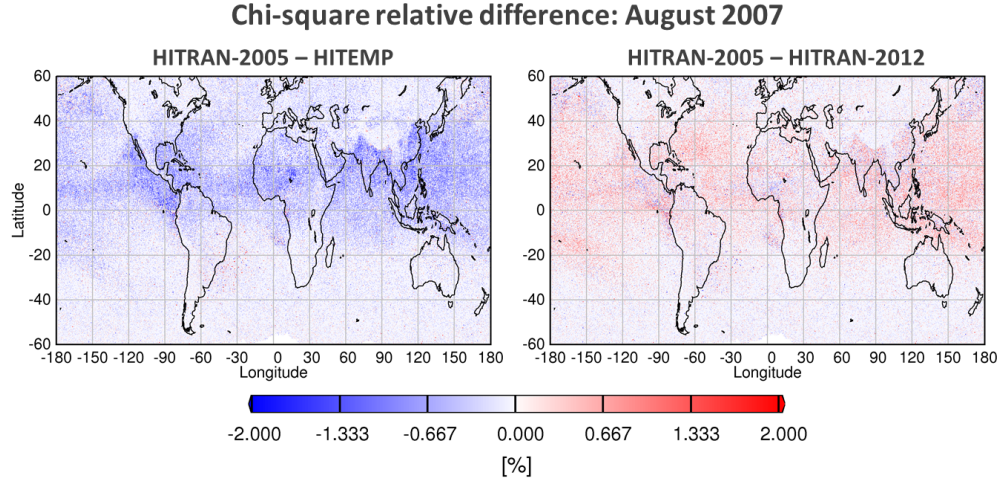


**Figure 3.12:** Global maps of chi-square relative differences between glyoxal retrievals from OMI measurements using different water vapour cross-sections for August 2007. Relative differences between HITRAN–2005 and HITEMP (left), and HITRAN–2005 and HITRAN–2012 (right).

**Table 3.2:** Chi-square relative difference and  $P$  values from the Wilcoxon signed-rank test for five regions have been computed, using as reference water vapour cross-section the one from the HITRAN–2005 database (Rothman et al., 2005).

	Rel. diff. max. (Chi-square)	Africa $P_{\text{chis}}$	China $P_{\text{chis}}$	NA $P_{\text{chis}}$	Pacific $P_{\text{chis}}$	Desert $P_{\text{chis}}$
HITRAN–2008	2.0 %	0.395	0.218	0.350	0.176	0.350
HITEMP	-1.5 %	0.511	0.227	0.235	0.054	0.001
HITRAN–2012	1.0 %	0.603	0.981	0.702	0.785	0.874

in the retrieval. It should also be noted that the chi-square becomes worse when using the water vapour cross-section from the HITEMP database (see Fig. 3.12, left). However, the chi-square relative differences obtained between retrievals using HITRAN–2005 and HITRAN–2012 Rothman et al. (2013) are even smaller and not larger than 1.0 % (see Fig. 3.12, right).

## 3.2 OPTIMIZATION OF THE GLYOXAL RETRIEVAL FROM SATELLITE MEASUREMENTS

In order to evaluate the significance in the change of chi-square, a statistical test was performed between retrievals using HITRAN-2005 and the other water vapour cross-sections. As the chi-square values are non-normally distributed, the Wilcoxon signed-rank test is used, where the null hypothesis assumes that two populations have an identical distribution at the significance level of 0.05 ( $P$  value). If the  $P$  values are larger than 0.05, the chi-square values are not significantly different in the glyoxal retrievals, and if they are smaller than 0.05, the difference is considered to be significant. In Table 3.2, the  $P$  values ( $P_{\text{chis}}$ ) obtained for five selected regions (Africa, China, North America (NA), Pacific, and desert) are summarized.  $P_{\text{chis}} > 0.05$  were obtained for almost all regions with the exception of  $P_{\text{chis}}$  over the desert between glyoxal–HITRAN–2005 and glyoxal–HITEMP retrievals, which is smaller than 0.05. However, the chi-square values are not improved using the HITEMP water vapour cross-section and also over the desert it is well known that there are interference problems due to sand reflectance (Richter et al., 2011). Thus, the chi-square relative differences among the different retrievals are considered not to be significant. Despite that, there are some differences in glyoxal SCs between retrievals, however these are rather small and to this point it is not clear which cross-section produces better values. For that reason, the decision was taken to use the water vapour cross-section from the HITRAN–2005 database in our retrieval.

### 3.2.6 The effects of clouds on the glyoxal retrieval

In the CHOCHO retrieval a number of corrections and their effects need to be taken into account. This section is focused on investigating the effect of cloud screening in the glyoxal retrieval. Clouds are highly reflective and usually above a CHOCHO pollution layer, because CHOCHO amounts are expected to be close to the surface. Clouds have significant effects on trace gas retrievals from satellite observations in the ultraviolet and visible spectral ranges. Only 5–15 % of all measurements of spatial resolutions of  $10 \times 10 \text{ km}^2$  are cloud-free pixels (Krijger et al., 2007). Clouds can shield the trace gases below them from top of atmosphere observations. Furthermore, clouds can enhance the visibility of trace gases above them due to the larger spectral reflectance compared to most ground surfaces. In addition, clouds can enhance the visibility of trace gases in their upper part due to multiple scattering by increasing the light path of photons in this altitude range. These effects of clouds on the light path depend on the cloud fraction, cloud height, trace gas profile, aerosol loading and surface

### 3. GLYOXAL RETRIEVAL FROM SATELLITE MEASUREMENTS

**Table 3.3:** Regions selected for test the glyoxal SC dependence on cloud fraction (Fig. 3.14).

	<b>Latitude [°]</b>	<b>Longitude [°]</b>	<b>Month</b>
Region 1	$39.0 \pm 2.0$	$-68.0 \pm 2.0$	August 2007
Region 2	$47.5 \pm 2.5$	$-7.5 \pm 2.5$	August 2007
Region 3	$-10.0 \pm 5.0$	$7.5 \pm 2.5$	August 2007
Region 4	$-5.0 \pm 5.0$	$22.5 \pm 7.5$	August 2007
Region 5	$23.0 \pm 7.0$	$102.0 \pm 10.0$	April 2007

reflectivity (Krijger et al., 2007).

In this study, the parameter used for investigating the effects of clouds on the glyoxal fields is the cloud fraction. For OMI CHOCHO retrievals, a cloud screening is applied based on the OMI O<sub>4</sub> cloud product (Acarreta et al., 2004). For GOME–2 (A and B) and SCIAMACHY, a cloud screening based on the algorithm Fast Retrieval Scheme for Clouds from the Oxygen A band (FRESCO+) is applied (Wang et al., 2008). In Fig. 3.13, global glyoxal SC fields are compared for different cloud fraction ranges ( $0.0 < CF < 0.1$ ;  $0.0 < CF < 0.3$ ;  $0.5 < CF < 1.0$ ) for August 2007. The figure shows that the difference between the first two is only moderate and more significant for the last case, because the tropospheric glyoxal signal is reduced over hot-spots and enhanced over ocean in comparison of the other two. This enhancement over ocean and some land areas in cloudy measurements could be related to transport events (see Sect. 5.3.2).

Thus, five different regions over ocean and land have been selected in order to evaluate the dependence of glyoxal SCs from the cloud fraction threshold (see Table 3.3). Figure 3.14 shows the CHOCHO SC dependence on cloud fraction for five regions characterized by outflow and biomass burning hot-spots from OMI and GOME–2A measurements. The dependence on the cloud fraction for the five regions is similar for both instruments with the major differences found for regions 3 and 5 (land areas). Regions 1, 2, and 3 correspond to areas over ocean, where usual outflow of glyoxal is observed. CHOCHO SCs increase for high cloud fraction, showing a similar behaviour for regions 1 and 2, while in region 3 the CHOCHO SC are high for most cloud fractions and have some differences between both instruments, which could be related to the transport events that

### 3.2 OPTIMIZATION OF THE GLYOXAL RETRIEVAL FROM SATELLITE MEASUREMENTS

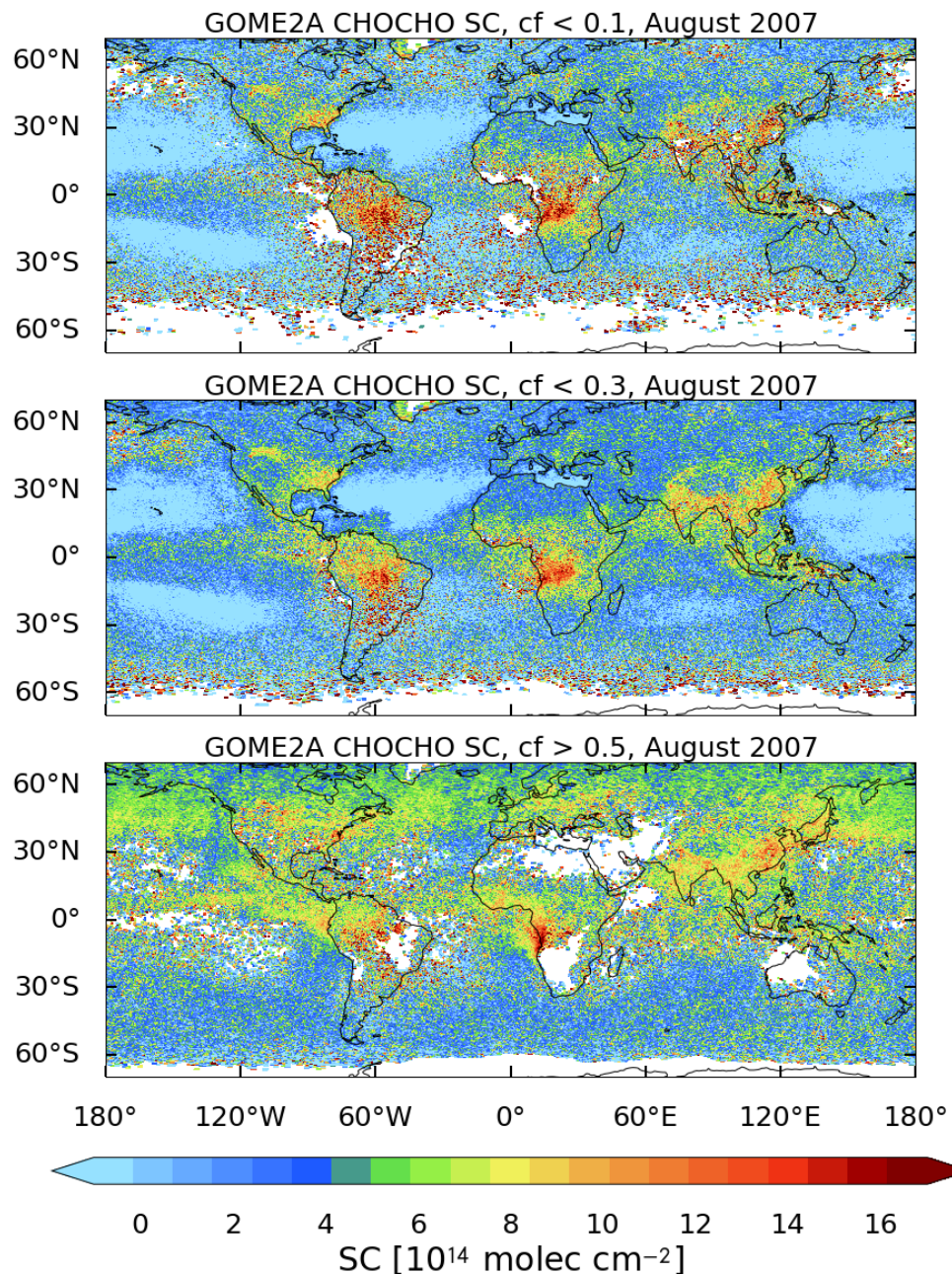


**Figure 3.13:** Comparison of CHOCHO SCs retrieved from GOME-2A measurements for August 2007 using different cloud fraction selection criteria, 0 to 0.1 (top), 0 to 0.3 (middle), and 0.5 to 1 (bottom).

### 3. GLYOXAL RETRIEVAL FROM SATELLITE MEASUREMENTS

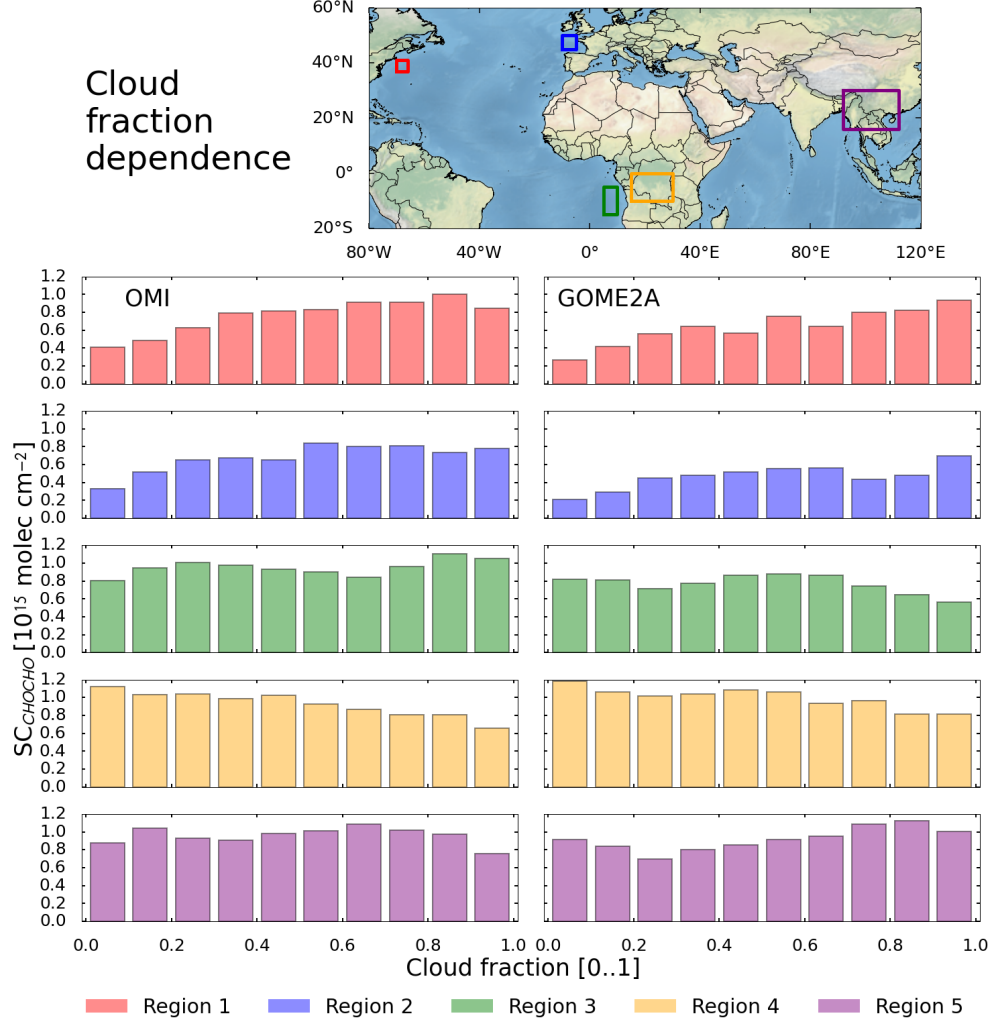


**Figure 3.14:** Glyoxal SC dependence on the cloud fraction for five selected regions in OMI and GOME-2A measurements. For region 1 to 4, the measurements correspond to August 2007, while for region 5 April 2007 data is shown.

have been observed over this region (see Sect. 5.3.2). For region 4, the glyoxal SCs increase for lower cloud fractions indicating that CHOCHO is close to the surface (Vrekoussis et al., 2009), in fact glyoxal amounts over this region are large due to pyrogenic emissions. For region 5, where transport of glyoxal has been observed similar to region 3, especially during the biomass burning season (March–April), the dependence on cloud fraction is not clear and high glyoxal

## 3.2 OPTIMIZATION OF THE GLYOXAL RETRIEVAL FROM SATELLITE MEASUREMENTS

columns are found for all cloud fractions. Glyoxal has as primary source biomass burning (produced close to the surface, similar as in region 4), however it also is produced during the oxidation process of other VOC which can occur at high altitudes and thus, glyoxal may have this behaviour.

In order to reduce the effect of clouds in the glyoxal retrieval, a cloud fraction threshold of 0.3 is applied, because glyoxal SCs decrease for cloud fraction thresholds larger than 0.3 over “hot-spots”, where large glyoxal amounts are expected close to the surface (and not at high altitudes because of its short lifetime). However, more tests are needed in order to properly asses the effect of clouds and aerosols on the glyoxal retrieval from satellite measurements.

### 3.2.7 The reference spectrum

For satellite retrieval of traces gases by the DOAS method, normally a solar irradiance spectrum is used as reference spectrum as shown in Fig. 2.9. However, for instruments using an imaging spectrometer such as OMI, offsets (“stripes”) are sometimes observed between viewing directions (solar and terrestrial) due to different sources such as small differences in the dark current correction or pixel damage. In Fig. 3.15 (left), an example of OMI glyoxal SC for an orbit measured on 12 August 2007 is shown and stripes between the different viewing directions are observed. Therefore, a correction needs to be applied to the OMI measurements for an optimum quality of the retrieved SCs.

The approach consists of a statistical evaluation of a large dataset of CHO-CHO SCs over a limited region, and the assumption that the CHOCHO VCs do not depend on the viewing direction in that region (Boersma et al., 2007). Here, we assume that the variations in glyoxal air mass factor are small close to the equator and only correct for the change in viewing zenith angle. The median SC is computed for a number of measurements over a selected region (lat. 30° N–30° S; long. 160° E–140° W), and the mean deviation from this value for each viewing direction is computed. Then, the pattern is corrected for all SCs by adding it as an offset. The corrected orbit shows a significant reduction of the stripes between the different viewing directions in comparison to the retrieval without the correction (Fig. 3.15, middle).

However, one alternative in the glyoxal retrieval would be to use as background spectrum a daily backscattered spectrum (known as Earthshine spectrum) measured over a region where glyoxal levels are low. This approach has

### 3. GLYOXAL RETRIEVAL FROM SATELLITE MEASUREMENTS

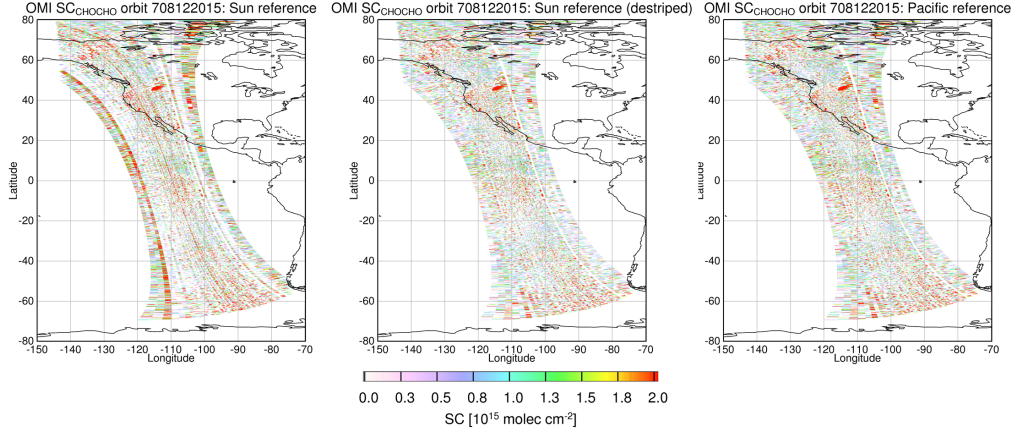


**Figure 3.15:** Glyoxal SCs retrieved from OMI data (orbit 16362) using the Sun spectrum as reference with (middle) and without (left) desstriping correction, and using the Pacific region as a reference spectrum (right).

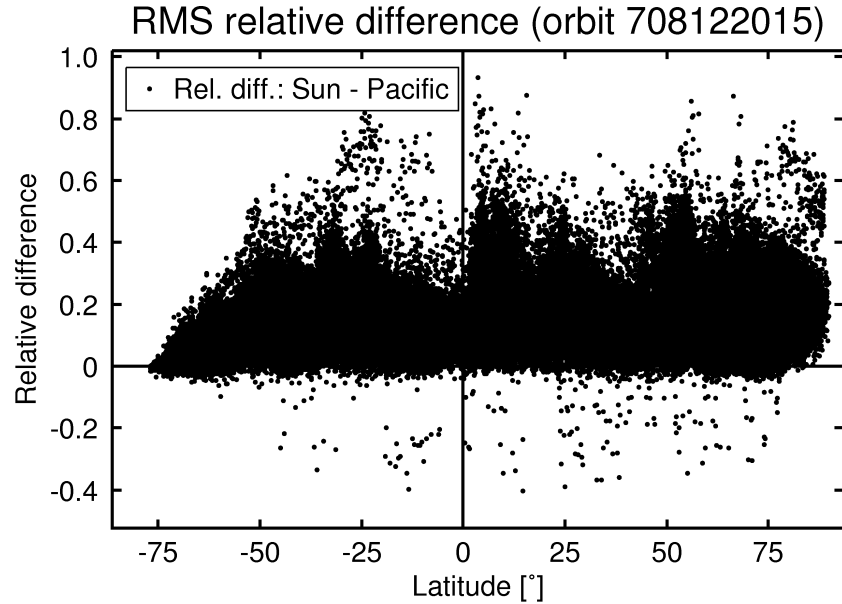


**Figure 3.16:** RMS relative differences  $\left( \frac{\text{RMS}_{\text{sun}} - \text{RMS}_{\text{Pacific}}}{\text{RMS}_{\text{Sun}}} \right)$  obtained from the OMI glyoxal retrieval for the orbit 16362 between retrievals using the Sun spectrum and Pacific region as reference spectrum.

### 3.2 OPTIMIZATION OF THE GLYOXAL RETRIEVAL FROM SATELLITE MEASUREMENTS

**Table 3.4:** CHOCHO retrieval settings for reference spectrum intercomparison for OMI measurements.

	Retrieval 1	Retrieval 2
Instrument		OMI
Fitting window		433–460 nm
Polynomial		4
Cross-sections		CHOCHO, O <sub>3</sub> (223 K), NO <sub>2</sub> (220 K and 294 K) O <sub>4</sub> , H <sub>2</sub> O <sub>vap</sub> , H <sub>2</sub> O <sub>liq</sub> , Ring
Cloud fraction	0.3	
Ref. spectrum	Sun (fixed)	Pacific region (daily)

already been applied in the retrieval of iodine monoxide (IO) from SCIAMACHY (Schönhardt et al., 2008), HCHO from GOME (De Smedt et al., 2008), and most recently NO<sub>2</sub> from OMI measurements (Anand et al., 2015). In all cases, a reduction of residual instrumental noise has been observed, which is introduced by differences between the viewing mode of measurements (solar and terrestrial) as is mentioned above. Thus, daily backscattered spectra averaged over a remote Pacific region (lat. 50° N–50° S; long. 160°–235°) have been used as reference spectrum in the glyoxal retrieval. The glyoxal SCs retrieved by using the Earth-shine spectrum as reference show no stripes between viewing directions in the OMI CHOCHO SCs (Fig. 3.15, right), and also a significant reduction in the residuals is observed. In Fig. 3.16, RMS relative differences between glyoxal retrievals using the Sun as reference (destriped) and those using the Pacific region are shown. The observed improvement in the retrieval is generally up to 20% in RMS and in some cases it is up to 40%.

In addition, when using the Pacific region as reference spectrum, the interferences with liquid water over remote Pacific areas are partially cancelled out. Similar improvements are observed for glyoxal retrievals from SCIAMACHY and GOME–2 (A and B) measurements, when a region over the Pacific is used as reference spectrum.

In order to evaluate the impact of the reference spectrum on the glyoxal SC, monthly mean glyoxal SCs retrieved by using the Sun (retrieval 1) and the Pacific region (retrieval 2) as reference spectrum are compared. Table 3.4 summarizes

### 3. GLYOXAL RETRIEVAL FROM SATELLITE MEASUREMENTS

**Table 3.5:** Regions selected for Fig. 4.3.

	Abbrev.	Latitude [°]	Longitude [°]
N-America	NA	$33.5 \pm 6.5$	$-83.5 \pm 10.5$
S-America	SA	$-5.0 \pm 4.0$	$-50.5 \pm 6.5$
C-Africa	AFC	$-2.0 \pm 14.0$	$9.5 \pm 24.5$
India	IND	$26.0 \pm 8.0$	$81.0 \pm 13.0$
NE-China	CHN	$33.5 \pm 6.5$	$116.5 \pm 6.5$
Australia	AUS	$-14.5 \pm 4.5$	$136.5 \pm 9.5$

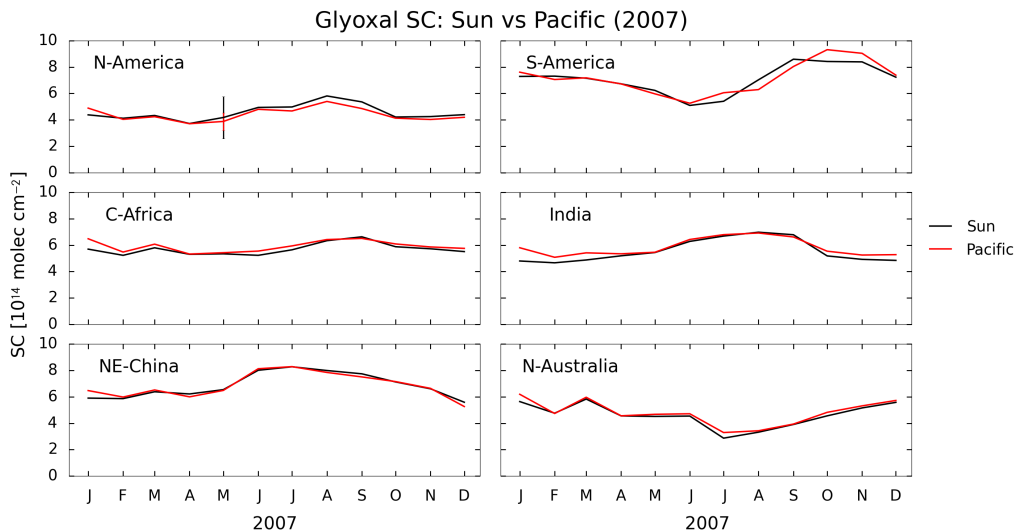


**Figure 3.17:** Comparison of glyoxal SCs over 6 selected regions (see Table 3.5) between retrievals using the Sun spectrum and Pacific region as reference spectrum for 2007.

the main fitting parameters used in the glyoxal retrievals from OMI. For this comparison, six regions over continents with large production of glyoxal from biogenic, anthropogenic and pyrogenic sources have been selected (see Table 3.5).

In Fig. 3.17, time series of monthly mean CHOCHO SCs over these six regions are shown for the year 2007. The monthly observations are averaged within each of the areas. The temporal variabilities of both retrievals have a very good consistency and overall good agreement between them for all six regions. However,

### 3.2 OPTIMIZATION OF THE GLYOXAL RETRIEVAL FROM SATELLITE MEASUREMENTS

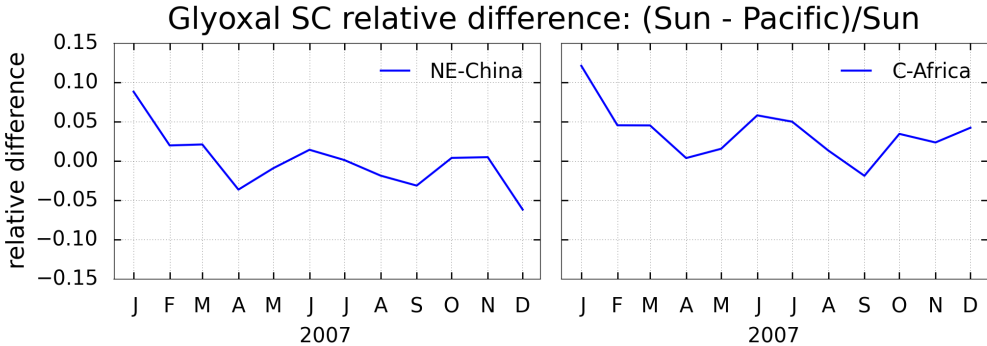


**Figure 3.18:** Glyoxal SC relative differences  $\left( \frac{SC_{\text{sun}} - SC_{\text{Pacific}}}{SC_{\text{Sun}}} \right)$  obtained from the OMI glyoxal retrieval for 2007 between retrievals using the Sun spectrum and Pacific region as reference spectrum.

on closer inspection some differences between retrievals are observed for January in all regions, corresponding to relative differences of about 14% (see Fig. 3.18). For the other months in 2007, these differences decrease to 5% and are sometimes even smaller for most regions, S-America being an exception where the differences are more pronounced for several months. These differences over S-America could be related to interferences in the measurements over the Southern Atlantic Anomaly (SAA)<sup>3</sup>.

In addition, correlation coefficients are determined by assuming a linear relationship between glyoxal SCs from retrievals 1 and 2 for the same four of the six selected regions above (see Table 3.5). The computations were performed using daily mean glyoxal SCs for both retrievals. The correlation coefficients obtained for all regions are larger than 0.97 and slopes are nearly 1, which proves the strong correlation and agreement between the retrievals.

The differences found between retrievals are small and the improvement in the fit residual using the Pacific region as reference is significant, and no stripes are introduced due to the different viewing modes of the measurements (solar and terrestrial). The Pacific region is used as reference spectrum in the glyoxal

<sup>3</sup>The SAA is a region where the Earth's inner Van Allen radiation belt comes closest to the Earth's surface, leading to an increase of energetic particles flux in this area. Thus satellites orbiting the Earth are exposed to high radiation levels (more than usual) causing technical problems in the measurements from these. This effect is due to the non-concentricity of the Earth and its magnetic dipole, being SAA the near area where the Earth's magnetic field is weaker relative to an idealized Earth centered dipole field.

### 3. GLYOXAL RETRIEVAL FROM SATELLITE MEASUREMENTS

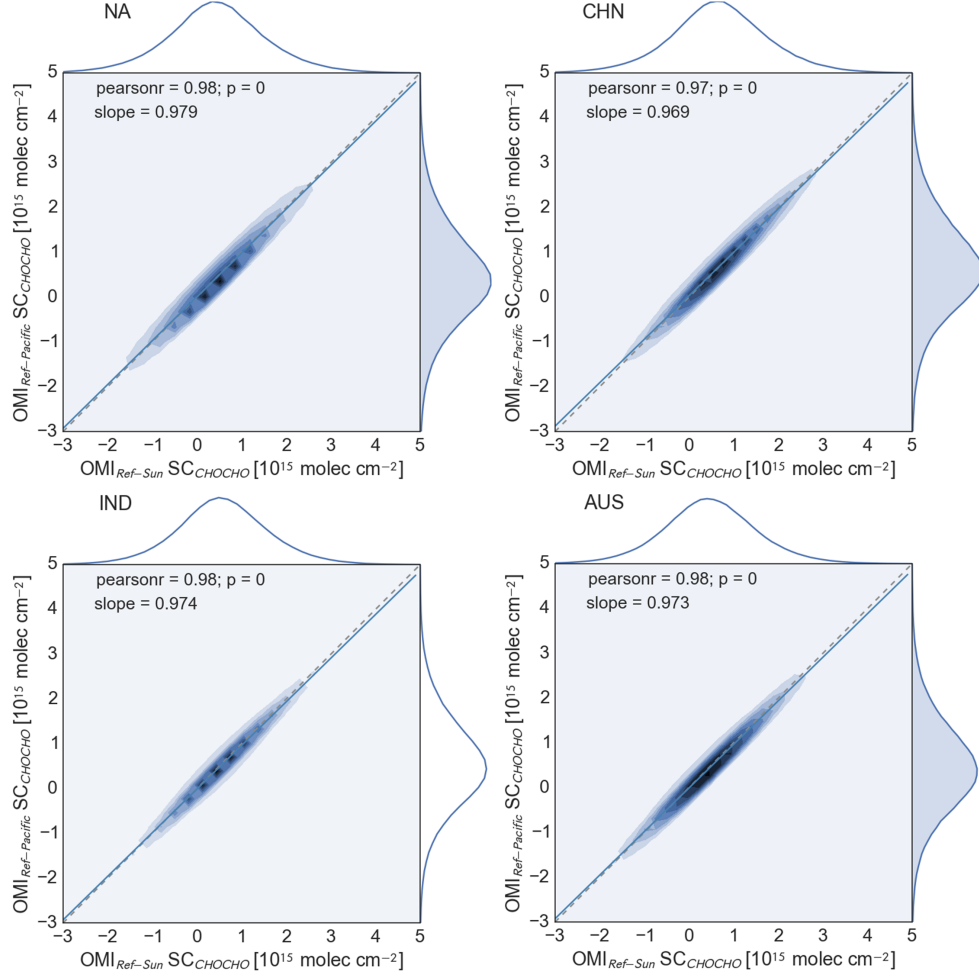


**Figure 3.19:** Correlation plots for 4 selected regions (see Table 3.5) between glyoxal columns retrieved using Sun and Pacific region as reference spectrum for 2007. Additionally, the respective distribution of each dataset are showed.

retrieval for OMI and applied to the SCIAMACHY and GOME–2 (A and B) as well. Despite the fact that these instruments are not imaging spectrometers as OMI, there are other causes of interferences introduced by using a Sun spectrum as reference in the glyoxal retrieval. In Fig. 3.20 (blue line), glyoxal SCs retrieved from GOME–2A measurements over the Pacific ( $30^{\circ}$ S– $30^{\circ}$ N,  $180^{\circ}$ – $240^{\circ}$ E) using similar fitting parameters to retrieval 1 (see Table 3.4), but using as reference a Sun spectrum are shown. CHOCHO SCs show a seasonal variability over the

### 3.3 GLYOXAL DETECTION LIMITS AND ERRORS

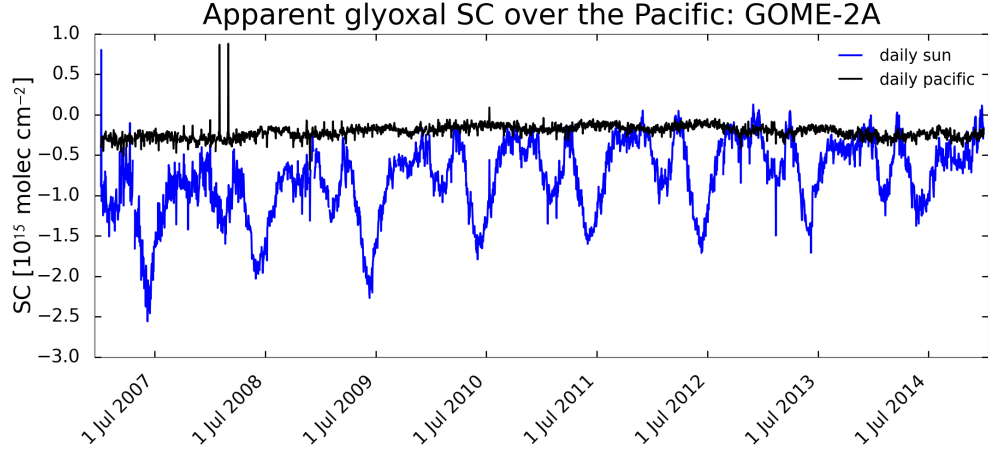


**Figure 3.20:** Comparison of GOME–2A glyoxal SCs over the Pacific using daily Sun reference spectrum and daily Region as reference spectrum from 2007 to 2014.

Pacific and very large negative SCs, which are introduced by problems in the daily Sun reference spectrum. Similar behaviour is observed for NO<sub>2</sub> SCs over the Pacific (Andreas Richter, personal communication), which are also associated with artefacts introduced by the Sun reference spectrum. However, if daily spectra from the Pacific region are used in the retrieval (retrieval 2), the number of negative glyoxal SCs is reduced and no seasonal variability is observed (Fig. 3.20, black line).

## 3.3 Glyoxal detection limits and errors\*

When investigating the uncertainty of the retrieved glyoxal columns, several effects have to be taken into account. Photon-shot noise, related to the number of photons collected in a single measurement and governed by the probability distribution of incoming photons (Burrows et al., 2011), together with readout noise and the dark signal in the detector, are the main sources of random errors in the radiance measurements. Systematic errors in the slant columns are introduced by uncertainties in reference spectra, an imperfect wavelength calibration, and instrumental features (Boersma et al., 2004; De Smedt et al., 2008; Vrekoussis et al., 2009; Lerot et al., 2010). These, combined with other parameters

---

\* Parts of this section have been previously published as part of Alvarado et al. (2014).

### 3. GLYOXAL RETRIEVAL FROM SATELLITE MEASUREMENTS

such as the limited penetration of solar radiation due to scattering effects in the atmosphere, determine the total uncertainty of the retrieved glyoxal SCs. In this study, these systematic errors are estimated as described by Wittrock (2006) to be around  $6.0 \times 10^{14}$  molec cm $^{-2}$  in the SC.

In addition, the air mass factor calculations introduce more uncertainties in the results (Boersma et al., 2004) as well as the influence of clouds and aerosols, which lead to significant uncertainties in satellite retrievals (Wang et al., 2008; Vrekoussis et al., 2009).

Moreover, some offset errors can be introduced for weak absorbers in the DOAS retrieval (Wittrock, 2006). For example, the solar irradiance entering the Earth's atmosphere varies with time, the greatest changes being observed in the ultraviolet spectral region, however the irradiance variability occurs at almost all wavelengths. This solar irradiance variability is associated with the 11 years solar cycle (22 years magnetic cycle), and the solar rotation (27 days). These cycles are the periods of changes in the Sun, which include changes in the ejection of solar material and solar radiation, as well as changes in the numbers of sunspots, flares and other manifestations. All these variabilities can introduce interferences in the satellite retrievals, especially for weak absorbers such as glyoxal. In Fig. 3.21 (top), time series of glyoxal SCs retrieved from SCIAMACHY, OMI and GOME–2 (A and B) measurements over the Pacific region ( $30^{\circ}$ S– $30^{\circ}$ N,  $180^{\circ}$ – $240^{\circ}$ E) using retrieval 1 (see Table 3.4) are shown. The retrieval 1 uses a single solar reference spectrum, which has been measured on 15 July 2007 for OMI, SCIAMACHY and GOME–2A, and on 15 July 2014 for GOME–2B. CHOCHO SCs show a similar temporal oscillation in SC for all instruments, which most likely are introduced by the solar irradiance variability. The Magnesium II core-to-wing ratio (MgII index) is used as proxy for the solar variability (Snow et al., 2014). Then, composite MgII index time series are compared with the glyoxal SCs (Fig. 3.21, top). The comparison shows that CHOCHO SCs variation follow very well the variability of the MgII index. These variations have a cycle of 27 days, which corresponds to the solar rotation and is an evidence for the influence of solar variation in the glyoxal retrieval by introducing changes in the SC. In order to account for these effects, the normalization method of columns introduced in Vrekoussis et al. (2009) has been applied, which consists of computing the mean of the slant columns over an area in the remote Pacific Ocean (lat.:  $0^{\circ} \pm 60^{\circ}$ ; long.:  $180^{\circ} \pm 30^{\circ}$ ), and subtracting this value from all the measurements of the same day. Similar as before, time series of glyoxal SCs have been computed for all instruments after applying the normalization correction (Fig. 3.21,

### 3.3 GLYOXAL DETECTION LIMITS AND ERRORS

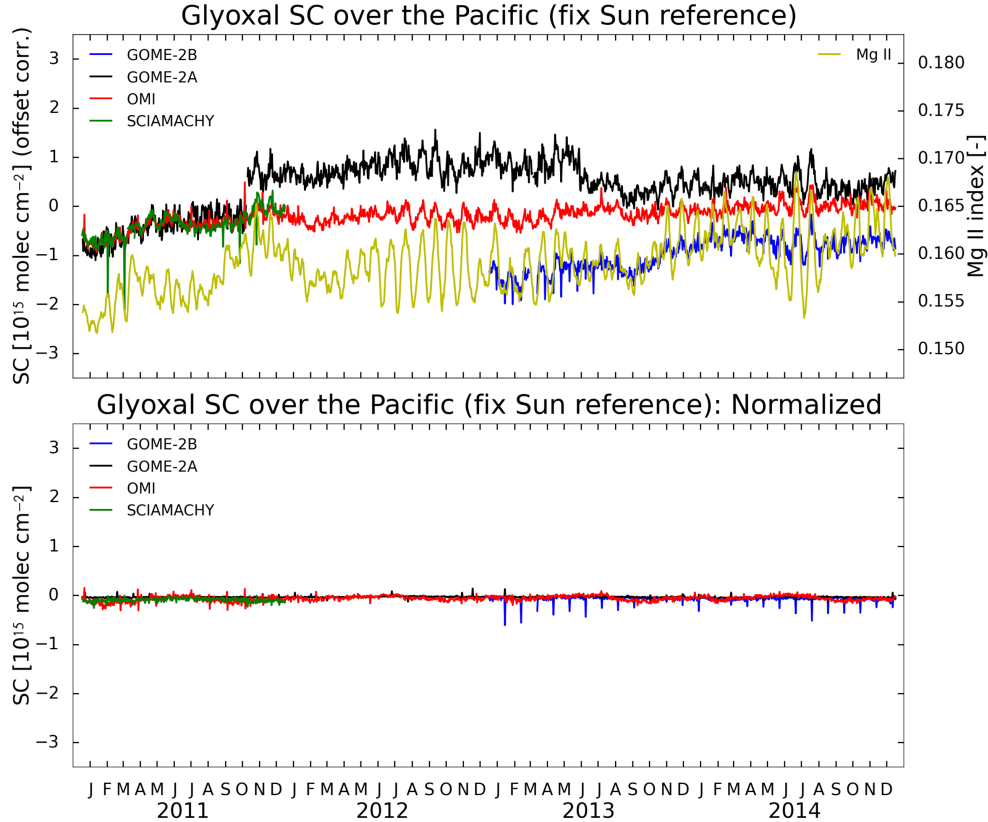


**Figure 3.21:** CHOCHO SCs retrieved over the Pacific using a fix Sun reference spectrum without normalization, MgII index (top), and glyoxal SCs after applying the normalization correction (bottom) for OMI, SCIAMACHY and GOME-2(A and B) from 2011 to 2014. The fixed Sun reference spectrum corresponds to a measurement on 15 July 2007 for OMI, SCIAMACHY and GOME-2A, and on 15 July 2014 for GOME-2B.

bottom). After applying the normalization correction, the glyoxal SC variability is removed and also the offsets between datasets. In addition, in order to account for the glyoxal background a slant column of  $1.6 \times 10^{14}$  molec  $\text{cm}^{-2}$  is then added to the global field similar to the values found over the Pacific by Sinreich et al. (2010).

For the computation of the detection limit, the minimum glyoxal slant columns detectable with the DOAS retrieval from OMI measurements are estimated for an ideal case of a single measurement as described by Vrekoussis et al. (2009).

### 3. GLYOXAL RETRIEVAL FROM SATELLITE MEASUREMENTS

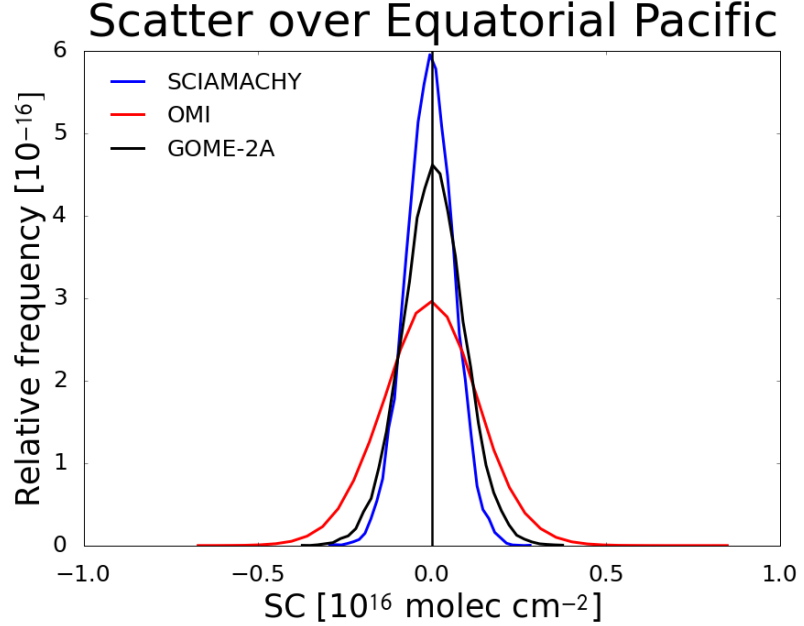


**Figure 3.22:** Distribution of CHOCHO SCs for OMI, SCIAMACHY and GOME-2A over a clean equatorial ocean region ( $5^{\circ}$ S– $5^{\circ}$ N,  $160$ – $200^{\circ}$ E) for August 2007.

This detection limit is given by the ratio between the root mean square (RMS) at the residual and the maximum differential absorption cross-section of the trace gas of interest ( $\sigma_{CHOCHO}$ ). The typical RMS for a single measurement in a region where high glyoxal amounts are found (indicating ideal measurement conditions, e.g. Africa) is around  $3 \times 10^{-4}$  for OMI,  $9 \times 10^{-5}$  for SCIAMACHY, and  $8 \times 10^{-5}$  for GOME-2A and the maximum of the CHOCHO absorption cross-section is  $5.5 \times 10^{-19} \text{ cm}^2 \text{ molec}^{-1}$ . Thus, the SC detection limit for the ideal case and a single measurement of OMI, SCIAMACHY, and GOME-2A are around  $5.5 \times 10^{14} \text{ molec cm}^{-2}$ ,  $1.6 \times 10^{14} \text{ molec cm}^{-2}$ , and  $1.4 \times 10^{14} \text{ molec cm}^{-2}$ , respectively, using a typical RMS for a region where high glyoxal amounts are found. This limit is reduced by averaging over time or space to compute monthly means.

For comparison, the scatter of SCs over a clean region in the equatorial Pacific ( $5^{\circ}$ S– $5^{\circ}$ N,  $160$ – $200^{\circ}$ E) has been computed for August 2007. As illustrated in Fig. 3.22, the SC scatter shows a distribution around zero for the three instruments with FWHM of  $3.0 \times 10^{15} \text{ molec cm}^{-2}$ ,  $2.0 \times 10^{15} \text{ molec cm}^{-2}$ ,

### 3.4 SUMMARY

and  $1.6 \times 10^{15}$  molec cm $^{-2}$  and a standard deviation of  $1.3 \times 10^{15}$  molec cm $^{-2}$ ,  $8.9 \times 10^{14}$  molec cm $^{-2}$ ,  $6.8 \times 10^{14}$  molec cm $^{-2}$ , respectively, which are of the same order of magnitude as obtained for the detection limit by the theoretical approach above. OMI glyoxal SCs present a larger scatter than the GOME–2A and SCIAMACHY instrument, which could be related to instrumental features.

## 3.4 Summary

An improved and homogenized glyoxal retrieval has been developed for four different satellite instruments, which expands the dataset available of glyoxal to 12 years from morning and afternoon orbits. Sensitivity tests on synthetic data as well as on OMI, GOME–2 (A and B), and SCIAMACHY measurements over selected regions provided useful information for the selection of DOAS fitting window and the most appropriate polynomial degree for this study. Moreover, two approaches for the reduction of the liquid water interference over clear water oceans have been evaluated, finding that including the liquid water absorption cross-section in the DOAS fit leads to the best reduction of unphysical negative glyoxal values over oceans and nearly no differences over land are found. For the first time, possible interferences by tropospheric NO $_2$  over areas with large anthropogenic emissions have been investigated. A high-temperature NO $_2$  absorption cross-section representing near-surface NO $_2$  has been introduced in the retrieval, leading to a significant reduction of glyoxal over these areas and an improved fit quality.

Investigation of the impact of different water vapour cross-sections in the fit shows that for OMI data, this does not seem to be a critical factor. This is in contrast to ground-based MAX-DOAS observations, where water vapour absorption can interfere strongly with the retrievals, in particular in the tropic regions (Sinreich et al., 2007, 2010).

In spite of the progress made on the glyoxal retrieval and its homogenisation for different satellite platforms, the resulting datasets are still noisy and depend critically on the details of the selection made for the retrieval. Further improvements in signal-to-noise and consistency are needed to make full use of the synergy between measurements from instruments in morning and afternoon orbits. In addition, the effects of clouds and aerosols on the air mass factors need to be taken into account, in particular for biomass burning scenarios, where these can play an important role in the detection of glyoxal transport events.

# 4

## Observations of glyoxal from space

### 4.1 Introduction

Despite the increase in the number of studies about glyoxal from space, more detailed description of the behaviour and global distribution is needed.

Wittrock et al. (2006) published the first global simultaneous observation of HCHO and CHOCHO by the SCIAMACHY instrument. The highest concentrations of both species were found over areas with large biogenic isoprene emissions and also in regions with anthropogenic emissions and biomass burning (tropical and sub-tropical regions).

Kurosu et al. (2007) reported observations from OMI of seasonally resolved global distribution of HCHO and CHOCHO during twelve months over regions of biomass burning and anthropogenic sources. These results were compared with ground based measurements, as well as with simulations from the chemistry transport model (CTM).

Millet et al. (2008), Fu et al. (2008) and Barkley et al. (2008) reported spatial distributions of isoprene emissions derived from OMI HCHO columns, SCIAMACHY CHOCHO columns, and GOME HCHO columns, respectively. Millet et al. (2008) compared HCHO columns in June-August over north America with the CTM. They compared emissions derived from OMI to a state-of-science bottom-up isoprene emission inventory from MEGAN (Model of Emissions of Gases and Aerosols from Nature), and found consistent results between both,

## 4.1 INTRODUCTION

however the results derived from OMI were lower than isoprene emissions determined by MEGAN. Fu et al. (2008) published global budgets of atmospheric CHOCHO and methylglyoxal, and the implications for formation of SOA. They compared CHOCHO on a global scale between the CTM and SCIAMACHY measurements, finding highest values and good agreement over biomass burning regions. Also, the SCIAMACHY results showed that a large source over the ocean is missing in CTM. Barkley et al. (2008) presented a study of isoprene emissions derived from GOME and compared them with simulated results from a CTM using the MEGAN bottom-up inventory over South America. These results showed a qualitative consistency among the CTM, *in situ* ground based results, airborne concentration profiles of isoprene, and GOME HCHO columns. However, the agreement was not so good in the wet season. Myriokefalitakis et al. (2008) published a study on the influence of natural and anthropogenic secondary sources on the CHOCHO global distribution. They calculated by a global CTM (TM4-ECPL) the chemical production of CHOCHO ( $56 \text{ Tg yr}^{-1}$ ) with around 30% of anthropogenic origin. According to this model the anthropogenic contribution to CHOCHO over tropical regions is about 3–20%, while over urban areas it can be as large as 70%. Also, the model result showed a good agreement with the earlier study by Wittrock et al. (2006).

Vrekoussis et al. (2009) reported largest values of CHOCHO over tropical and sub-tropical regions as part of a study of temporal and spatial variability of CHOCHO from the SCIAMACHY instrument. This result was associated with high biological activity and plumes from vegetation fires. They also found the highest values during the warm and dry seasons due to the enhancement of biogenic activities and/or biomass burning from natural and man-made fires. A study by Stavrakou et al. (2009a) confirms the high emissions of CHOCHO from natural sources, however the amount of these sources is still unknown and the comparison with simulated CHOCHO columns led to a good agreement between both, but with underestimation in the simulated columns. Later, Vrekoussis et al. (2010) published the first HCHO and CHOCHO columns retrieved from the GOME-2 instrument over regions with enhanced biogenic emissions. They used the ratio of CHOCHO to HCHO to classify the different sources. These results were compared with SCIAMACHY observations showing good agreement between both instruments for 2007–2008. Lerot et al. (2010) reported an improved retrieval for CHOCHO from GOME-2 measurements and compared the results with model calculations. This study showed good agreement with the results found by Vrekoussis et al. (2010). The highest CHOCHO values were

## 4. OBSERVATIONS OF GLYOXAL FROM SPACE

found over continental tropical regions and the comparison with the simulated results showed that there are missing CHOCHO sources in the model. Another study over China by Liu et al. (2012) compared CHOCHO satellite observations with model simulated values. This comparison showed a large unknown source of CHOCHO over China. They attributed this missing source to an underestimation of aromatics emissions.

Most recent studies by Chan Miller et al. (2014), and Alvarado et al. (2014) reported on OMI retrievals of CHOCHO. Chan Miller et al. (2014) similar to Alvarado et al. (2014), showed glyoxal pattern with high values associated to regions with dense vegetations and biomass burning. In addition, Alvarado et al. (2014) presented the correlation map with Fire Radiate Power (FRP) as an indicator of glyoxal emissions from fires.

This chapter's focus is on a detailed description of glyoxal globally and also over selected "hot-spots". In addition, correlations with different indicators of biogenic activities (Enhanced Vegetation Index: EVI), pyrogenic emissions (Fire Radiate Power: FRP), and anthropogenic activities ( $\text{NO}_2$  vertical columns) are analysed in order to identify the possible sources of glyoxal.

### 4.2 Global observations and satellite intercomparison

In order to evaluate the quality and consistency of the improved glyoxal retrieval presented in Chap. 3, a comparison among instruments has been performed using homogenized fitting parameters for all datasets. Table 4.1 summarizes the main fitting parameters used in the glyoxal retrievals from SCIAMACHY, OMI, and GOME–2 (A and B) measurements.

The glyoxal slant columns have been retrieved from SCIAMACHY, OMI, and GOME–2 (A and B) measurements and converted to vertical columns by using AMFs as is described in the Sect. 2.4.8. Glyoxal vertical columns comprising a dataset of more than twelve years (2003–2014) of global CHOCHO observations. As no stratospheric column of glyoxal is expected, no stratospheric correction is necessary. Then, the vertical column represents the tropospheric CHOCHO vertical column. Figure 4.1 shows the global CHOCHO VCs for the four instruments averaged for the periods of 2003–2011 (SCIAMACHY), 2005–2014 (OMI), 2007–2014 (GOME–2A), and 2013–2014 (GOME–2B). Enhanced CHOCHO VCs are observed mainly in the tropical and sub-tropical areas (e.g.

## 4.2 GLOBAL OBSERVATIONS AND SATELLITE INTERCOMPARISON

**Table 4.1:** CHOCHO retrieval settings for the instrument intercomparison.

Parameters	
Instrument	SCIAMACHY, OMI, GOME–2 (A and B)
Fitting window	433–460 nm
Polynomial	4
Cross-sections	CHOCHO, O <sub>3</sub> (223 K), NO <sub>2</sub> (220 K and 294 K) O <sub>4</sub> , H <sub>2</sub> O <sub>vap</sub> ,H <sub>2</sub> O <sub>liq</sub> ,Ring
Cloud fraction	≤0.3
Ref. spectrum	Pacific region (daily)

Central and South America, Africa, India, Indonesia and South-eastern China), with CHOCHO VCs of about  $4 \times 10^{14}$  molec cm<sup>-2</sup>. At mid-latitudes, the glyoxal VCs are moderate and about  $2.5 \times 10^{14}$  molec cm<sup>-2</sup> are distinguishable over the southern USA, Europe and Australia. The high glyoxal values originate mostly from regional sources of the precursors of VOC due to its short lifetime (2–3 h). These regions are characterized by strong biogenic and pyrogenic emissions, as well as pollution induced by anthropogenic activities.

The global pattern of glyoxal VCs from the four instruments are similar (see Fig. 4.1), with their maxima located over the same regions. However, the magnitude of glyoxal vertical columns varies, GOME–2 (A and B) CHOCHO VCs being larger than those of SCIAMACHY and OMI. Figure 4.2 shows absolute differences between OMI and SCIAMACHY VCs (left), as well as OMI and GOME–2A VCs (right), all averages for 2007–2011. The OMI glyoxal VCs are generally smaller than those from SCIAMACHY and GOME–2A, mainly in tropical regions.

Additionally, monthly mean VCs from the OMI, GOME–2 (A and B) and SCIAMACHY instruments are used in order to compare those columns over regions where large amounts of glyoxal are found. In Fig. 4.3 (top), time series of monthly mean CHOCHO VCs over 6 regions (see Table 3.5) are shown for the period 2003–2014. The monthly observations are averaged within each of the areas, which represent different environments with large glyoxal production (biogenic, anthropogenic and pyrogenic sources). The seasonal variabilities of the datasets have an overall good consistency. However, OMI glyoxal VCs are

#### 4. OBSERVATIONS OF GLYOXAL FROM SPACE

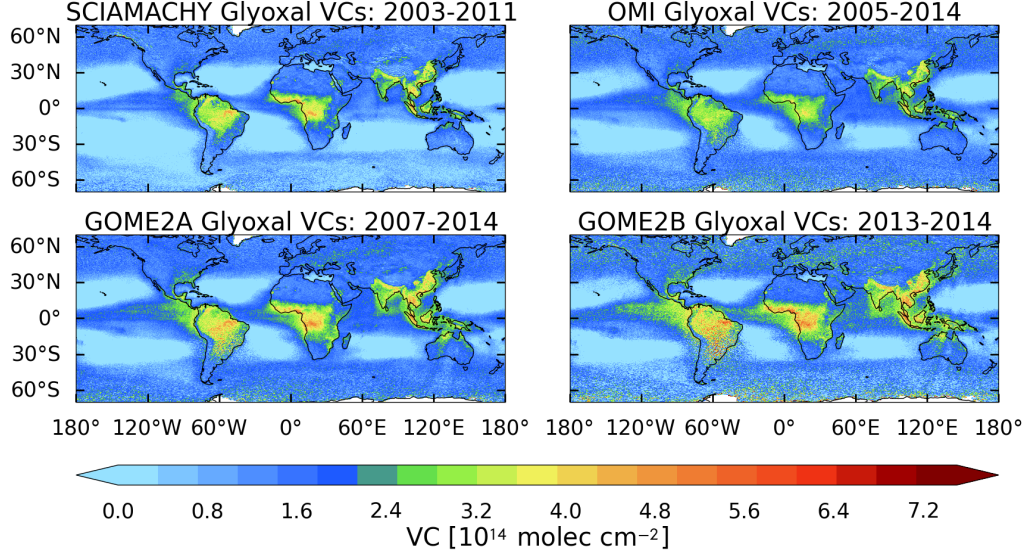


**Figure 4.1:** Global means of CHOCHO VCs retrieved from SCIAMACHY, OMI, GOME-2(A and B) for the period 2003–2011, 2005–2014, 2007–2014, and 2013–2014 respectively.

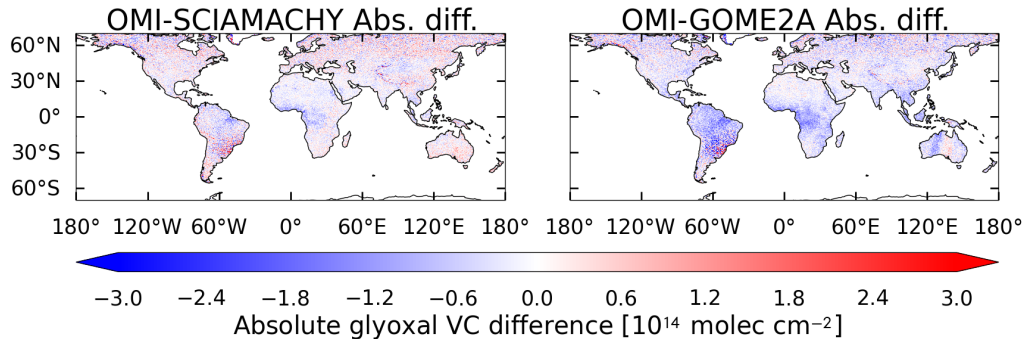


**Figure 4.2:** Global absolute differences between CHOCHO VCs from OMI and SCIAMACHY, as well as OMI and GOME-2A for the period 2007–2011.

often lower than SCIAMACHY and GOME-2 (A and B), especially since 2010. This tendency of decreasing OMI glyoxal VCs is more evident for regions within latitudes 30° S–5° N (C-Africa: AFC, S-America: SA, Australia: AUS) similar to those observed in the global maps (see Fig. 4.1). In contrast, the glyoxal VCs for regions with latitudes larger than 5° N show a very good agreement

## 4.2 GLOBAL OBSERVATIONS AND SATELLITE INTERCOMPARISON

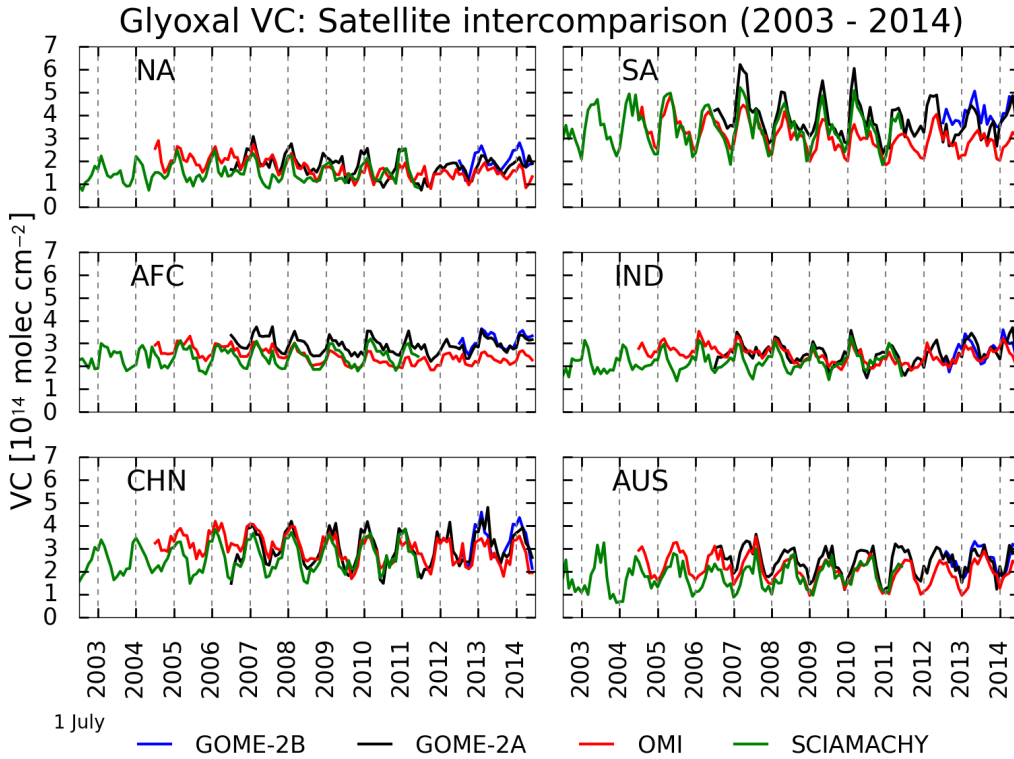


**Figure 4.3:** Comparison of monthly averaged CHOCHO VCs from GOME–2B (blue line), GOME–2A (black line), OMI (red line) and SCIAMACHY (green line) data for 6 selected regions over different environments during 2003–2014. These regions are the same as defined in Table 3.5.

among instruments. Also, the seasonal variation is less pronounced in almost all regions for the OMI instrument. Some of these differences could be related to the different overpass times at the satellites, sampling different VOC emissions and photochemical regimes. Additionally, this result is consistent with the observed diurnal variation of HCHO by De Smedt et al. (2015) as well as with the diurnal variation computed from ground-based measurements as shown in this work (see Chap. 6), with a maximum corresponding to morning hours between 10:00 and 11:00 hour local time, which is closer in time to the overpass of GOME–2 (A and B) and SCIAMACHY.

In addition, the amplitude of seasonal variability of glyoxal VCs is larger in North America and Africa than in South America, China, Australia and India, which is possibly related to less variation in the emissions from vegetation

## 4. OBSERVATIONS OF GLYOXAL FROM SPACE

in those areas. Good agreement between products are found over regions with large anthropogenic activities (e.g. China). Despite the differences found between products, the homogenized glyoxal retrieval offer useful and consistent information for the analysis of VOCs from different sources.

### 4.2.1 Interannual variability

Annual averages of CHOCHO VCs from GOME–2A between 2007 and 2014 are used to investigate the interannual variability of glyoxal (see Fig. 4.4). The annual averages show a similar pattern every year, where each individual yearly average of CHOCHO VCs confirms that high amounts of glyoxal VCs are found over tropical and subtropical regions characterized by dense vegetation (e.g. tropical forest of Amazonia), biomass burning (e.g. central Africa and the sub-Saharan Africa), and with high anthropogenic emissions (e.g. Beijing, China), as well as those that have a mixture of the three sources. Annual changes of glyoxal are not clearly observed, however on closer inspection some regions show variations from year to year, specially those that are dominated by pyrogenic emissions (e.g. central Africa and Brazil). These changes can be related to many factors, such as variability in the number of fire events and decrease or increase in the precipitation levels over these regions. The possible causes of variability in glyoxal and VOC in general will be discussed in more detail in the sections below.

### 4.2.2 Seasonal variation

In order to study the seasonal variability of glyoxal, averages of CHOCHO VCs for Northern Hemispheric winter (DJF), spring (MAM), summer (JJA), and autumn (SON) are presented for GOME–2A data (see Fig. 4.5). These are averaged for the respective seasons within the time period 2007 to 2014. The maps show that the highest levels of CHOCHO are found in the tropical and sub-tropical regions as has been observed in the interannual variability. The CHOCHO VCs vary with the season, the maxima and minima corresponding to the respective summer and winter. This is consistent with the fact that the biogenic emissions increase in the warm periods and thus the CHOCHO production is enhanced. Whereas the largest CHOCHO amounts are found in Africa north of the equator in DJF, maximum CHOCHO production is observed in JJA over central Africa due to fire emissions. The maximum of CHOCHO in South Amer-

## 4.2 GLOBAL OBSERVATIONS AND SATELLITE INTERCOMPARISON

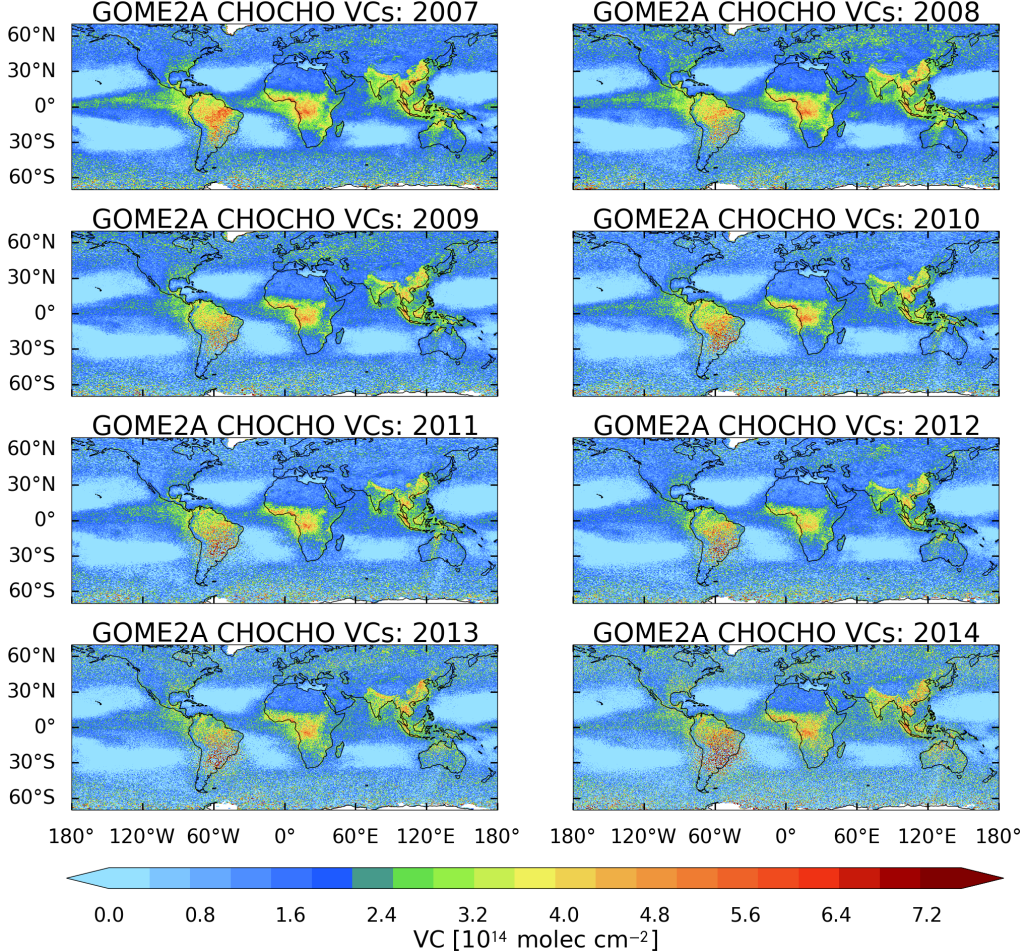


**Figure 4.4:** Yearly averages maps of CHOCHO VCs from GOME–2A between 2007 and 2014. The annual means are similar for all years, being glyoxal levels high for the earliest years.

ica occurs in SON, in agreement with the largest fire activity and the highest NO<sub>2</sub> (produced from fire emissions) levels during that season (Schreier et al., 2014). Close to the equator, the CHOCHO seasonal variation is quite smooth, suggesting that CHOCHO is mostly produced by biogenic sources from tropical forests (Guenther et al., 2006). In contrast, CHOCHO from biogenic sources at higher latitudes has a clear seasonal cycle with the maximum in JJA (e.g. Southeast US), which corresponds to the vegetation growth cycle. No significant differences were found between seasons over highly populated regions (e.g.

## 4. OBSERVATIONS OF GLYOXAL FROM SPACE

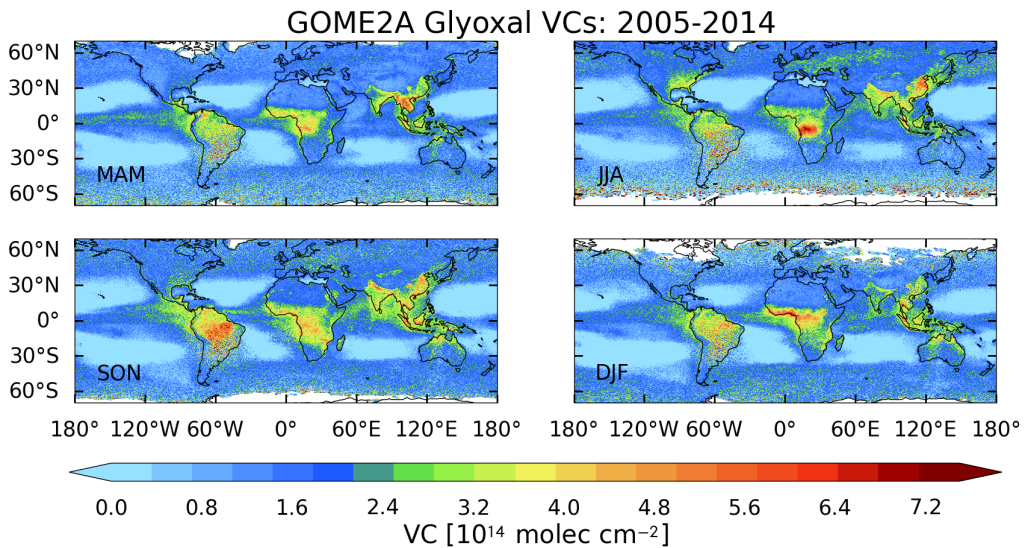


**Figure 4.5:** Seasonal means of GOME–2A CHOCHO VCs for winter (DJF), spring (MAM), summer (JJA), and autumn (SON) for the period 2007–2014. The CHOCHO VCs vary with the season, the maxima and minima corresponding to the respective summer and winter for each hemisphere.

Southeast China), most likely as a result of different sources contributing to the CHOCHO amounts at different times of the year (e.g. anthropogenic emissions in DJF, biogenic production in MAM). Similar patterns are observed for the glyoxal VCs retrieved from SCIAMACHY, OMI and GOME–2B measurements.

## 4.3 Identification of glyoxal sources

### 4.3.1 Biogenic emissions\*

It is well known that one of the main sources of trace gases in the atmosphere are biogenic emissions. The global maps of glyoxal show that high values are found over regions such as south America, continental Africa, south of Asia and, to a lesser extent, the southeastern US, which correspond to areas with dense vegetation (see Fig. 4.1). Around 55% of global glyoxal amounts released to the

---

\* Part of this subsection has been previously published as part of Alvarado et al. (2015).

### 4.3 IDENTIFICATION OF GLYOXAL SOURCES

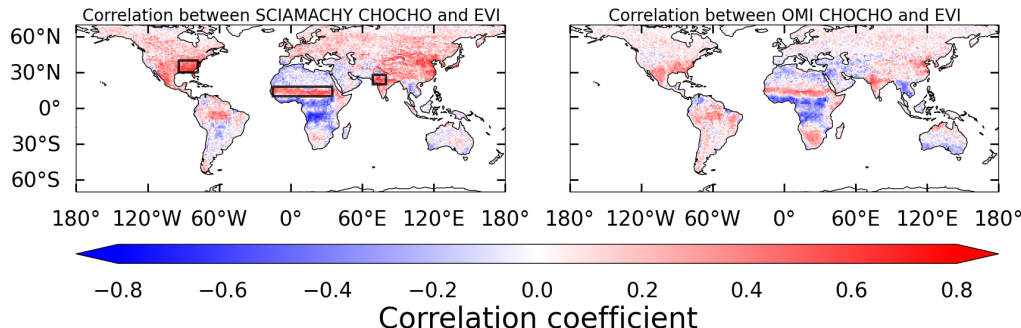


**Figure 4.6:** Pearson coefficient correlation map between CHOCHO VC and EVI over continental regions 2005–2014.

atmosphere result from the oxidation of biogenic VOC, where isoprene oxidation is responsible for 90%, while the remaining sources are ethane and monoterpenes (Stavrakou et al., 2009a).

In order to investigate the link between glyoxal and biogenic activities, correlation coefficients between CHOCHO and enhanced vegetation index (EVI) were computed, where EVI represents a measure of vegetation “greenness”, a composite property of leaf chlorophyll and canopy cover, which can be retrieved from the MODerate resolution Imaging Spectroradiometers (MODIS) on board NASA’s Terra and Aqua satellites Jiang et al. (2008). Investigating a possible linear relationship between CHOCHO VCs from OMI and SCIAMACHY and EVI from Aqua and Terra satellites respectively, monthly mean values of CHOCHO VCs and EVI with a grid resolution of  $0.5 \text{ deg} \times 0.5 \text{ deg}$  were used in the calculations. Figure 4.6 shows a global map of correlation coefficients between SCIAMACHY CHOCHO and EVI Terra (morning instruments) and OMI CHOCHO and EVI Aqua (afternoon instruments) for the time periods 2007–2014 and 2005–2014, respectively. The highest correlations between CHOCHO and EVI were found for three regions (Southeastern USA, Africa north of equator, and Northwest India), even correlation coefficients larger than 0.8 were found over these areas (see Fig. 4.6). Time series of spatially averaged monthly means were computed for the three regions (see Fig. 4.6, black boxes) and are shown in Fig. 4.7. The seasonal behaviour of glyoxal and EVI are in good correspondence for all three regions, which leads to the conclusion that the dominant source of glyoxal is biogenic emissions. This is in agreement with the results obtained for one year of analysis of SCIAMACHY CHOCHO VCs and EVI by Vrekoussis et al. (2009). Addition-

#### 4. OBSERVATIONS OF GLYOXAL FROM SPACE

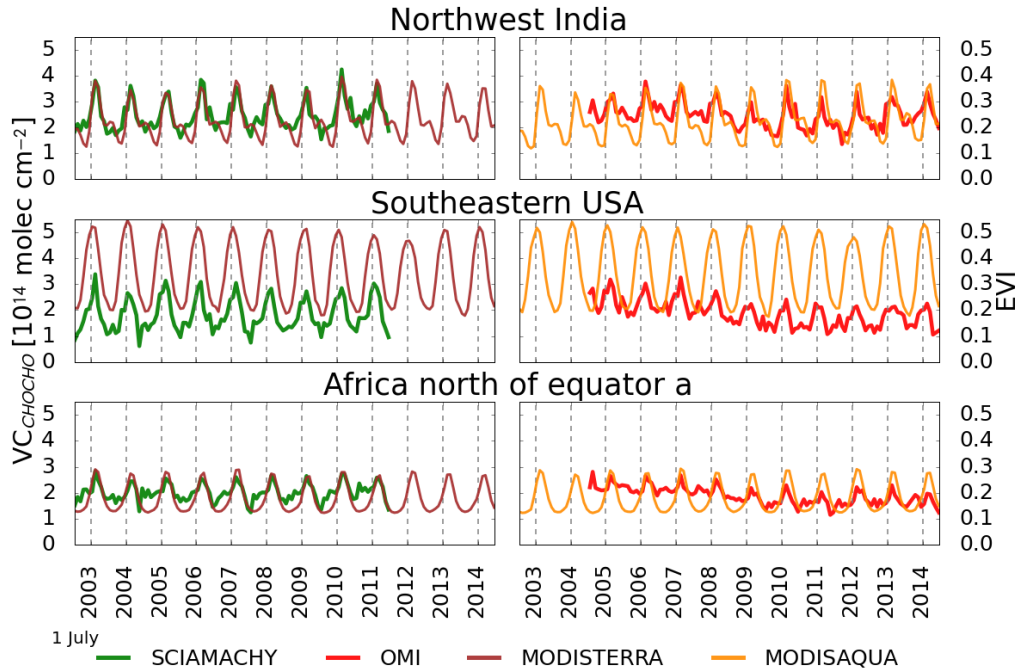


**Figure 4.7:** Time series of glyoxal VCs and EVI over regions, where high correlation coefficients were found for 2005–2014 (Africa north of equator, Southeastern USA, and Northwest India; black boxes in Fig. 4.6).

ally, some differences are observed between SCIAMACHY and OMI CHOCHO VCs, which are not observed between Terra and Aqua EVI, these differences could be related to the photochemical regime of VOC. Maxima of glyoxal VCs are found in the warm seasons for both instruments, probably caused by the increase isoprenes emissions, which also corresponds to the major growth phase of plants. Negative correlations between CHOCHO VCs and EVI were found over regions in Africa, which are characterized by high pyrogenic emissions as discussed in the section below.

##### 4.3.2 Pyrogenic emissions\*

Another main source of glyoxal in the atmosphere is pyrogenic emissions, which together with biogenic emissions are one of the main contributors of trace

---

\* Part of this subsection has been previously published as part of Alvarado et al. (2014).

### 4.3 IDENTIFICATION OF GLYOXAL SOURCES

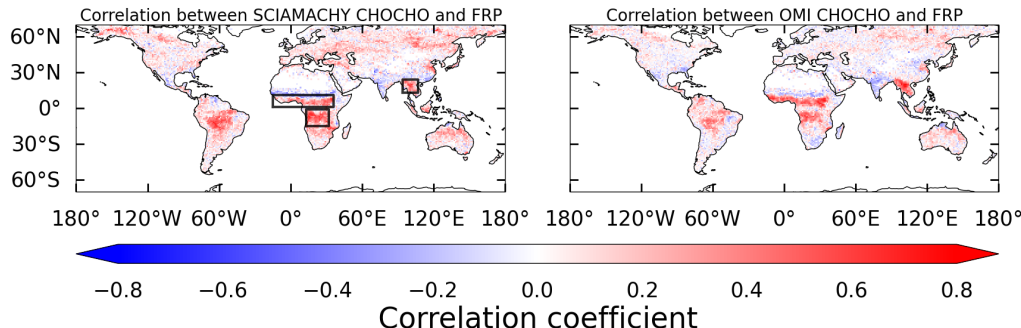


**Figure 4.8:** Pearson correlation coefficients of FRP and CHOCHO VCs over continental regions from 2005 to 2014.

gases to the atmosphere over tropical and sub-tropical areas, and are estimated to contribute 18 % of the global CHOCHO levels (Stavrakou et al., 2009a). Around 60 % of this glyoxal is believed to be emitted directly by the fires and the rest by secondary production (Stavrakou et al., 2009a). It is well known that large fire events occur during the warm season in Africa. In order to identify the regions with largest production of CHOCHO from fires, correlation coefficients between CHOCHO VCs and fire radiative power (FRP) are presented. FRP is a measure of outgoing radiant heat from fires (in units of  $\text{wattcm}^{-2}$ ), which can be retrieved from the MODIS Terra and Aqua similar to EVI (Justice et al., 2002).

As for biogenic emissions, a linear relationship is assumed between glyoxal and FRP. The calculations were performed with a grid resolution of  $0.5^\circ \times 0.5^\circ$  using monthly means of OMI and SCIAMACHY CHOCHO VCs and FRP from MODIS Aqua and Terra, respectively. High correlation coefficients are found over Africa south of the equator and Myanmar–Thailand (see Fig. 4.8), which correspond to regions with large fire activities during the dry season. Also, some negative correlation coefficients are observed in Fig. 4.8, which correspond to regions dominated by biogenic emissions as shown in Vrekoussis et al. (2010). A linear relationship between tropospheric  $\text{NO}_2$  VCs and FRP was already shown by Schreier et al. (2014). They demonstrated a strong link between the seasonal cycles of tropospheric  $\text{NO}_2$  and FRP for the main biomass burning regions. In this study, we found a comparable connection between CHOCHO and FRP for two similar regions in Africa as shown in Schreier et al. (2014). The time series of spatially averaged monthly means are shown in Fig. 4.9 for the three regions. Although pyrogenic emissions contribute only about 18 % to the global budget

#### 4. OBSERVATIONS OF GLYOXAL FROM SPACE

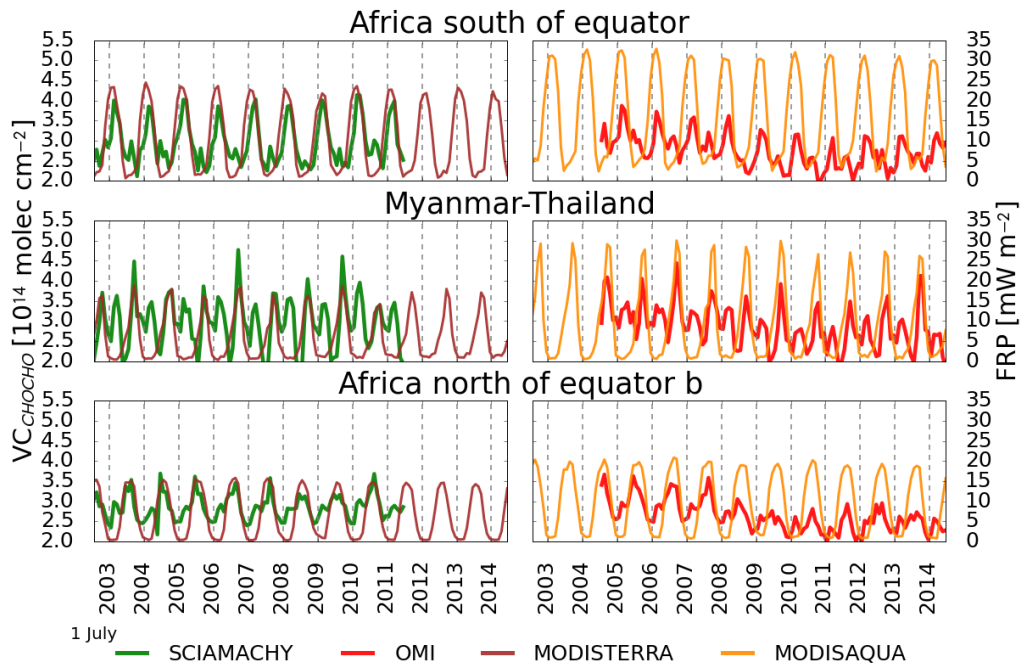


**Figure 4.9:** Time series of glyoxal and FRP over region where high correlation coefficient were found for 2005–2014 (Africa north of equator b, Africa south of equator, and Myanmar–Thailand: black boxes Fig. 4.8).

of CHOCHO (Stavrakou et al., 2009a), there clearly exist some regions where fires are the dominant source of glyoxal and where good agreement in seasonal behaviour is found with FRP. Additional peaks are observed in CHOCHO VCs during the wet season in all three regions. As there is no significant fire activity during this time, these peaks are most likely caused by biogenic sources. In addition, similar to regions with high correlation between EVI and CHOCHO VCs, the GOME–2A CHOCHO columns are higher than those from OMI.

##### 4.3.3 Anthropogenic emissions

In the global maps of glyoxal, some hot-spots can be identified over regions with large populations (e.g., Los Angeles, USA; Pearl River Delta, China). About 27 % of the global glyoxal originated from anthropogenic activities (Stavrakou et al., 2009a). About 60 % of this are produced by acetylene oxidation, 20 % are due to primary glyoxal, and about 15 % are formed from aromatics. To identify

#### 4.3 IDENTIFICATION OF GLYOXAL SOURCES

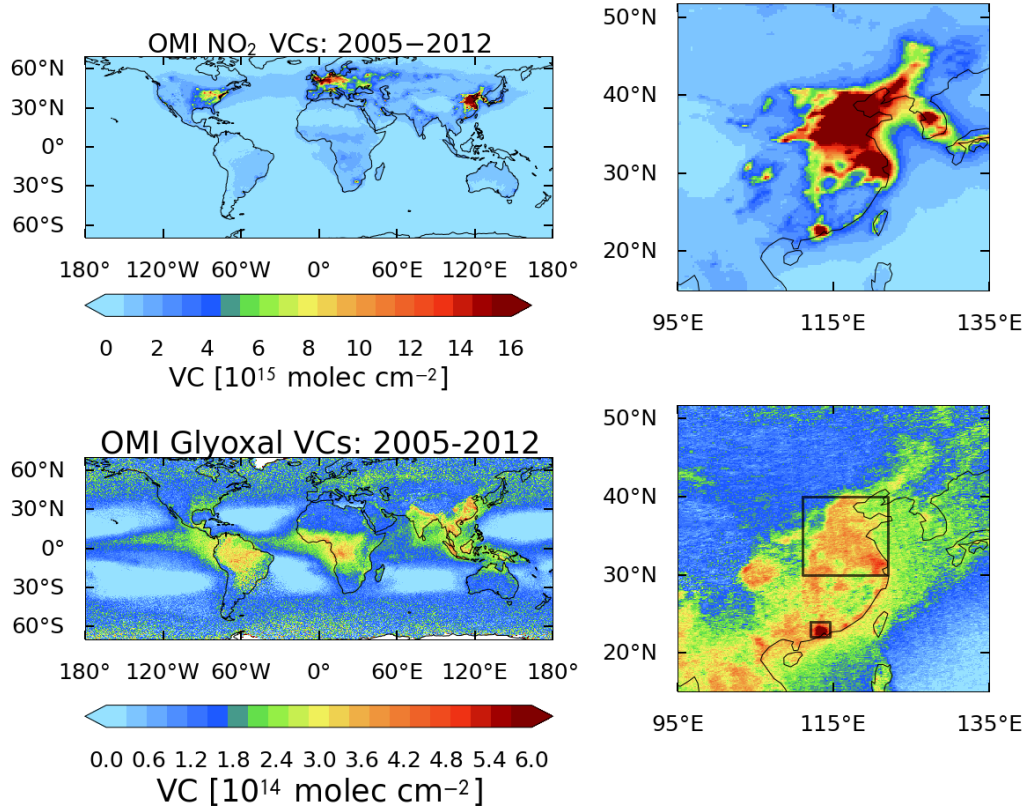


**Figure 4.10:** Averaged global maps of CHOCHO and tropospheric NO<sub>2</sub> VCs (left) and zoom maps of CHOCHO and tropospheric NO<sub>2</sub> over China (right) for period of 2005–2012.

regions where the dominant sources of glyoxal are anthropogenic, tropospheric NO<sub>2</sub> VCs from OMI measurements are used (Hilboll et al., 2013), as tropospheric NO<sub>2</sub> is a tracer of anthropogenic activities, in particular combustion of fossil fuels (Richter et al., 2005). Tropospheric NO<sub>2</sub> and CHOCHO VCs from OMI measurements are shown in Fig. 4.10, where both gases present clearly different spatial distributions (CHOCHO: mainly over tropical and sub-tropical regions; NO<sub>2</sub>: mainly over regions with large populations, China, Europe and USA). At closer inspection, CHOCHO VCs have a similar spatial distribution to tropospheric NO<sub>2</sub> VCs over China (see Fig. 4.10, right), the hot-spots over the Pearl River Delta (PRD) and Northeastern China (NE-China) being clearly visible.

In order to investigate this further, Pearson correlation coefficients between CHOCHO and tropospheric NO<sub>2</sub> VCs over two regions are computed (see Fig. 4.11,

## 4. OBSERVATIONS OF GLYOXAL FROM SPACE

right, black boxes). The calculations were performed with a grid resolution of  $0.5^\circ \times 0.5^\circ$  using monthly means of OMI CHOCHO and NO<sub>2</sub> VCs from 2005 to 2012. The Pearson correlation coefficient obtained for PRD and NE-China region are 0.7 and 0.4, respectively (see Fig. 4.11, top). The higher correlation between CHOCHO and tropospheric NO<sub>2</sub> corresponds to the PRD region, which includes large metropolis, and the combination of all these cities form one of the most densely populated regions in the world, having a population of about 57 million. As in this region, there are not only anthropogenic but also biogenic and pyrogenic sources, the analysis was repeated using only winter months (more tropospheric NO<sub>2</sub> is emitted). The correlation between the datasets increases significantly, being 0.62 and 0.81 for NE-China and PRD, respectively (see Fig. 4.11, bottom). This increase is especially pronounced over NE-China, where the biogenic contribution is significant in summer due to increased isoprene emissions during this period. In contrast to PRD region where the emission of glyoxal from vegetation is less.

### 4.4 “Hot-spot” areas of glyoxal and comparison with indicators of different sources

After the description of the global glyoxal VC distribution and comparison among instruments, its seasonal and annual variation and correlations with possible sources, closer inspection over areas where the glyoxal levels are high will be performed. For that, 21 regions have been selected on the globe (see Fig. 4.12, black boxes), which are representative of continental distribution of glyoxal, and these have been grouped by regions. Additionally, mean values of EVI, FRP and NO<sub>2</sub> VCs are compared with glyoxal for the different seasons, in order to investigate the possible dominant sources for each glyoxal “hot-spot”. For consistency, all datasets have been regridded to the same resolution ( $0.5^\circ \times 0.5^\circ$ ).

#### 4.4.1 North and Central America

For this region, two different locations are used (Southeastern USA and Central America: see Fig. 4.12, boxes 1–3). Figure 4.13 shows the comparison of normalized mean values of CHOCHO VCs to EVI (biogenic), FRP (Pyrogenic), and tropospheric NO<sub>2</sub> VCs (anthropogenic) for the different seasons from morn-

#### 4.4 “HOT-SPOT” AREAS OF GLYOXAL AND COMPARISON WITH INDICATORS OF DIFFERENT SOURCES

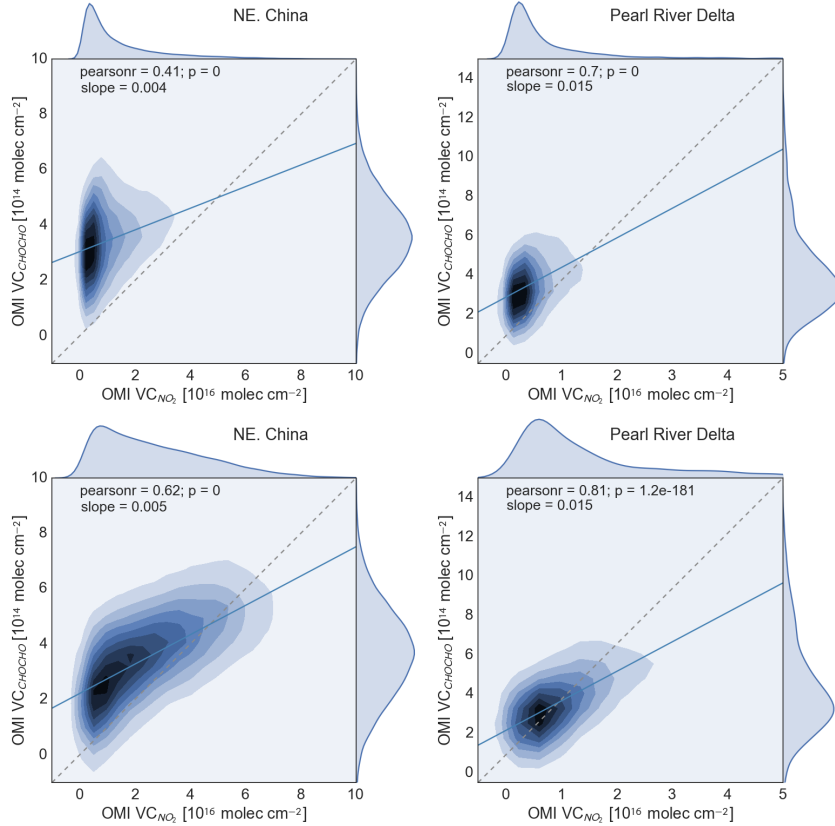


**Figure 4.11:** Density correlation plots between CHOCHO and tropospheric NO<sub>2</sub> VCs for two selected areas over China (see Fig. 4.10, black boxes) computed including all data between 2005 and 2012 (Top) and only taking into account the months corresponding to winter season (bottom).

ing and afternoon instruments over Southeastern USA and Central America for the period 2007–2011. In general, the variability of glyoxal VCs among the seasons for Central America are less pronounced than for the Southeastern USA (see Fig. 4.13). The mean values from Central America are higher than those of the Southeastern USA. In addition, the variability of glyoxal VCs over the Southeastern USA is in agreement with the variability of EVI over this region, the maximum for both quantities occurring during JJA (see Fig. 4.13, top), which corresponds to the warm season and thus a major release of isoprene during the growth of plants. In the case of Central America, the glyoxal amounts are almost constant during MAM ( $2.3\text{--}2.8 \times 10^{14}$  molec cm<sup>-2</sup>), JJA ( $2.1\text{--}2.7 \times 10^{14}$  molec cm<sup>-2</sup>),

#### 4. OBSERVATIONS OF GLYOXAL FROM SPACE

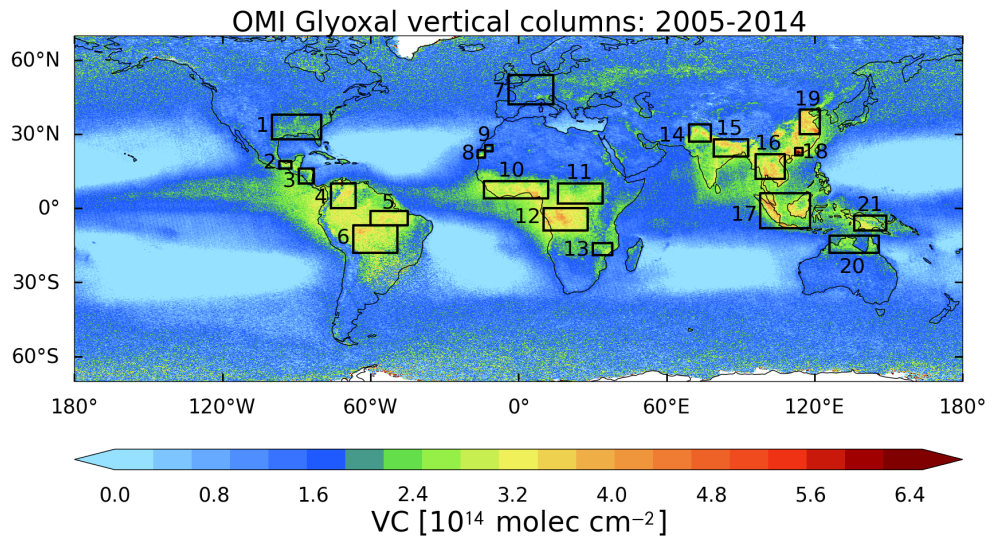


**Figure 4.12:** Selected “hot-spots” of CHOCHO VCs over continental regions: black boxes 1–21.

and SON ( $2.4\text{--}3.2 \times 10^{14}$  molec  $\text{cm}^{-2}$ ), however slightly lower values are observed during DJF ( $1.8\text{--}2.3 \times 10^{14}$  molec  $\text{cm}^{-2}$ ) (see Fig. 4.13, bottom). This is consistent with the variability of EVI and FRP during the seasons, high FRP values during MAM and low values for the other three seasons, and the opposite for EVI, high values during JJA and SON and lower during MAM and DJF. On the other side, tropospheric  $\text{NO}_2$  VCs behave similarly as glyoxal VCs over the seasons for Central America, however over Southeastern USA, the glyoxal VCs decrease for DJF but the  $\text{NO}_2$  VCs increase significantly during that period due to the increased anthropogenic emissions and decrease of light, which lead to less  $\text{NO}_2$  photolysis.

Additionally, the values of CHOCHO and  $\text{NO}_2$  from morning orbits are higher than those from afternoon and the opposite is observed for EVI and FRP (higher in the afternoon than those from morning). These differences in the case of glyoxal and nitrogen dioxide could be related to different overpass times at the satellites, sampling different emissions and photochemical regimes as we have mentioned above.

#### 4.4 “HOT-SPOT” AREAS OF GLYOXAL AND COMPARISON WITH INDICATORS OF DIFFERENT SOURCES

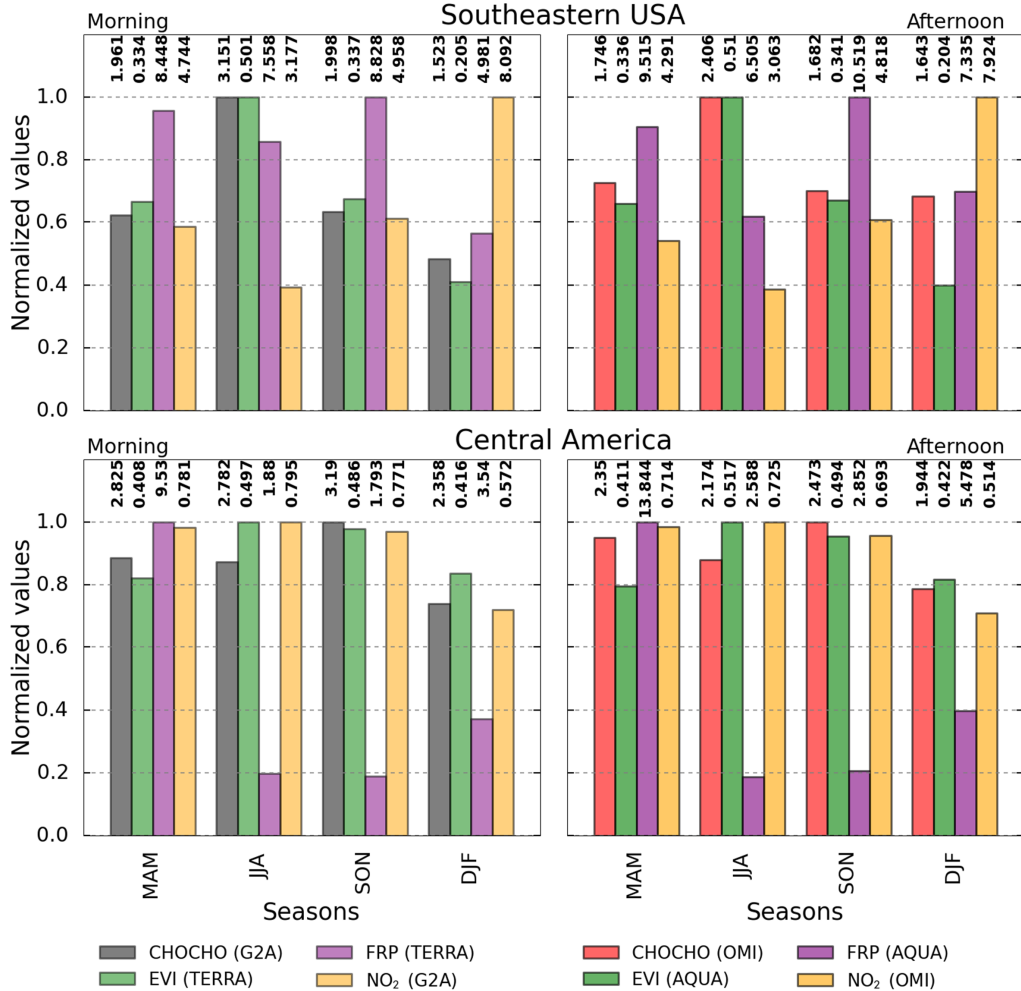


**Figure 4.13:** Seasonal means of CHOCHO VCs [ $10^{14}$  molec  $\text{cm}^{-2}$ ], FRP [ $\text{mW m}^{-2}$ ], EVI and NO<sub>2</sub> VCs [ $10^{15}$  molec  $\text{cm}^{-2}$ ] normalized to the respective maximum over each region from morning and afternoon instruments over Southeastern USA and Central America during 2007–2011.

#### 4.4.2 South America

Regions over the tropical rainforests of Amazonia have been selected (South America a, b and c: see Fig. 4.12, boxes 4–6). South America is characterized by dense vegetation. However, the large abundance of glyoxal over this region is not only produced by VOC induced by biogenic activities (high values of EVI in

#### 4. OBSERVATIONS OF GLYOXAL FROM SPACE

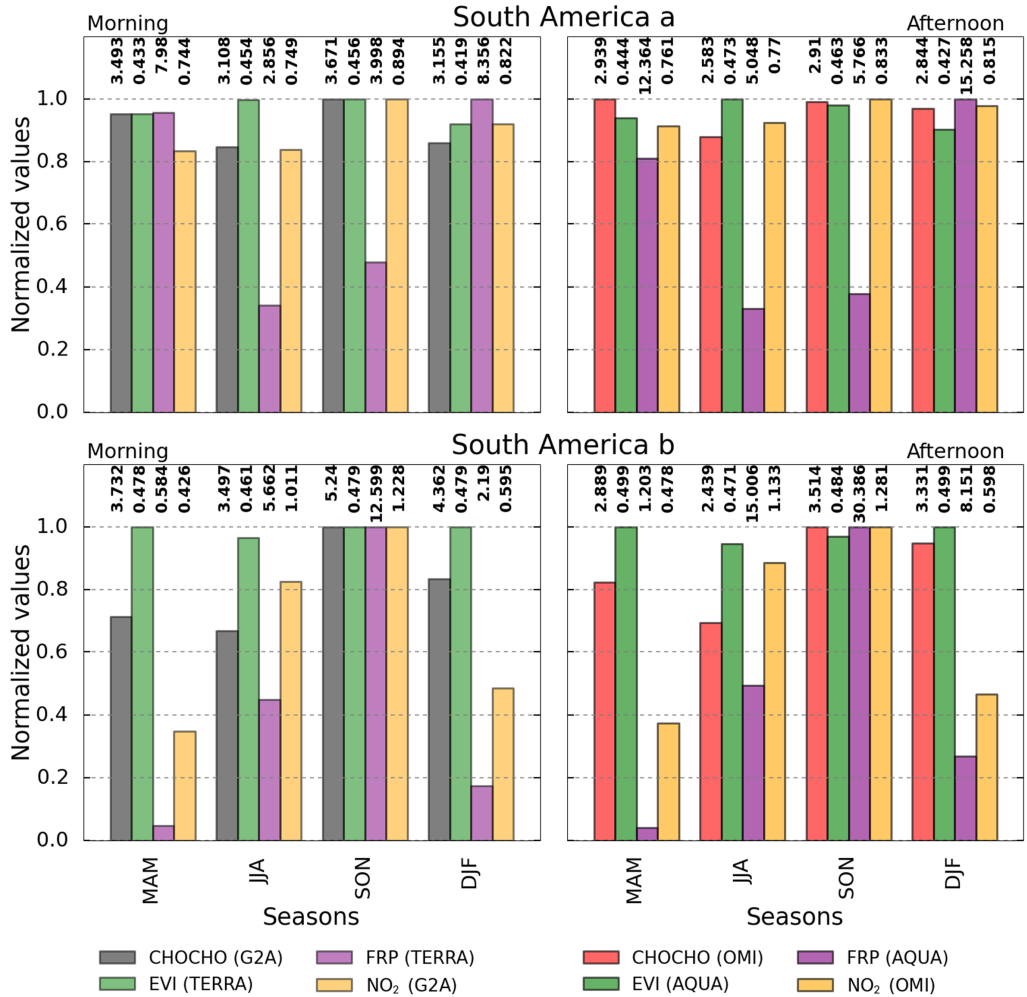


**Figure 4.14:** Seasonal means of CHOCHO VCs [ $10^{14}$  molec  $\text{cm}^{-2}$ ], FRP [ $\text{mW m}^{-2}$ ], EVI and NO<sub>2</sub> VCs [ $10^{15}$  molec  $\text{cm}^{-2}$ ] normalized to the respective maximum over each region from morning and afternoon instruments over South America (a and b, Fig. 4.12, boxes 4–3) during 2007–2011.

comparison to other regions, e.g. North and Central America), but also by pyrogenic emissions. Figure 4.14 shows the comparison of mean normalized values of CHOCHO VCs, EVI, FRP, and tropospheric NO<sub>2</sub> VCs for different seasons from morning and afternoon instruments over South America (a and b) for the period 2007–2011. In South America a, the glyoxal values remains almost con-

#### 4.4 “HOT-SPOT” AREAS OF GLYOXAL AND COMPARISON WITH INDICATORS OF DIFFERENT SOURCES

stant during the seasons, with a very small increase during SON (see Fig. 4.14, top). However, over South America b and c, there is a clear maximum in the glyoxal VCs during SON, which also corresponds to a maximum in FRP. Although pyrogenic emissions contribute less systematically than biogenic emissions, their occurrence coincides with maximum amounts of glyoxal VCs. The glyoxal VCs over South America vary between  $2.5 \times 10^{14}$  and  $3.7 \times 10^{14}$  molec cm $^{-2}$  for MAM,  $2.2 \times 10^{14}$  and  $3.5 \times 10^{14}$  molec cm $^{-2}$  for JJA,  $2.9 \times 10^{14}$  and  $5.2 \times 10^{14}$  molec cm $^{-2}$  for SON, and between  $2.8 \times 10^{14}$  and  $4.3 \times 10^{14}$  molec cm $^{-2}$  for DFJ. These values are almost twice as large as those observed over North America. In addition, South America b and c behave very similar through the seasons in glyoxal, EVI, FRP and NO<sub>2</sub> levels. The glyoxal VCs behave similar to EVI over the seasons, which remains constant during all seasons, and only have differences when glyoxal increased due to fire emissions (increase of FRP). Additionally, similar to glyoxal, the values of EVI and FRP over South America are higher than those from North America, but with lower NO<sub>2</sub> levels. Thus, the dominant sources of glyoxal over this region are VOC produced by biogenic emission, and with a maximum in SON induced by pyrogenic emissions.

##### 4.4.3 Europe and Western Sahara

An European region and two “hot-spots” over Western Sahara have been selected (see Fig. 4.12, boxes 7–9). Europe has been characterized by high population density and thus large anthropogenic emissions. The levels of CHOCHO over Europe are moderately low in comparison to those from North and South America. These values vary between  $1.5 \times 10^{14}$  and  $2.1 \times 10^{14}$  molec cm $^{-2}$  (see Fig. 4.15, top), with a maximum during the warm season (JJA), when major isoprene emissions occur due to the increase of temperature. Also, the variability of EVI and FRP values behaves similarly to glyoxal with the maximum during the same period (JJA) as is shown in Fig 4.15, top. In contrast, the contribution from fires over this region is low in comparison to South America or Africa, which is clearly observed in the low FRP values over this region. Additionally, as consequence of large anthropogenic activities over Europe, large NO<sub>2</sub> VCs are found (Hilboll et al., 2013).

In addition, Fig. 4.15 (bottom) shows mean values normalized to the maximum over one of two regions selected over Western Sahara. For the two “hot-spots”, the values for EVI are very low and zero for FRP. Also, the NO<sub>2</sub> VCs are lower than those obtained over Europe, but as similar order of magnitude of those

#### 4. OBSERVATIONS OF GLYOXAL FROM SPACE

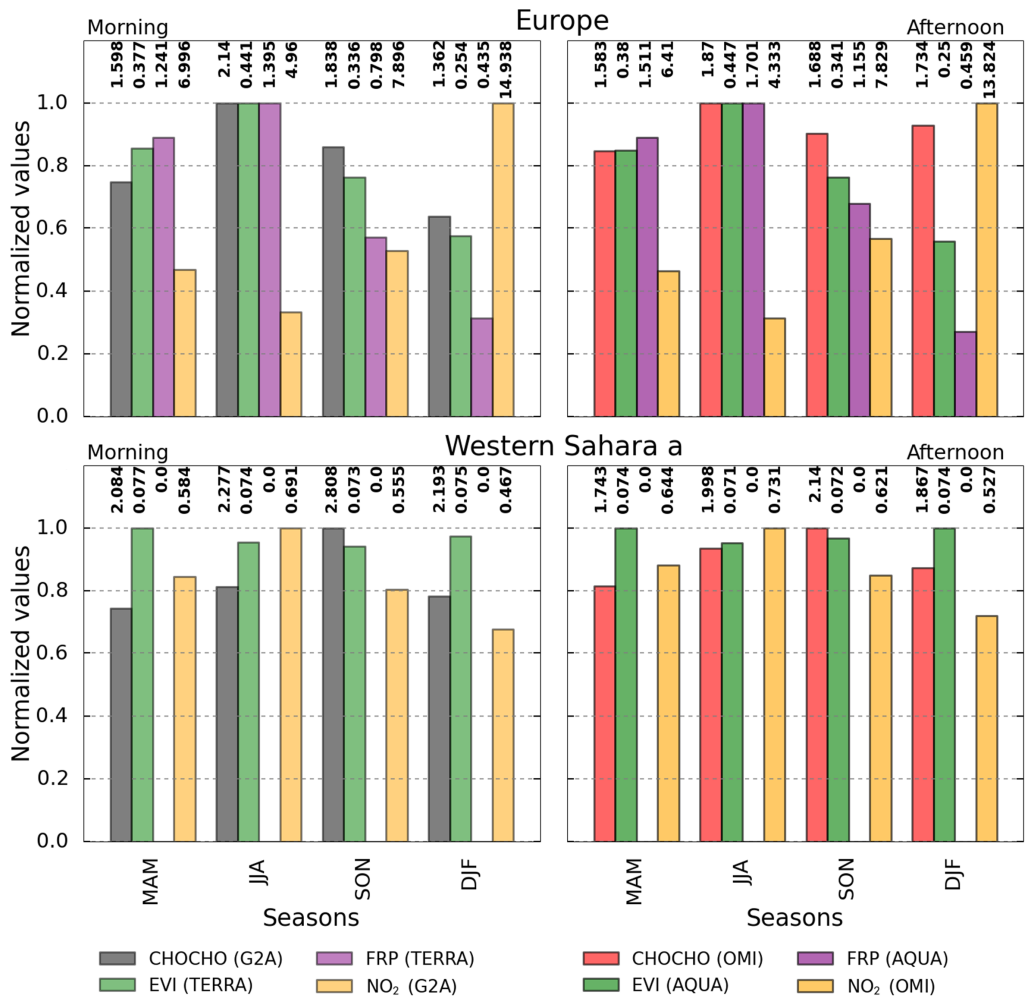


**Figure 4.15:** Seasonal means of CHOCHO VCs [ $10^{14}$  molec  $\text{cm}^{-2}$ ], FRP [ $\text{mW m}^{-2}$ ], EVI and NO<sub>2</sub> VCs [ $10^{15}$  molec  $\text{cm}^{-2}$ ] normalized to the respective maximum over each region from morning and afternoon instruments over Europe and Western Sahara a, Fig. 4.12, boxes 7–8) during 2007–2011.

obtained over South America. Also, NO<sub>2</sub> values behave almost constant through the seasons. The glyoxal levels over these two “hot-spots” are higher than those from Europe and they vary between  $1.7 \times 10^{14}$  and  $2.9 \times 10^{14}$  molec  $\text{cm}^{-2}$ . Despite the high values of glyoxal over these regions, no correlation is found with EVI, FRP and NO<sub>2</sub>, which are associated to biogenic, pyrogenic, and anthropogenic

#### 4.4 “HOT-SPOT” AREAS OF GLYOXAL AND COMPARISON WITH INDICATORS OF DIFFERENT SOURCES

emissions, respectively. Thus, the probable source of glyoxal over Western Sahara is unknown and further investigation will be need, however it is out of the scope of this study.

##### 4.4.4 Africa

Africa is one of the continental regions with the most vegetation, similar to South America, which implies large emissions of VOC and thus high glyoxal levels are observed. Additionally, biomass burning is a common phenomenon over this area, which is a contributor of glyoxal levels (Vrekoussis et al., 2009). Four regions have been selected over Africa, two north of the equator and two south of it (see Fig. 4.12, boxes 10–13). In order to investigate the variability of glyoxal and its relation with indicators of different sources (biogenic, pyrogenic and anthropogenic), a comparison of mean normalized values of CHOCHO VCs, EVI, FRP, and tropospheric NO<sub>2</sub> VCs for different seasons from morning and afternoon instruments over two of four regions selected in Africa for the period 2007–2011 are shown in Fig. 4.14. The CHOCHO VCs vary between  $1.8 \times 10^{14}$  and  $3.9 \times 10^{14}$  molec cm<sup>-2</sup> for MAM,  $1.7 \times 10^{14}$  and  $5.1 \times 10^{14}$  molec cm<sup>-2</sup> for JJA,  $2.7 \times 10^{14}$  and  $4.2 \times 10^{14}$  molec cm<sup>-2</sup> for SON, and between  $2.4 \times 10^{14}$  and  $4.3 \times 10^{14}$  molec cm<sup>-2</sup> for DJF. The maxima for each region are found in the season with large wild and savanna fires, which is correlated with the high values in FRP during the season. For Africa north of the equator, this maximum corresponds to DJF, while for Africa south of the equator to JJA and SON. Also, NO<sub>2</sub> values follow a similar variability over these regions (see Fig. 4.14). In addition, the values found in EVI are larger than those found over Europe and North America, but comparable in order of magnitude to those from South America, which varies between 0.22 and 0.46 and represent the dense vegetation found in Africa and South America. Despite the large fire activities over these African regions, the dominant source is biogenic emission, because in contrast to South America where the difference between the peaks of glyoxal during the wet and dry seasons are large, the background of glyoxal over Africa remains always high and the variability in the amplitudes of CHOCHO VCs is less pronounced in most of the regions selected, showing small influence of biomass burnig season on the total CHOCHO levels.

## 4. OBSERVATIONS OF GLYOXAL FROM SPACE

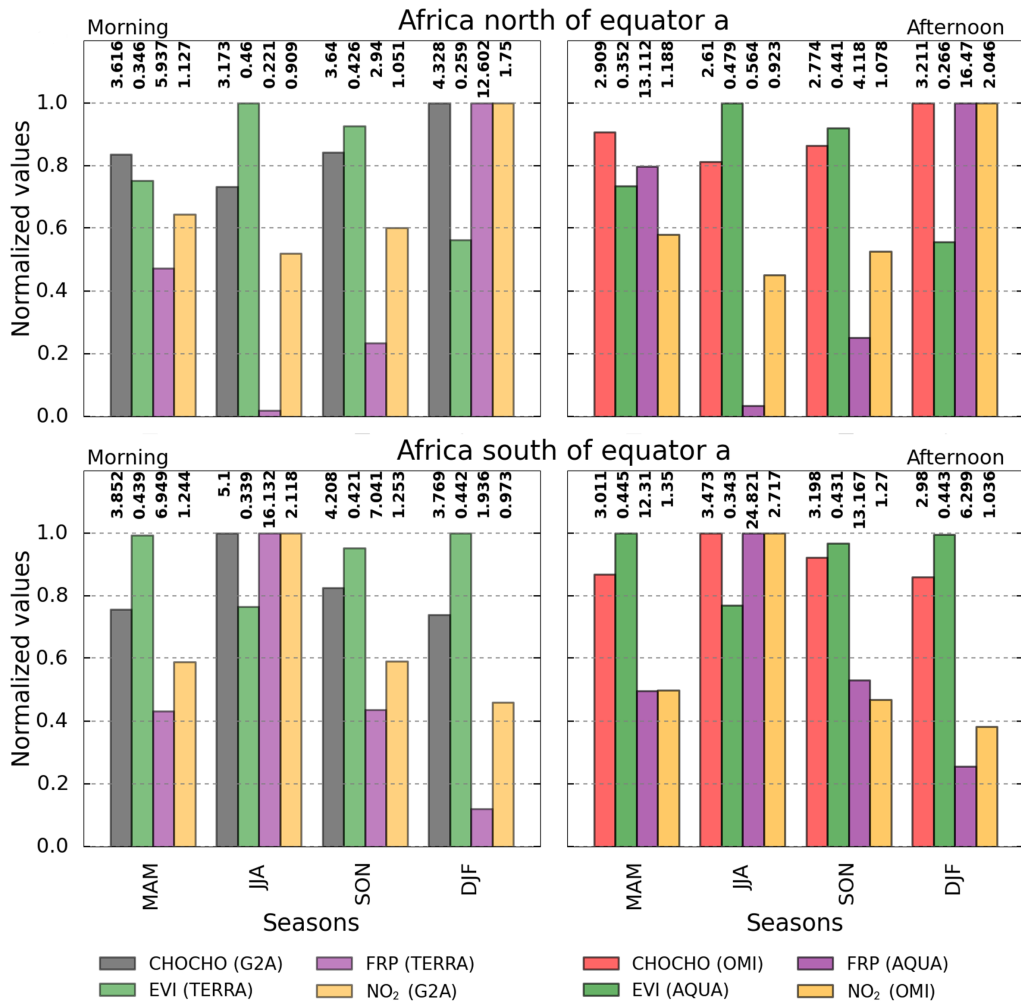


**Figure 4.16:** Seasonal means of CHOCHO VCs [ $10^{14}$  molec  $\text{cm}^{-2}$ ], FRP [ $\text{mW m}^{-2}$ ], EVI and NO<sub>2</sub> VCs [ $10^{15}$  molec  $\text{cm}^{-2}$ ] normalized to the respective maximum over each region from morning and afternoon instruments over two Africa regions (see Fig. 4.12, boxes 10–12) during 2007–2011.

### 4.4.5 Asia

Six “hot-spots” have been selected over Asia (see Fig. 4.12, boxes 11–19). Two over India and China, and one over Thailand and Indonesia. The Northeast China region is controlled by strong biogenic as well as pyrogenic emissions

#### 4.4 “HOT-SPOT” AREAS OF GLYOXAL AND COMPARISON WITH INDICATORS OF DIFFERENT SOURCES

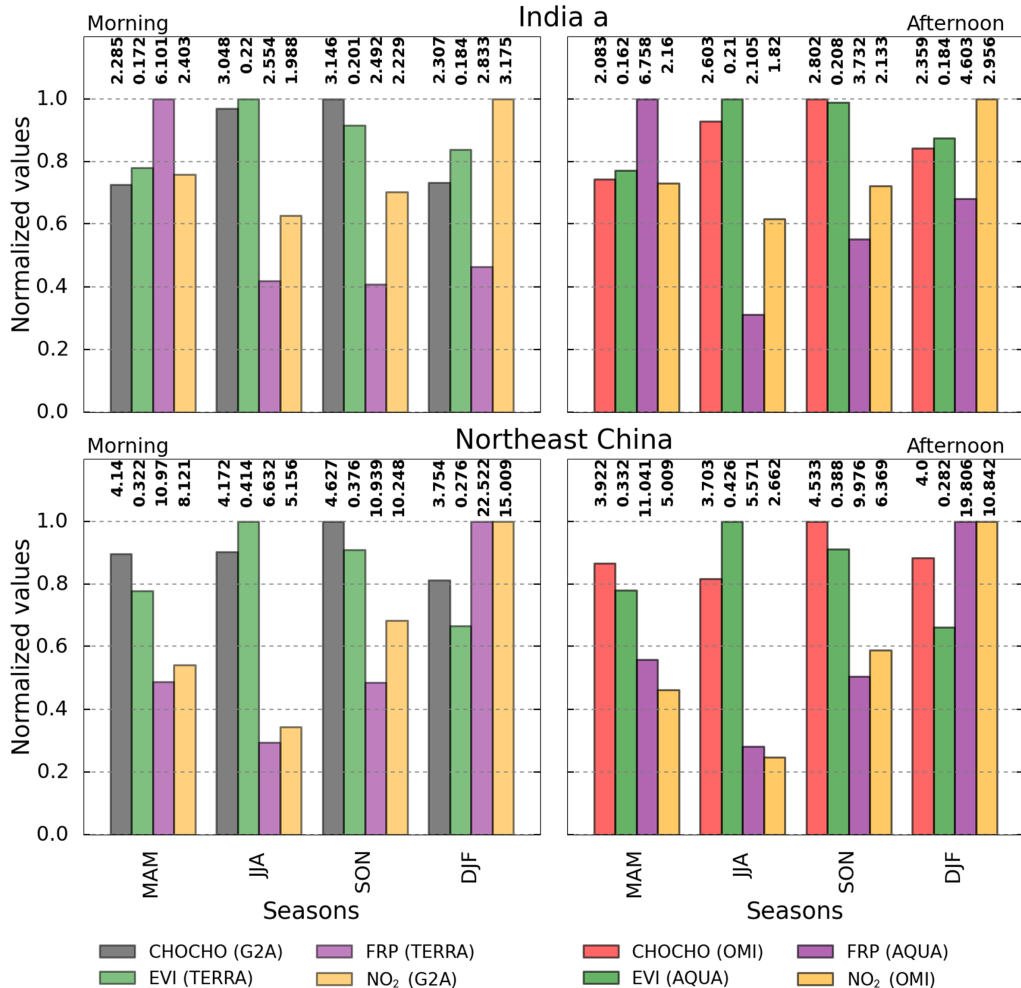


**Figure 4.17:** Seasonal means of CHOCHO VCs [ $10^{14}$  molec  $\text{cm}^{-2}$ ], FRP [mW  $\text{m}^{-2}$ ], EVI and NO<sub>2</sub> VCs [ $10^{15}$  molec  $\text{cm}^{-2}$ ] normalized to the respective maximum over each region from morning and afternoon instruments over India and Northeast China, (Fig. 4.12, boxes 14–19) during 2007–2011.

(Stavrakou et al., 2009b), while the Pearl-River-Delta region is mainly dominated by anthropogenic activities (high amounts of NO<sub>2</sub> are observed as well), but also has some contribution from fires and biogenic emissions as is reflected in the values for FRP and EVI, respectively. Figure 4.17 shows seasonal means normalized to the respective maximum over each region of CHOCHO VCs, EVI,

## 4. OBSERVATIONS OF GLYOXAL FROM SPACE

FRP, and NO<sub>2</sub> VCs for two of six selected “hot-spots” in Asia for 2007–2011. The glyoxal VCs are high for most of the regions in comparison of those columns obtained over Africa and South America and these behave different depending on the season and latitude. CHOCHO VCs have large influence for most of source production of VOC (biogenic, pyrogenic and anthropogenic), in fact despite that the major source of glyoxal is natural, in Asia there is a large contribution from fires and also from anthropogenic emissions, which can be observed in the Fig. 4.17, where depending on the season the high glyoxal values correlate to the respective indicator (e.g. JJA: EVI, SON: FRP, DFJ: NO<sub>2</sub>). In addition, the glyoxal columns vary between  $2.0 \times 10^{14}$  and  $4.5 \times 10^{14}$  molec cm<sup>-2</sup> for MAM,  $2.4 \times 10^{14}$  and  $4.2 \times 10^{14}$  molec cm<sup>-2</sup> for JJA,  $2.8 \times 10^{14}$  and  $4.6 \times 10^{14}$  molec cm<sup>-2</sup> for SON, and between  $2.3 \times 10^{14}$  and  $4.0 \times 10^{14}$  molec cm<sup>-2</sup> for DJF. Additionally, Fig. 4.17 shows seasonal behaviour is relatively similar for India and Northeast China, with the maximum values being retrieved during SON. In general, similar to another regions, the values of glyoxal from the morning instruments are larger than those from the afternoon instruments for almost all seasons. However, in the Northeastern China and Pearl-River-Delta regions, the glyoxal level from afternoon instrument during DFJ (winter season) the values are larger than those from morning (see Fig. 4.17, bottom), which also correspond to high levels of NO<sub>2</sub> over this region. This is consistent with results obtained from ground-based measurements over highly polluted areas by Volkamer et al. (2005a), where glyoxal showed a maximum at noon (close to the overpass time of OMI). However, in measurements performed over Athens and Nairobi from ground based measurements, the maximum of glyoxal is found in the morning (see Chap. 6), nevertheless the chemistry, topography and population density of these cities are different and thus different behaviors in glyoxal is expected.

### 4.4.6 Oceania

Two regions have been selected for Oceania (Northern Australia and New Guinea: see Fig. 4.12, boxes 20–21). Northern Australia is characterized by large diversity of environments such as desert, tropical subtropical and others. The region selected over Australia is dominated by large vegetations and periods of biomass burning. However, New Guinea is characterized by dense vegetation, having EVI values comparable to those from Africa and South America. Figure 4.17 shows seasonal means of CHOCHO VCs, EVI, FRP, and tropospheric NO<sub>2</sub> VCs normalized to the respective seasonal maximum over Australia and

#### 4.4 “HOT-SPOT” AREAS OF GLYOXAL AND COMPARISON WITH INDICATORS OF DIFFERENT SOURCES

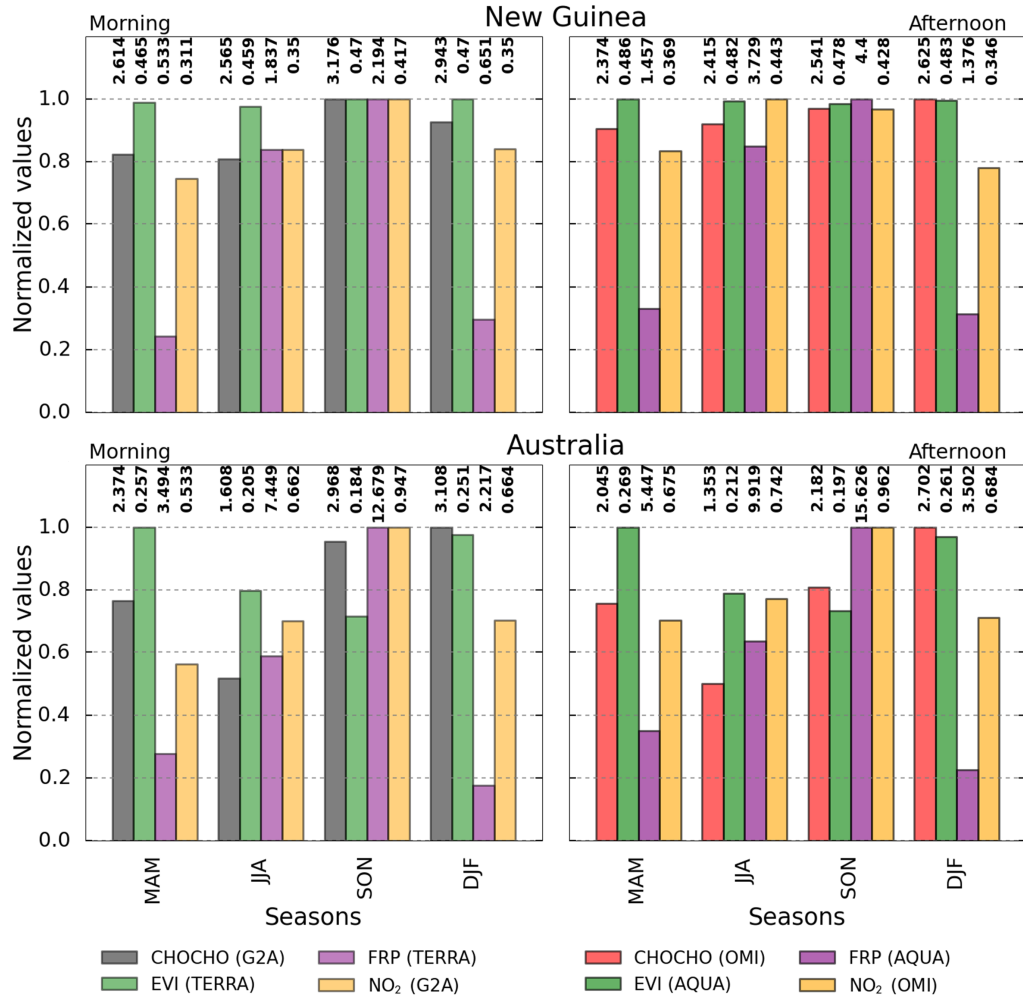


**Figure 4.18:** Seasonal means of CHOCHO VCs [ $10^{14}$  molec  $\text{cm}^{-2}$ ], FRP [ $\text{mW m}^{-2}$ ], EVI and NO<sub>2</sub> VCs [ $10^{15}$  molec  $\text{cm}^{-2}$ ] normalized to the respective maximum over each region from morning and afternoon instruments over Australia and New Guinea (see Fig. 4.12, boxes 20–21) during 2007–2011.

New Guinea for 2007–2011. CHOCHO columns over New Guinea vary between  $2.3 \times 10^{14}$  and  $2.6 \times 10^{14}$  molec  $\text{cm}^{-2}$  for MAM,  $2.4 \times 10^{14}$  and  $2.5 \times 10^{14}$  molec  $\text{cm}^{-2}$  for JJA,  $2.5 \times 10^{14}$  and  $3.2 \times 10^{14}$  molec  $\text{cm}^{-2}$  for SON, and between  $2.6 \times 10^{14}$  and  $2.9 \times 10^{14}$  molec  $\text{cm}^{-2}$  for DJF, while in Northern Australia the glyoxal levels are slightly smaller for some seasons than those obtained over New Guinea

## 4. OBSERVATIONS OF GLYOXAL FROM SPACE

and vary between  $2.0 \times 10^{14}$  and  $2.3 \times 10^{14}$  molec cm $^{-2}$  for MAM,  $1.3 \times 10^{14}$  and  $1.6 \times 10^{14}$  molec cm $^{-2}$  for JJA,  $2.1 \times 10^{14}$  and  $2.9 \times 10^{14}$  molec cm $^{-2}$  for SON, and  $2.7 \times 10^{14}$  and  $3.1 \times 10^{14}$  molec cm $^{-2}$  for DJF. This is also reflected by the values of EVI over these regions. The EVI values for New Guinea are almost twice as large (0.47) as those from Australia (0.27). A seasonality in FRP is observed over Australia which corresponds to the maximum in glyoxal over this area. On the other hand, the NO<sub>2</sub> levels over these regions remain almost constant through the seasons. Thus, most likely, the main influence of glyoxal over these regions is biogenic emission (mainly for New Guinea) and fires as well (for both regions, but more strongly over Northern Australia), and probably, to a lesser degree, contribution from anthropogenic sources.

## 4.5 Summary

A global description of glyoxal retrieved from four different instruments shows that the largest levels are located in the tropical and subtropical regions, where dense vegetation can be found. In the northern and southern hemisphere, a clear seasonal pattern for glyoxal was found with the maximum for summer season.

The comparison of glyoxal VCs retrieved from measurements of OMI, GOME–2 (A and B), and SCIAMACHY shows good overall agreement in the seasonal behaviour. However, OMI glyoxal columns are systematically lower than those columns observed by SCIAMACHY and GOME–2 (A and B), especially for recent years (since 2010). This observation is even more evident in OMI CHOCHO VCs for regions within latitudes 30°S–5°N. In addition, the amplitude of the seasonal variation for OMI is smaller than for the other instruments. Significant differences were found over regions with large anthropogenic emissions. Moreover, a similar seasonal behaviour is observed among the four products, although less pronounced in the OMI product.

Correlation coefficients between EVI and CHOCHO columns larger than 0.8 have been found over regions characterized by dense vegetation, where the computed time series of EVI and glyoxal columns show strong and in-phase seasonal variations. Moreover, the maxima of glyoxal were found during the warm seasons, as a consequence of the increase in the isoprene emissions. Additionally, strong negative correlations between glyoxal columns and EVI were found over Africa, caused by large fire events in these regions, which mainly occur outside the growing season. The correlation coefficients between FRP and CHOCHO VCs over

## 4.5 SUMMARY

these regions are larger than 0.8 and the time series of FRP and glyoxal VCs show strong and in-phase seasonal variation. However, the source contribution over these regions is not only due to fires, because the background signal of glyoxal is large in these areas. Most likely due to the biogenic contribution, also an additional peak in glyoxal is found in the wet season which also could be related to biogenic influences.

Finally, a detailed comparison between glyoxal, EVI, FRP, and tropospheric NO<sub>2</sub> over 21 regions have been performed in order to characterize the possible sources of glyoxal in these regions. It is clear that the dominant source of glyoxal is biogenic emissions because in most of the regions it was observed to follow the behaviour of EVI. However, there are regions where the strong fire events become an important source for glyoxal, similarly this can be observed for regions with an important influence from anthropogenic emissions.

# 5

## Identification of VOC sources and case studies

### 5.1 Introduction

VOC play an important role in the atmosphere and have a significant influence on atmospheric composition (Vrekoussis et al., 2010; Curci et al., 2010). VOC originate from natural and anthropogenic sources as well as from fire emissions. VOC commonly have a short atmospheric lifetime between fractions of a day to months. On a global scale, the biogenic emissions are ten times larger than those produced by anthropogenic sources (Atkinson and Arey, 2003). VOC are emitted by oceans and plants as part of a complex system, in particular trees. Also, anthropogenic and fire emissions contribute to the total amounts of VOC in the atmosphere with about  $161\text{--}186 \text{ Tg C yr}^{-1}$  (Stavrakou et al., 2009b), and  $33\text{--}49 \text{ Tg C yr}^{-1}$  (Andreae and Merlet, 2001), respectively. Although the main pathways of biogenic VOC release to the atmosphere have been relatively well-known for many years, the uncertainties in total emissions are large since the amounts emitted depend on several parameters, e.g. on plant species, temperature, humidity and the condition of the plant.

For a better understanding and identification of VOC sources, Vrekoussis et al. (2010) used the ratio of CHOCHO to HCHO to classify the different sources. CHOCHO and HCHO are mainly emitted from natural and anthro-

## 5.2 RATIO OF GLYOXAL TO FORMALDEHYDE ( $R_{GF}$ )

pogenic sources as well as during fire events. Although the sources and chemistry are similar in many respects, the variation in production efficiency for different sources can be used to better constrain source attribution of VOC. This approach for source identification of VOC has already been used for ground and satellite based instruments (e.g. Vrekoussis et al., 2010; DiGangi et al., 2012; Li et al., 2013; Kaiser et al., 2015). However, different values of ratios have been reported in the literature and no clear agreement between them was found.

The first attempts to identify source types using the ratio of glyoxal to formaldehyde ( $R_{GF}$ ) from satellite measurement were reported by Wittrock et al. (2006) and Vrekoussis et al. (2009). Both studies used SCIAMACHY observations, which were limited to specific regions. Later, Vrekoussis et al. (2010) also computed the ratio from GOME-2A observations. From these studies, for places with known biogenic emissions, ratios in the range of 0.4–0.6 were found, while for regions with high anthropogenic emissions lower ratios were found in comparison to those from biogenic influence.

In the previous chapter, the correlation of glyoxal with indicators of biogenic, pyrogenic and anthropogenic emissions were evaluated. In order to extend our analysis, computation of the ratio of CHOCHO to HCHO for identify VOC sources is performed. In addition, analysis of temporal evolution of ratios globally and also for selected hot-spots is presented. Additionally, two selected case studies are presented.

## 5.2 Ratio of glyoxal to formaldehyde ( $R_{GF}$ )

In this study, GOME-2A data are used for computation of the ratio of glyoxal to formaldehyde. HCHO VCs have been retrieved as is described by Wittrock et al. (2006). Figure 5.1 shows global average maps of CHOCHO and HCHO VCs retrieved from GOME-2A measurements from 2007 to 2014. CHOCHO and HCHO VCs have similar global patterns with highest levels over tropical and subtropical regions, which are characterized by dense vegetation and fire activities. Some “hot-spots” are also found over highly populated cities for both species, which could be associated to anthropogenic emissions. In spite of the similarity of the global pattern, differences are found over some regions most likely due to difference in production efficiency of these VOC species. Furthermore, outflow of glyoxal is observed over ocean regions while for formaldehyde it is not observed. Previous studies associated this glyoxal to an unknown oceanic source (Vrekoussis

## 5. IDENTIFICATION OF VOC SOURCES AND CASE STUDIES

et al., 2010), because the lifetime of glyoxal is too short for such a transport event. Nevertheless, it will be discussed again in the following sections.

The  $R_{GF}$  have been computed using monthly mean gridded data of CHOCHO and HCHO VCs with a spatial resolution of  $1.0^\circ \times 1.0^\circ$ . These ratios have been averaged by season for the whole period (2007–2014). Figure 5.2 shows average  $R_{GF}$  for the four seasons for 2007–2014. Individual ratios show a large scatter, but some differences in the pattern of  $R_{GF}$  values among regions where biogenic sources are expected and those areas where the dominant sources of VOC are associated to anthropogenic and pyrogenic emissions can be found.  $R_{GF}$  has a clear seasonal behaviour, the large ratios being found over regions dominated by anthropogenic and pyrogenic emissions, and low values where the dominant source is natural. Also, there are regions where the  $R_{GF}$  variability is not clear.  $R_{GF}$  behaves similar to glyoxal over the seasons (see Fig. 4.5), with an increase during the warm season when more release of VOC from natural sources is observed.

For a better identification and assessment of VOC sources, a comparison of  $R_{GF}$  with EVI, FRP,  $\text{NO}_2$  over nine selected regions is performed (see Fig. 4.3: 1–Southeastern USA, 4–South America a, 6–South America c, 10–Africa north of equator a, 12–Africa south of equator a, 14–India a, 15–India b, 18–Pearl River Delta, and 19–Northeast China). For consistency, all datasets have been regridded to the same spatial resolution ( $0.5^\circ \times 0.5^\circ$ ). Figure 5.3 shows ratios of glyoxal to formaldehyde over the season for the nine selected regions for 2007–2014.  $R_{GF}$  behaves different for each region, however for most of the regions the lowest  $R_{GF}$  correspond to seasons with larger EVI (e.g. warm season for Southeastern USA, India, Pearl River Delta, and Northeast China). The opposite is observed when FRP and  $\text{NO}_2$  VCs increase, an increase of  $R_{GF}$  is observed. EVI values have a significant increase in the warm season for Southeastern USA, India, China, but over regions characterized by dense vegetation (e.g. South America, and Africa south of equator), the observed ratios are nearly constant over the seasons. Similar behaviour is found for EVI values with differences between seasons close to zero.

It is clear that  $R_{GF}$  varies quite strongly among the regions, in fact different vegetation types and land covers are expected for all these areas (see Fig. 5.4). For example, Southeastern USA, India, Pearl River Delta, and Northeast China are mainly characterized by a combination of croplands, woody savannas, and evergreen broadleaf forest, in contrast to South America, and Africa south of equator which are mainly dominated by evergreen broadleaf forest, savannas and

## 5.2 RATIO OF GLYOXAL TO FORMALDEHYDE ( $R_{GF}$ )

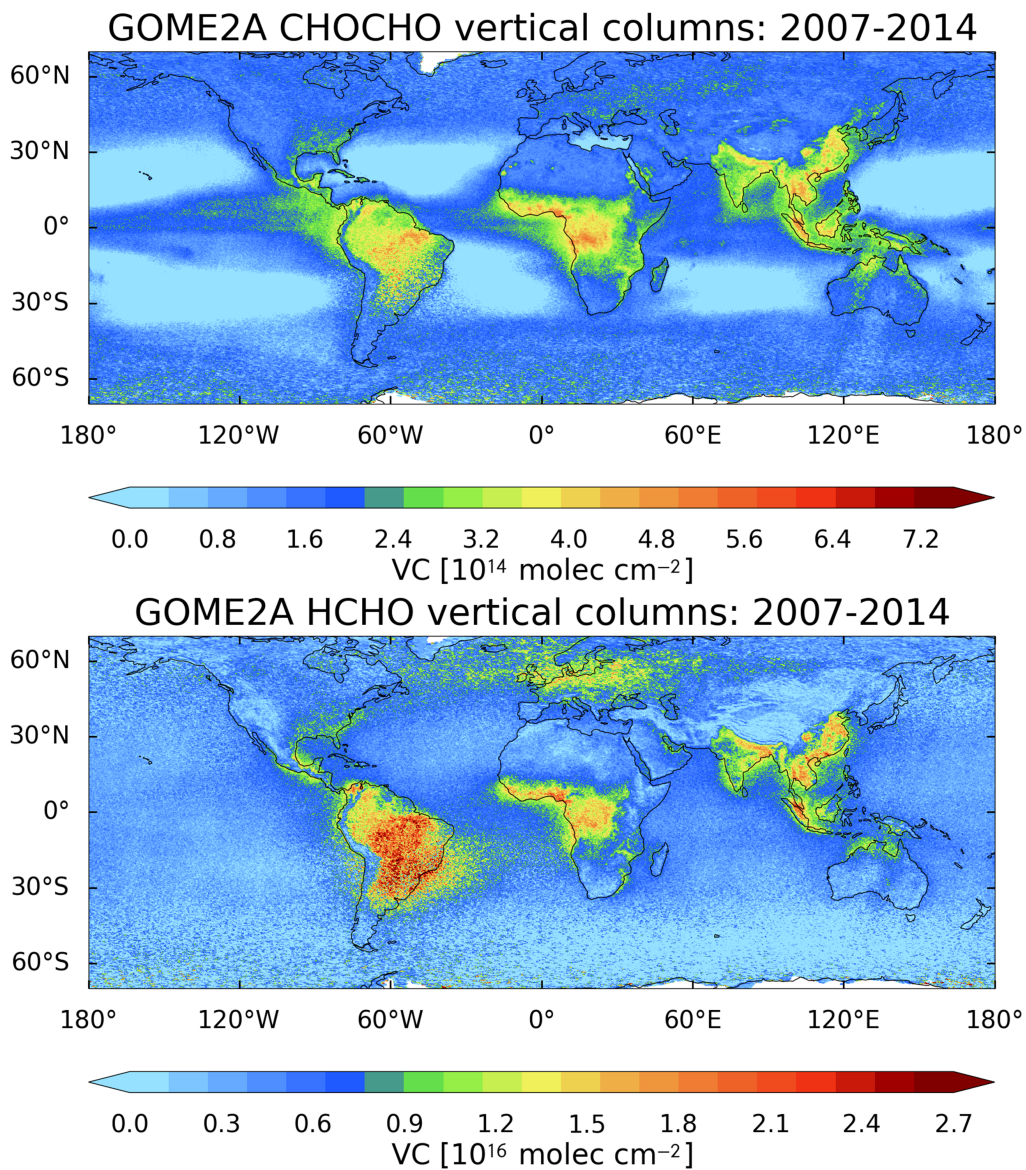


**Figure 5.1:** Global average maps of glyoxal and formaldehyde VCs for 2007–2014 from GOME–2A measurements. The global distributions of CHOCHO and HCHO are similar, high values being found over tropical and sub-tropical regions, where large extensions of vegetation are found. Outflow of glyoxal is observed over ocean regions whereas this is not observed for formaldehyde.

## 5. IDENTIFICATION OF VOC SOURCES AND CASE STUDIES

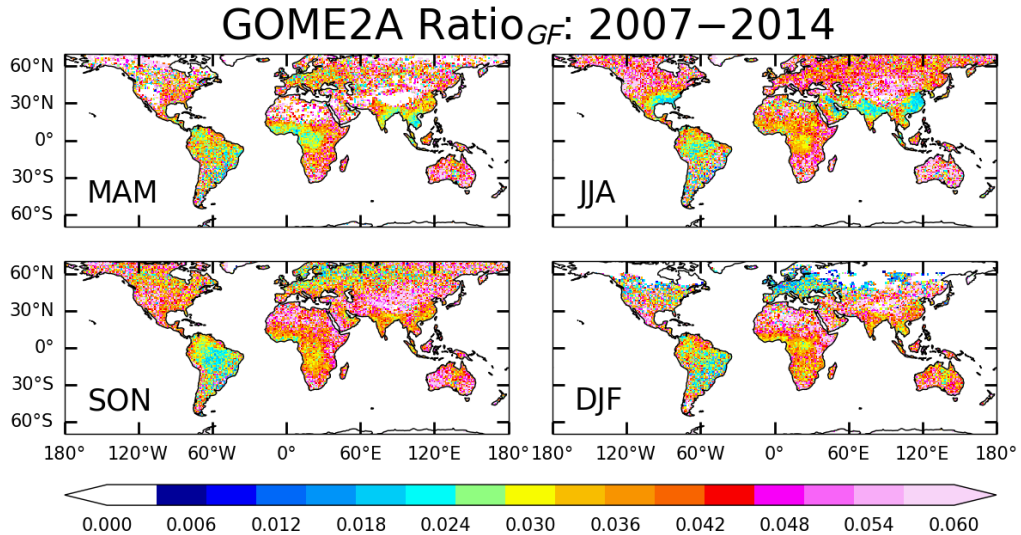


**Figure 5.2:** Seasonal global averaged ratio of glyoxal to formaldehyde from GOME–2A data for period between 2007 and 2014.

woody savannas. Another important difference between these regions is the temperature between seasons, strong changes are observed for subtropical regions (e.g. Southeastern USA, India and China) and nearly no changes for tropical areas (e.g. South America and Africa south of equator), subtropical regions are usually hotter than tropical regions during summer. In addition, the population density in regions such as Southeastern USA, India or China is higher than in South America, and Africa south of equator. Therefore, depending on the vegetation type, temperature and population, the ratio of glyoxal to formaldehyde varies. Values between 0.015 and 0.029 are found for those regions where strong changes of temperature are observed between seasons and also for regions where the dominant vegetation type is evergreen broadleaf forest (e.g. South America). For regions where there is also a large contribution from fire emissions, the ratios are large and nearly constant over the season (e.g. Africa south of equator). This assessment is in contrast with earlier results obtained by Vrekoussis et al. (2010), which associated large ratios to regions dominated by biogenic emissions and small R<sub>GF</sub> to regions with anthropogenic emissions as dominant source. However, it is important to mention that Vrekoussis et al. (2010) have computed the R<sub>GF</sub> for a complete period of two years and not by season. If the ratios obtained here are averaged over all seasons, then for regions such as Southeastern USA, China, India where large contributions from anthropogenic sources is expected

## 5.2 RATIO OF GLYOXAL TO FORMALDEHYDE ( $R_{GF}$ )

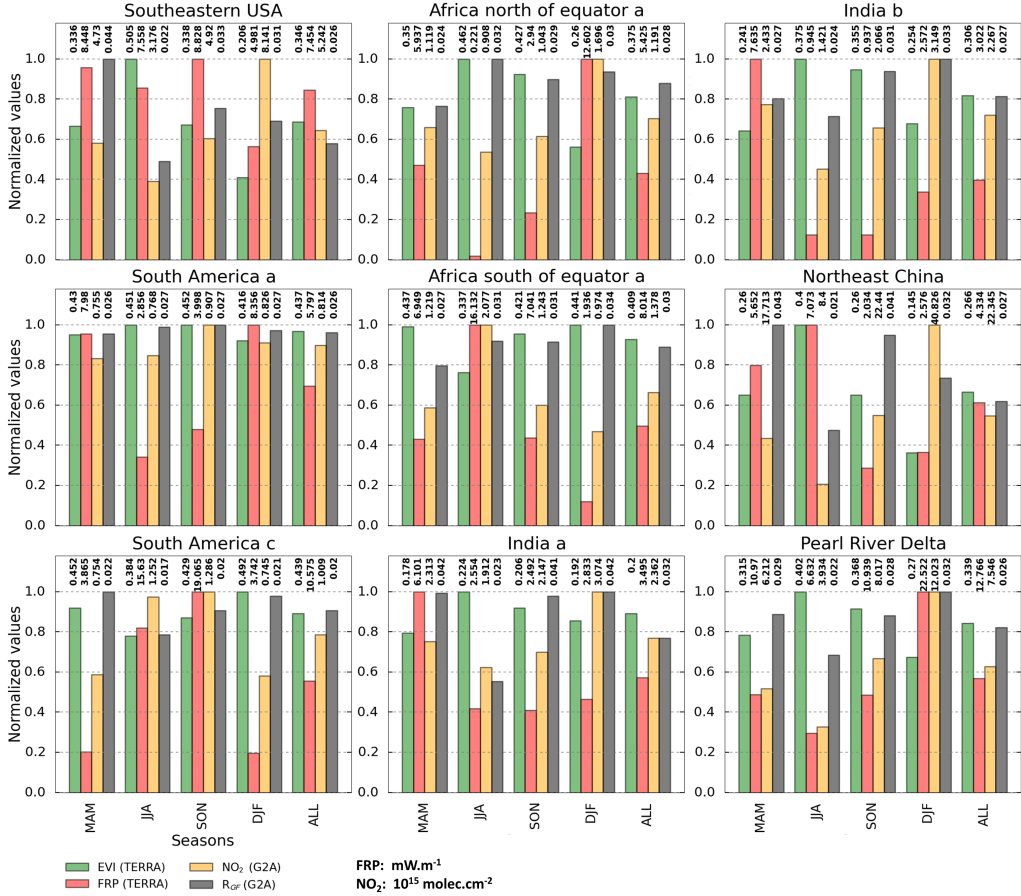


**Figure 5.3:** Temporal variation of GOME-2A  $R_{GF}$  for nine selected regions compared with indicators of biogenic, anthropogenic and pyrogenic emissions for 2007–2014.

during winter, the  $R_{GF}$  is in general smaller than 0.03 and for regions that are characterized by dense tropical vegetation, large ratios are found. The assessment performed here is in agreement with the results obtained by Kaiser et al. (2015). Thus, the assignment of  $R_{GF}$  to the different sources emissions of VOC needs to take into account all the factors that can affect these emissions such as vegetation type, temperature, humidity and population. Useful information for the identification of VOC sources can be obtained with this approach, but a more accurate process is needed in order to have a better identification of VOC sources and combination with model studies for the assessment of  $R_{GF}$  to the VOC sources.

## 5. IDENTIFICATION OF VOC SOURCES AND CASE STUDIES

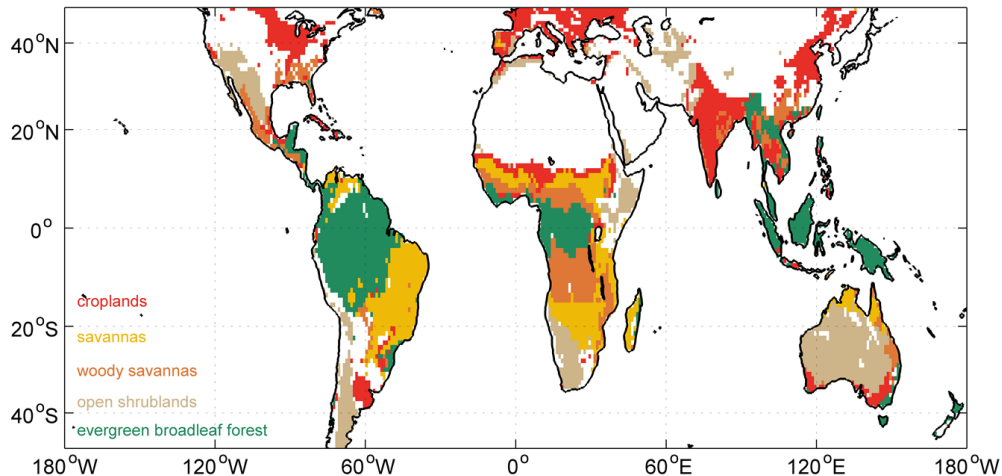


**Figure 5.4:** Global land cover map with different biomass types. The areas selected for the comparison between EVI, FRP and NO<sub>2</sub> are mainly cover by evergreen broadleaf forest (green), open shrublands (beige), woody savannas (orange), savannas (yellow), and croplands (red) (from Schreier et al. (2014)).

### 5.3 Case studies

#### 5.3.1 Glyoxal as an indicator of pyrogenic emissions: Russian fires in summer 2010\*

In this study, we have found connections between CHOCHO and fire radiative power for three regions as shown in Sect. 4.3.2. Although pyrogenic emissions contribute only about 18 % to the global budget of CHOCHO (Stavrakou et al., 2009a), there are some regions where fires are the dominant source of glyoxal and where good agreement in seasonal behaviour is found with FRP. Thus, in order to investigate the connection of glyoxal and pyrogenic emissions closer, a large fire event is studied here.

In summer 2010, unprecedented temperature anomalies causing severe drought in some areas of European Russia resulted in the outbreak of many wildfires (Shvidenko et al., 2011). Beginning in mid-July, the number of fires showed

\* This subsection has been previously published as part of Alvarado et al. (2014).

### 5.3 CASE STUDIES

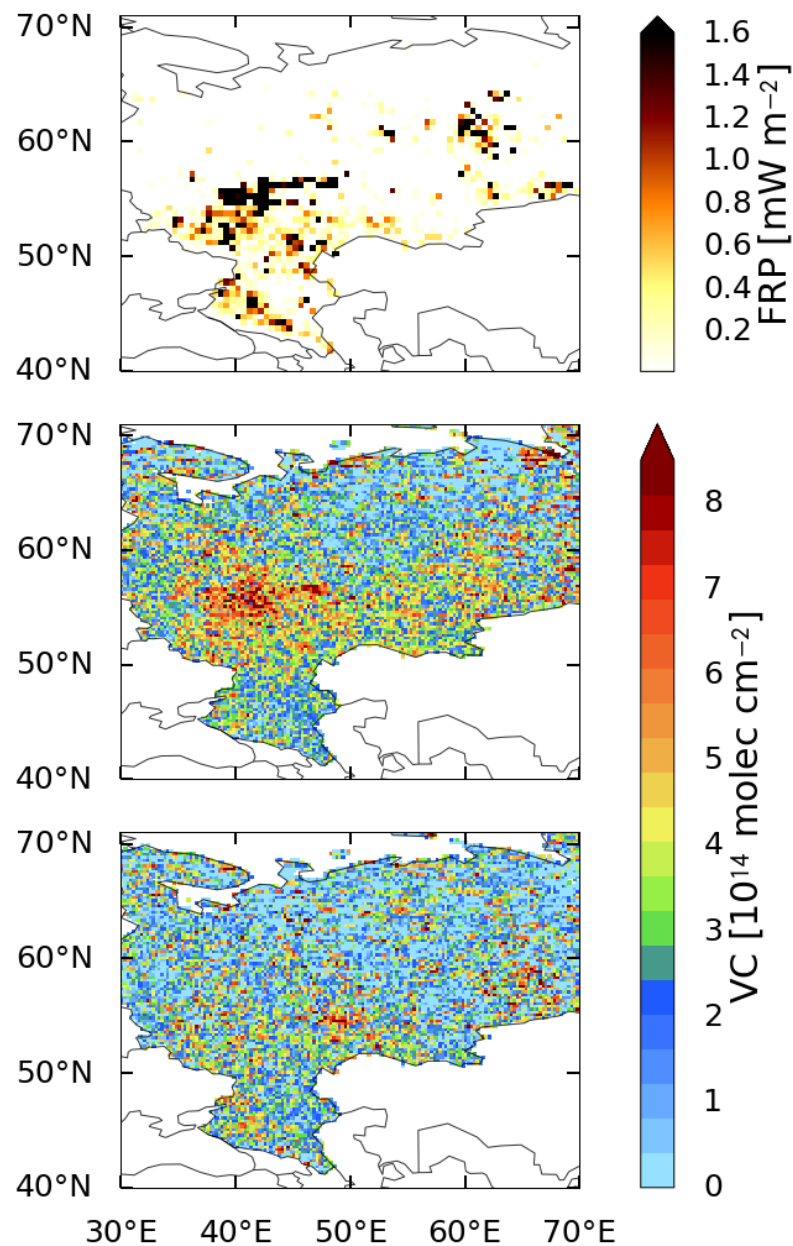


**Figure 5.5:** Maps of fire radiative power (top) and glyoxal VCs (middle) over Russia from 22 July to 18 August 2010, as well as glyoxal VCs for the same period in 2009 (bottom). Clearly an enhancement of glyoxal VCs is observed as consequence of emissions of VOC from the fire activity.

## 5. IDENTIFICATION OF VOC SOURCES AND CASE STUDIES

a steadily increase in occurrence until the end of July, followed by a decrease in August (Parshutkina et al., 2011).

The wildfires around Moscow created elevated atmospheric levels of carbon monoxide (CO),  $\text{NO}_x$ ,  $\text{O}_3$ , sulfur dioxide ( $\text{SO}_2$ ), methane ( $\text{CH}_4$ ), carbon dioxide ( $\text{CO}_2$ ), ammonia ( $\text{NH}_3$ ), formic acid ( $\text{HCOOH}$ ) and aerosol load, affecting air quality and human health (Yurganov et al., 2011; Elansky et al., 2011; Konovalov et al., 2011; van Donkelaar et al., 2011; R'Honi et al., 2013). Here, we show that high levels of glyoxal have also been produced from these wildfires.

For this case study, we use the 24 h assimilation data of FRP from the Global Fire Assimilation System (GFASv1.0) (Kaiser et al., 2012). Briefly, GFASv1.0 spatially aggregates all valid observations of fire and non-fire from the two MODIS instruments onto a horizontal resolution of  $0.5^\circ \times 0.5^\circ$  and calculates the total FRP sums for each grid cell. Further details about the daily 24 h assimilated GFASv1.0 FRP product, which we use for the following analysis of Russian wildfires can be found in Kaiser et al. (2012).

The geographical distributions of the 24 h assimilated FRP and the tropospheric vertical columns of CHOCHO are shown in Fig. 5.5 (top and middle) for the period 22 July to 18 August 2010, which represents the main part of the fire period. The largest fire activity is observed in the east of Moscow and this is also where the highest CHOCHO VCs are found, although it is a region with usually rather low glyoxal levels (see Fig. 5.5, bottom). This is a clear indication of glyoxal emissions from forest fires. Another hot-spot of fire activity during the selected time period is observed between  $60^\circ$  and  $65^\circ$  N and  $60^\circ$  and  $65^\circ$  E. However, these fires are much less intense and thus, the magnitude of the observed CHOCHO columns is lower.

### 5.3.2 Glyoxal transport event

Wittrock et al. (2006) and Vrekoussis et al. (2009) observed large amounts of glyoxal over ocean regions, where no sources of glyoxal are expected. Due to the short lifetime of glyoxal, the long-range transport of glyoxal is also very unlikely. However, in this study some possible transport of glyoxal produced from fire emissions has been identified. To illustrate the nature of CHOCHO transport events, one example is analysed and compared with model simulation trajectories.

### 5.3 CASE STUDIES

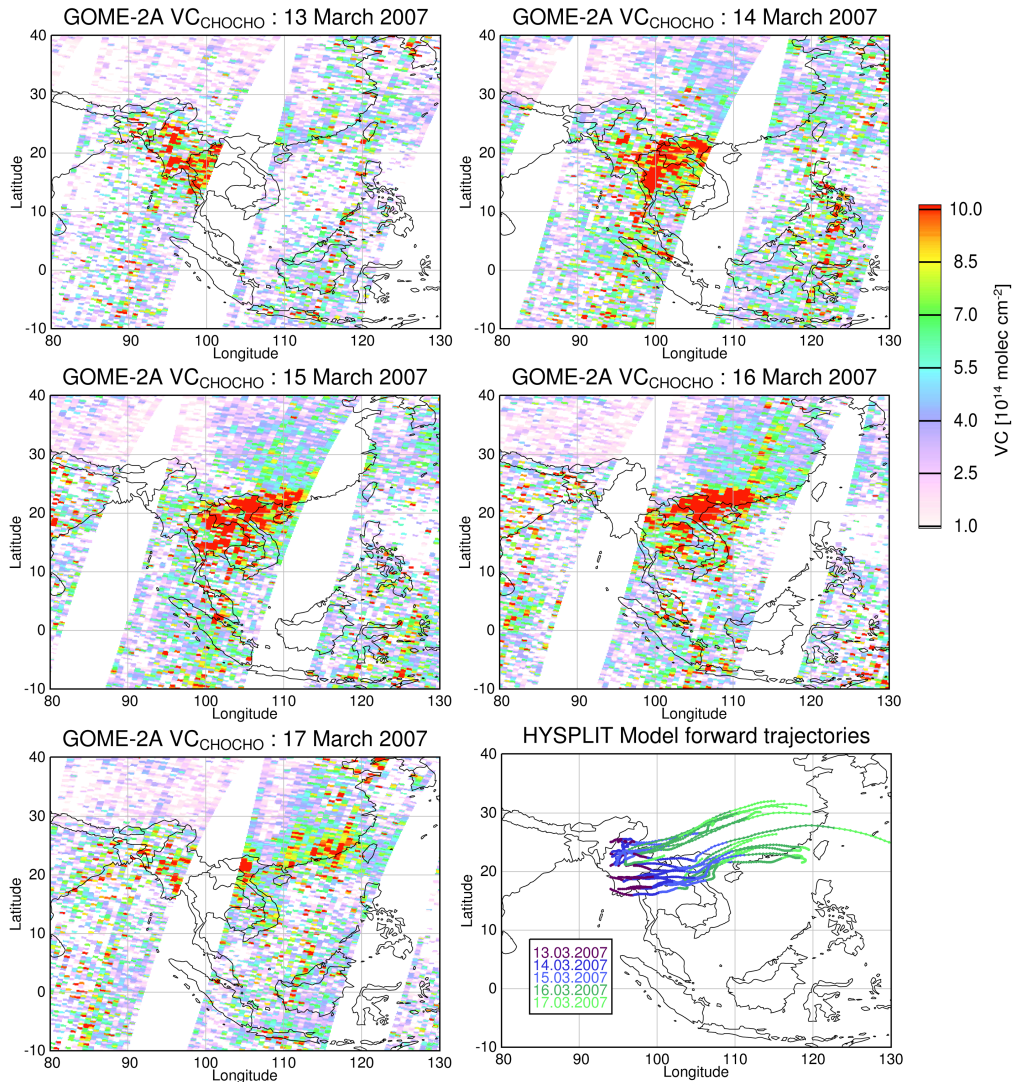


**Figure 5.6:** High CHOCHO levels detected over Myanmar-Thailand-Laos from 13 to 17 March of 2007. The glyoxal high levels partially follows forward trajectories of the air masses simulated with HYSPLIT (right).

#### Southeast Asia (Myanmar-Thailand-Laos)

The agricultural fire season (March-April) in Southeast Asia spreads smoke across a large portion of Myanmar, Thailand, and Laos. These fires create elevated atmospheric levels of many different gases in the atmosphere, e.g. CO, NO<sub>x</sub>, O<sub>3</sub>, SO<sub>2</sub>, CO<sub>2</sub>, HCHO, CHOCHO and aerosols affecting air quality. On

## 5. IDENTIFICATION OF VOC SOURCES AND CASE STUDIES

March 13, 2007, elevated levels of glyoxal are observed over Myanmar as a result of fire activities in the region. The elevated levels remain visible for some days and move through Thailand and Laos until they dispersed.

In order to investigate if the air mass follows the same trajectories as the plume of elevated glyoxal levels, the web-based version of the HYbrid Single-Particle Lagrangian Integrated Trajectory (HYSPLIT) model (Stein et al., 2015; Rolph) from the National Oceanic and Atmospheric Administration (NOAA) was used for the calculation of airmass forward trajectories. HYSPLIT is a system for the calculation of simple air parcel trajectories, based on the Global Data Assimilation System (GDAS) meteorological databases. In this study, forward trajectories at an altitude of 500 m above sea level are calculated for the selected region with high CHOCHO levels ( $VCs > 7.5 \times 10^{14} \text{ molec cm}^{-2}$ ). The ensemble tracks of air masses, starting 12 hours prior to the observations of high glyoxal amounts from 13 to 17 March 2007.

Figure 5.6 shows maps of glyoxal from 13 to 17 of March 2007, and the forward trajectories computed with HYSPLIT model. The glyoxal high levels partially follows forward trajectories of the air masses simulated with HYSPLIT. One explanation of longer life time of glyoxal emitted from fires is that glyoxal in the lower troposphere layer is mixed with aerosols, and its lifetime becomes longer due to recycling processes. This first time transport event observed for glyoxal could explain the reason of large amounts of glyoxal over oceanic areas, because over South America and Africa south of the equator, large fire events take place and similar recycling processes could lead to an enhanced lifetime of glyoxal. More investigation is needed in order to study all possible reasons of extended atmospheric lifetime of glyoxal under these conditions, but that is out of scope of this research.

### 5.4 Summary

The ratio of glyoxal to formaldehyde has been computed from GOME-2A measurements from 2007 to 2014. The  $R_{GF}$  show a clear seasonality similar to that of glyoxal. On closer inspection over nine selected regions, the variation  $R_{GF}$  depends on the vegetation type and temperature. The comparison of  $R_{GF}$  with indicators of biogenic (EVI), pyrogenic (FRP), and anthropogenic ( $\text{NO}_2$ ) emissions also vary, for most of the regions being low when large EVI was observed and large when high FRP and  $\text{NO}_2$  was found. These results are in agreement

## 5.4 SUMMARY

with the assessment performed by Kaiser et al. (2015) for the assignment of  $R_{GF}$  to the different source emissions of VOC. Many factors such as vegetation type, temperature, humidity, and population play an important role in the behaviour of  $R_{GF}$  for different regions. Thus, the ratios of glyoxal to formaldehyde can be used as a tool for the identification of VOC sources from satellite, however a more accurate process is needed in order to have a better identification of VOC sources.

The CHOCHO retrieval has been applied to study pyrogenic activities for the large Russian wildfire during August 2010. It was shown that the location and temporal pattern of the retrieved glyoxal columns is closely linked with the fire radiative power observations, indicating that in these areas, pyrogenic emissions dominate the glyoxal signal and thus glyoxal can also be used as an indicator of fires emissions.

For the first time, evidence for transport events of glyoxal have been found in the GOME–2A data. A case study over Southeast Asia has been investigated, where the elevated levels of glyoxal were found to follow the trajectories of air masses simulated with HYSPLIT. As glyoxal lifetime is short in the atmosphere, possible recycling processes in a mixing layer with aerosols could be the reason of the extended atmospheric lifetime of glyoxal in such plumes.

# 6

## Glyoxal, formaldehyde, and nitrogen dioxide retrievals from MAX-DOAS measurements

### 6.1 Introduction

From the ground both, direct-light DOAS and MAX-DOAS observations can be performed. They both utilise light from natural sources such as the sun or the moon. The use of other stars as light source has also been reported (Platt and Stutz, 2008). In the last decade, MAX-DOAS has been introduced and shown to be a powerful technique for the detection of tropospheric species, because their “off-axis” observational geometries (see Fig. 2.13 ) are mainly sensitive to measuring trace gases in the troposphere (Hönninger et al., 2004; Wittrock et al., 2004; Wagner et al., 2004; Heckel et al., 2005; Pinardi et al., 2012). This is because the incoming photons have a longer path through lower layers (small elevation angles) than photons at large elevation angles (see Fig. 2.13 ). As a consequence, these observations have an increased sensitivity to atmospheric absorbers close to the surface, such as HCHO and CHOCHO. The MAX-DOAS configuration has been applied for detection of NO<sub>2</sub>, HCHO, CHOCHO, SO<sub>2</sub>, and BrO (Bobrowski et al., 2003; Hönninger et al., 2004; Wittrock et al., 2004; Heckel et al., 2005; Sinreich et al., 2007; Pikelnaya et al., 2007; Vlemmix et al.,

## 6.1 INTRODUCTION

2010; Irie et al., 2011; Wagner et al., 2011; Pinardi et al., 2012; Peters et al., 2012; Li et al., 2013). Also, It has been used to retrieve information on the vertical distribution of both trace gases and aerosols (Wagner et al., 2004; Li et al., 2010). In addition, measurements with MAX-DOAS configuration can be used as a link for validation between satellite observation, and model calculation (Wittrock, 2006; Brinksma et al., 2008).

In 2002 and 2003, the first measurements of HCHO with MAX-DOAS were performed in the Po-Valley in Italy (Heckel et al., 2005; Wagner et al., 2011). The first study of CHOCHO with the MAX-DOAS technique was reported by Sinreich et al. (2007). These measurements were part of the ICARTT campaign in 2004, and reported mixing ratios between 40 ppt and 140 ppt with a maximum at noon for Cambridge, USA during summer 2004. Later, Hak et al. (2005) reported on an intercomparison of HCHO results among MAX-DOAS, long-path (LP) DOAS (active DOAS), the chromatographic technique, Fourier Transform Infrared (FTIR), and Hantzsch-type *in-situ* instruments. These results showed a good agreement among all instruments with the exception of one Hantzsch instrument. Wittrock (2006) presented results of MAX-DOAS measurements from the Cabauw campaign in summer 2005 and satellite observations, finding a good agreement between the tropospheric columns of HCHO and CHOCHO with satellite observations, and demonstrated that MAX-DOAS is a powerful tool for long-term observation of tropospheric species. A study performed by MacDonald et al. (2012) for the rainforest canopy in Borneo with MAX-DOAS and LP-DOAS in spring and summer 2008 observed a maximum of HCHO and CHOCHO at 4.5 ppt and 1.6 ppt respectively, with consistent agreement between MAX-DOAS and LP-DOAS columns. Vigouroux et al. (2009) compared SCIAMACHY, MAX-DOAS and FTIR HCHO total columns over a tropical region, finding good agreement between daily mean total columns of HCHO from MAX-DOAS and FTIR, and also a very good agreement with SCIAMACHY observations during the same period. Later, Fried et al. (2011) compared aircraft and ground-based measurement of HCHO during the INTEX-B campaign, finding a good agreement between both configurations. More recently, a study by Pinardi et al. (2012) presents an intercomparison exercise of HCHO columns retrieved from different instruments that participated in the CINDI campaign during summer 2009. The mean differences found are no larger than 15% on slant columns. Thus, MAX-DOAS instruments have demonstrated the capabilities for detection of HCHO and CHOCHO in long-term observations and the link with satellite observations and model calculations.

## 6. GLYOXAL, FORMALDEHYDE, AND NITROGEN DIOXIDE RETRIEVALS FROM MAX-DOAS MEASUREMENTS

In this chapter, results of HCHO, CHOCHO, and NO<sub>2</sub> retrieved from MAX-DOAS measurement over two different locations (Athens and Nairobi) are presented. Sensitivity studies have been performed in order to optimize the retrieval parameters of HCHO, CHOCHO, and NO<sub>2</sub>. In addition, an analysis of the temporal evolution of the three gases has been performed for the two locations, which are part of the Bremian DOAS Network for Atmospheric Measurements (BREDOM). Also, the ratio of glyoxal to formaldehyde ( $R_{GF}$ ) was evaluated in order to constrain VOC emission types (Vrekoussis et al., 2010; DiGangi et al., 2012; Li et al., 2013) and the formaldehyde to dioxide nitrogen ratio ( $R_{FN}$ ) for the study of O<sub>3</sub> production rates (Duncan et al., 2010; Ortega et al., 2015).

### 6.2 Measurement sites

The geographic location of the measurement sites can be seen in the map in Fig. 6.1. The red stars represent stations that are part of the BREDOM network, one is located in Athens, Greece and the other in Nairobi, Kenia. The purple star represents the location where the Multi-Axis DOAS-Comparison campaign for Aerosols and Trace gases (MAD-CAT) in Mainz, Germany took place. However, results from the campaign are not shown here.

#### 6.2.1 Athens

Athens is the capital and largest city of Greece. It is located in the Southeast of Europe, having a population of 3.1 millions inhabitants over an area of 38.9 km<sup>2</sup>. Athens is characterized by a typical Mediterranean climate, with hot summers and mild winters. The summer corresponds to the months June to August, which are usually dry and hot with temperatures between 19 °C and 28 °C (see Fig. 6.2). During summer, the city is also prone to smog formation most likely due to the increase of temperature and the photochemistry. Spring and autumn are from March to May and from September to November, respectively. Rainfall is sparse from mid October to mid April, and sometimes showers fall during summer (see Fig. 6.3).

The BREDOM MAX-DOAS instrument is installed in Penteli (30° N, 23° E) at an altitude of 500 meters above sea level in the building of the National Observatory of Athens (more details about the instrument can be found in Sect. 2.5.1). Figure 6.4 shows the eight different azimuth viewing direction of the MAX-DOAS

## 6.2 MEASUREMENT SITES

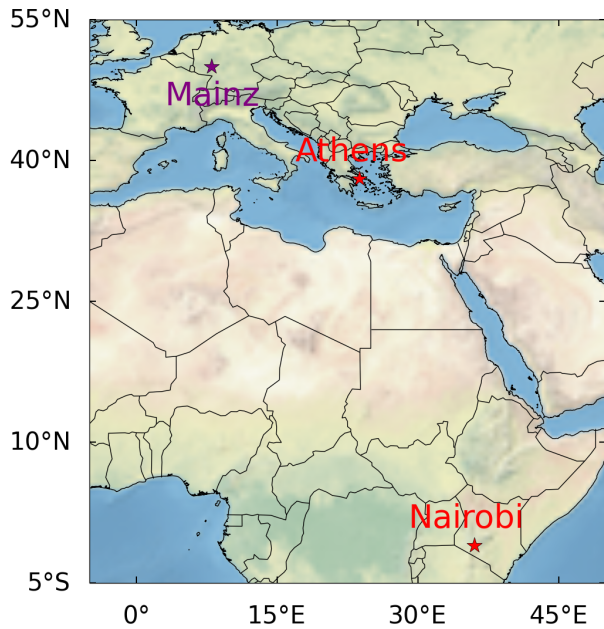


**Figure 6.1:** Overview map of locations where MAX-DOAS instruments are measuring. In red are the measurement sites that are part of the BREDOM network and in purple the location where MAD-CAT campaign took place.

instrument over Athens. These directions are looking over open ocean (W), airport (A), southern part of the city (R), old centre (S), Piraeus harbour (T), Olympic stadium (U), northern suburbs of the city (V), and a region with biogenic background (B). The MAX-DOAS instrument is measuring at elevations angles of  $0^\circ$ ,  $1^\circ$ ,  $2^\circ$ ,  $3^\circ$ ,  $4^\circ$ ,  $6^\circ$ ,  $8^\circ$ ,  $15^\circ$ , and  $30^\circ$  in fact, there are additional elevations in some directions. The reference spectrum is measured at the zenith ( $90^\circ$ ). Here, measurements from January 2013 to December 2014 are analysed.

### 6.2.2 Nairobi

Nairobi is the capital and largest city of Kenya. It is located in the central east of Africa, having a population of 3.2 millions inhabitants over an area of  $696 \text{ km}^2$ . Nairobi has a tropical climate, with temperatures between  $12^\circ\text{C}$  and  $27^\circ\text{C}$  (see Fig. 6.5). The winter corresponds to months between July and September, which are usually dry and mid-cold. The summer months are from December to March

## 6. GLYOXAL, FORMALDEHYDE, AND NITROGEN DIOXIDE RETRIEVALS FROM MAX-DOAS MEASUREMENTS

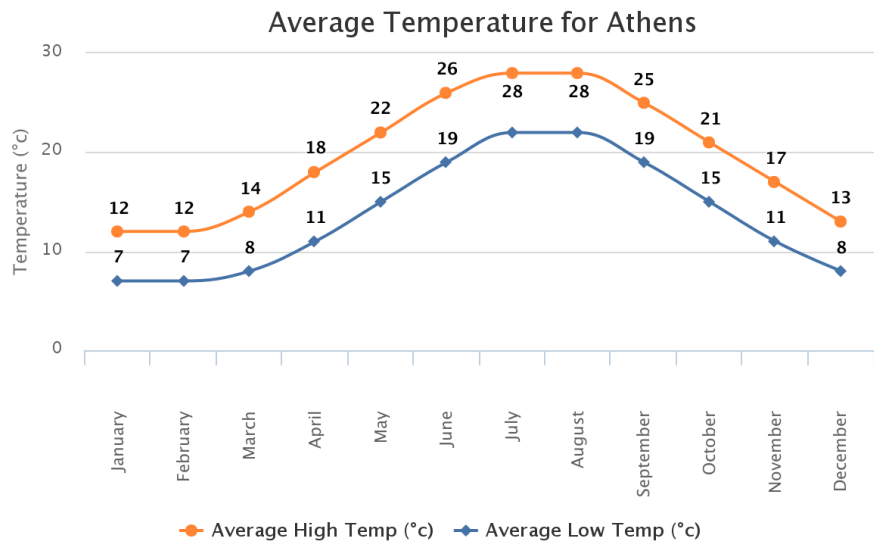


**Figure 6.2:** Maxima and minima of average temperature for Athens (from <http://www.worldweatheronline.com>).

with temperatures between 13 °C and 28 °C (see Fig. 6.5). The rest of the months are characterized by rainfall and wet conditions (see Fig. 6.6).

The BREDOM MAX-DOAS instrument is installed in the building of the United Nations Environment Programme of Kenya (1°S, 36°E) at an altitude of 1600 meters above sea level. Figure 6.7 shows the azimuth viewing direction of the MAX-DOAS instrument over Nairobi. This direction is looking over the city and a national park. The MAX-DOAS instrument is measuring at elevations angles between 0° and 30°. The reference spectrum is measured at the zenith (90°). Here, measurements from January 2011 to December 2014 are analysed.

Despite its large population, Nairobi also has a large extension of vegetation. Thus, it is interesting to compare the results from Athens and Nairobi in order to obtain a better understanding of sources for production of VOC and NO<sub>x</sub>.

## 6.2 MEASUREMENT SITES

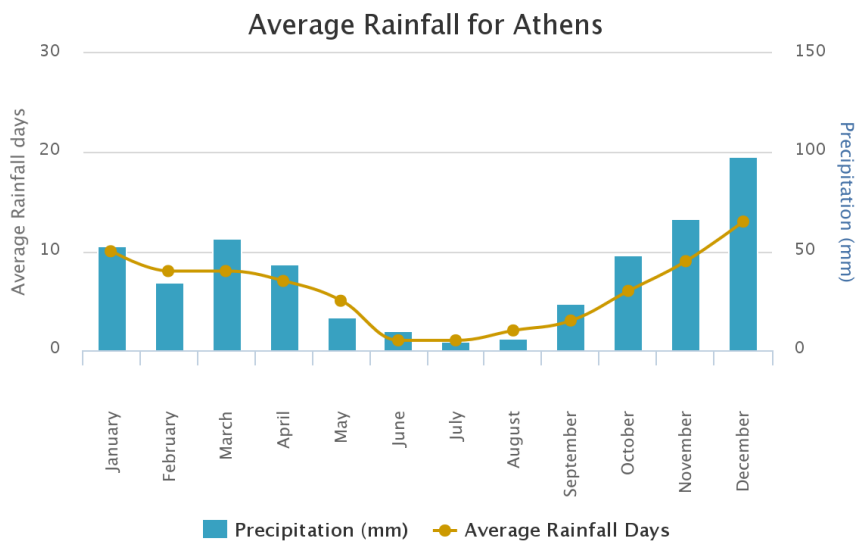


**Figure 6.3:** Maxima and minima of average rainfall for Athens (from <http://www.worldweatheronline.com>).

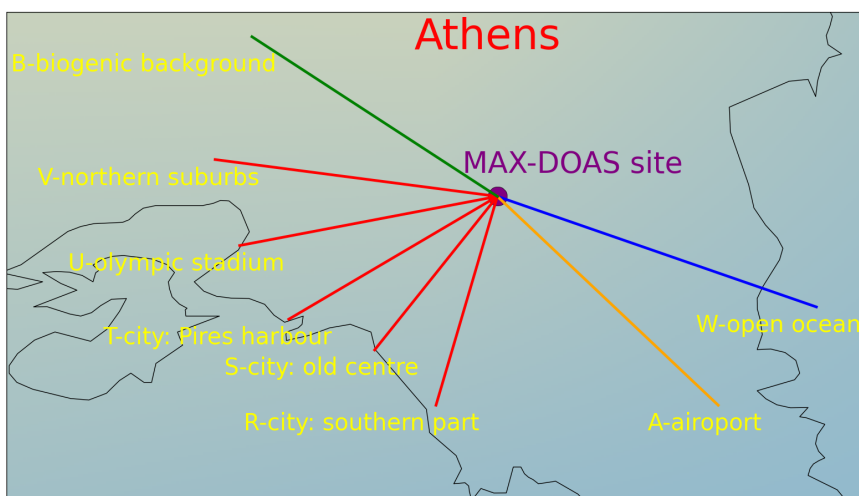


**Figure 6.4:** Location and azimuth viewing direction of the MAX-DOAS instrument in Athens. The lines represent the different azimuth viewing directions to which the instrument is looking.

## 6. GLYOXAL, FORMALDEHYDE, AND NITROGEN DIOXIDE RETRIEVALS FROM MAX-DOAS MEASUREMENTS

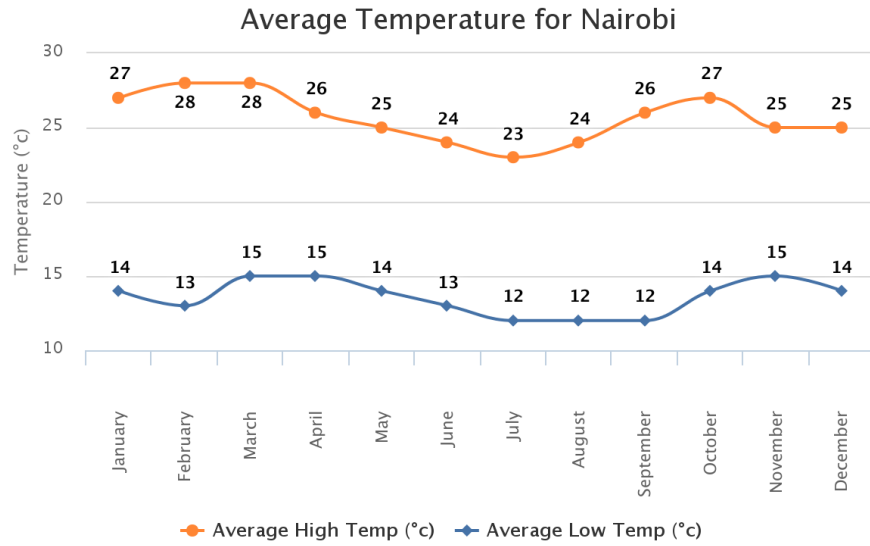


**Figure 6.5:** Maxima and minima of average temperature for Nairobi, Kenya (from <http://www.worldweatheronline.com>).

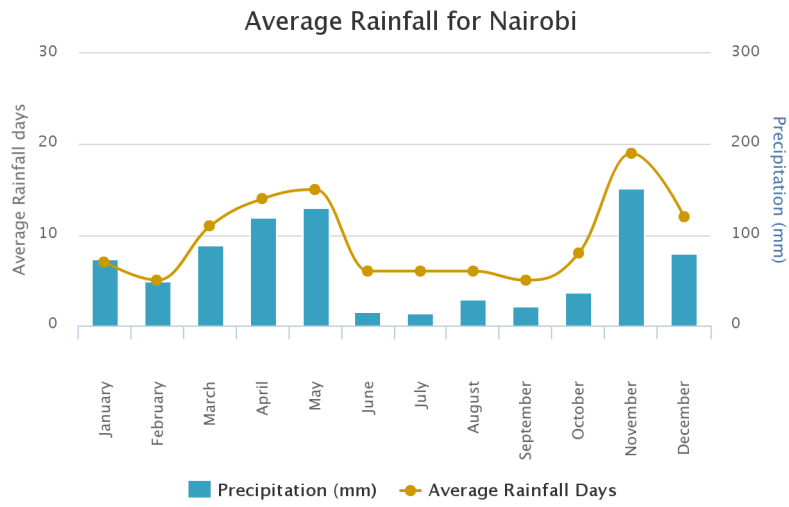


**Figure 6.6:** Maxima and minima of average rainfall for Nairobi, Kenya (from <http://www.worldweatheronline.com>).

## 6.3 SENSITIVITY STUDY ON THE RETRIEVALS OF CHOCHO, HCHO AND NO<sub>2</sub>

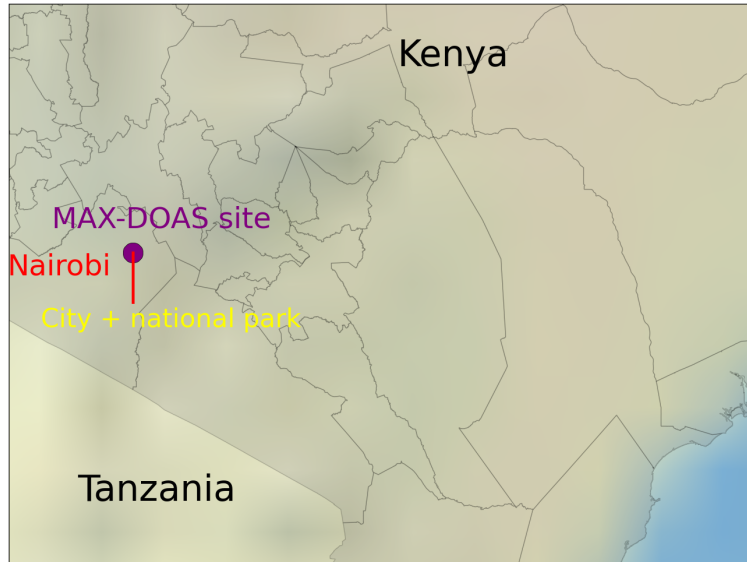


**Figure 6.7:** Location and azimuth viewing direction of the MAX-DOAS instrument in Nairobi. The red line represents the azimuth viewing direction to which the instrument is looking and a distance of 20 km.

## 6.3 Sensitivity study on the retrievals of CHOCHO, HCHO and NO<sub>2</sub>

During the last two decades, many efforts have been taken in order to improve the retrieval of smaller absorbers such as HCHO and CHOCHO. However, the uncertainties are still large in comparison to strong absorbers such as NO<sub>2</sub>. Nevertheless, the number of algorithms and definition of parameters used in the NO<sub>2</sub> retrievals are still broad, which sometimes show consistent results but also large differences, depending on the wavelength window, polynomial and cross-sections included of interfering species in the retrieval. Therefore, the focus of this section is to find the optimal retrieval parameters for HCHO, CHOCHO and NO<sub>2</sub>, based on sensitivity studies as is described below.

For the formaldehyde, glyoxal and nitrogen dioxide sensitivity studies, measurements performed in Athens have been used. A systematic variation of parameters has been performed to find the optimal parameter set for each specie. The parameters evaluated were the cross-sections included in the retrieval, the fitting window, and the polynomial degree. First, a day with good weather (specially

## 6. GLYOXAL, FORMALDEHYDE, AND NITROGEN DIOXIDE RETRIEVALS FROM MAX-DOAS MEASUREMENTS

with good visibility) was selected. In order to chose a day where the amounts of HCHO, CHOCHO, and NO<sub>2</sub> are high, preliminary retrievals were performed using parameter sets that have been used in other studies. During the measurement period, many days with large amounts of HCHO, CHOCHO, and NO<sub>2</sub> slant columns have been found. From this priori evaluation, measurements from 25.06.2013 have been identified as a good test day. After this initial phase, the systematic analysis of the measurements was performed, varying the start and end wavelength limits in the intervals used in the DOAS fit, the cross-sections included, and the polynomial degree in the fit.

- **start wavelength:** intervals between 335 nm and 340 nm, 420 nm and 437 nm, 405 nm and 435 nm for HCHO, CHOCHO, and NO<sub>2</sub> respectively.
- **end wavelength:** intervals between 343 nm and 364 nm, 442 nm and 460 nm, 440 nm and 500 nm for HCHO, CHOCHO, and NO<sub>2</sub> respectively.
- **cross-sections:** HCHO at 297 K (Meller and Moortgat, 2000), O<sub>3</sub> for temperatures of 223 K, 243 K, 273 K, and 293 K (Bogumil et al., 2003), NO<sub>2</sub> at 220 K and 294 K (Vandaele et al., 1998), CHOCHO at 298 K (Volkamer et al., 2005b), BrO (Fleischmann et al., 2004), O<sub>4</sub> at 293 K (Thalman and Volkamer, 2013), H<sub>2</sub>O vapour at 296 K (Rothman et al., 2010), and Ring (Vountas et al., 1998). The temperature dependence on O<sub>3</sub> and BrO absorption are evaluated for the formaldehyde retrieval, while NO<sub>2</sub> temperature dependence is tested in the glyoxal and nitrogen dioxide retrievals.
- **polynomial order:** 2 to 5

Every combination of parameters was applied to the 36 measurements of the day at an elevation angle of 2° and using as reference spectrum the zenith measurement closest in time. The combination of these parameters gives more than  $2.0 \times 10^5$  fits for each measurement. In order to compensate the stray-light effect, a constant intensity offset was applied.

Figures 6.8, 6.9, and 6.10 show the mean RMS obtained from the retrievals of HCHO, CHOCHO, and NO<sub>2</sub> computed for all possible combinations of start and end wavelengths for each combination of cross-sections, and different polynomial orders. Clearly, when the number of cross-sections used in the retrieval increase, the mean RMS decreases, the reduction in mean RMS being more significant when the stronger absorbers in the wavelength range of interest are included. For

### 6.3 SENSITIVITY STUDY ON THE RETRIEVALS OF CHOCHO, HCHO AND NO<sub>2</sub>

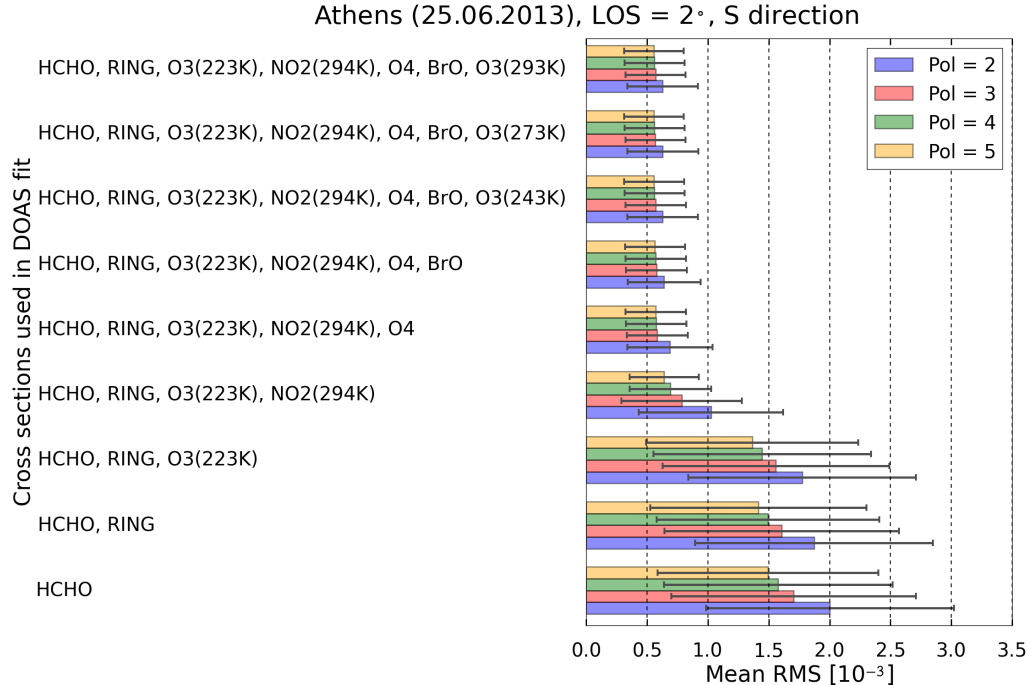


**Figure 6.8:** The mean RMS for formaldehyde retrievals with their respective standard deviation as error bar computed over all possible fitting windows for each combination of cross-sections and different polynomials (colour bars) for measurements performed in Athens during 25 June 2013, elevation angle of 2° and azimuth direction of 52.5° (S direction, see Fig. 6.4).

HCHO, the most pronounced reduction of the mean RMS is achieved by adding the Ring, stratospheric O<sub>3</sub>, tropospheric NO<sub>2</sub>, and O<sub>4</sub> cross-sections. Adding BrO and a higher temperatures O<sub>3</sub> (accounting for tropospheric contribution) cross-sections gives a small improvement in the mean RMS as well. For the ozone high temperature cross-sections, this improvement is nearly independent on which one is used, however the 293 K cross-section led to the most noticeable improvement and is the one used in our HCHO retrieval. Additionally, the order of polynomial that gives the smallest mean RMS corresponds to 5 (see Fig. 6.8).

For CHOCHO, the most significant reduction in the mean RMS is achieved by adding Ring, stratospheric O<sub>3</sub> and NO<sub>2</sub>, O<sub>4</sub>, water vapour and high temperature NO<sub>2</sub> (294 K) cross-sections, this last accounting for the tropospheric contribution over regions with large anthropogenic emissions as suggested in (Alvarado et al.,

## 6. GLYOXAL, FORMALDEHYDE, AND NITROGEN DIOXIDE RETRIEVALS FROM MAX-DOAS MEASUREMENTS

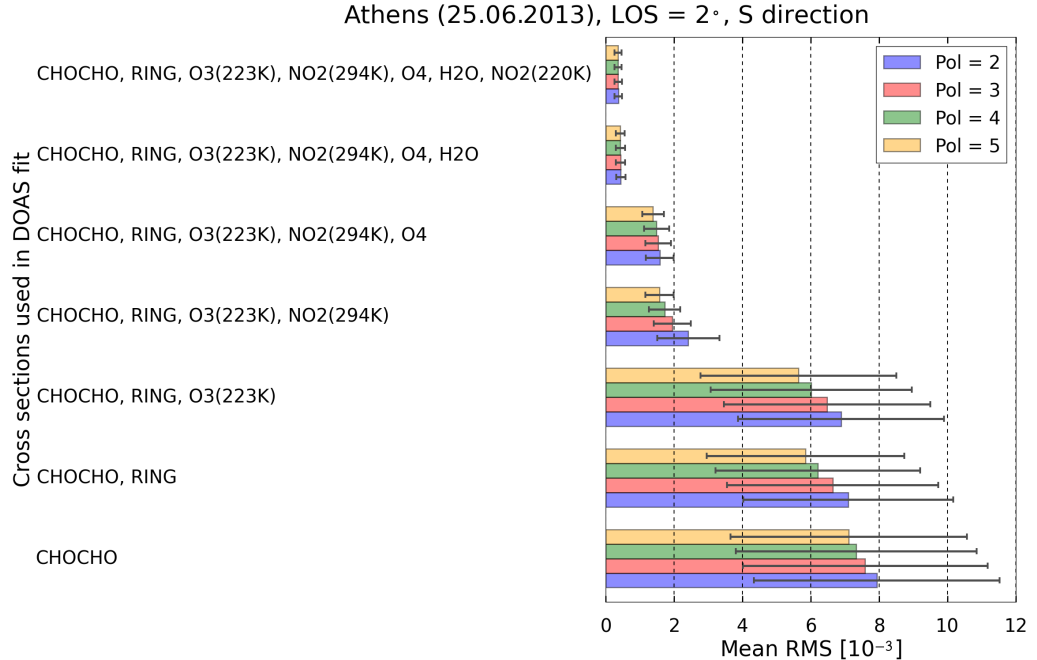


**Figure 6.9:** The mean RMS for glyoxal retrievals with their respective standard deviation as error bar computed over all possible fitting windows for each combination of cross-sections and different polynomials (colour bars) for measurements performed in Athens during 25 June 2013, elevation angle of 2° and azimuth direction of 52.5° (S direction, see Fig. 6.4).

2014). A polynomial of order 4 is used although polynomial degrees of 3 and 5 give similar mean residuals.

For NO<sub>2</sub>, the introduction of O<sub>4</sub> and H<sub>2</sub>O cross-sections in the retrieval led to the most significant reduction in the mean RMS (see Fig. 6.10), because strong absorption bands of O<sub>4</sub> and H<sub>2</sub>O are found in the visible wavelength range. Also, a slight improvement is observed with the introduction of Ring, stratospheric O<sub>3</sub> and NO<sub>2</sub> (220 K) in the retrieval. A polynomial of order 5 gives the smallest mean residual.

After choosing the polynomial and cross-sections that are used in the retrievals of HCHO, CHOCHO, and NO<sub>2</sub>, the selection of the most appropriate fitting window has been done based on root mean square and fitting error for each retrieval. The RMS and fit error as function of start and end limits of

### 6.3 SENSITIVITY STUDY ON THE RETRIEVALS OF CHOCHO, HCHO AND NO<sub>2</sub>

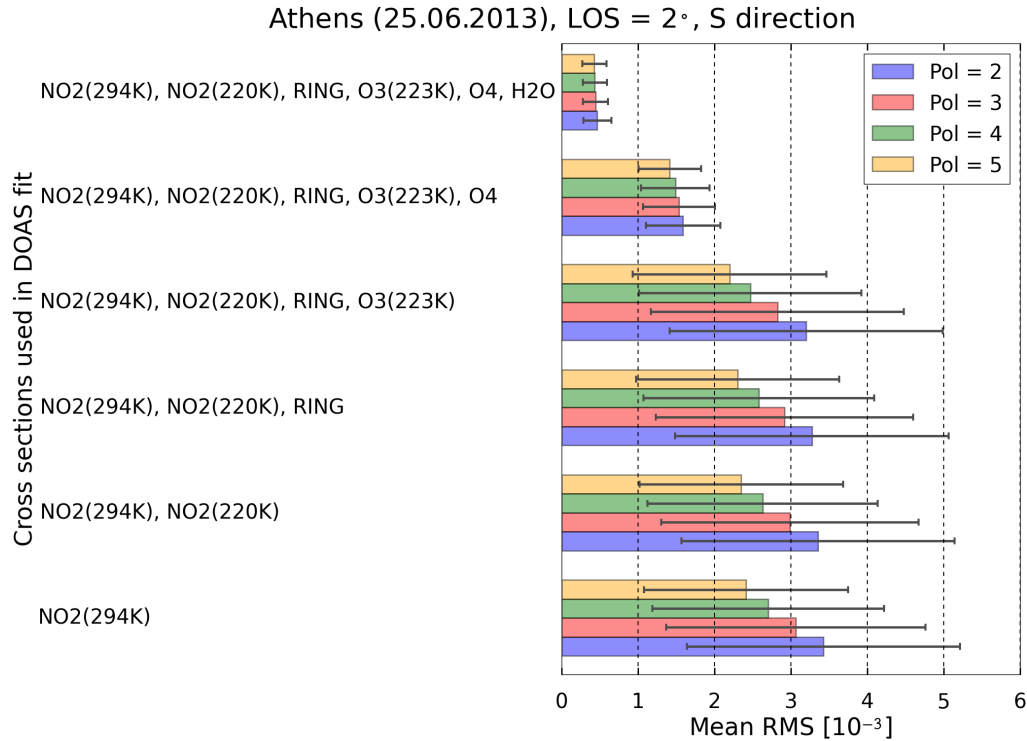


**Figure 6.10:** The mean RMS for nitrogen dioxide retrievals with their respective standard deviation as error bar computed over all possible fitting windows for each combination of cross-sections and different polynomials (colour bars) for measurements performed in Athens during 25 June 2013, elevation angle of 2° and azimuth direction of 52.5° (S direction, see Fig. 6.4).

fitting intervals at steps of 0.5 nm are shown in Fig. 6.11. The wavelength limits chosen for each gas take into account the most representative absorption bands. Every point in the plot represents the average RMS and fitting error over 36 spectra in order to limit the effect of measurement noise. For HCHO, the start wavelengths have been limited to 335 nm due to instrumental limitations. Fitting windows between 335 nm and 360 nm have been used in previous studies for retrieving formaldehyde from MAX-DOAS measurements (Peters et al., 2012; Pinardi et al., 2013). The minimum fitting error for each retrieval combined with the smallest RMS is highlighted by a dark-red box in Fig. 6.11. The variability of RMS with the fitting windows is low in comparison with the fit error variability. For HCHO and CHOCHO only wavelength ranges for which the fit-

## 6. GLYOXAL, FORMALDEHYDE, AND NITROGEN DIOXIDE RETRIEVALS FROM MAX-DOAS MEASUREMENTS

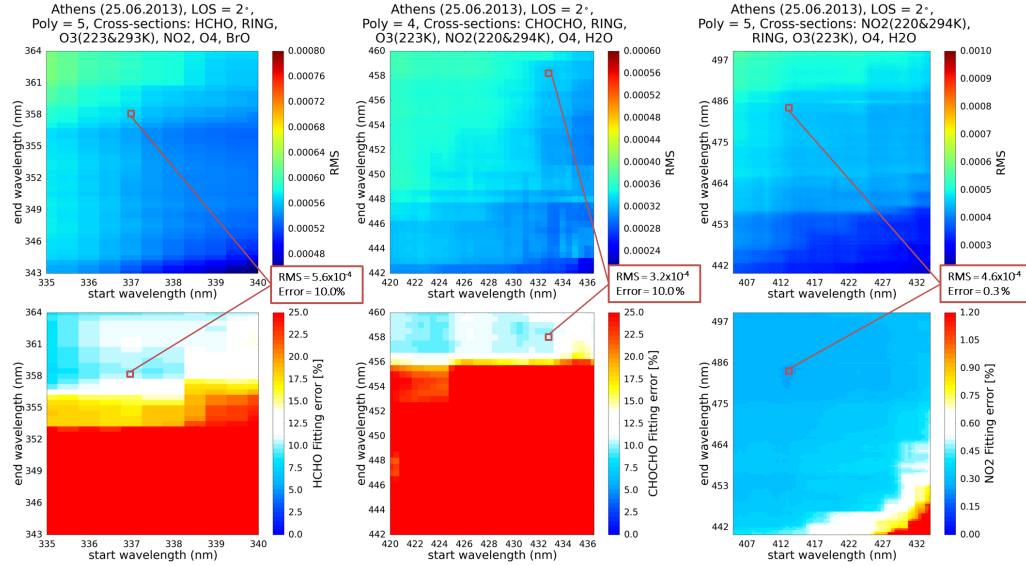


**Figure 6.11:** Colour mapping of fit errors and RMS of HCHO, CHOCHO, and NO<sub>2</sub> for different wavelength with start limits of 335–340 nm, 420–437 nm, 405–435 nm and end limits of 343–364 nm, 442–460 nm, 440–500 nm respectively from measurements performed at 2° elevation angle over Athens on Tuesday, 25 June 2013.

ting error is below 12% are considered. In the case of CHOCHO, this result is in agreement with the one obtained for satellite measurements, being below 12% for wavelength ranges that include the strong absorption band of glyoxal (larger than 456 nm) and this limits the end wavelength to the range between 456 and 460 nm. Only start wavelengths in the range of 432–436 nm are considered, because the RMS increases for wavelengths below 432 nm, and also the CHOCHO differential slant columns (DSC) pattern is largely variable for these wavelengths (see Appendix). Finally, the combined lowest fit error with the low RMS in these wavelength ranges led to the fitting window between 433 nm and 458 nm. Similar fitting windows have already been used for retrieving glyoxal from ground and satellite measurements (Sinreich et al., 2010; Alvarado et al., 2014).

The lowest fit error in HCHO retrievals corresponds to ranges with start wavelengths of 335–338.5 nm and end wavelengths of 357–364 nm, lowest error being found for the fitting window between 335 nm and 358.5 nm. However, the RMS is high for this wavelength range and thus the selected fitting window corresponds to wavelengths between 337 nm and 358 nm, which led to a lower RMS and simi-

## 6.3 SENSITIVITY STUDY ON THE RETRIEVALS OF CHOCHO, HCHO AND NO<sub>2</sub>

**Table 6.1:** Parameters used for retrieve HCHO, CHOCHO, and NO<sub>2</sub> from MAX-DOAS measurements

<b>Parameters</b>	<b>Gas to retrieve</b>		
	<i>Formaldehyde</i>	<i>Glyoxal</i>	<i>Nitrogen dioxide</i>
<b>Cross sections</b>			
HCHO (297 K)	+	-	-
CHOCHO (298 K)	-	+	-
NO <sub>2</sub> (220 K)	-	+	+
NO <sub>2</sub> (294 K)	+	+	+
O <sub>3</sub> (223 K)	+	+	+
O <sub>3</sub> (293 K)	+	-	-
O <sub>4</sub> (293 K)	+	+	+
H <sub>2</sub> O <sub>vap</sub> (296 K)	-	+	+
BrO	+	-	-
Ring	+	+	+
<b>Fitting window</b>	337–358 nm	433–458 nm	413–485 nm
<b>Polynomial</b>	5	4	5

lar fit error as the wavelength interval between 335 nm and 358.5 nm. Moreover, the HCHO DSCs for these wavelength ranges are similar and no large variability is observed as was the case in CHOCHO DSCs. For the NO<sub>2</sub> retrieval, the variation in fit error and RMS is lower than for HCHO and CHOCHO, because the absorption of NO<sub>2</sub> is stronger than those of HCHO and CHOCHO. Thus, most of all possible combinations of start and end wavelengths give fit errors below 1.2%, however for the selection of NO<sub>2</sub> fitting window, only wavelengths with start limits of 400–425 nm and end limits of 450–500 nm are considered. The lowest fit errors are found for start wavelengths of 412–414 nm and end wavelengths of 482–486 nm (see Fig. 6.11, bottom-right), which correspond to fit errors below 0.25%. For these wavelength intervals, the lowest RMS is obtained for the wavelength range extended from 413 nm to 485 nm. The final settings for retrieving each gas are summarized in the Table 6.1.

## 6. GLYOXAL, FORMALDEHYDE, AND NITROGEN DIOXIDE RETRIEVALS FROM MAX-DOAS MEASUREMENTS

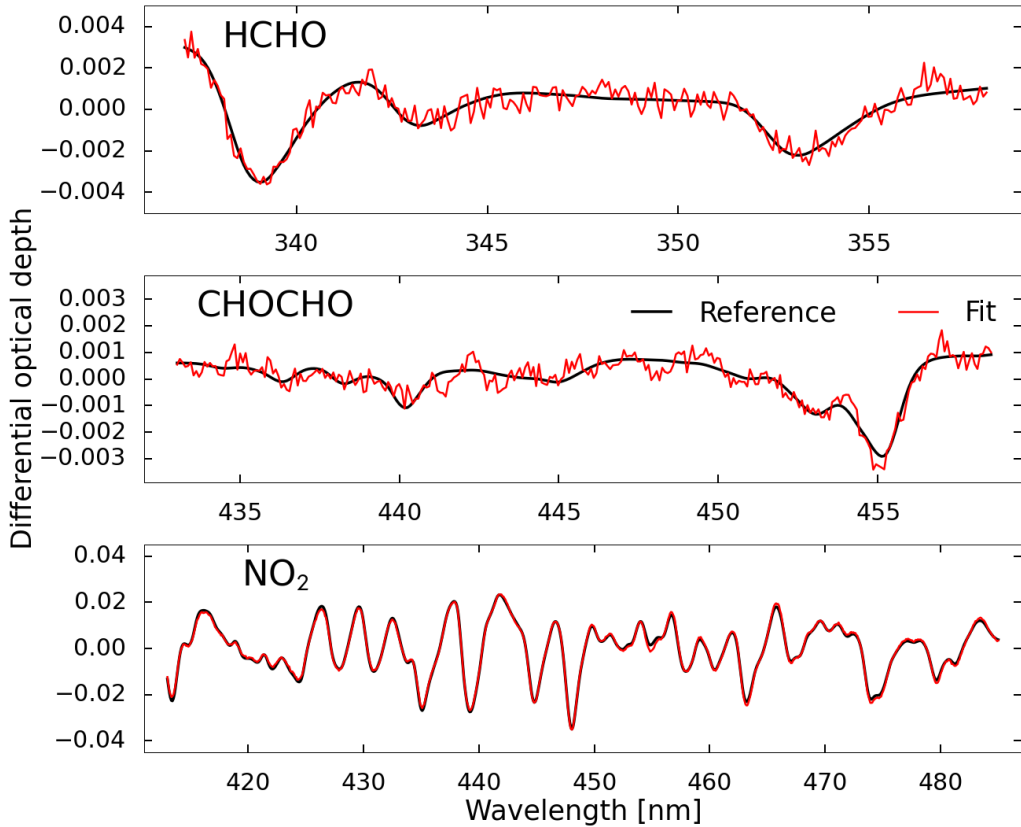


**Figure 6.12:** Example fits for HCHO, CHOCHO, and NO<sub>2</sub> from a measurement performed at 2° elevation over Athens on the morning of 25 June 2013 (9:53:08, local time). The black lines show the reference cross-section and the red lines the fit for each gas.

Typical fit examples for HCHO, CHOCHO, and NO<sub>2</sub> retrieved from a measurement performed at 2° elevation angle over Athens on Tuesday, 25 June 2013 in the morning are shown in Fig. 6.12. The agreement between reference cross-sections for HCHO, CHOCHO, and NO<sub>2</sub> (black line) and the respective fits (red line) is very good, specially for wavelengths where the main absorption bands are found, leading to a fit error for each gas about of 5.27%, 4.15%, and 0.24% respectively.

## 6.4 RESULTS AND DISCUSSION

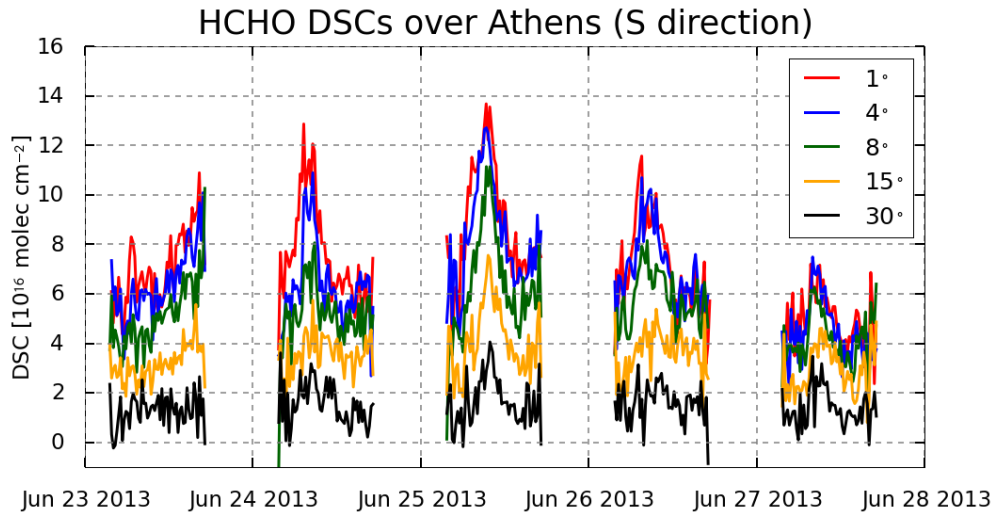


**Figure 6.13:** Time series of HCHO DSCs retrieved from the MAX-DOAS measurements over Athens at elevation angles of  $1^\circ$ ,  $4^\circ$ ,  $8^\circ$ ,  $15^\circ$  and  $30^\circ$  in the S direction for the period between 23 (Sunday) and 27 (Thursday) June 2013.

## 6.4 Results and Discussion

In this section, the main results obtained from the retrievals of HCHO, CHOCHO, and NO<sub>2</sub> from the MAX-DOAS measurements over Athens and Nairobi are presented.

### 6.4.1 Athens

Figures 6.13, 6.14, and 6.15 show time series from Sunday (23 June 2013) to Thursday (27 June 2013) of HCHO, CHOCHO, and NO<sub>2</sub> DSCs retrieved from the MAX-DOAS measurements over Athens at an azimuth angle of  $52.5^\circ$  (S direction, see Fig. 6.4) and elevation angles of  $1^\circ$ ,  $4^\circ$ ,  $8^\circ$ ,  $15^\circ$ , and  $30^\circ$ . These days are mostly cloud free with the exception of 26 June 2013 in the afternoon.

The separation between elevation angles is clear for all days due to the good visibility. The HCHO, CHOCHO, and NO<sub>2</sub> DSCs have a very pronounced diurnal variation with a maximum around noon for most of the days. However, on Sunday (23 June 2013) no diurnal variation is observed, which could be related

## 6. GLYOXAL, FORMALDEHYDE, AND NITROGEN DIOXIDE RETRIEVALS FROM MAX-DOAS MEASUREMENTS

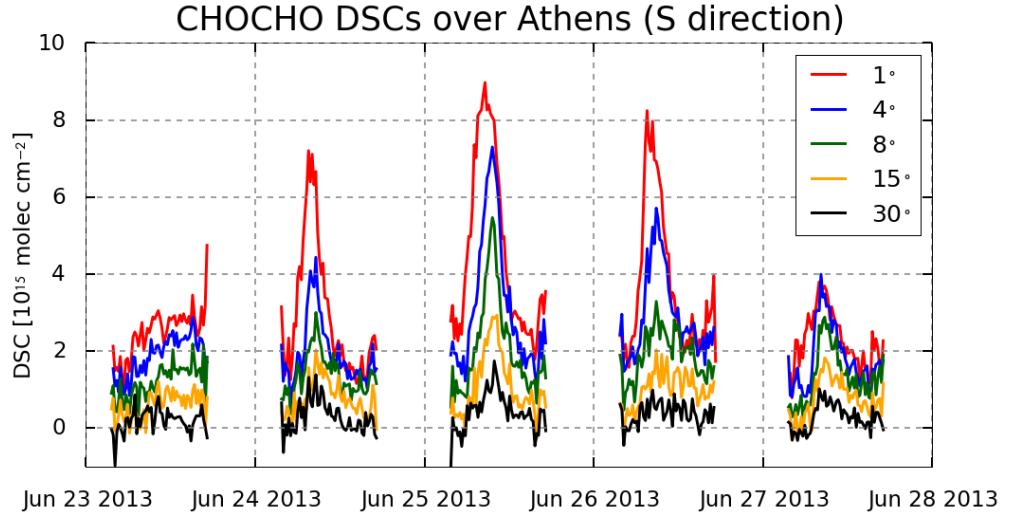


**Figure 6.14:** Time series of CHOCHO DSCs retrieved from the MAX-DOAS measurements over Athens at elevation angles of 1°, 4°, 8°, 15° and 30° in the S direction for the period between 23 (Sunday) and 27 (Thursday) June 2013.

to the lower amount of emissions from vehicles, as well as from industry. The lowest DSCs for the three gases are found on Sunday in comparison to the weekly days. The temporal variability of DSCs for the three gases is similar, the largest HCHO, CHOCHO, and NO<sub>2</sub> DSCs being found on 25 June 2013. In contrast, the variation from one day to another (e.g. 24 and 25 June 2013) is less pronounced for HCHO than for CHOCHO and NO<sub>2</sub>. For these five days, the HCHO DSCs vary between 0 and  $1.4 \times 10^{17}$  molec cm<sup>-2</sup>, while for CHOCHO, DSCs are between 0 and  $9 \times 10^{15}$  molec cm<sup>-2</sup> and for NO<sub>2</sub> between 0 and  $2.9 \times 10^{17}$  molec cm<sup>-2</sup>.

In order to compare the columns obtained with satellite measurements or with results obtained from other stations, the DSCs need to be converted to VC, which is usually done as is described in the Sect. 2.4.8. For simplicity, a geometrical approximation is used here. This approach has already been validated in many studies for the computation of vertical columns (e.g. Li et al., 2013). A differential AMF (DAMF) has to be computed, which is defined as the difference of AMF between the off-axis direction ( $\theta \neq 90^\circ$ ) and the zenith ( $\theta = 90^\circ$ ). Then, the AMF for off-axis and the zenith view can be estimated as  $1/\sin(\theta)$  and 1 respectively. For this study, a measurement at elevation angle of 15° as off-axis is used for the determination of the “geometric” VC.

## 6.4 RESULTS AND DISCUSSION

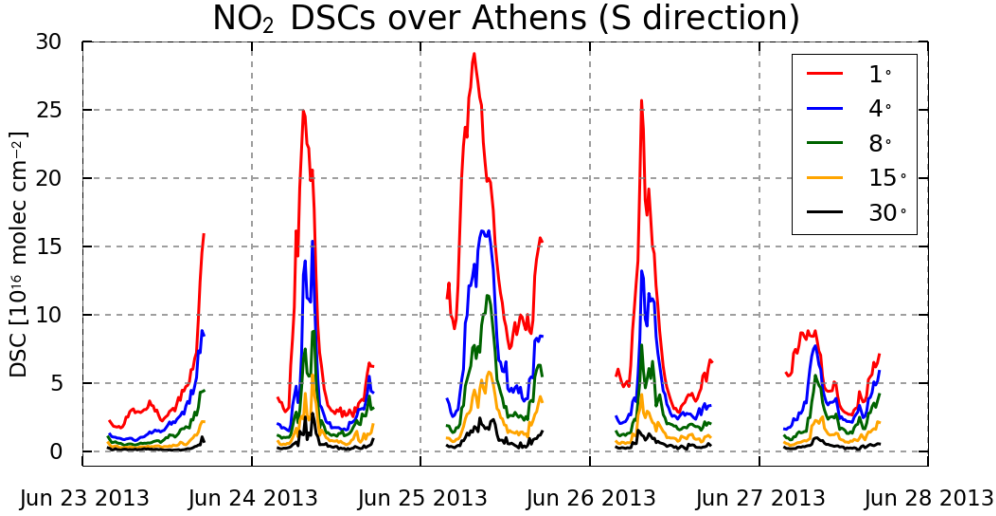


**Figure 6.15:** Time series of NO<sub>2</sub> DSCs retrieved from the MAX-DOAS measurements over Athens at elevation angles of 1°, 4°, 8°, 15° and 30° in the S-direction for the period between 23 (Sunday) and 27 (Thursday) June 2013.

Thus, the trace gas VC<sub>geo</sub> can be written as,

$$VC_{geo} = \frac{DSC_\theta}{DAMF_\theta} = \frac{DSC_{15^\circ}}{DAMF_{15^\circ}} = \frac{DSC_{15^\circ}}{(1/\sin(15^\circ)) - 1} \quad (6.1)$$

Additionally, a quality test is applied in order to filter the VC<sub>geo</sub>. This consists of comparing the VCs obtained using an elevation angle at 8° and 15°. If the relative difference between both VCs ( $\frac{VC_{15^\circ} - VC_{8^\circ}}{(VC_{15^\circ} + VC_{8^\circ})/2}$ ) is larger than 20%, the VC is not used as final product.

Figure 6.16 shows monthly mean HCHO, CHOCHO, and NO<sub>2</sub> VCs over Athens for morning (5:00–12:00), afternoon (12:00–19:00), and all day (5:00–19:00) from January 2013 to December 2014, which have been computed by using the geometrical approach described above. For the computation of monthly means, only months that have more than 10 days of measurements are taken into account. The monthly mean HCHO VCs for the morning, afternoon and all show a similar temporal behaviour, the main differences being found between afternoon and those from morning and all. The HCHO VCs from morning and all are in good agreement, in fact the maximum for every day of formaldehyde is found in the morning time (see Fig. 6.17, top), which probably is dominant factor

## 6. GLYOXAL, FORMALDEHYDE, AND NITROGEN DIOXIDE RETRIEVALS FROM MAX-DOAS MEASUREMENTS

in the computation of daily mean HCHO VCs (all) and most likely originates from direct emissions from local combustion events during the peak hours. The seasonal behaviour is similar for 2013 and 2014, which have the maximum during summer (June–July–August), which also most likely corresponds to an increase in the emissions of VOC by the vegetation during this season. The monthly values of HCHO VCs for 2013 and 2014 are of the same order of magnitude and about of  $2 - 7.0 \times 10^{15}$  molec cm $^{-2}$ .

The monthly mean CHOCHO VCs show a less pronounced seasonality in comparison to the one observed for HCHO VCs, in particular for 2014, where the values are nearly constant for most months, with a slightly increase during summer (see Fig. 6.16, middle). However, in 2013 two peaks of glyoxal are clearly observed (June and October), which are also observed for formaldehyde. Similar to HCHO, glyoxal amounts increase for the period corresponding to the warm season, which also corresponds to the growth of plants and thus, major release of isoprene and monoterpene from vegetation. In addition, the anthropogenic contributions play an important role in the amounts of formaldehyde and glyoxal, the contribution of anthropogenic sources to glyoxal being less important. Despite the fact that sources of glyoxal and formaldehyde are similar, the efficiency in the production of these could be the reason for the more pronounced seasonal behaviour of formaldehyde. The CHOCHO VCs computed for morning, afternoon, and all day show a similar temporal behaviour during 2013–2014, the VCs being slightly higher in the morning than in the afternoon. This is consistent to the observations for formaldehyde, as the glyoxal maximum is found during the morning period (see Fig. 6.17, middle). The glyoxal VCs vary between  $1.5 \times 10^{14}$  molec cm $^{-2}$  and  $3.4 \times 10^{14}$  molec cm $^{-2}$ .

In contrast to formaldehyde and glyoxal, NO<sub>2</sub> VCs for morning, afternoon and all vary more (see Fig. 6.16, bottom). NO<sub>2</sub> is mainly emitted by anthropogenic sources and as Athens is a city with high population density, a large contribution from fossil fuel combustion and industry is expected. The tendency of NO<sub>2</sub> from morning and afternoon measurement is not clear, in some months the values from the morning are higher than those from the afternoon, but also the opposite is observed. The highest monthly values of NO<sub>2</sub> VCs are found in the winter season, where more emissions by heating are expected. This is in good agreement to the observations from satellite over regions with large anthropogenic emission (e.g. North East China). The NO<sub>2</sub> VCs oscillate between  $2.0 \times 10^{15}$  molec cm $^{-2}$  and  $8.0 \times 10^{15}$  molec cm $^{-2}$  with the maximum corresponding to December 2014.

## 6.4 RESULTS AND DISCUSSION

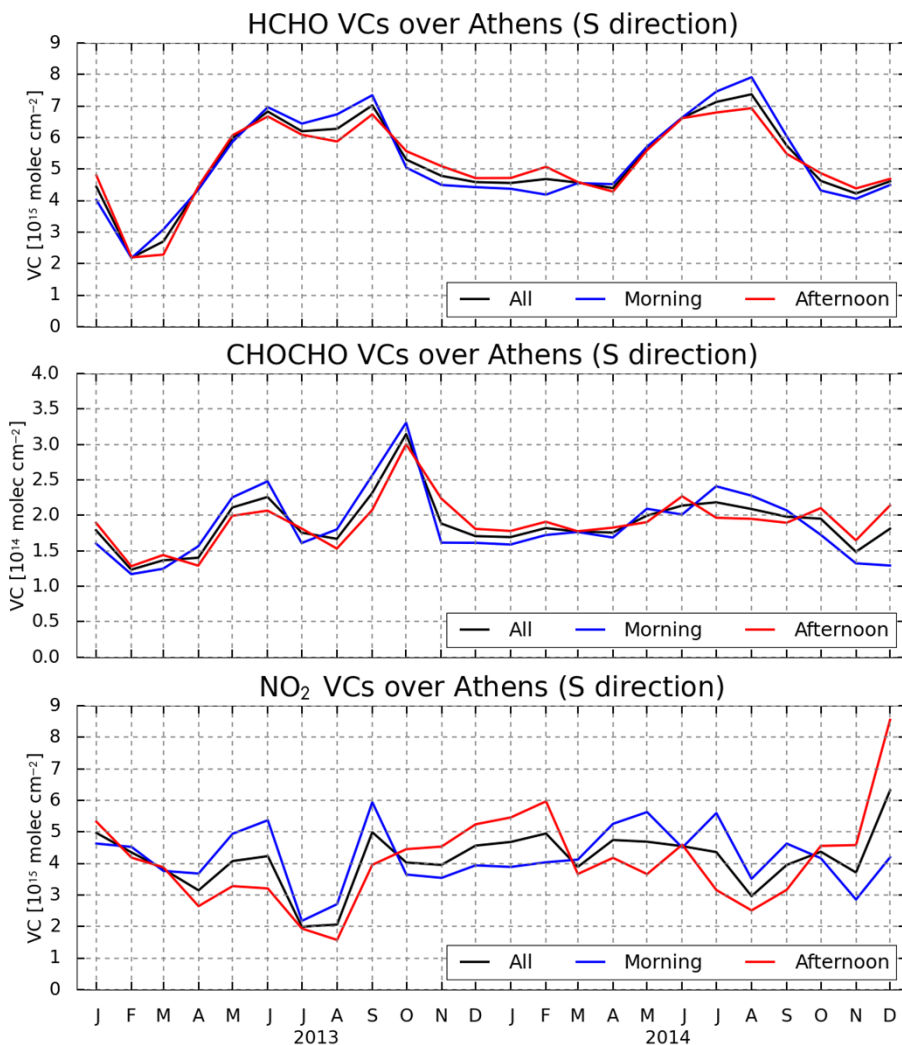


**Figure 6.16:** Monthly means HCHO, CHOCHO, and NO<sub>2</sub> VCs computed by using the geometrical approximation on 8° elevation angle over Athens for the S direction from January 2013 to December 2014.

Despite that the morning, afternoon, and all VCs have a similar temporal behaviour, the diurnal variation of HCHO, CHOCHO, and NO<sub>2</sub> VCs show differences. Figure 6.17 shows normalized means of HCHO, CHOCHO, and NO<sub>2</sub> VCs for 10 days. These diurnal variations have been computed from 18 to 27 June 2013, which are cloud free days. The measurements from every day have been binned into 1 hour steps and then normalized to the corresponding daily

## 6. GLYOXAL, FORMALDEHYDE, AND NITROGEN DIOXIDE RETRIEVALS FROM MAX-DOAS MEASUREMENTS

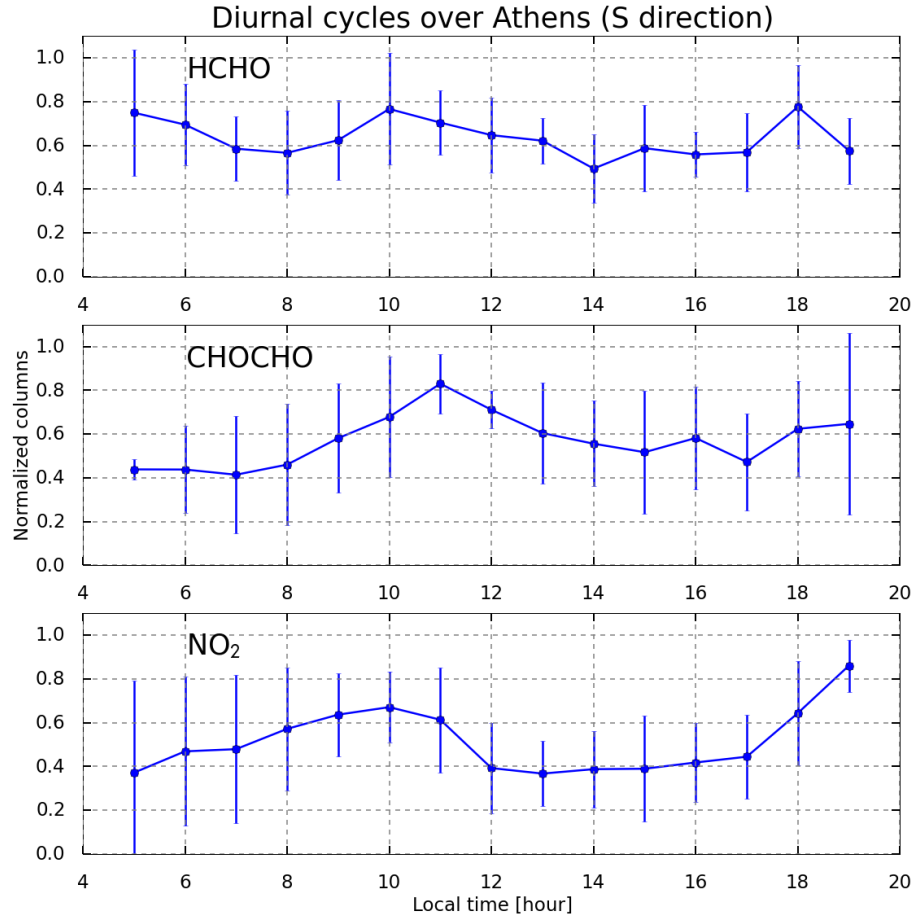


**Figure 6.17:** Diurnal variation of HCHO, CHOCHO, and NO<sub>2</sub> VCs retrieved over Athens for 10 cloud free days from 18 to 27 June 2013.

maximum, so that the increase of vertical columns from day to day will not affect the diurnal variation. In general, the diurnal cycles for CHOCHO and NO<sub>2</sub> behave similar with morning build-up and noon maximum, but NO<sub>2</sub> then decreases and has second maximum in the evening. While HCHO nearly no diurnal cycle. The diurnal cycles for each gas show the maxima in the morning, NO<sub>2</sub> and CHOCHO are low in the early morning and increase after peak hour (major vehicle traffic) and decrease in the afternoon. The NO<sub>2</sub> diurnal cycle has a similar behaviour as seen from model results (Blechschmidt et al., in preparation), with a maximum at 10:00 hour local time for both and decreasing around noon and an increase again after 17:00 hour local time (see Fig. 6.17, bottom). In

## 6.4 RESULTS AND DISCUSSION

contrast, the diurnal cycle of CHOCHO VCs shows a more symmetric evolution during the day with maximum around 11:00 hour at local time (see Fig. 6.17, middle). A similar result has already been found over Mexico city by Volkamer et al. (2005a), however the maximum corresponded to 12:00 hour local time. In contrast, Li et al. (2013) reported glyoxal amounts measured in Southern China and found that the CHOCHO diurnal cycle has a maximum in the early morning as consequence of oxydation of VOC in the previous night by OH radicals. These different results could be consequence of different dominant sources in the production of glyoxal over each region (e.g. anthropogenic or biogenic).

Additionally, HCHO, CHOCHO, and NO<sub>2</sub> VCs have been retrieved for eight different azimuth directions over Athens (see Fig. 6.4). Figure 6.18 shows monthly mean vertical columns computed from daily means that take into account measurements from 5:00 to 19:00 hours (all). For the three trace gases, the temporal evolutions are similar in the eight azimuth directions, the lowest VCs being found in the W (ocean) and A (airport) directions. These differences between azimuth viewing directions is more evident for CHOCHO and NO<sub>2</sub> VCs. Thus, the azimuth variation of HCHO VCs shows a quite homogeneous distribution, while for CHOCHO, and NO<sub>2</sub> is not. However, in the weekly and daily variation of HCHO, CHOCHO, and NO<sub>2</sub> VCs from the different azimuth viewing directions, large gradients can be found due to horizontal transport carry out by wind.

Finally, in order to investigate the sources of VOC over Athens, the ratio of glyoxal to formaldehyde ( $R_{GF}$ ) has been computed for the S direction. Although, HCHO and CHOCHO are mainly produced in the oxidation processes of hydrocarbons, they have different pathways of formation and precursors (Vrekouassis et al., 2010; DiGangi et al., 2012; Kaiser et al., 2015). The ratio of formaldehyde to nitrogen dioxide ( $R_{FN}$ ) can be used to investigate the ozone production rates of precursor species of VOC and NO<sub>x</sub> (Martin et al., 2004a; Duncan et al., 2010; Li et al., 2013; Ortega et al., 2015). The interpretation of these ratios is highly variable and depends on many factors (e.g. season, location). Figure 6.19 shows monthly mean  $R_{GF}$  over Athens for 2013 and 2014. The  $R_{GF}$  has a clear seasonal variation with large ratios corresponding to the cold season (winter: December–January–February) and low values to the warm season (summer: June–July–August). These ratios vary between 0.028 to 0.06, the maximum found for October 2013 and the minimum in August 2013. For the warm season, ratios oscillate between 0.028 and 0.033. These ratios could be associated to biogenic sources of VOC, because during summer an increase of temperature lead to a major release of BVOC from vegetation. These ratios are slightly larger than

## 6. GLYOXAL, FORMALDEHYDE, AND NITROGEN DIOXIDE RETRIEVALS FROM MAX-DOAS MEASUREMENTS

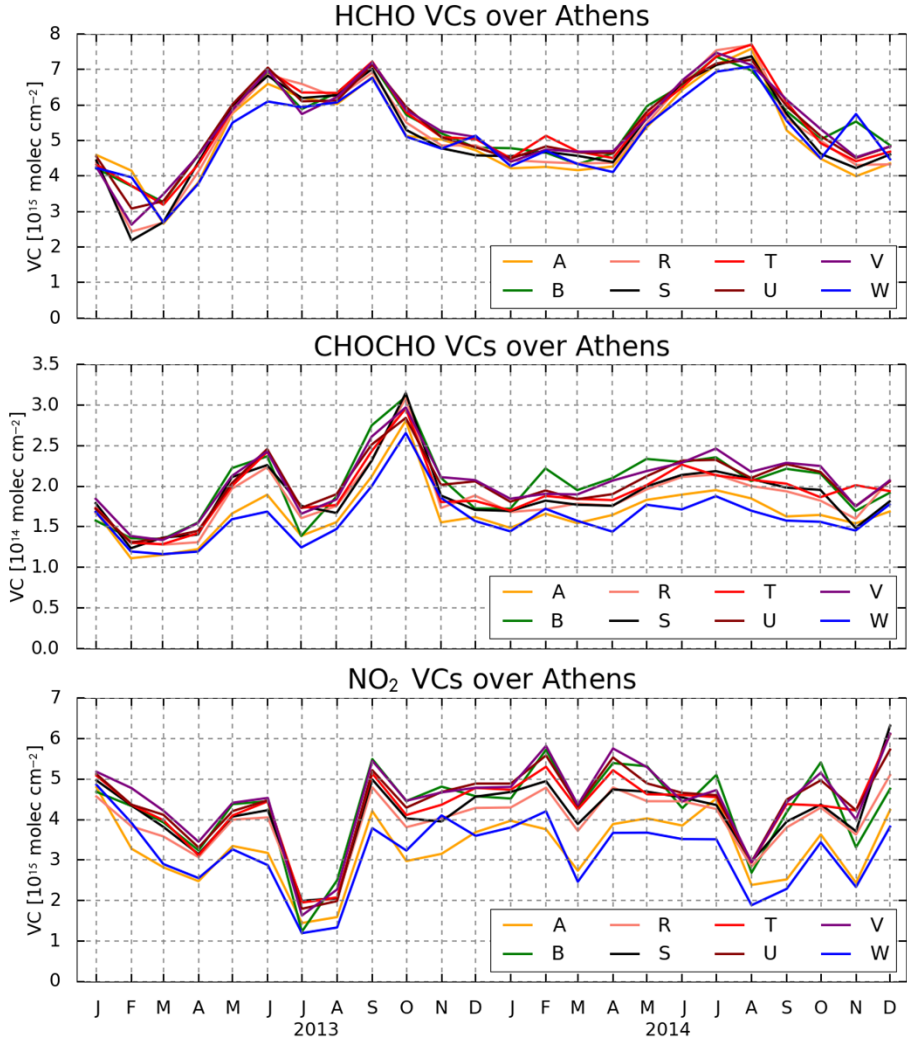


**Figure 6.18:** Monthly means of HCHO, CHOCHO, and NO<sub>2</sub> VCs over Athens for eight different azimuth directions, which are focused over different sources for period 2013–2014.

those found by DiGangi et al. (2012) from in-situ measurements over two rural regions during summer time. The ratios obtained by DiGangi et al. (2012) vary between 0.019 and 0.030 for most days, smaller than those found in our study. However, the measurement regions are characterized by large biogenic influence, they associated these small ratios to biogenic sources of VOC. In contrast, Athens is a city with high population density and despite the larger biogenic emission

## 6.4 RESULTS AND DISCUSSION

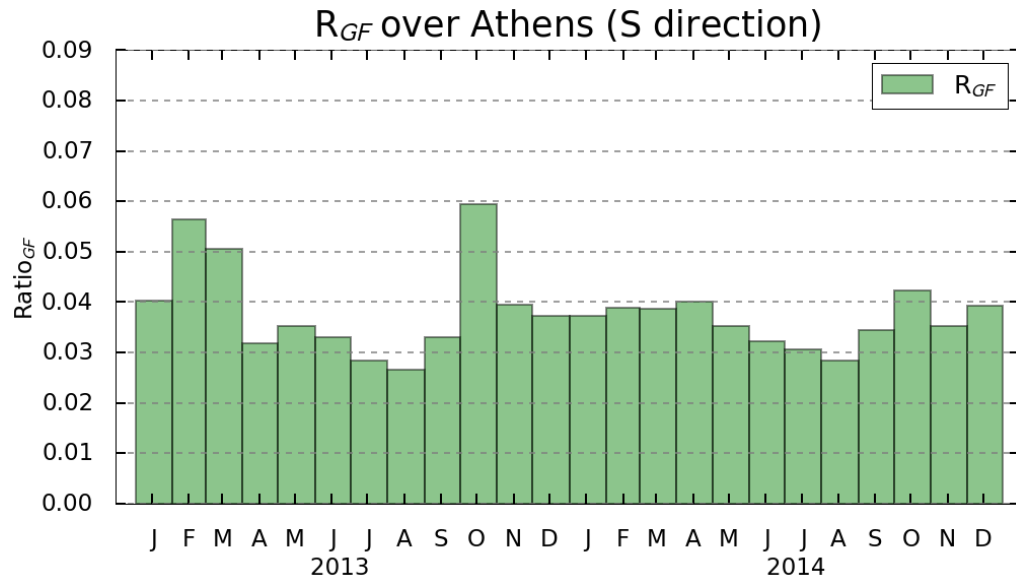


**Figure 6.19:** Ratio of glyoxal to formaldehyde ( $R_{GF}$ ) obtained for the S direction over Athens for 2013 and 2014.

expected in summer, the anthropogenic contribution still remains, and thus  $R_{GF}$  in Athens during summer time could be a result from BVOC with some influence from AVOC, because the ratios obtained from this study are monthly means and not daily as in DiGangi et al. (2012). In the monthly means, the production of glyoxal and formaldehyde from day to day can change due to the different sources that emit VOC over Athens. DiGangi et al. (2012) also found an enhancement of  $R_{GF}$  during a fire event, which is in agreement with results obtained from satellite observations over regions characterized by a large number of fire events (Kaiser et al., 2015) and associated to pyrogenic and anthropogenic sources. Thus, large ratios observed during winter season in this study could be due to the anthropogenic contribution to production of AVOC.

Additionally, by using the ratio of formaldehyde to nitrogen dioxide, the relative sensitivity of  $O_3$  formation to precursor species of VOC and  $NO_x$  is investigated over Athens as is inferred from this ratio. Because, the formation of ozone can drive by reducing the emissions of VOC or  $NO_x$ , and they are referred to VOC-limited and  $NO_x$ -limited photochemical regimes. Duncan et al. (2010) characterized the relationship between  $R_{FN}$  and  $O_3$  production in the United States, by combining a model study and satellite observation, and suggested

## 6. GLYOXAL, FORMALDEHYDE, AND NITROGEN DIOXIDE RETRIEVALS FROM MAX-DOAS MEASUREMENTS

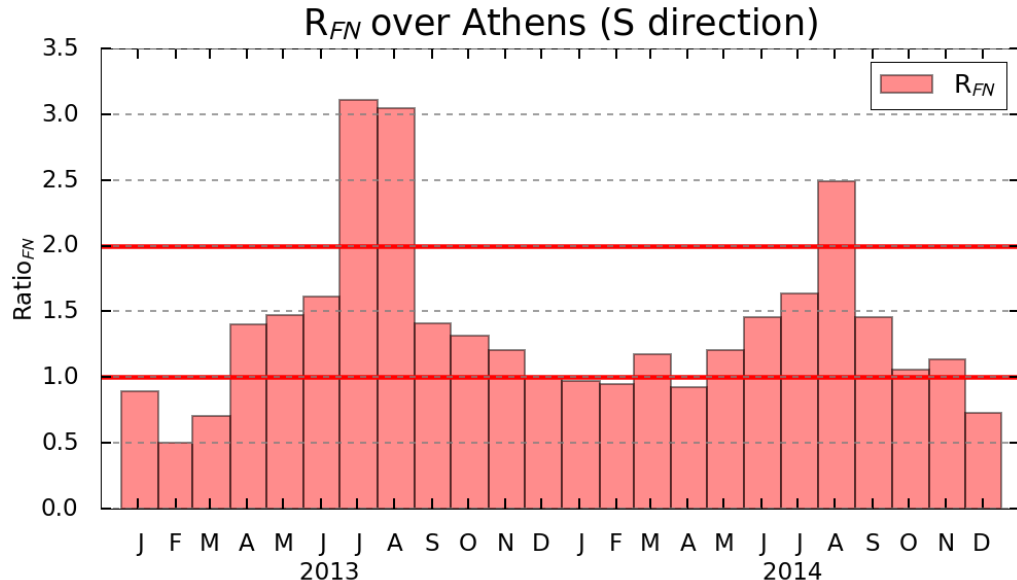


**Figure 6.20:** Monthly means ratios of formaldehyde to nitrogen dioxide ( $R_{FN}$ ) for the S direction over Athens during 2013 and 2014.

three regimes:  $R_{FN} < 1$  for VOC-limited,  $R_{FN} > 2$  for  $\text{NO}_x$ -limited, and  $R_{FN}$  between 1 and 2 for transition regimes, where both (VOC-limit and  $\text{NO}_x$ -limit) may reduce the ozone production. Figure 6.20 shows monthly mean  $R_{FN}$  over Athens for 2013 and 2014. The  $R_{FN}$  behave opposite to the  $R_{GF}$ , the large ratios during the warm season and small values in the cold season. These ratios are between 0.5 and 3.0 with the minimum found in February 2013 (0.5), while the maximum is found during July 2013 (3.1). Thus, in the summer months  $\text{O}_3$  production is  $\text{NO}_x$ -limited and only in winter it is VOC-limited, while the rest of the year it is in the intermediate regime.

### 6.4.2 Nairobi

Figures 6.21, 6.22, and 6.23 show HCHO, CHOCHO, and  $\text{NO}_2$  DSCs retrieved from the MAX-DOAS measurements over Nairobi at elevation angles of  $1^\circ$ ,  $4^\circ$ ,  $8^\circ$ ,  $15^\circ$ , and  $30^\circ$  from Wednesday (23 January 2013) to Sunday (27 January 2013). These days are mostly cloud free. As described above, Nairobi is a city with large population, however there are also large vegetation extensions and the instrument is in the direction of a national park.

## 6.4 RESULTS AND DISCUSSION

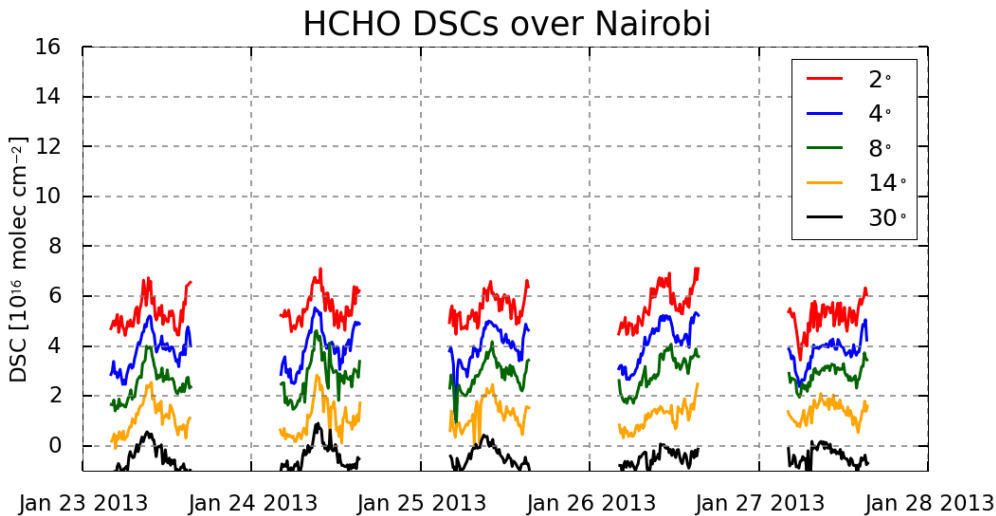


**Figure 6.21:** Time series of HCHO DSCs retrieved from MAX-DOAS measurements over Nairobi at elevation angles of 2°, 4°, 8°, 14° and 30° for the period between 23 (Wednesday) and 27 (Sunday) January 2013.

The separation of the retrieved DSCs between different elevation angles is clear for these five days due to the good visibility. The HCHO DSCs have a very pronounced diurnal variation with the maximum around noon for most of days, which is not clear for CHOCHO, and NO<sub>2</sub> DSCs (see Figs 6.22 and 6.23). Moreover, some HCHO DSCs for the 30° elevation angle are negatives due to instrumental problems as mirror degradation (this has working for more than 12 years). The CHOCHO, and NO<sub>2</sub> DSCs show an increase in the afternoon, while the maximum in DSC varies between days, being mostly found around noon (late morning or early afternoon) for CHOCHO and mainly in the afternoon for NO<sub>2</sub>. On Sunday (27 January 2013) the diurnal variation is less pronounced than during week days. Moreover, a significant reduction in the DSCs for the three gases is observed for Sunday in comparison of week days, which could be related to reduced amount of emissions from vehicles similar to Athens (see Sect. 6.4.1). The day to day variations of DSCs for CHOCHO and NO<sub>2</sub> is similar, higher amounts of these gases being observed on 26 January 2013 (Saturday). In contrast, HCHO DSCs are nearly constant with only a slight decrease on Sunday. The HCHO is varying between 0 and  $7 \times 10^{16}$  molec cm<sup>-2</sup>, CHOCHO between 0 and  $4.5 \times 10^{15}$  molec cm<sup>-2</sup> and NO<sub>2</sub> columns are between 0 and  $9.5 \times 10^{16}$  molec cm<sup>-2</sup>.

## 6. GLYOXAL, FORMALDEHYDE, AND NITROGEN DIOXIDE RETRIEVALS FROM MAX-DOAS MEASUREMENTS

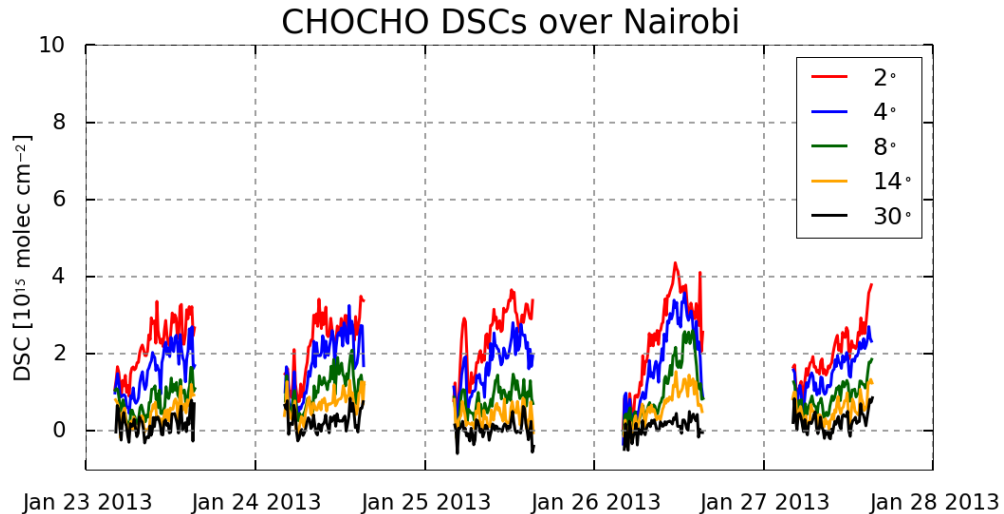


**Figure 6.22:** Time series of CHOCHO DSCs retrieved from the MAX-DOAS measurements over Nairobi at elevation angles of 2°, 4°, 8°, 14° and 30° for the period between 23 (Wednesday) and 27 (Sunday) January 2013.

These DSCs retrieved over Nairobi are converted to VCs using equation 6.1 as is described in Sect. 6.4.1. However, instead of using the elevation angle at 15°, an angle at 14° is used, because for the years of interest the measurement at 15° was not performed.

In order to investigate the diurnal variation of HCHO, CHOCHO, and NO<sub>2</sub> VCs, means of VCs normalized to the corresponding daily maximum for 10 days from 15 to 25 February 2013 (summer time in Nairobi) have been computed. These days are characterized by be cloud free conditions. The measurements from every day have been binned into 1 hour steps. Figure 6.24 shows the diurnal variation of HCHO, CHOCHO, and NO<sub>2</sub>, which is quite similar for all three species. However, the increase during the day occurs at a different time for each gas. HCHO and NO<sub>2</sub> VCs are slightly higher in the morning and decrease to a minimum at 8:00 and 9:00 hour (local time), respectively. These elevated levels for the early morning could be related to vehicle emissions in the peak hours, which is more evident for HCHO and NO<sub>2</sub> as they are directly related to anthropogenic emissions. In the case of HCHO, a maximum is reached around 11:00 hours, keeping the levels high and nearly constant until 16:00 hours, when the amounts of formaldehyde start to decrease. In contrast, NO<sub>2</sub> levels keep increasing until the maximum is reached around 15:00 hour, and them remain

## 6.4 RESULTS AND DISCUSSION

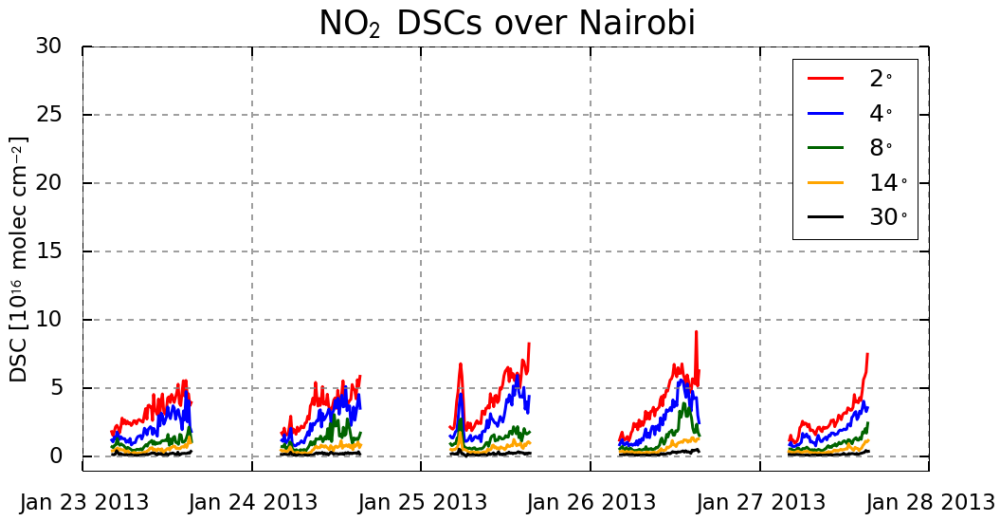


**Figure 6.23:** Time series of NO<sub>2</sub> DSCs retrieved from the MAX-DOAS measurements over Nairobi at elevation angles of 2°, 4°, 8°, 14° and 30° for the period between 23 (Wednesday) and 27 (Sunday) January 2013.

nearly constant until the end of the day. For CHOCHO during the morning, the behaviour is nearly constant and lower with a minimum at 8:00 hour. CHOCHO levels start to increase around 10:00 hours until a maximum is reached around noon (12:00 hours). These high levels remain constant until 16:00 hours, when they start to decrease again. These diurnal variations show that the behaviour of the three gases during the day is most likely dominated by photolysis and increase of temperature, because the tropical regions are characterized by intense sun light between 10:00 and 15:00 hours during summer time with a significant increase of temperature. In fact the increase of temperate also causes an increase in the isoprene emissions over regions with large vegetation (Duncan et al., 2010). The diurnal behaviour observed in Nairobi is different than in Athens, which could be related to the difference in sources and sinks over each city.

Figure 6.25 shows monthly mean HCHO, CHOCHO, and NO<sub>2</sub> VCs over Nairobi for morning (5:00–12:00), afternoon (12:00–19:00), and all day (5:00–19:00) from January 2011 to December 2014. The computation of monthly means has been performed similar to Athens (see Sect. 6.4.1). The monthly mean VCs show a similar temporal behaviour for the three gases, the most notable differences between time periods (morning, afternoon, all) are found for formaldehyde and glyoxal. In contrast, the NO<sub>2</sub> VCs for the three time periods

## 6. GLYOXAL, FORMALDEHYDE, AND NITROGEN DIOXIDE RETRIEVALS FROM MAX-DOAS MEASUREMENTS

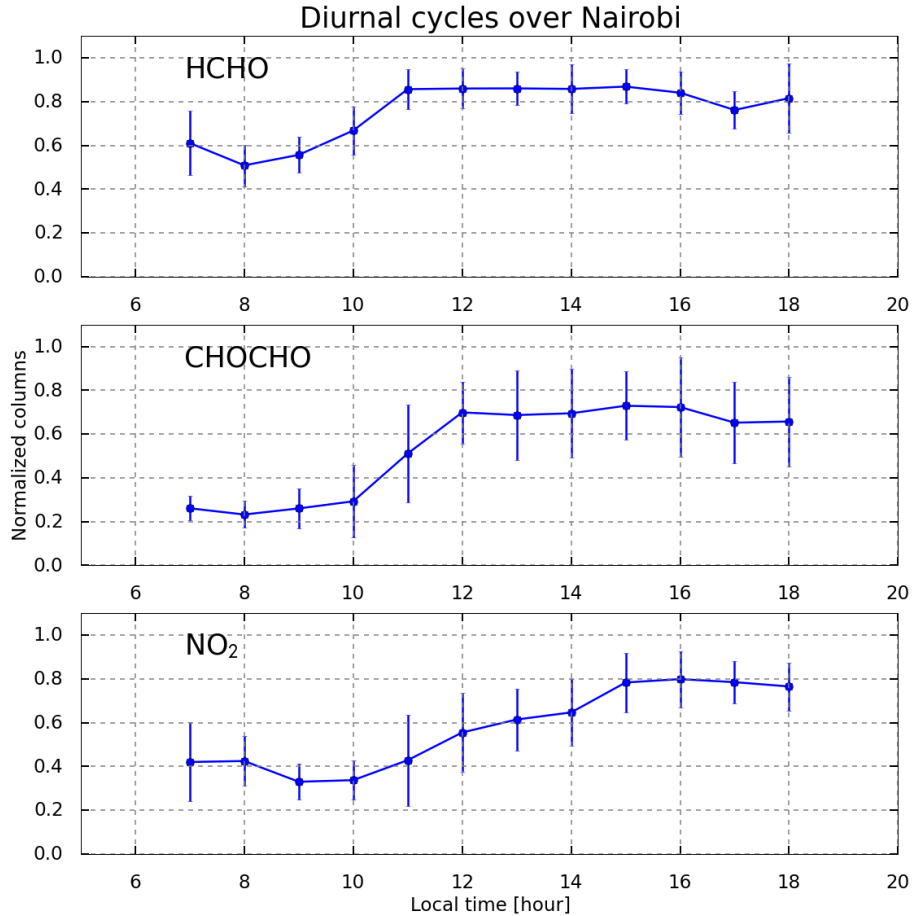


**Figure 6.24:** Diurnal variation of HCHO, CHOCHO, and NO<sub>2</sub> VCs retrieved over Nairobi for 10 cloud free days from 15 to 25 February 2013.

are very similar. The VCs of the afternoon period are larger than those from the morning time, as expected from the daily variations showing higher levels of formaldehyde, glyoxal and nitrogen dioxide between late morning and afternoon time (see Fig. 6.24). The seasonal behaviour for glyoxal and NO<sub>2</sub> VCs is similar from year to year with the exception of 2014 for glyoxal. In contrast, the seasonal variability for formaldehyde is not clear, a slight increase being found during winter time (June–July–August–September) for every year. The maximum of CHOCHO and NO<sub>2</sub> VCs for every year is observed during winter similar to formaldehyde, however the seasonal variability of these two gases is much more pronounced. The HCHO VCs vary between  $3.0 \times 10^{15}$  molec cm<sup>-2</sup>

## 6.4 RESULTS AND DISCUSSION

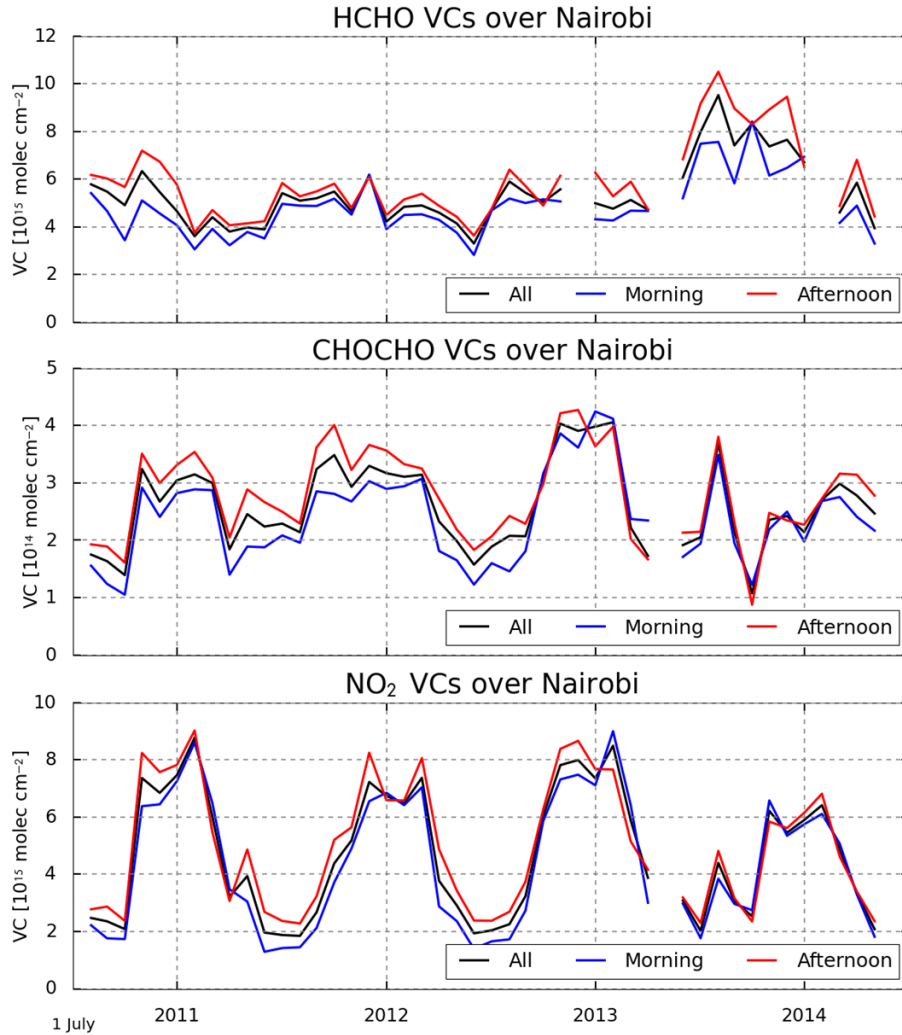


**Figure 6.25:** Monthly means of HCHO, CHOCHO, and NO<sub>2</sub> VCs computed by using the geometrical approach over Nairobi from January 2011 to December 2014.

and  $11.0 \times 10^{15}$  molec  $\text{cm}^{-2}$ , and for CHOCHO between  $1.0 \times 10^{14}$  molec  $\text{cm}^{-2}$  and  $4.5 \times 10^{15}$  molec  $\text{cm}^{-2}$ , while NO<sub>2</sub> VCs between  $2.0 \times 10^{15}$  molec  $\text{cm}^{-2}$  and  $9.0 \times 10^{15}$  molec  $\text{cm}^{-2}$ .

Similar to Athens, the ratios of glyoxal to formaldehyde and formaldehyde to nitrogen dioxide have been computed in order to investigate the sources of production of VOC and the ozone production rates to NO<sub>x</sub> limit and VOC limit

## 6. GLYOXAL, FORMALDEHYDE, AND NITROGEN DIOXIDE RETRIEVALS FROM MAX-DOAS MEASUREMENTS

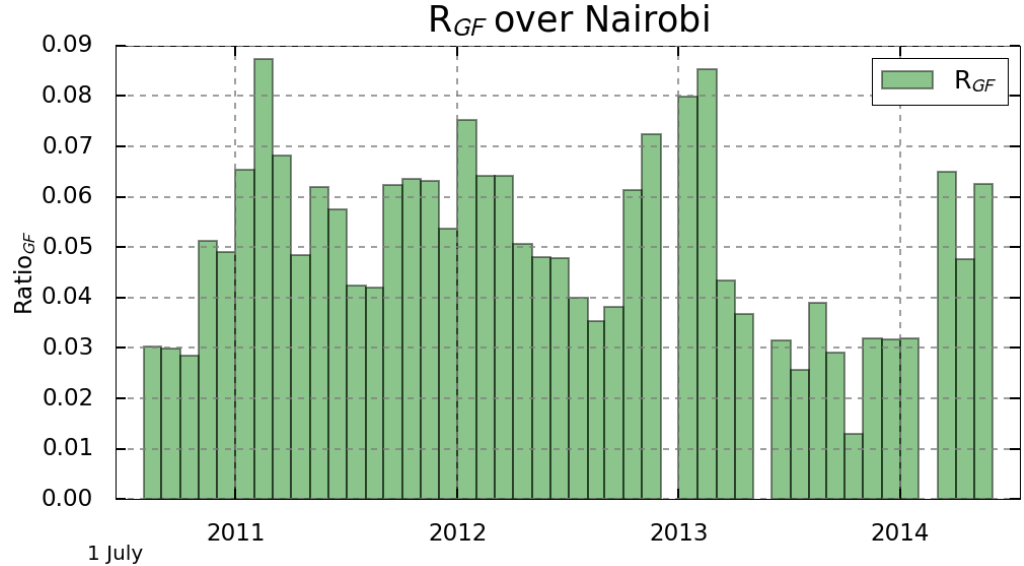


**Figure 6.26:** Monthly means ratios of glyoxal to formaldehyde ( $R_{GF}$ ) over Nairobi from January 2011 to December 2014.

as well. Fig. 6.26 shows monthly mean  $R_{GF}$  over Nairobi between 2011 and 2014. The  $R_{GF}$  has a clear seasonal variation with large ratios corresponding to cold season (winter: June–July–August–September) and low ratios in the warm season (summer: December–January–February–March). These ratios vary between 0.015 to 0.085, the maximum being found in August 2011 and the minimum in April 2014. For the warm season, ratios range between 0.015 and 0.060 are found. Low ratios similar to Athens, could be associated to biogenic sources of VOC, because during summer more isoprenes are emitted by vegetation due to the temperature dependence of these, especially over Nairobi, where large extensions of vegetation are found in the direction of instrument view. The  $R_{GF}$  over Nairobi are larger than those observed by DiGangi et al. (2012), however Nairobi is a city with large anthropogenic contribution as well. Thus, significant differences would be expected between both regions, because the measurement site in DiGangi et al. (2012) is characterized mainly by biogenic influence. The largest ratios are found for June–July–August–September, which corresponds to winter months and is characterized for regions with anthropogenic activities and fire events (DiGangi et al., 2012; Kaiser et al., 2015).

Figure 6.27 shows monthly mean  $R_{FN}$  values computed for Nairobi from 2011 to 2014. The  $R_{FN}$  have a strong seasonality following the behaviour of  $\text{NO}_2$  with

## 6.4 RESULTS AND DISCUSSION

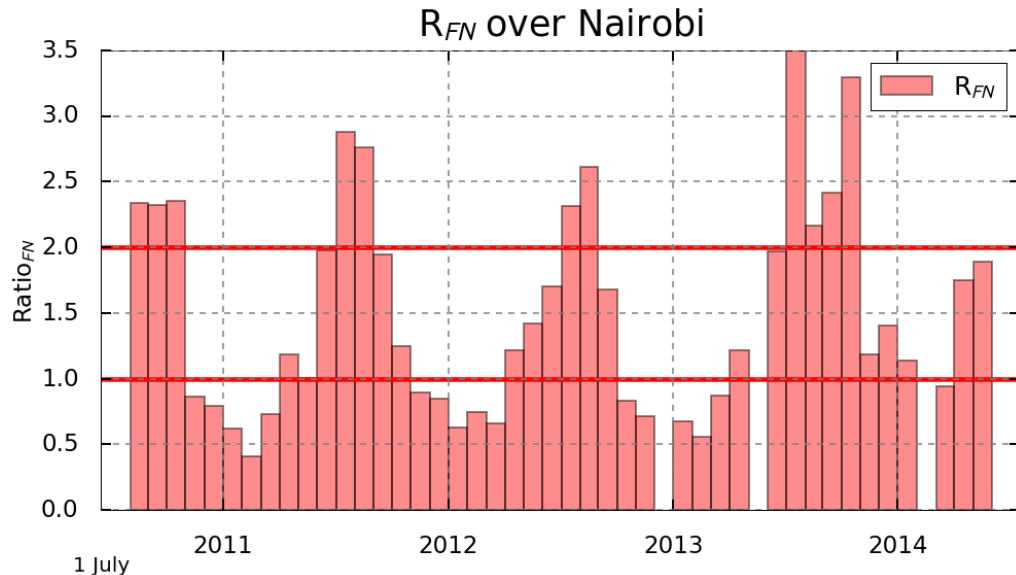


**Figure 6.27:** Monthly means ratios of formaldehyde to nitrogen dioxide ( $R_{FN}$ ) over Nairobi from January 2011 to December 2014.

large ratios observed in summer and small from winter. During summer the ratio varies between 2 and 3.5 and for winter between 0.4 and 1.5. Thus, following the characterization suggested by Duncan et al. (2010), the values obtained for summer correspond to  $\text{NO}_x$ -limited. This could be a consequence of the large isoprene emission from vegetation during that season and it is consistent with the small  $R_{GF}$  values. While for winter, the values correspond to VOC-limited, which could be a consequence of higher anthropogenic emissions during winter. These ratios are about the same order of magnitude with the ones found by (Duncan et al., 2010) over Los Angeles, USA. For the rest of the months the  $R_{FN}$  corresponds to the transition regime.

### 6.4.3 Comparison between Athens and Nairobi

Despite the similar population size of Athens and Nairobi, many differences are found between the results obtained in each city. First, the weather in Nairobi is mostly stable without strong changes in the temperatures as cities located very north or south in the hemisphere such as Athens. The rainfall and temperatures over Nairobi in average are higher than in Athens. Also, the vegetation exten-

## 6. GLYOXAL, FORMALDEHYDE, AND NITROGEN DIOXIDE RETRIEVALS FROM MAX-DOAS MEASUREMENTS

sion for Nairobi is larger than in Athens. These differences in weather could be the reasons of most pronounced seasonal cycle of CHOCHO and NO<sub>2</sub> VCs for Nairobi (increase of temperature during summer more emissions from biogenic sources), however the background signal of the these gases is larger in Athens than in Nairobi, which could be explained by the major anthropogenic influence in Athens. The diurnal cycles for both regions are different, which could be related to the time of sources in these and the weather conditions. Nevertheless, the diurnal cycles from Athens is in agreement with those found by Volkamer et al. (2005a) in Mexico city for CHOCHO and model results by Blechschmidt et al. (in preparation) for NO<sub>2</sub>. The R<sub>GF</sub> is larger for Nairobi than Athens (see Fig. 6.19 and 6.26), however the lower values for both regions correspond to their respective summer (increase of temperature means more isoprene emissions from vegetation), and the higher for their respective winter season (more anthropogenic emissions). The R<sub>FN</sub> have their maxima during winter season for both stations and the minima correspond to summer season, which is the opposite to the R<sub>GF</sub>. Thus, we could conclude that the main sources of VOC in Athens are mainly due to anthropogenic emissions with minor influences from biogenic sources, and for Nairobi these sources are mainly biogenic with some contribution from anthropogenic emissions. In spite the many differences and consistencies found between results from both station, further work is need to done in order to a better characterization of the VOC sources over Athens and Nairobi.

### 6.5 Summary

HCHO, CHOCHO, and NO<sub>2</sub> columns have been retrieved from MAX-DOAS measurements for two locations (Athens and Nairobi), based on a systematic analysis of fitting windows, polynomial orders, and interfering cross-sections for each species. For both locations, the measured HCHO, CHOCHO, and NO<sub>2</sub> SCs have been converted to VCs using a geometrical approach.

Diurnal cycles of HCHO, CHOCHO, and NO<sub>2</sub> VCs have been computed for both locations. In spite of the similar population size, the diurnal variations at both stations are different. This difference could be related to the different weather conditions (Nairobi tropical climate and Athens mediterranean climate) but, more importantly, due to the different types of sources, because the vegetation extensions in Nairobi are larger than in Athens. Also, the diurnal cycle of

## 6.5 SUMMARY

glyoxal and NO<sub>2</sub> are similar to observations by Volkamer et al. (2005a) in Mexico city and model results by Blechschmidt et al. (in preparation) over densely populated cities like Athens.

Monthly mean VCs have been computed for each gas for three time periods (morning, afternoon and all day), finding a good agreement among the three data sets for both locations. The monthly mean time series of VCs show the maximum for each year during June–July–August. However, in the case of Athens, this corresponds to summer season while for Nairobi, it is winter season. Generally, the VCs over Nairobi are larger than these VCs obtained for Athens.

The R<sub>GF</sub> and R<sub>FN</sub> show a strong seasonality for both locations. The R<sub>GF</sub> are high for winter season and small for summer season. The opposite is also true for R<sub>FN</sub> (high for summer and small for winter). From these ratios, some information about the type of sources can be inferred from both location. For Athens, these ratios indicate mainly anthropogenic sources with some biogenic contribution during summer to VOC, and mainly biogenic sources for Nairobi with some contribution from pyrogenic and anthropogenic emissions.

# 7

## Conclusions and Outlook

### Glyoxal satellite retrieval

In this thesis, an improved and homogenized glyoxal retrieval has been developed for four different satellite instruments, which expands the data set available of glyoxal to more than 12 years of morning and afternoon orbits. Sensitivity tests on synthetic data as well as on OMI, GOME-2 (A and B), and SCIA-MACHY measurements over selected regions provided useful information for the selection of DOAS fitting windows and the most appropriate polynomial degree for this study. Two approaches for the reduction of the liquid water interference over clear water oceans have been evaluated, finding that including the liquid water absorption cross-section in the DOAS fit leads to the reduction of negative glyoxal values over oceans and nearly no differences over land. For the first time, possible interferences by tropospheric NO<sub>2</sub> over areas with large anthropogenic emissions have been investigated. A high-temperature NO<sub>2</sub> absorption cross-section representing near-surface NO<sub>2</sub> has been introduced in the retrieval, leading to a significant reduction of glyoxal over these areas and an improved fit quality.

Investigation of the impact of different water vapour cross-sections in the fit shows that for OMI data, this does not seem to be a critical factor. This is in contrast to ground-based MAX-DOAS observations, where water vapour absorption can interfere strongly with the retrievals, in particular in the Tropics.

In spite of the progress made on glyoxal retrieval and its homogenisation

for different satellite platform, the resulting datasets are still noisy and depend critically on the details of the selections made for the retrieval. Further improvements in signal-to-noise and consistency are needed to make full use of the synergy between measurements from instruments in morning and afternoon orbits. In addition, the effects of clouds and aerosols on the air mass factors need to be taken into account, in particular for biomass burning scenarios, where these can play an important role in the detection of glyoxal transport events.

## Interpretation of satellite data

A global analysis of glyoxal retrieved from four different instrument shows that the largest levels are located in the tropical and subtropical regions, where more dense vegetation is found. In the northern and southern hemisphere, a clear seasonality of glyoxal is present with the maximum in the summer season.

The comparison of glyoxal vertical columns retrieved from measurements of OMI, GOME-2 (A and B), and SCIAMACHY shows good overall agreement in the seasonal behaviour. However, OMI glyoxal columns are systematically lower than the vertical columns observed by SCIAMACHY and GOME-2 (A and B), especially for the most recent years (since 2011). This decrease in OMI CHOCHO VCs is most evident for regions in the latitude range 30° S–5° N. In addition, the amplitude of the seasonal variation for OMI is smaller than that of the other instruments. Significant differences were found over regions with large anthropogenic emissions. A similar seasonal behaviour is observed among the four products, although less pronounced in the OMI product.

Correlation coefficients between EVI and CHOCHO columns larger than 0.8 have been found over areas characterized by dense vegetation, where the computed time series of EVI and glyoxal columns show strong and in-phase seasonal variations. The maxima of glyoxal were found during the warm seasons, as a consequence of increases in isoprene emissions. Strong negative correlation between glyoxal columns and EVI was found over Africa caused by large fire events in these regions, which mainly occur outside the growing season. The correlation coefficient between FRP and CHOCHO VCs over these regions are larger than 0.8 and the time series of FRP and glyoxal VCs show strong and in-phase seasonal variation. However, the sources contribution over these regions is not only from fires, because the background signal of glyoxal is large, most likely due to the biogenic contribution. An additional peak in glyoxal is found in the wet

## 7. CONCLUSIONS AND OUTLOOK

season which could be related to biogenic influence.

Finally, a detailed comparison between glyoxal, EVI, FRP, and NO<sub>2</sub> over 21 regions has been performed in order to characterize the possible sources of glyoxal in these regions. It is clear that the dominant source of glyoxal is biogenic emission, because in most of the regions it follows the behaviour of EVI. There are some regions where strong fire events become an important source in the production of glyoxal, and others with an important influence from anthropogenic emissions.

The ratio of glyoxal to formaldehyde has been computed from GOME-2A measurements from 2007 to 2014. The R<sub>GF</sub> shows a clear seasonality similar to that of glyoxal. On a closer inspection over nine selected regions the variation R<sub>GF</sub> turns out to depend on the vegetation type and temperature. The comparison of R<sub>GF</sub> with indicators of biogenic (EVI), pyrogenic (FRP), and anthropogenic (NO<sub>2</sub>) emissions also vary, with most of the regions being low when large EVI is observed and large when high FRP and NO<sub>2</sub> is found. These results are in agreement with the assessment performed by Kaiser et al. (2015) for the assignment of R<sub>GF</sub> to the different source emissions of VOC. In addition, many factors such as vegetation type, temperature, humidity, and population play an important role in the behaviour of R<sub>GF</sub> for different regions. Thus, the ratios of glyoxal to formaldehyde can be used as a tool for the identification of VOC sources from satellites, however a more accurate process is needed in order to have a better identification of VOC sources.

The CHOCHO retrieval has been applied to identify pyrogenic activities for the large Russian wildfire during August 2010. It was shown that the location and temporal pattern of the retrieved glyoxal columns are closely linked to the fire radiative power observations, indicating that in these areas, pyrogenic emissions dominate the glyoxal signal and thus glyoxal can also be used of indicator of fire emissions.

For the first time transport events of glyoxal have been identified. A case study over Southeast Asia was investigated, where high levels of glyoxal follow the trajectories of air masses simulated with HYSPLIT. As glyoxal lifetime is short in the atmosphere, a possible recycling process in a mixing layer with aerosols could be the reason of an extended lifetime of glyoxal under these conditions.

## Ground-based MAX-DOAS measurements

HCHO, CHOCHO, and NO<sub>2</sub> columns have been retrieved from MAX-DOAS measurements for two locations (Athens and Nairobi), based on a systematic analysis of fitting windows, polynomial orders, and interfering cross sections for each species. For both locations, the measured HCHO, CHOCHO, and NO<sub>2</sub> SCs have been converted to VCs using a geometrical approach.

Diurnal cycles of HCHO, CHOCHO, and NO<sub>2</sub> VCs have been computed for both locations. In spite of the similar population size, the diurnal variations at both stations are different. This difference could be related to the different weather conditions (Nairobi tropical climate and Athens mediterranean climate); but most importantly due to the type of sources, because the vegetation extension in Nairobi is larger than in Athens. The diurnal cycles of glyoxal and NO<sub>2</sub> are similar as seen from measurement in Mexico city and model results over densely populated cities as Athens.

Monthly mean VCs have been computed for each gas for three periods of time (morning, afternoon and all), finding a good agreement among the three data sets for both locations. The monthly mean time series of VCs show the maximum for each year during June–July–August. However, in the case of Athens, this corresponds to summer season while for Nairobi, it is winter season. Generally, the VCs obtained for Nairobi are larger than the VCs obtained in Athens.

The R<sub>GF</sub> and R<sub>FN</sub> have a strong seasonality for both locations. The R<sub>GF</sub> are high during winter season and small for summer season. The opposite is true for R<sub>FN</sub> (high for summer and small for winter). From these ratios, some information about the type of source can be inferred from both location. For Athens, these are mainly anthropogenic with some biogenic contribution during summer to VOC, and mainly biogenic for Nairobi with some contribution from pyrogenic and anthropogenic emissions.

## Outlook

As shown by this thesis, satellite and ground-based measurements are an invaluable tool to observe glyoxal and have a better understanding of VOC in the atmosphere. However, the number of assumptions made in the retrieval still provide many possibilities to improve the glyoxal product. Especially, more efforts have to be invested in accounting for cloud and aerosol effects on the

## 7. CONCLUSIONS AND OUTLOOK

air mass factors calculation, in particular in the case of biomass burning when atmospheric aerosol levels are high. Also, in order to better quantify the observed CHOCHO columns, in terms of surface concentrations, detailed information on the glyoxal profile is needed for different environments.

For improved interpretation possibilities of the VOC, trajectory analysis can be used to identify sources and transport path ways of HCHO and CHOCHO observed in the satellite data. Both forward trajectories (mainly from locations of fires but also from areas with expected biogenic emissions) and backward trajectories (from interesting satellite measurement locations and the ground-based instrument) can be used. The outcome will provide statistics on the relation between source regions and HCHO/CHOCHO columns observed as a function of season.

Also, selected trajectories and trajectory groups need to be used to drive a chemistry box model with input from up-to-date emission inventories and to compare the columns determined from multiple runs of the model with those observed from satellite to verify the consistency of the emissions used.

The methods presented in this thesis open the path for interpretation of the available long-term multiple instrument datasets with the possibility of including data from future missions (e.g. GOME-2/Metop-C, Sentinel 4 and 5) for the analysis in a consistent manner.



## Appendix

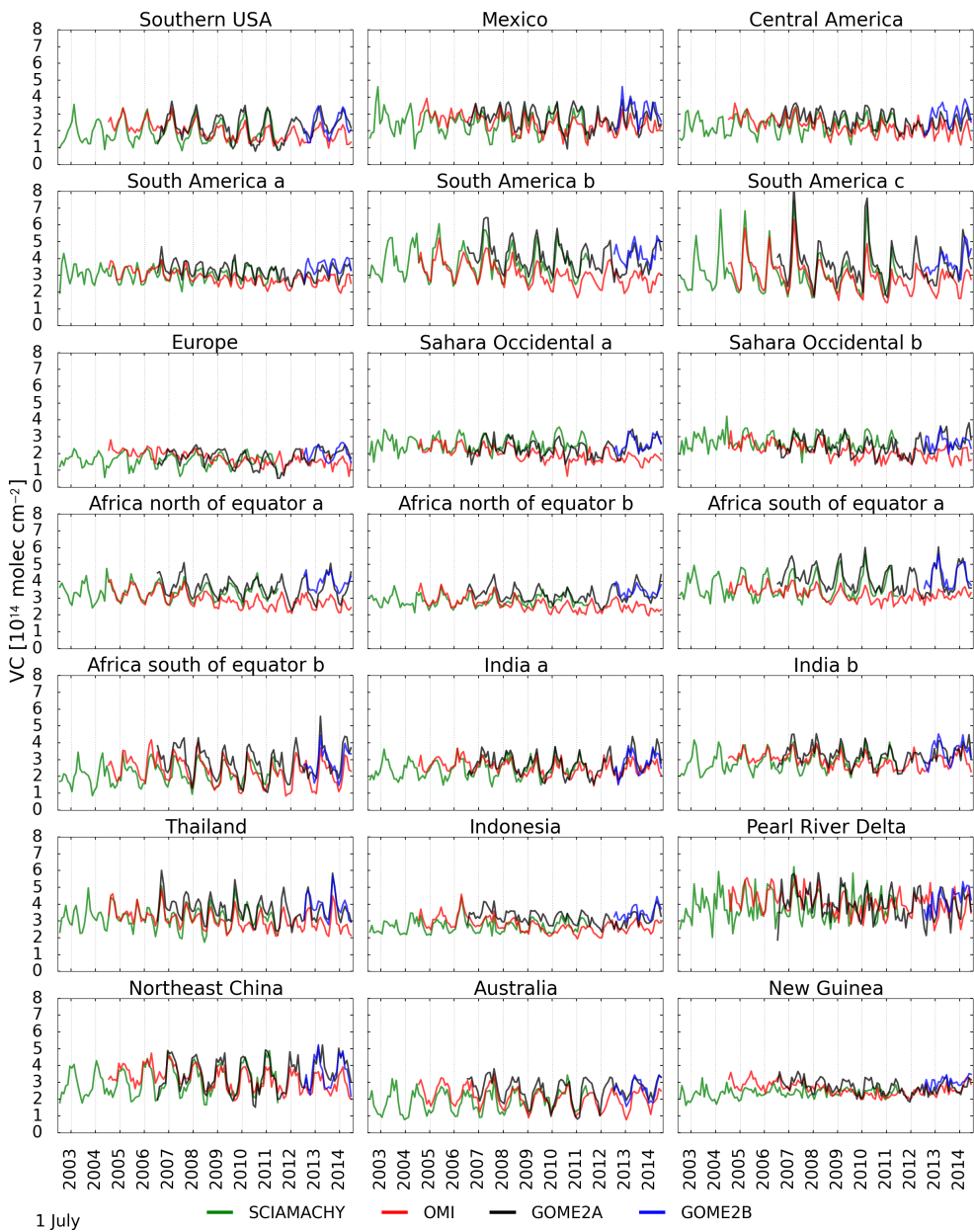


**Figure A.1:** Comparison of monthly averaged CHOCHO VCs from GOME–2B (blue line), GOME–2A (black line), OMI (red line) and SCIAMACHY (green line) data for 21 selected “hot-spots” from different environments during 2003–2014. These regions are the same as defined in Fig. 4.12.

# Bibliography

- Abbot, D. S., Palmer, P. I., Martin, R. V., Chance, K. V., Jacob, D. J., and Guenther, A.: Seasonal and interannual variability of North American isoprene emissions as determined by formaldehyde column measurements from space, *Geophysical Research Letters*, 30, 2003.
- Acarreta, J. R., De Haan, J. F., and Stammes, P.: Cloud pressure retrieval using the O<sub>2</sub>-O<sub>2</sub> absorption band at 477 nm, *Journal of Geophysical Research: Atmospheres*, 109, 2004.
- Alvarado, L. M. A., Richter, A., Vrekoussis, M., Wittrock, F., Hilboll, A., Schreier, S. F., and Burrows, J. P.: An improved glyoxal retrieval from OMI measurements, *Atmos. Meas. Tech.*, 7, 4133–4150, 2014.
- Alvarado, L. M. A., Richter, A., Vrekoussis, M., Wittrock, F., Hilboll, A., Schreier, S. F., and Burrows, J. P.: Investigating the Link Between Glyoxal and Biogenic Activities, in: *Towards an Interdisciplinary Approach in Earth System Science*, edited by Lohmann, G., Meggers, H., Unnithan, V., Wolf-Gladrow, D., Notholt, J., and Bracher, A., Springer Earth System Sciences, pp. 59–65, Springer International Publishing, 2015.
- Alvarado Bonilla, L. M. A.: Determinación de niveles de formaldehído en San Salvador con espectroscopia óptica de absorción diferencial (DOAS), Universidad de El Salvador, San Salvador, 2011.
- Anand, J. S., Monks, P. S., and Leigh, R. J.: An improved retrieval of tropospheric NO<sub>2</sub> from space over polluted regions using an Earth radiance reference, *Atmos. Meas. Tech.*, 8, 1519–1535, 2015.

## BIBLIOGRAPHY

- Andreae, M. O. and Merlet, P.: Emission of trace gases and aerosols from biomass burning, *Global Biogeochemical Cycles*, 15, 955–966, 2001.
- Atkinson, R.: Atmospheric chemistry of VOCs and NO<sub>x</sub>, *Atmospheric Environment*, 34, 2063–2101, 2000.
- Atkinson, R. and Arey, J.: Gas-phase tropospheric chemistry of biogenic volatile organic compounds: a review, *Atmospheric Environment*, 37, Supplement 2, 197–219, 2003.
- ATSDR: Toxicological Profile: Formaldehyde, Technical note, U.S. Department of Health and Human Services, Public Health Service, Atlanta, GA, 1999.
- Barkley, M. P., Palmer, P. I., Kuhn, U., Kesselmeier, J., Chance, K., Kurosu, T. P., Martin, R. V., Helmig, D., and Guenther, A.: Net ecosystem fluxes of isoprene over tropical South America inferred from Global Ozone Monitoring Experiment (GOME) observations of HCHO columns, *Journal of Geophysical Research: Atmospheres*, 113, 2008.
- Bobrowski, N., Hönniger, G., Galle, B., and Platt, U.: Detection of bromine monoxide in a volcanic plume, *Nature*, 423, 273–276, 2003.
- Boeke, N. L., Marshall, J. D., Alvarez, S., Chance, K. V., Fried, A., Kurosu, T. P., Rappenglück, B., Richter, D., Walega, J., Weibring, P., and Millet, D. B.: Formaldehyde columns from the Ozone Monitoring Instrument: Urban versus background levels and evaluation using aircraft data and a global model, *Journal of Geophysical Research*, 116, D05 303, 2011.
- Boersma, K. F., Eskes, H. J., and Brinksma, E. J.: Error analysis for tropospheric NO<sub>2</sub> retrieval from space, *Journal of Geophysical Research: Atmospheres*, 109, 2004.
- Boersma, K. F., Eskes, H. J., Veefkind, J. P., Brinksma, E. J., van der A, R. J., Sneep, M., van den Oord, G. H. J., Levelt, P. F., Stammes, P., Gleason, J. F., and Bucsela, E. J.: Near-real time retrieval of tropospheric NO<sub>2</sub> from OMI, *Atmos. Chem. Phys.*, 7, 2103–2118, 2007.
- Bogumil, K., Orphal, J., Homann, T., Voigt, S., Spietz, P., Fleischmann, O., Vogel, A., Hartmann, M., Kromminga, H., Bovensmann, H., Frerick, J., and Burrows, J.: Measurements of molecular absorption spectra with the SCIA-MACHY pre-flight model: instrument characterization and reference data for

## BIBLIOGRAPHY

- atmospheric remote-sensing in the 230–2380 nm region, *Journal of Photochemistry and Photobiology A: Chemistry*, 157, 167–184, 2003.
- Bovensmann, H., Burrows, J. P., Buchwitz, M., Frerick, J., Noël, S., Rozanov, V. V., Chance, K. V., and Goede, A. P. H.: SCIAMACHY: Mission Objectives and Measurement Modes, *Journal of the Atmospheric Sciences*, 56, 127–150, 1999.
- Brinkmann, R. T.: Rotational Raman Scattering in Planetary Atmospheres, *Astrophysical Journal*, pp. 1087–1093, 1968.
- Brinksma, E. J., Pinardi, G., Volten, H., Braak, R., Richter, A., Schönhardt, A., Roozendael, M. v., Fayt, C., Hermans, C., Dirksen, R. J., Vlemmix, T., Berkhouit, A. J. C., Swart, D. P. J., Oetjen, H., Wittrock, F., Wagner, T., Ibrahim, O. W., Leeuw, G. d., Moerman, M., Curier, R. L., Celarier, E. A., Cede, A., Knap, W. H., Veefkind, J. P., Eskes, H. J., Allaart, M., Rothe, R., Piters, A. J. M., and Levelt, P. F.: The 2005 and 2006 DANDELIONS NO<sub>2</sub> and aerosol intercomparison campaigns, *Journal of Geophysical Research*, 113, D16S46, 2008.
- Burrows, J., Hötzle, E., Goede, A., Visser, H., and Fricke, W.: SCIAMACHY—scanning imaging absorption spectrometer for atmospheric cartography, *Acta Astronautica*, 35, 445–451, 1995.
- Burrows, J. P., Weber, M., Buchwitz, M., Rozanov, V., Ladstätter-Weißenmayer, A., Richter, A., DeBeek, R., Hoogen, R., Bramstedt, K., Eichmann, K.-U., Eisinger, M., and Perner, D.: The Global Ozone Monitoring Experiment (GOME): Mission Concept and First Scientific Results, *Journal of the Atmospheric Sciences*, 56, 151–175, 1999.
- Burrows, J. P., Platt, U., and Borrell, P.: Tropospheric Remote Sensing from Space, in: *The Remote Sensing of Tropospheric Composition from Space*, edited by Burrows, J. P., Borrell, P., Platt, U., Guzzi, R., Platt, U., and Lanzerotti, L. J., *Physics of Earth and Space Environments*, pp. 1–65, Springer Berlin Heidelberg, 2011.
- Callies, J., Corpaccioli, E., Eisinger, M., Hahne, A., and Lefebvre, A.: GOME-2 - Metop's second-generation sensor for operational ozone monitoring, *ESA Bulletin*, 102, 28–36, 2000.

## BIBLIOGRAPHY

- Chan Miller, C., Gonzalez Abad, G., Wang, H., Liu, X., Kurosu, T., Jacob, D. J., and Chance, K.: Glyoxal retrieval from the Ozone Monitoring Instrument, *Atmos. Meas. Tech.*, 7, 3891–3907, 2014.
- Chance, K. and Kurucz, R. L.: An improved high-resolution solar reference spectrum for earth's atmosphere measurements in the ultraviolet, visible, and near infrared, *Journal of Quantitative Spectroscopy and Radiative Transfer*, 111, 1289–1295, 2010.
- Chance, K., Palmer, P. I., Spurr, R. J. D., Martin, R. V., Kurosu, T. P., and Jacob, D. J.: Satellite observations of formaldehyde over North America from GOME, *Geophysical Research Letters*, 27, 3461–3464, 2000.
- Cook, P. A., Savage, N. H., Turquety, S., Carver, G. D., O'Connor, F. M., Heckel, A., Stewart, D., Whalley, L. K., Parker, A. E., Schlager, H., Singh, H. B., Avery, M. A., Sachse, G. W., Brune, W., Richter, A., Burrows, J. P., Purvis, R., Lewis, A. C., Reeves, C. E., Monks, P. S., Levine, J. G., and Pyle, J. A.: Forest fire plumes over the North Atlantic: p-TOMCAT model simulations with aircraft and satellite measurements from the ITOP/ICARTT campaign, *Journal of Geophysical Research: Atmospheres*, 112, 2007.
- Curci, G., Palmer, P. I., Kurosu, T. P., Chance, K., and Visconti, G.: Estimating European volatile organic compound emissions using satellite observations of formaldehyde from the Ozone Monitoring Instrument, *Atmos. Chem. Phys.*, 10, 11 501–11 517, 2010.
- De Smedt, I., Müller, J.-F., Stavrakou, T., van der A, R., Eskes, H., and Van Roozendael, M.: Twelve years of global observations of formaldehyde in the troposphere using GOME and SCIAMACHY sensors, *Atmos. Chem. Phys.*, 8, 4947–4963, 2008.
- De Smedt, I., Stavrakou, T., Hendrick, F., Danckaert, T., Vlemmix, T., Pinardi, G., Theys, N., Lerot, C., Gielen, C., Vigouroux, C., Hermans, C., Fayt, C., Veefkind, P., Müller, J.-F., and Van Roozendael, M.: Diurnal, seasonal and long-term variations of global formaldehyde columns inferred from combined OMI and GOME-2 observations, *Atmos. Chem. Phys. Discuss.*, 15, 12 241–12 300, 2015.
- DiGangi, J. P., Henry, S. B., Kammrath, A., Boyle, E. S., Kaser, L., Schnitzhofer, R., Graus, M., Turnipseed, A., Park, J.-H., Weber, R. J., Hornbrook, R. S.,

## BIBLIOGRAPHY

- Cantrell, C. A., Maudlin III, R. L., Kim, S., Nakashima, Y., Wolfe, G. M., Kajii, Y., Apel, E., Goldstein, A. H., Guenther, A., Karl, T., Hansel, A., and Keutsch, F. N.: Observations of glyoxal and formaldehyde as metrics for the anthropogenic impact on rural photochemistry, *Atmos. Chem. Phys.*, 12, 9529–9543, 2012.
- Dufour, G., Szopa, S., Barkley, M. P., Boone, C. D., Perrin, A., Palmer, P. I., and Bernath, P. F.: Global upper-tropospheric formaldehyde: seasonal cycles observed by the ACE-FTS satellite instrument, *Atmos. Chem. Phys.*, 9, 3893–3910, 2009.
- Duncan, B. N., Yoshida, Y., Olson, J. R., Sillman, S., Martin, R. V., Lamsal, L., Hu, Y., Pickering, K. E., Retscher, C., Allen, D. J., and Crawford, J. H.: Application of OMI observations to a space-based indicator of NO<sub>x</sub> and VOC controls on surface ozone formation, *Atmospheric Environment*, 44, 2213–2223, 2010.
- Elansky, N. F., Mokhov, I. I., Belikov, I. B., Berezina, E. V., Elokhov, A. S., Ivanov, V. A., Pankratova, N. V., Postylyakov, O. V., Safronov, A. N., Skorokhod, A. I., and Shumskii, R. A.: Gaseous admixtures in the atmosphere over Moscow during the 2010 summer, *Izvestiya, Atmospheric and Oceanic Physics*, 47, 672–681, 2011.
- EPA: Environmental Protection Agency – Nitrogen Dioxide (NO<sub>2</sub>).
- Fehsenfeld, F., Calvert, J., Fall, R., Goldan, P., Guenther, A. B., Hewitt, C. N., Lamb, B., Liu, S., Trainer, M., Westberg, H., and Zimmerman, P.: Emissions of volatile organic compounds from vegetation and the implications for atmospheric chemistry, *Global Biogeochemical Cycles*, 6, 389–430, 1992.
- Fleischmann, O. C., Hartmann, M., Burrows, J. P., and Orphal, J.: New ultraviolet absorption cross-sections of BrO at atmospheric temperatures measured by time-windowing Fourier transform spectroscopy, *Journal of Photochemistry and Photobiology A: Chemistry*, 168, 117–132, 2004.
- Fried, A., Lee, Y.-N., Frost, G., Wert, B., Henry, B., Drummond, J. R., Hübner, G., and Jobson, T.: Airborne CH<sub>2</sub>O measurements over the North Atlantic during the 1997 NARE campaign: Instrument comparisons and distributions, *Journal of Geophysical Research*, 107, 4039, 2002.

## BIBLIOGRAPHY

- Fried, A., Cantrell, C., Olson, J., Crawford, J. H., Weibring, P., Walega, J., Richter, D., Junkermann, W., Volkamer, R., Sinreich, R., Heikes, B. G., O'Sullivan, D., Blake, D. R., Blake, N., Meinardi, S., Apel, E., Weinheimer, A., Knapp, D., Perring, A., Cohen, R. C., Fuelberg, H., Shetter, R. E., Hall, S. R., Ullmann, K., Brune, W. H., Mao, J., Ren, X., Huey, L. G., Singh, H. B., Hair, J. W., Riemer, D., Diskin, G., and Sachse, G.: Detailed comparisons of air-borne formaldehyde measurements with box models during the 2006 INTEX-B and MILAGRO campaigns: potential evidence for significant impacts of unmeasured and multi-generation volatile organic carbon compounds, *Atmos. Chem. Phys.*, 11, 11 867–11 894, 2011.
- Fu, T.-M., Jacob, D. J., Palmer, P. I., Chance, K., Wang, Y. X., Barletta, B., Blake, D. R., Stanton, J. C., and Pilling, M. J.: Space-based formaldehyde measurements as constraints on volatile organic compound emissions in east and south Asia and implications for ozone, *Journal of Geophysical Research: Atmospheres*, 112, 2007.
- Fu, T.-M., Jacob, D. J., Wittrock, F., Burrows, J. P., Vrekoussis, M., and Henze, D. K.: Global budgets of atmospheric glyoxal and methylglyoxal, and implications for formation of secondary organic aerosols, *Journal of Geophysical Research: Atmospheres*, 113, 2008.
- González Abad, G., Liu, X., Chance, K., Wang, H., Kurosu, T. P., and Suleiman, R.: Updated Smithsonian Astrophysical Observatory Ozone Monitoring Instrument (SAO OMI) formaldehyde retrieval, *Atmos. Meas. Tech.*, 8, 19–32, 2015.
- Grainger, J. F. and Ring, J.: Anomalous Fraunhofer Line Profiles, *Nature*, 193, 762–762, 1962.
- Guenther, A., Hewitt, C. N., Erickson, D., Fall, R., Geron, C., Graedel, T., Harley, P., Klinger, L., Lerdau, M., McKay, W. A., Pierce, T., Scholes, B., Steinbrecher, R., Tallamraju, R., Taylor, J., and Zimmerman, P.: A global model of natural volatile organic compound emissions, *Journal of Geophysical Research: Atmospheres*, 100, 8873–8892, 1995.
- Guenther, A., Geron, C., Pierce, T., Lamb, B., Harley, P., and Fall, R.: Natural emissions of non-methane volatile organic compounds, carbon monoxide, and oxides of nitrogen from North America, *Atmospheric Environment*, 34, 2205–2230, 2000.

## BIBLIOGRAPHY

- Guenther, A., Karl, T., Harley, P., Wiedinmyer, C., Palmer, P. I., and Geron, C.: Estimates of global terrestrial isoprene emissions using MEGAN (Model of Emissions of Gases and Aerosols from Nature), *Atmos. Chem. Phys.*, 6, 3181–3210, 2006.
- Hak, C., Pundt, I., Trick, S., Kern, C., Platt, U., Dommen, J., Ordóñez, C., Prévôt, A. S. H., Junkermann, W., Astorga-Lloréns, C., Larsen, B. R., Melqvist, J., Strandberg, A., Yu, Y., Galle, B., Kleffmann, J., Lörzer, J. C., Braathen, G. O., and Volkamer, R.: Intercomparison of four different in-situ techniques for ambient formaldehyde measurements in urban air, *Atmos. Chem. Phys.*, 5, 2881–2900, 2005.
- Heckel, A., Richter, A., Tarsu, T., Wittrock, F., Hak, C., Pundt, I., Junkermann, W., and Burrows, J. P.: MAX-DOAS measurements of formaldehyde in the Po-Valley, *Atmos. Chem. Phys.*, 5, 909–918, 2005.
- Hewson, W., Bösch, H., Barkley, M. P., and De Smedt, I.: Characterisation of GOME-2 formaldehyde retrieval sensitivity, *Atmos. Meas. Tech.*, 6, 371–386, 2013.
- Hilboll, A., Richter, A., Rozanov, A., Hodnebrog, O., Heckel, A., Solberg, S., Stordal, F., and Burrows, J. P.: Improvements to the retrieval of tropospheric NO<sub>2</sub> from satellite – stratospheric correction using SCIAMACHY limb/nadir matching and comparison to Oslo CTM2 simulations, *Atmos. Meas. Tech.*, 6, 565–584, 2013.
- Houweling, S., Dentener, F., and Lelieveld, J.: The impact of nonmethane hydrocarbon compounds on tropospheric photochemistry, *Journal of Geophysical Research: Atmospheres*, 103, 10 673–10 696, 1998.
- Hönninger, G., von Friedeburg, C., and Platt, U.: Multi axis differential optical absorption spectroscopy (MAX-DOAS), *Atmos. Chem. Phys.*, 4, 231–254, 2004.
- Irie, H., Takashima, H., Kanaya, Y., Boersma, K. F., Gast, L., Wittrock, F., Brunner, D., Zhou, Y., and Van Roozendael, M.: Eight-component retrievals from ground-based MAX-DOAS observations, *Atmospheric Measurement Techniques*, 4, 1027–1044, 2011.
- Jacob, D. J.: Heterogeneous chemistry and tropospheric ozone, *Atmospheric Environment*, 34, 2131–2159, 2000.

## BIBLIOGRAPHY

- Jiang, Z., Huete, A. R., Didan, K., and Miura, T.: Development of a two-band enhanced vegetation index without a blue band, *Remote Sensing of Environment*, 112, 3833–3845, 2008.
- Justice, C., Giglio, L., Korontzi, S., Owens, J., Morisette, J., Roy, D., Descloitres, J., Alleaume, S., Petitcolin, F., and Kaufman, Y.: The MODIS fire products, *Remote Sensing of Environment*, 83, 244–262, 2002.
- Kaiser, J., Wolfe, G. M., Min, K. E., Brown, S. S., Miller, C. C., Jacob, D. J., deGouw, J. A., Graus, M., Hanisco, T. F., Holloway, J., Peischl, J., Pollack, I. B., Ryerson, T. B., Warneke, C., Washenfelder, R. A., and Keutsch, F. N.: Reassessing the ratio of glyoxal to formaldehyde as an indicator of hydrocarbon precursor speciation, *Atmos. Chem. Phys.*, 15, 7571–7583, 2015.
- Kaiser, J. W., Heil, A., Andreae, M. O., Benedetti, A., Chubarova, N., Jones, L., Morcrette, J.-J., Razinger, M., Schultz, M. G., Suttie, M., and van der Werf, G. R.: Biomass burning emissions estimated with a global fire assimilation system based on observed fire radiative power, *Biogeosciences*, 9, 527–554, 2012.
- Kampa, M. and Castanas, E.: Human health effects of air pollution, *Environmental Pollution*, 151, 362–367, 2008.
- Kansal, A.: Sources and reactivity of NMHCs and VOCs in the atmosphere: A review, *Journal of Hazardous Materials*, 166, 17–26, 2009.
- Konovalov, I. B., Beekmann, M., Kuznetsova, I. N., Yurova, A., and Zvyagintsev, A. M.: Atmospheric impacts of the 2010 Russian wildfires: integrating modelling and measurements of an extreme air pollution episode in the Moscow region, *Atmos. Chem. Phys.*, 11, 10 031–10 056, 2011.
- Koppmann, R.: *Volatile Organic Compounds in the Atmosphere*, Blackwell Publishing Ltd, 2007.
- Krijger, J. M., van Weele, M., Aben, I., and Frey, R.: Technical Note: The effect of sensor resolution on the number of cloud-free observations from space, *Atmos. Chem. Phys.*, 7, 2881–2891, 2007.
- Kurosu, T. P., Chance, K., Liu, X., Volkamer, R., Fu, T.-M., Millet, D., and Jacob, D. J.: Seasonally resolved global distributions of glyoxal and formaldehyde

## BIBLIOGRAPHY

- observed from the Ozone Monitoring Instrument on EOS Aura, in: Proceeding of Anais XIII Simpósio Brasileiro de Sensoriamento Remoto, 2007.
- Ladstätter-Weißenmayer, A., Heland, J., Kormann, R., von Kuhlmann, R., Lawrence, M. G., Meyer-Arnek, J., Richter, A., Wittrock, F., Ziereis, H., and Burrows, J. P.: Transport and build-up of tropospheric trace gases during the MINOS campaign: comparision of GOME, in situ aircraft measurements and MATCH-MPIC-data, *Atmos. Chem. Phys.*, 3, 1887–1902, 2003.
- Lerot, C., Stavrakou, T., De Smedt, I., Müller, J.-F., and Van Roozendael, M.: Glyoxal vertical columns from GOME-2 backscattered light measurements and comparisons with a global model, *Atmos. Chem. Phys.*, 10, 12 059–12 072, 2010.
- Levelt, P., van den Oord, G., Dobber, M., Malkki, A., Visser, H., Vries, J. d., Stammes, P., Lundell, J., and Saari, H.: The ozone monitoring instrument, *IEEE Transactions on Geoscience and Remote Sensing*, 44, 1093 – 1101, 2006.
- Li, X., Brauers, T., Shao, M., Garland, R. M., Wagner, T., Deutschmann, T., and Wahner, A.: MAX-DOAS measurements in southern China: retrieval of aerosol extinctions and validation using ground-based in-situ data, *Atmos. Chem. Phys.*, 10, 2079–2089, 2010.
- Li, X., Brauers, T., Hofzumahaus, A., Lu, K., Li, Y. P., Shao, M., Wagner, T., and Wahner, A.: MAX-DOAS measurements of NO<sub>2</sub>, HCHO and CHOCHO at a rural site in Southern China, *Atmos. Chem. Phys.*, 13, 2133–2151, 2013.
- Liu, Z., Wang, Y., Vrekoussis, M., Richter, A., Wittrock, F., Burrows, J. P., Shao, M., Chang, C.-C., Liu, S.-C., Wang, H., and Chen, C.: Exploring the missing source of glyoxal (CHOCHO) over China, *Geophysical Research Letters*, 39, 2012.
- MacDonald, S. M., Oetjen, H., Mahajan, A. S., Whalley, L. K., Edwards, P. M., Heard, D. E., Jones, C. E., and Plane, J. M. C.: DOAS measurements of formaldehyde and glyoxal above a south-east Asian tropical rainforest, *Atmos. Chem. Phys.*, 12, 5949–5962, 2012.
- Martin, R. V.: Satellite remote sensing of surface air quality, *Atmospheric Environment*, 42, 7823–7843, 2008.

## BIBLIOGRAPHY

- Martin, R. V., Fiore, A. M., and Van Donkelaar, A.: Space-based diagnosis of surface ozone sensitivity to anthropogenic emissions, *Geophysical Research Letters*, 31, 2004a.
- Martin, R. V., Parrish, D. D., Ryerson, T. B., Jr, D. K. N., Chance, K., Kurosu, T. P., Jacob, D. J., Sturges, E. D., Fried, A., and Wert, B. P.: Evaluation of GOME satellite measurements of tropospheric NO<sub>2</sub> and HCHO using regional data from aircraft campaigns in the southeastern United States, *Journal of Geophysical Research*, 109, D24307, 2004b.
- Meller, R. and Moortgat, G. K.: Temperature dependence of the absorption cross sections of formaldehyde between 223 and 323 K in the wavelength range 225–375 nm, *Journal of Geophysical Research: Atmospheres*, 105, 7089–7101, 2000.
- Millet, D. B., Jacob, D. J., Boersma, K. F., Fu, T.-M., Kurosu, T. P., Chance, K., Heald, C. L., and Guenther, A.: Spatial distribution of isoprene emissions from North America derived from formaldehyde column measurements by the OMI satellite sensor, *Journal of Geophysical Research: Atmospheres*, 113, 2008.
- Myrokefalitakis, S., Vrekoussis, M., Tsigaridis, K., Wittrock, F., Richter, A., Brühl, C., Volkamer, R., Burrows, J. P., and Kanakidou, M.: The influence of natural and anthropogenic secondary sources on the glyoxal global distribution, *Atmos. Chem. Phys.*, 8, 4965–4981, 2008.
- Nicolet, M.: On the molecular scattering in the terrestrial atmosphere : An empirical formula for its calculation in the homosphere, *Planetary and Space Science*, 32, 1467–1468, 1984.
- Ortega, I., Koenig, T., Sinreich, R., Thomson, D., and Volkamer, R.: The CU 2-D-MAX-DOAS instrument – Part 1: Retrieval of 3-D distributions of NO<sub>2</sub> and azimuth-dependent OVOC ratios, *Atmos. Meas. Tech.*, 8, 2371–2395, 2015.
- Palmer, P. I., Jacob, D. J., Chance, K., Martin, R. V., Spurr, R. J. D., Kurosu, T. P., Bey, I., Yantosca, R., Fiore, A., and Li, Q.: Air mass factor formulation for spectroscopic measurements from satellites: Application to formaldehyde retrievals from the Global Ozone Monitoring Experiment, *Journal of Geophysical Research: Atmospheres*, 106, 14 539–14 550, 2001.
- Parshutkina, I. P., Sosnikova, E. V., Grishina, N. P., Stulov, E. A., Plaude, N. O., and Monakhova, N. A.: Atmospheric aerosol characterization in 2010

## BIBLIOGRAPHY

- anomalous summer season in the Moscow region, Russian Meteorology and Hydrology, 36, 355–361, 2011.
- Peters, E., Wittrock, F., Großmann, K., Frieß, U., Richter, A., and Burrows, J. P.: Formaldehyde and nitrogen dioxide over the remote western Pacific Ocean: SCIAMACHY and GOME-2 validation using ship-based MAX-DOAS observations, *Atmos. Chem. Phys.*, 12, 11 179–11 197, 2012.
- Peters, E., Wittrock, F., Richter, A., Alvarado, L. M. A., Rozanov, V. V., and Burrows, J. P.: Liquid water absorption and scattering effects in DOAS retrievals over oceans, *Atmos. Meas. Tech. Discuss.*, 7, 5027–5073, 2014.
- Pikelnaya, O., Hurlock, S. C., Trick, S., and Stutz, J.: Intercomparison of multi-axis and long-path differential optical absorption spectroscopy measurements in the marine boundary layer, *Journal of Geophysical Research*, 112, D10S01, 2007.
- Pinardi, G., Van Roozendael, M., Abuhassan, N., Adams, C., Cede, A., Clémer, K., Fayt, C., Frieß, U., Gil, M., Herman, J., Hermans, C., Hendrick, F., Irie, H., Merlaud, A., Navarro Comas, M., Peters, E., Piters, A. J. M., Puente-dura, O., Richter, A., Schönhardt, A., Shaiganfar, R., Spinei, E., Strong, K., Takashima, H., Vrekoussis, M., Wagner, T., Wittrock, F., and Yilmaz, S.: MAX-DOAS formaldehyde slant column measurements during CINDI: intercomparison and analysis improvement, *Atmospheric Measurement Techniques Discussions*, 5, 6679–6732, 2012.
- Pinardi, G., Van Roozendael, M., Abuhassan, N., Adams, C., Cede, A., Clémer, K., Fayt, C., Frieß, U., Gil, M., Herman, J., Hermans, C., Hendrick, F., Irie, H., Merlaud, A., Navarro Comas, M., Peters, E., Piters, A. J. M., Puente-dura, O., Richter, A., Schönhardt, A., Shaiganfar, R., Spinei, E., Strong, K., Takashima, H., Vrekoussis, M., Wagner, T., Wittrock, F., and Yilmaz, S.: MAX-DOAS formaldehyde slant column measurements during CINDI: intercomparison and analysis improvement, *Atmospheric Measurement Techniques*, 6, 167–185, 2013.
- Platt, U. and Stutz, J.: Differential Optical Absorption Spectroscopy: Principles and Applications, Springer, 2008.
- R'Honi, Y., Clarisse, L., Clerbaux, C., Hurtmans, D., Duflot, V., Turquety, S.,

## BIBLIOGRAPHY

- Ngadi, Y., and Coheur, P.-F.: Exceptional emissions of NH<sub>3</sub> and HCOOH in the 2010 Russian wildfires, *Atmos. Chem. Phys.*, 13, 4171–4181, 2013.
- Richter, A.: Absorptionsspektroskopische Messungen stratosphärischer Spuren-gase über Bremen, 53° N, Ph.D. thesis, University of Bremen, 1997.
- Richter, A., Burrows, J. P., Nüß, H., Granier, C., and Niemeier, U.: Increase in tropospheric nitrogen dioxide over China observed from space, *Nature*, 437, 129–132, 2005.
- Richter, A., Begoin, M., Hilboll, A., and Burrows, J. P.: An improved NO<sub>2</sub> retrieval for the GOME-2 satellite instrument, *Atmos. Meas. Tech.*, 4, 1147–1159, 2011.
- Rolph, G.D., G. R.: READY - Real-time Environmental Applications and Dis-play sYstem.
- Rothman, L., Jacquemart, D., Barbe, A., Chris Benner, D., Birk, M., Brown, L., Carleer, M., Chackerian Jr., C., Chance, K., Coudert, L., Dana, V., Devi, V., Flaud, J.-M., Gamache, R., Goldman, A., Hartmann, J.-M., Jucks, K., Maki, A., Mandin, J.-Y., Massie, S., Orphal, J., Perrin, A., Rinsland, C., Smith, M., Tennyson, J., Tolchenov, R., Toth, R., Vander Auwera, J., Varanasi, P., and Wagner, G.: The HITRAN 2004 molecular spectroscopic database, *Journal of Quantitative Spectroscopy and Radiative Transfer*, 96, 139–204, 2005.
- Rothman, L., Gordon, I., Barbe, A., Benner, D., Bernath, P., Birk, M., Boudon, V., Brown, L., Campargue, A., Champion, J.-P., Chance, K., Coudert, L., Dana, V., Devi, V., Fally, S., Flaud, J.-M., Gamache, R., Goldman, A., Jacquemart, D., Kleiner, I., Lacome, N., Lafferty, W., Mandin, J.-Y., Massie, S., Mikhailenko, S., Miller, C., Moazzen-Ahmadi, N., Naumenko, O., Nikitin, A., Orphal, J., Perevalov, V., Perrin, A., Predoi-Cross, A., Rinsland, C., Rotger, M., Šimečková, M., Smith, M., Sung, K., Tashkun, S., Tennyson, J., Toth, R., Vandaele, A., and Vander Auwera, J.: The HITRAN 2008 molecular spectroscopic database, *Journal of Quantitative Spectroscopy and Radiative Transfer*, 110, 533–572, 2009.
- Rothman, L., Gordon, I., Barber, R., Dothe, H., Gamache, R., Goldman, A., Perevalov, V., Tashkun, S., and Tennyson, J.: HITEMP, the high-temperature molecular spectroscopic database, *Journal of Quantitative Spectroscopy and Radiative Transfer*, 111, 2139–2150, 2010.

## BIBLIOGRAPHY

- Rothman, L. S., Gordon, I. E., Babikov, Y., Barbe, A., Chris Benner, D., Bernath, P. F., Birk, M., Bizzocchi, L., Boudon, V., Brown, L. R., Campargue, A., Chance, K., Cohen, E. A., Coudert, L. H., Devi, V. M., Drouin, B. J., Fayt, A., Flaud, J. M., Gamache, R. R., Harrison, J. J., Hartmann, J. M., Hill, C., Hodges, J. T., Jacquemart, D., Jolly, A., Lamouroux, J., Le Roy, R. J., Li, G., Long, D. A., Lyulin, O. M., Mackie, C. J., Massie, S. T., Mikhailenko, S., Müller, H. S. P., Naumenko, O. V., Nikitin, A. V., Orphal, J., Perevalov, V., Perrin, A., Polovtseva, E. R., Richard, C., Smith, M. A. H., Starikova, E., Sung, K., Tashkun, S., Tennyson, J., Toon, G. C., Tyuterev, V. G., and Wagner, G.: The HITRAN2012 molecular spectroscopic database, *Journal of Quantitative Spectroscopy and Radiative Transfer*, 130, 4–50, 2013.
- Rozanov, V., Rozanov, A., Kokhanovsky, A., and Burrows, J.: Radiative transfer through terrestrial atmosphere and ocean: Software package SCIATRAN, *Journal of Quantitative Spectroscopy and Radiative Transfer*, 2013.
- Schreier, S. F., Richter, A., Kaiser, J. W., and Burrows, J. P.: The empirical relationship between satellite-derived tropospheric NO<sub>2</sub> and fire radiative power and possible implications for fire emission rates of NO<sub>x</sub>, *Atmos. Chem. Phys.*, 14, 2447–2466, 2014.
- Schönhardt, A.: DOAS measurements of iodine monoxide from satellite, Ph.D. thesis, University of Bremen, 2009.
- Schönhardt, A., Richter, A., Wittrock, F., Kirk, H., Oetjen, H., Roscoe, H. K., and Burrows, J. P.: Observations of iodine monoxide columns from satellite, *Atmos. Chem. Phys.*, 8, 637–653, 2008.
- Seinfeld, J. H. and Pandis, S. N.: *Atmospheric Chemistry and Physics: From Air Pollution to Climate Change*, Wiley-Interscience, Hoboken, N.J, 2nd edn., 2006.
- Setokuchi, O.: Trajectory calculations of OH radical- and Cl atom-initiated reaction of glyoxal: atmospheric chemistry of the HC(O)CO radical, *Physical Chemistry Chemical Physics*, 13, 6296–6304, 2011.
- Shvidenko, A. Z., Shchepashchenko, D. G., Vaganov, E. A., Sukhinin, A. I., Maksyutov, S. S., McCallum, I., and Lakyda, I. P.: Impact of wildfire in Russia between 1998–2010 on ecosystems and the global carbon budget, *Doklady Earth Sciences*, 441, 1678–1682, 2011.

## BIBLIOGRAPHY

- Sinreich, R., Volkamer, R., Filsinger, F., Friess, U., Kern, C., Platt, U., Sebastian, O., and Wagner, T.: MAX-DOAS detection of glyoxal during ICARTT 2004, *Atmos. Chem. Phys.*, 7, 1293–1303, 2007.
- Sinreich, R., Coburn, S., Dix, B., and Volkamer, R.: Ship-based detection of glyoxal over the remote tropical Pacific Ocean, *Atmos. Chem. Phys.*, 10, 11359–11371, 2010.
- Snow, M., Weber, M., Machol, J., Viereck, R., and Richard, E.: Comparison of Magnesium II core-to-wing ratio observations during solar minimum 23/24, *Journal of Space Weather and Space Climate*, 4, A04, 2014.
- Stavrakou, T., Müller, J.-F., De Smedt, I., Van Roozendael, M., Kanakidou, M., Vrekoussis, M., Wittrock, F., Richter, A., and Burrows, J. P.: The continental source of glyoxal estimated by the synergistic use of spaceborne measurements and inverse modelling, *Atmos. Chem. Phys.*, 9, 8431–8446, 2009a.
- Stavrakou, T., Müller, J.-F., De Smedt, I., Van Roozendael, M., van der Werf, G. R., Giglio, L., and Guenther, A.: Evaluating the performance of pyrogenic and biogenic emission inventories against one decade of space-based formaldehyde columns, *Atmos. Chem. Phys.*, 9, 1037–1060, 2009b.
- Stein, A. F., Draxler, R. R., Rolph, G. D., Stunder, B. J. B., Cohen, M. D., and Ngan, F.: NOAA's HYSPLIT Atmospheric Transport and Dispersion Modeling System, *Bulletin of the American Meteorological Society*, 96, 2059–2077, 2015.
- Tadić, J., Moortgat, G. K., and Wirtz, K.: Photolysis of glyoxal in air, *Journal of Photochemistry and Photobiology A: Chemistry*, 177, 116–124, 2006.
- Thalman, R. and Volkamer, R.: Temperature dependent absorption cross-sections of O<sub>2</sub>–O<sub>2</sub> collision pairs between 340 and 630 nm and at atmospherically relevant pressure, *Physical Chemistry Chemical Physics*, 15, 15371–15381, 2013.
- Thomas, W., Hegels, E., Slijkhuis, S., Spurr, R., and Chance, K.: Detection of biomass burning combustion products in Southeast Asia from backscatter data taken by the GOME Spectrometer, *Geophysical Research Letters*, 25, 1317–1320, 1998.

## BIBLIOGRAPHY

- USGCRP: Strategic Plan of the U.S. Climate Change Science Program, Tech. rep., U.S. Global Change Research Program, Washington, DC, USA, 2003.
- van Donkelaar, A., Martin, R. V., Levy, R. C., da Silva, A. M., Krzyzanowski, M., Chubarova, N. E., Semutnikova, E., and Cohen, A. J.: Satellite-based estimates of ground-level fine particulate matter during extreme events: A case study of the Moscow fires in 2010, *Atmospheric Environment*, 45, 6225–6232, 2011.
- Vandaele, A., Hermans, C., Simon, P., Carleer, M., Colin, R., Fally, S., Mérienne, M., Jenouvrier, A., and Coquart, B.: Measurements of the NO<sub>2</sub> absorption cross-section from 42000 cm<sup>-1</sup> to 10000 cm<sup>-1</sup> (238–1000 nm) at 220 K and 294 K, *Journal of Quantitative Spectroscopy and Radiative Transfer*, 59, 171–184, 1998.
- Vigouroux, C., Hendrick, F., Stavrakou, T., Dils, B., De Smedt, I., Hermans, C., Merlaud, A., Scolas, F., Senten, C., Vanhaelewijn, G., Fally, S., Carleer, M., Metzger, J.-M., Müller, J.-F., Van Roozendael, M., and De Mazière, M.: Ground-based FTIR and MAX-DOAS observations of formaldehyde at Réunion Island and comparisons with satellite and model data, *Atmos. Chem. Phys.*, 9, 9523–9544, 2009.
- Vlemmix, T., Piters, A. J. M., Stammes, P., Wang, P., and Levelt, P. F.: Retrieval of tropospheric NO<sub>2</sub> using the MAX-DOAS method combined with relative intensity measurements for aerosol correction, *Atmos. Meas. Tech.*, 3, 1287–1305, 2010.
- Vogel, L., Sihler, H., Lampel, J., Wagner, T., and Platt, U.: Retrieval interval mapping: a tool to visualize the impact of the spectral retrieval range on differential optical absorption spectroscopy evaluations, *Atmos. Meas. Tech.*, 6, 275–299, 2013.
- Volkamer, R., Molina, L. T., Molina, M. J., Shirley, T., and Brune, W. H.: DOAS measurement of glyoxal as an indicator for fast VOC chemistry in urban air, *Geophysical Research Letters*, 32, 2005a.
- Volkamer, R., Spietz, P., Burrows, J., and Platt, U.: High-resolution absorption cross-section of glyoxal in the UV–vis and IR spectral ranges, *Journal of Photochemistry and Photobiology A: Chemistry*, 172, 35–46, 2005b.

## BIBLIOGRAPHY

- Volkamer, R., San Martini, F., Molina, L. T., Salcedo, D., Jimenez, J. L., and Molina, M. J.: A missing sink for gas-phase glyoxal in Mexico City: Formation of secondary organic aerosol, *Geophysical Research Letters*, 34, 2007.
- Vountas, M., Rozanov, V., and Burrows, J.: Ring effect: Impact of rotational Raman scattering on radiative transfer in earth's atmosphere, *Journal of Quantitative Spectroscopy and Radiative Transfer*, 60, 943–961, 1998.
- Vrekoussis, M., Wittrock, F., Richter, A., and Burrows, J. P.: Temporal and spatial variability of glyoxal as observed from space, *Atmos. Chem. Phys.*, 9, 4485–4504, 2009.
- Vrekoussis, M., Wittrock, F., Richter, A., and Burrows, J. P.: GOME-2 observations of oxygenated VOCs: what can we learn from the ratio glyoxal to formaldehyde on a global scale?, *Atmos. Chem. Phys.*, 10, 10 145–10 160, 2010.
- Wagner, T., Dix, B., Friedeburg, C. v., Frieß, U., Sanghavi, S., Sinreich, R., and Platt, U.: MAX-DOAS O<sub>4</sub> measurements: A new technique to derive information on atmospheric aerosols—Principles and information content, *Journal of Geophysical Research*, 109, D22 205, 2004.
- Wagner, T., Beirle, S., Brauers, T., Deutschmann, T., Frieß, U., Hak, C., Halla, J. D., Heue, K. P., Junkermann, W., Li, X., Platt, U., and Pundt-Gruber, I.: Inversion of tropospheric profiles of aerosol extinction and HCHO and NO<sub>2</sub> mixing ratios from MAX-DOAS observations in Milano during the summer of 2003 and comparison with independent data sets, *Atmos. Meas. Tech.*, 4, 2685–2715, 2011.
- Wallace, J. M. and Hobbs, P. V.: *Atmospheric Science: an introductory survey*, vol. 92 of *International Geophysics Series*, Academic Press, 2nd edn., 2006.
- Wang, P., Stammes, P., van der A, R., Pinardi, G., and van Roozendael, M.: FRESCO+: an improved O<sub>2</sub> A-band cloud retrieval algorithm for tropospheric trace gas retrievals, *Atmos. Chem. Phys.*, 8, 6565–6576, 2008.
- Williams, J.: Organic Trace Gases in the Atmosphere: An Overview, *Environmental Chemistry*, 1, 125–136, 2004.
- Wittrock, F.: The retrieval of oxygenated volatile organic compounds by remote sensing techniques, Ph.D. thesis, University of Bremen, 2006.